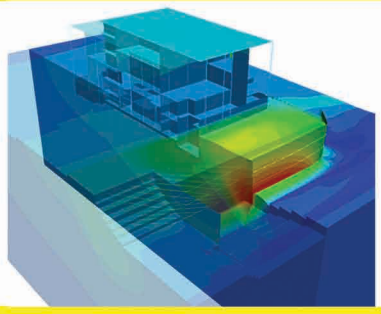
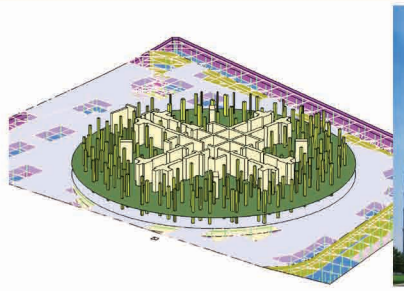

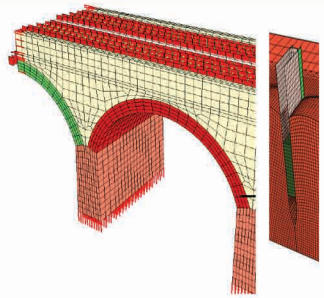
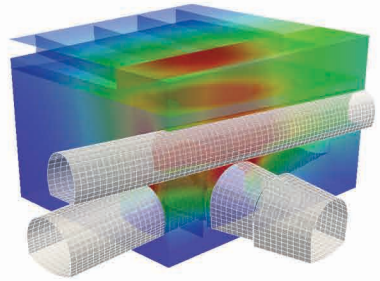
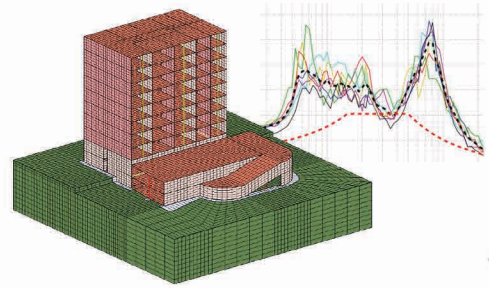
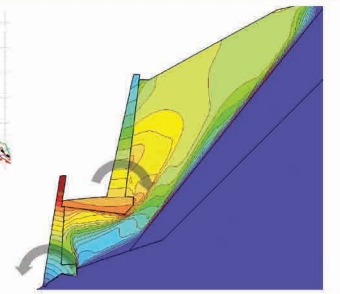

NUMERICS IN GEOTECHNICS AND STRUCTURES 2015

Edited by
Th. Zimmermann
A.Truty
K. Podleś

ROSSOLIS & ZACE

NUMERICS IN GEOTECHNICS AND STRUCTURES

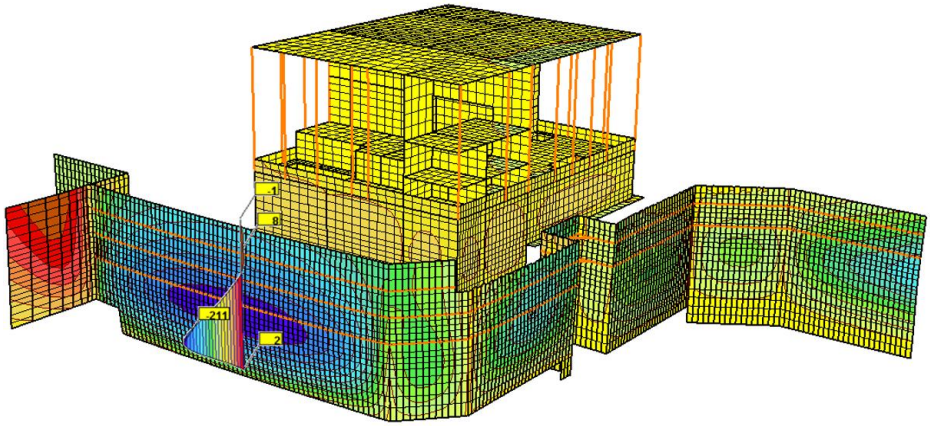

1985-2015, 30 years Z_SOIL®.PC

NUMERICS IN GEOTECHNICS AND STRUCTURES 2015

Edited by
Thomas Zimmermann
Andrzej Truty
Krzysztof Podleś

The texts of the various papers in this volume were set individually by typists under the supervision of each of the authors concerned.

PUBLISHER:
Rossolis Editions & Zace Services Ltd., Switzerland

ISBN 9 782940 365982

PRINTED IN POLAND

Preface

This book reunites a selection of contributions presented at the yearly meeting on “NUMERICS IN GEOTECHNICS & STRUCTURES”, which took place on the 28th of August 2015 at the Swiss Federal Institute of Technology, in Lausanne. 2015 marks the 30th anniversary of ZSOIL.PC, which came out in early 1985 after three years of intensive development at Zace Services Ltd, in Switzerland.

The initial software development started in 1982, under supervision of Thomas Zimmermann, following inspiring discussions about the need for such a tool with F.Vuilleumier (BG ingénieurs conseils SA) and B. Saugy (EPFL). A number of people joined the development team in the following years, and collaborations with the Swiss Federal Institute of Technology and several major engineering companies led to the software available today, which includes fully coupled two-phase media, partial saturation, thermal and humidity diffusion, full 3D capabilities, including structures, and dynamic analysis.

The present Version 2016, developed under supervision of A. Truty and Th. Zimmermann, and orchestrated by K. Podleś is now available, it introduces general dynamic capabilities, novel constitutive models, and full support of 64bits OS systems with a significant increase of speed and maximum problem size.

With over two thousand installations active worldwide in daily practice and in Universities and thousands of real-world cases studied, some of them illustrated in this book, ZSOIL.PC has become one of the most powerful tools available for the modern civil engineer.

Acknowledgements:

ZSOIL would not exist today in its present form without the contributions to the development of the following individuals: C. Rodriguez, B. Dendrou, B. Rebora, F. Delaraye , J. Diaz, M. Howe, E. Seker, E. Davalle, P.Droz, A.Urbanski, K.Podles, L.Vernier, W. Farra, B. Radic, S. Commend, A. Barry, Y. Li, A. Wroblewski, W. Atamaz-Sibai, Ph. Menétrey, A. Wiktor, B. Rutscho, D. Alvarez, R. Obrzud, M. Preisig.

The contributions to the validation of ZSOIL.PC by the following individuals are also acknowledged: U. Ekdahl, J.-L. Sarf, L. Labiouse, R. Gaerber, M. Kharchafi, A. Bisetti, J. L'Eplattenier, D. Tendon, F. Pellet, D. Collomb, S. Domon, C. Marzer, G. Roelfstra, C. Gindroz, M. Favre, P. Mayu, X. Marche, C. Carron, A. Mellal, F. Geiser, S. Kivell.

Financial and technical support by the following engineering companies is acknowledged: BG Ingénieurs Conseils, GEOS Ingénieurs Conseils SA, Genève, GVH Ingénieurs Civils EPF-SIA, INTRON SME, SRP AG, Brig, Stucky SA, Renens, Emch+Berger Holding AG, Bern.

Scientific support of the following laboratories of the Swiss Federal Institute of Technology is acknowledged: the Laboratory of Structural and Continuum Mechanics (Profs. F. Frey & Th. Zimmermann), the Laboratory of Rock Mechanics (Prof. F. Descoeudres) and the Laboratory of Soil Mechanics (Profs. L. Vulliet & L. Laloui).

Financial support of the Swiss Commission for Technology and Innovation (CTI) under grants 2672.1, 2387.1 and 2995.1, for version 4, and grant 4182.1, for version 6, is acknowledged.

Advice on finite element methodologies provided by T.J.R. Hughes (ICES, Austin TX) since the early days has often been crucial, his advices are gratefully acknowledged. The many inspiring discussions with J.P. Wolf (EPFL) throughout the years, with J-H. Prevost (Princeton Univ.) at the early stage of the project, and the fruitful collaborations with W. Ammann (GRF Davos), P. Roelfstra, E. Spacone (University "G.D'Annunzio" of Chieti-Pescara), D. Eyheramendy (Ecole Centrale de Marseille), and S. Yufin (Moscow State University of Civil Engineering) are also gratefully acknowledged.

Lausanne, August.2015

Thomas Zimmermann, Lausanne
Andrzej Truty, Cracow
Krzysztof Podleś, Cracow

NUMERICS IN GEOTECHNICS & STRUCTURES 2015

Preface

Modified Lee-Fenves plastic-damage model for concrete **1**
A. Truty, Th. Zimmermann

An orthotropic elasto-plasticdamage model of masonry. Implementation as ZSoil user model **25**
A. Urbański, F. Pachla, K. Wartak-Dobosz

Examples of large-scale simulations of soil-structure interaction with ZSoil **43**
R. Obrzud, K.Podleś

Computational Strategies for Retaining Structures in Steep Slopes **75**
J.M. Hohberg

Tackling liquefaction problems with ZSOIL **93**
S. Commend, S. Kivell

Dynamic time-history analyses **115**
M. Preisig

Fully coupled flow-deformation analysis on the impact of the dewatering confined water to the surrounding environment **129**
Yin Ji, Wu Jun, Guan Fei

Settlement prediction of super high-rise building based on the soil-foundation-superstructure interaction analysis **145**
Yin Ji, Xie Dongwu, Lu Zhinai

Steel Fiber Reinforced Concrete Beams and Slabs – a case record **159**
U. Ekdahl

Non-Linear Force-Deflection Application on the Existing Underground Train Station of Berne **177**
Ch. Berger

Modified Lee-Fenves plastic-damage model for concrete

Andrzej Truty*, Thomas Zimmermann**

**Cracow University of Technology, Poland*
Zace Services Ltd, Lausanne, Switzerland
*** Zace Services Ltd, Lausanne, Switzerland*

Keywords: Concrete, damage, plasticity.

Abstract

The presentation of a modified Lee-Fenves plastic-damage model for concrete [7][6] is the goal of this article. Major modifications of the model concern form of plastic flow potential, following the work by Omidi and Lotfi [11], variable dilatancy and modified yield condition, introduced to improve stress-strain characteristics generated in the tension-compression domain of the strength envelope. This model couples single surface elastoplasticity with hardening and an enhanced scalar damage allowing for description of stiffness degradation and corresponding stiffness recovery in cyclic tension-compression tests. The model is verified on a set of laboratory tests and on boundary value problems.

1. Introduction

In classical elastoplasticity with linear elastic kernel, used to model irreversible part of deformation, the relation between stress and strain state can be described in the following total form

$$\boldsymbol{\sigma} = \mathbf{E} : \left(\boldsymbol{\varepsilon} - \boldsymbol{\varepsilon}^{p} \right) \tag{1}$$

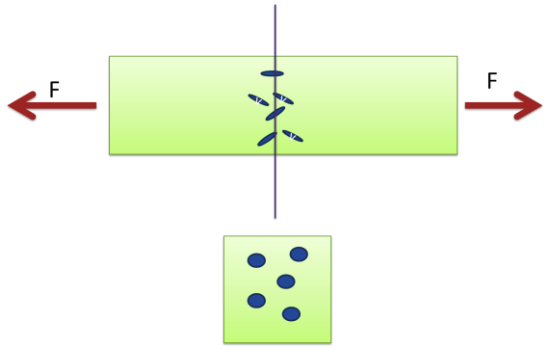

Figure 1: Damaged configuration (voids are represented by dark dots)

The lack of elastic stiffness degradation and lack of stiffness recovery in cyclic tension-compression tests is the major drawback of such elastic-plastic models. To remedy this important drawbacks several researchers worked out coupled damage-plasticity models. One of the simplest models, in which two independent damage variables are used, one for tensile and one for compressive damage, was proposed by Lee and Fenves [7],[6]. Their model, called from now on the reference model, uses several elements of the Barcelona model, developed earlier by Lubliner et al. [8] and then by Oller et al. [10]. Additional contributions to the subject were published by Krätzig and Pölling [4], Grassl and Jirásek [1], [2] and Omidi and Lotfi [11].

Contrary to classical elastoplasticity, continuum damage theory uses two stress configurations ie.: the nominal and the effective one (see Fig.1). This distinction is justified by the presence of voids (due to microcracks) and therefore one may consider the effective cross section (area of voids in the cross section is subtracted) and the nominal one (with full cross section). If we consider a 1D tensile test then the corresponding nominal and effective axial stress component can be defined as follows

$$\sigma = \frac{F}{A_o} \tag{2}$$

$$\sigma = \frac{F}{A_o - A_{voids}} \tag{3}$$

In order to generalize this concept to 2D/3D problems the following mapping rule from nominal to the effective stress configuration is used

$$\boldsymbol{\sigma} = \mathbf{D} : \boldsymbol{\sigma} \tag{4}$$

In the above expression $\mathbf{D}$ is a 4-th order mapping tensor while the ":" symbol represents the tensor product ($\sigma_{ij} = \mathbf{D}_{ijkl}\, \sigma_{kl}$). To distinguish between the two configurations effective stresses are always overlined (in matrix notation $\boldsymbol{\sigma}$ and in tensorial one σ_{ij}), while principal stresses are denoted by an extra hat put above the corresponding stress symbol (the nominal stress is denoted by $\hat{\sigma}_i$ and the effective stress by $\overline{\sigma}_i$). All stress/strain components positive in compression are underlined.

For sake of clarity a full model description, including the original Lee-Fenves formulation and all introduced modifications, is given in the paper. The paper is organized as follows. In section 2 a short summary of the reference model is given, in section 3 the calibration of model parameters is discussed, in section 4 numerical implementation is presented, in section 5 benchmarks are given and finally conclusions are drawn in section 6.

2. Components of the reference model

In the reference model an isotropic damage concept is adopted, although two damage variables are used separately for the tensile and compressive stress paths. Therefore the mapping tensor $\mathbf{D}$ is defined as follows

$$\mathbf{D} = \frac{1}{1-D}\mathbf{I} \tag{5}$$

where D is the current value of the damage parameter and $\mathbf{I}$ is the unit tensor.

Using the above mapping the relation between nominal and effective stress states can be written as

$$\boldsymbol{\sigma} = (1-D)\hat{\boldsymbol{\sigma}} \tag{6}$$

The resulting general form of the constitutive equation can be expressed as follows

$$\boldsymbol{\sigma} = (1-D)\mathbf{E} : \left(\boldsymbol{\varepsilon} - \boldsymbol{\varepsilon}^{p}\right) \tag{7}$$

where the effective elastic stiffness tensor is denoted by $\mathbf{E}$, while total strains and plastic strains are denoted by $\boldsymbol{\varepsilon}$ and $\boldsymbol{\varepsilon}^{p}$, respectively. As already mentioned two damage variables are used in the reference model

$$\boldsymbol{\kappa} = \left\{\kappa_c, \kappa_t\right\}^{\mathrm{T}} \tag{8}$$

These variables evolve with plastic straining according to the general evolution law which will be specified later on

$$\dot{\boldsymbol{\kappa}} = \dot{\lambda}\mathbf{H}(\boldsymbol{\sigma}, \boldsymbol{\kappa}) \tag{9}$$

where $\dot{\lambda}$ is the plastic multiplier while $\mathbf{H}$ is a diagonal matrix of hardening functions which are explicit functions of the current effective stress state and current damage variables. The current value of the damage parameter D is expressed as a function of the two damage variables κ_c, κ_t and current stiffness recovery parameter s

$$D = 1-(1-D_c(\kappa_c))(1-s(\hat{\boldsymbol{\sigma}})\, D_t(\kappa_t)) \tag{10}$$

D_c and D_t are damage parameters in compression and tension, respectively, their explicit forms will be given later on. The stiffness recovery parameter s, exclusively applied to the damage parameter for tension D_t, is defined as follows

$$s(\hat{\boldsymbol{\sigma}}) = s_o + (1-s_o)\, r(\hat{\boldsymbol{\sigma}}) \tag{11}$$

where s_o is a material parameter (assumed usually as $s_o = 0.2$) and effective stress domain function $r(\hat{\boldsymbol{\sigma}})$ is described by the following expression (here Macauley bracket $<\cdot>$ is used for $<x>=(x+|x|)/2$)

$$r(\hat{\boldsymbol{\sigma}}) = \frac{\sum_{i=1}^{3} < \hat{\boldsymbol{\sigma}}_i >}{\sum_{i=1}^{3} | \hat{\boldsymbol{\sigma}}_i |} \tag{12}$$

This function ranges from value 1.0 for pure uniaxial or multixial tensile state to 0.0 when all principal stresses are compressive.

The last two components of the model consist of the yield condition

$$F(\boldsymbol{\sigma}, \boldsymbol{\kappa}) = 0 \tag{13}$$

and a nonassociated plastic flow rule derived from the plastic potential G

$$\dot{\boldsymbol{\varepsilon}}^p = \dot{\lambda} \frac{\partial G}{\partial \boldsymbol{\sigma}} = \dot{\lambda}\, \mathbf{b} \tag{14}$$

A comprehensive description of all the components of the model is given in the following subsections.

2.1 Nominal stress, evolution law of damage variable and damage parameter in compression

In the reference model the nominal stress during plastic straining in uniaxial compression is approximated by the following composition of exponential functions

$$\underline{\sigma}_c = \underline{f}_{co}\left[(1+a_c)\exp(-b_c\, \varepsilon_c^p) - a_c \exp(-2\, b_c\, \varepsilon_c^p)\right] \tag{15}$$

where $\underline{f}_{co}$ is the initial value of the compressive uniaxial strength, a_c and b_c are material parameters and ε_c^p is the plastic hardening parameter. The evolution law for the hardening parameter is defined as follows

$$\dot{\varepsilon}_c^p = -(1 - r(\hat{\boldsymbol{\sigma}}))\, \dot{\varepsilon}_3^p \tag{16}$$

It is well known that softening models exhibit a pathological mesh dependency depending on the ductility of the post-peak branch in the stress-strain diagram. Hence regularization methods are needed to remedy the problem. Softening scaling, proposed long time ago by Mróz and Pietruszczak, is the the easiest method that can be used for plain concrete (but not necessarily for reinforced concrete). To use this method a normalized fracture energy g_c is defined as a material property

$$g_c = \frac{G_c}{l_c} = \int_0^{\infty} \underline{\sigma}_c(\varepsilon_c^p)\, d\varepsilon_c^p \tag{17}$$

where G_c is the fracture energy in compression while l_c is the characteristic length. For finite element implementation equation 17 is replaced by

$$g_c^h = \frac{G_c}{h^e} = \int_0^{\infty} \underline{\sigma}_c(\varepsilon_c^p)\, d\varepsilon_c^p \tag{18}$$

where h^e is the element size, this in order to maintain the fracture energy G_c constant after integration over the element.

The internal damage variable in compression κ_c expresses the percentage of released fracture energy in compression and it is defined as follows

$$\kappa_c = \frac{1}{g_c} \int_0^{\varepsilon_c^p} \underline{\sigma}_c(\varepsilon_c^p)\, d\varepsilon_c^p \tag{19}$$

Using equations (15) and (19) one may easily express the nominal stress σ_c in terms of the damage variable κ_c

$$\underline{\sigma}_c(\kappa_c) = \frac{\underline{f}_{co}}{a_c}\left(1 + a_c - \sqrt{\phi_c}\right)\sqrt{\phi_c} \tag{20}$$

$$\phi_c(\kappa_c) = \frac{2\, a_c\, b_c\, g_c(\kappa_c - 1)}{\underline{f}_{co}} + (1 + a_c)^2 \tag{21}$$

and rewrite the evolution law for damage variable $\dot{\kappa}_c$ in the following form

$$\dot{\kappa}_c = \frac{1}{g_c} \underline{\sigma}_c(\kappa_c)\dot{\varepsilon}_c^p \tag{22}$$

The first major difference between the reference and the modified models appears in the definition of the damage parameter in compression. In the reference model stiffness degradation occurs immediately with the plastic straining while in the modified one it can be delayed. The modified formula for the damage parameter D_c takes the form

$$D_c = 1 - \exp(-d_c < \varepsilon_c^p - \varepsilon_{c,D}^p >) \tag{23}$$

where $\varepsilon_{c,D}^p$ is the value of plastic hardening parameter ε_c^p at which stiffness degradation starts to occur and d_c is material parameter (note that $d_c \geq b_c$ to preserve hardening plasticity in terms of the effective stresses). In practice one may assume that in the uniaxial compression test stress level at which stiffness degradation takes place is equal to

$$\underline{\sigma}_{c,D} / \underline{f}_c = \frac{1}{\nu} \frac{f_t}{\underline{f}_c} \tag{24}$$

and $\underline{\sigma}_{c,D}/\underline{f}_c \geq f_{co}$. This is justified by the fact that corresponding transverse normal strain, in the uniaxial compression test, reaches value f_t/E. It is worth to mention that in the reference model $\varepsilon^p_{c,D} = 0$ which enforces the condition $\underline{\sigma}_{c,D}/\underline{f}_c = \underline{f}_{co}/\underline{f}_c$.

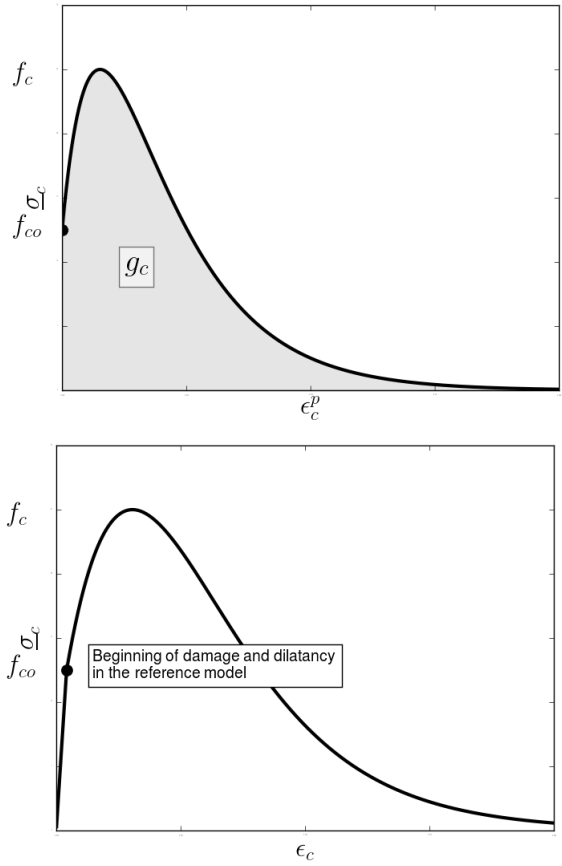

Figure 2: Definition of normalized fracture energy g_c and stress-strain diagram in the uniaxial compression test

By replacing the hardening parameter ε_c^p through the damage variable κ_c (with aid of equations (15) and (19)) the following expression for D_c is derived (here $\kappa_{c,D}$ is the damage variable value that corresponds to the $\varepsilon^p_{c,D}$)

$$D_c = \begin{cases} 0 & \text{for} \quad \kappa_c \le \kappa_{c,D} \\ 1 - \left(\dfrac{1 + a_c - \sqrt{\phi_c}}{a_c \; x_1} \right)^{d_c / b_c} & \text{for} \quad \kappa_c > \kappa_{c,D} \end{cases} \tag{25}$$

$$x_1 = \frac{1 + a_c - \sqrt{\phi_c(\kappa_{c,D})}}{a_c} \tag{26}$$

With aid of expression (25) one may derive the formula for the effective stress in uniaxial compression:

$$\underline{\sigma}_c(\kappa_c) = \begin{cases} \underline{f}_{co} \left(\dfrac{1 + a_c - \sqrt{\phi_c}}{a_c} \right) \sqrt{\phi_c} & \text{for} \quad \kappa_c \le \kappa_{c,D} \\ \dfrac{\underline{f}_{co}}{x_1^{-d_c / b_c}} \left(\dfrac{1 + a_c - \sqrt{\phi_c}}{a_c} \right)^{1 - d_c / b_c} \sqrt{\phi_c} & \text{for} \quad \kappa_c > \kappa_{c,D} \end{cases}$$

Notice that constant $x_1 = 1$ in the reference model.

2.2 Nominal stress, evolution law of damage variable and damage parameter in tension

The nominal softening stress under uniaxial tensile test conditions is approximated using the following expression

$$\sigma_t = f_{to} \left[(1 + a_t) \exp(-b_t \varepsilon_t^p) - a_t \exp(-2\, b_t \varepsilon_t^p) \right] \tag{27}$$

where f_{to} is the initial tensile strength, a_t and b_t are material parameters and ε_t^p is the plastic hardening parameter defined by the following evolution equation

$$\dot{\varepsilon}_t^p = r(\hat{\boldsymbol{\sigma}}) \, \dot{\varepsilon}_1^p \tag{28}$$

Here we may assume that the initial tensile strength f_{to} is equal to the tensile strength f_t. Therefore, there is no need to use the composition of two exponential functions to describe the post peak branch of the stress-strain diagram in tension and value of the a_t parameter can be set to zero.

Contrary to uniaxial compression the fracture energy in tension has a strong physical meaning and its value can be estimated according to standards (EC2 for instance). Strong softening effect in tension (due to cracking) leads to pathological mesh dependency in finite element simulations of plain concrete therefore the aforementioned softening scaling method is applied again. To use

this method a normalized fracture energy in tension g_t is defined as a material property

$$g_t = \frac{G_t}{l_c} = \int_0^{\infty} \sigma_t(\varepsilon_t^p)\, d\varepsilon_t^p \tag{29}$$

where l_c is the characteristic length. Again, for finite element implementations g_t is replaced by g_t^h and l_c by h^e.

The internal damage variable in tension κ_t expresses the percentage of released fracture energy in tension and it is defined as follows

$$\kappa_t = \frac{1}{g_t} \int_0^{\varepsilon_t^p} \sigma_t(\varepsilon_t^p)\, d\varepsilon_t^p = \frac{f_{to}}{g_t\, b_t}\left(1 - \exp\left(-b_t\, \varepsilon_t^p\right)\right) \tag{30}$$

Basing on equations (27) and (30) the evolution law for damage variable κ_t can be expressed as follows

$$\dot{\kappa}_t = \frac{1}{g_t} \sigma_t(\kappa_t) \dot{\varepsilon}_t^p \tag{31}$$

As there is no plastic straining before the peak tensile strength is achieved the damage parameter in tension D_t is defined as follows (stiffness degradation occurs immediately after start of plastic straining)

$$D_t = 1 - \exp\left(-d_t\, \varepsilon_t^p\right) \tag{32}$$

where d_t is a material parameter ($d_t \geq b_t$). If we express the hardening parameter ε_t^p in terms of κ_t then the expressions for the uniaxial nominal stress in tension, damage parameter D_t and uniaxial effective stress will take the form

$$\sigma_t(\kappa_t) = f_{to}(1 - \kappa_t) \tag{33}$$

$$D_t = 1 - (1 - \kappa_t)^{d_t/b_t} \tag{34}$$

$$\sigma_t(\kappa_t) = f_{to}\left(1 - \kappa_t\right)^{1 - d_t/b_t} \tag{35}$$

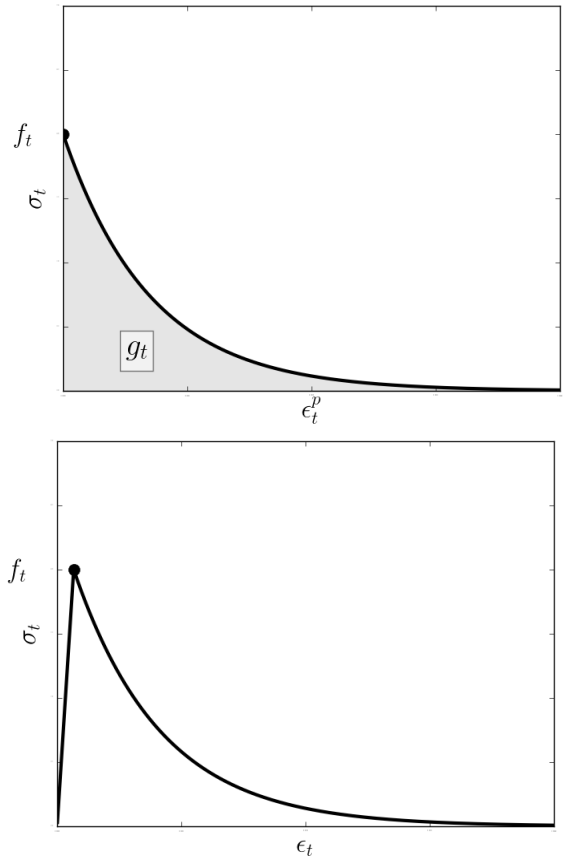

Figure 3: Definition of normalized fracture energy g_t and stress-strain diagram in uniaxial tensile test

2.3 Yield condition

In the reference model Lee and Fenves extended the plastic yield condition used in Barcelona model by Lubliner et al.[8] assuming that parameter β may vary during plastic straining. This condition is expressed as follows

$$F(\boldsymbol{\sigma}, \kappa_t, \kappa_c) = \frac{1}{1-\alpha}\left(\alpha\, I_1 + \sqrt{3\, J_2} + \beta(\kappa_t, \kappa_c) < \hat{\sigma}_{max} >\right) - c_c(\kappa_c) \tag{36}$$

where

$$\beta = \frac{c_c(\kappa_c)}{c_t(\kappa_t)}(1-\alpha) - (1+\alpha) \tag{37}$$

$$c_c = \underline{\sigma}_c(\kappa_c) \tag{38}$$

$$c_t = \sigma_t(\kappa_t) \tag{39}$$

The initial strength envelope for the reference model is drawn with a dashed line in Fig.4.

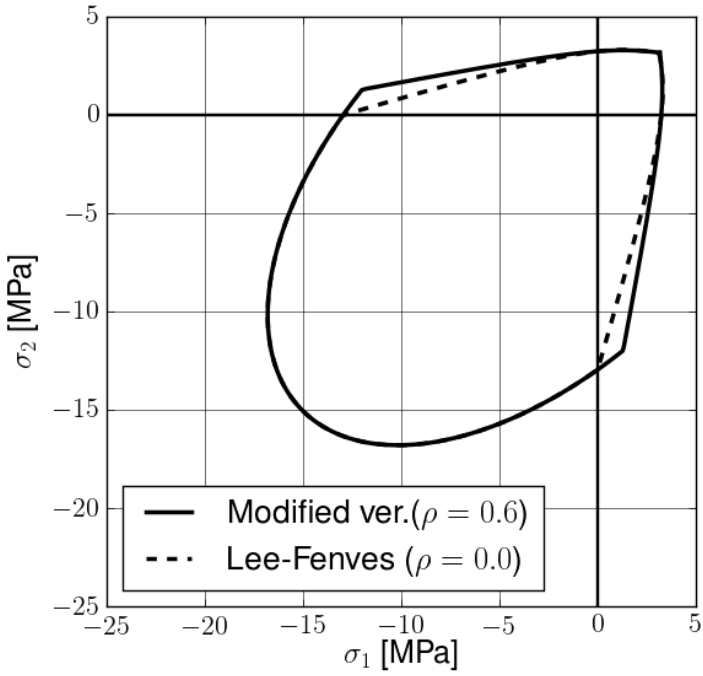

Figure 4: Initial strength envelopes for reference and modified model

It is obvious that this envelope in the tension-compression region will strongly undershoot bearing capacities for stress paths in that domain. To remedy the problem it is proposed here to modify the plastic yield condition by introducing parameter ρ ($\rho = 0.6$ was found here as optimal based on Kupfer's tests). The modified form of the yield condition takes the form of equation 40 (see envelope drawn with a solid line in Fig.4)

$$F(\boldsymbol{\sigma}, \kappa_t, \kappa_c) = \frac{1}{1-\alpha}\left(\alpha\, I_1 + \sqrt{3\, J_2} + \frac{\beta(\kappa_t, \kappa_c)}{1-\rho} < \hat{\sigma}_{max} - \rho\, c_t > \right) - c_c(\kappa_c) \tag{40}$$

2.4 Plastic flow rule

The Drucker-Prager (D-P) plastic potential is used in the flow rule of the reference model. The main benefit of using D-P is that principal stress directions in the trial state and after stress mapping on the current yield surface remain unchanged. This allows to carry out stress return procedure in the reduced principal stress space rather than in the full one. However, the major drawback of the D-P potential is that it generates an apex effect and may cause certain numerical problems (plastic flow direction is not unique) for stress paths in the tensile domain. To cancel this deficiency Omidi and Lotfi [11] introduced a simple correction to the plastic potential by rounding it near the apex (see Fig.5). The analytical form of the potential is then as follows

$$G(\bar{\boldsymbol{\sigma}}) = \sqrt{2\,J_2 + \beta_H^2} + \alpha_p^*\, I_1 \tag{41}$$

where stress invariants I_1 and J_2 are computed based on the effective stress state and $\beta_H = \alpha_d\ f_t\ \alpha_p$ ($\alpha_d = 1.0$ seems to be an optimal value).

In the reference model constant dilatancy is assumed ($\alpha_p^* = \alpha_p = \text{const}$). This assumption is too crude and requires to calibrate carefuly the α_p parameter to the dominant stress paths that may appear in analyzed problem.

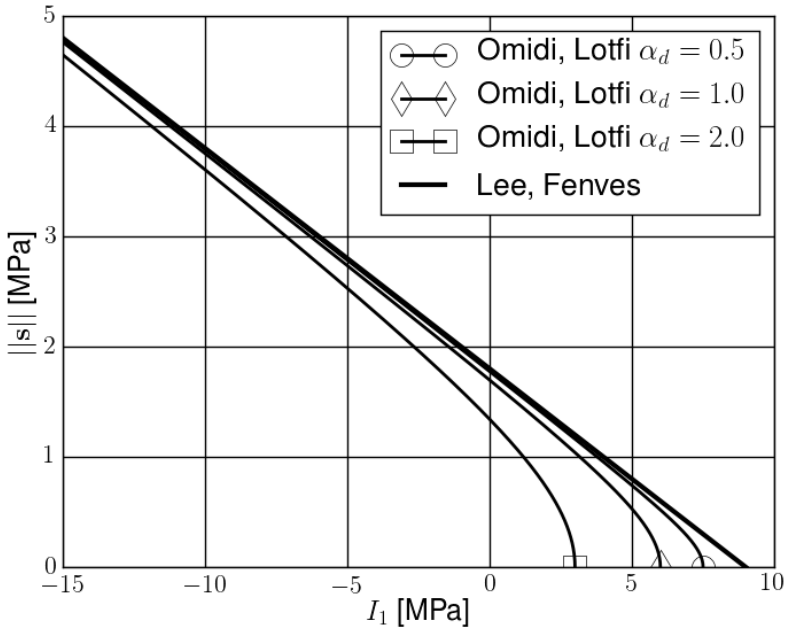

Figure 5: Smoothed plastic flow potential in $I_1 - \sqrt{J_2}$ plane

To enhance predictions of the model we propose a variable dilatancy law in which α_p^* is a function of the damage variables κ_t and κ_c. The following rule is proposed

$$\alpha_p^* = \alpha_{po}\ f_{\kappa_t}(\kappa_t) + (1 - f_{\kappa_t}(\kappa_t))\ f_{\kappa_c}(\kappa_c)\ \alpha_p \tag{42}$$

$$f_{\kappa_t}(\kappa_t) = \begin{cases} \frac{3}{2}\overline{\kappa}_t - \frac{1}{2}\overline{\kappa}_t^3 & \text{for} \quad \overline{\kappa}_t \le 1 \\ 1 & \text{for} \quad \overline{\kappa}_t > 1 \end{cases} \tag{43}$$

$$\overline{\kappa}_t = \frac{\kappa_t}{\kappa_{t,ref}} \qquad (\kappa_{t,ref} = 0.1) \tag{44}$$

$$f_{\kappa_c}(\kappa_c) = \begin{cases} 0 & \text{for} \quad \overline{\kappa}_c \le 0 \\ 3\overline{\kappa}_c^2 - 2\overline{\kappa}_c^3 & \text{for} \quad 0 \le \overline{\kappa}_c \le 1 \\ 1 & \text{for} \quad \overline{\kappa}_c > 1 \end{cases} \tag{45}$$

$$\overline{\kappa}_c = \frac{\kappa_c - \kappa_{c,dil}}{\kappa_{c,peak} - \kappa_{c,dil}} \tag{46}$$

Here $\kappa_{c,dil}$ and $\kappa_{c,peak}$ are values of damage variables corresponding to stress levels $\sigma_c/f_c = \underline{\sigma}_{c,dil}/\underline{f}_c$ and the $\sigma_c/f_c = 1$, respectively (in the uniaxial compression test). In this extended version dilatancy may vary during plastic straining; its value is kept zero as long as $\kappa_c \le \kappa_{c,dil}$ and then it grows up till α_p value at $\kappa_c = \kappa_{c,peak}$ (here a spline function is used). It is worth noting that in the uniaxial tensile test the resulting dilatancy parameter is equal to α_{po} while in the uniaxial compression to α_p. The smoothing parameter equals $\beta_H = \alpha_d\ f_t\ \alpha_{po}$.

3. Calibrating selected model parameters

3.1 Calibrating model parameters a_c, b_c and d_c

The a_c parameter can be evaluated once the ratio f_{co}/f_c is established (usually $f_{co}/f_c \ge 0.4$). If we assume that the peak compressive strength is equal to $\max(\underline{\sigma}_c) = \underline{f}_c$ then one may easily find that the extremum of $\underline{\sigma}_c$ is achieved at

$$\varepsilon_{c,extr}^{p} = -\frac{\ln\left(\frac{1}{2}\frac{1+a_c}{a_c}\right)}{b_c} \tag{47}$$

By substituting the $\varepsilon_{c,extr}^{p}$ to the general expression for $\underline{\sigma}_c$ (eq.(15)) the following relation is derived

$$\underline{f}_c = \frac{1}{4}\frac{\underline{f}_{co}(1+a_c)^2}{a_c} \tag{48}$$

Hence a_c parameter is equal to

$$a_c = 2\underline{f}_c/\underline{f}_{co} - 1 + 2\sqrt{(\underline{f}_c/\underline{f}_{co})^2 - \underline{f}_c/\underline{f}_{co}} \tag{49}$$

The two remaining parameters b_c and d_c can be estimated by preserving given normalized fracture energy $g_c = G_c/l_c$ value and damage parameter in compression $\tilde{D}_c$ at a given stress $\underline{\sigma}_c$ (see Fig.6).

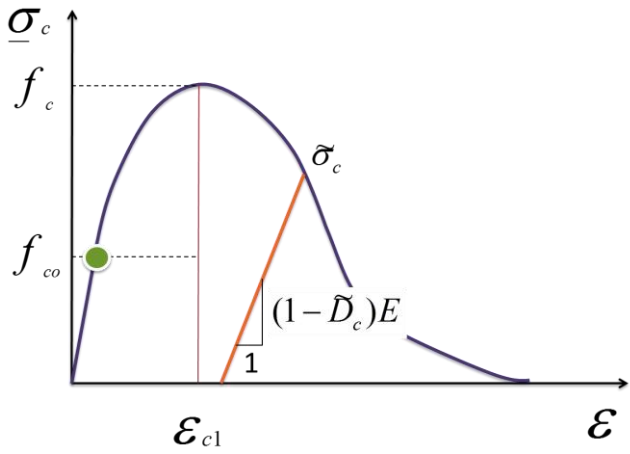

Figure 6: Calibration setup for d_c parameter

By using the expression for normalized fracture energy in compression (eq.(17)) one may easily derive value of b_c parameter

$$b_c = \frac{\underline{f}_{co}(1+a_c/2)}{g_c} \tag{50}$$

The corresponding d_c parameter is computed as

$$d_c = b_c \frac{\ln(1-\tilde{D}_c)}{\ln\left(\frac{1+a_c-\sqrt{\phi_c^*}}{x_1\, a_c}\right)} \tag{51}$$

where the ϕ_c^* value corresponds to the stress level value $\tilde{\sigma}_c/f_c$ (but on the post-peak branch).

It is worth to mention that strain at the peak ε_{c1} is not under control. Another important condition to be satisfied is such that $d_c \geq b_c$.

3.2 Calibrating model parameters b_t and d_t

In case of tensile domain $a_t = 0$ and calibration procedure is much simpler than in the compressive case. Once the normalized fracture energy g_t is known one may derive b_t parameter as

$$b_t = \frac{f_{to}}{g_t} \tag{52}$$

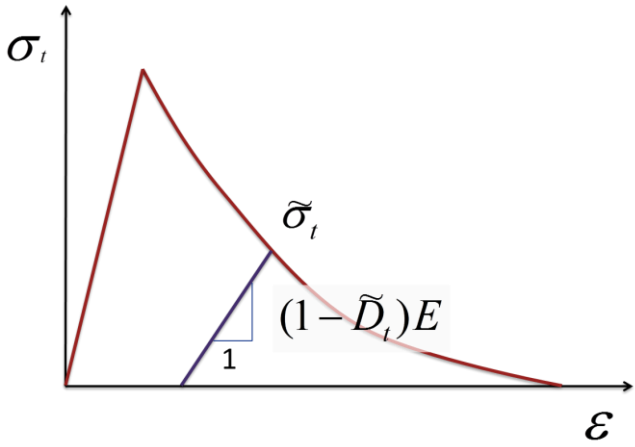

Figure 7: Calibration setup for d_t parameter

The d_t parameter is evaluated in a similar manner as the d_c one. Here we assume that for given stress value $\tilde{\sigma}_t$ damage factor in tension is known and

equal to $\tilde{D}_t$ (see Fig.(7)). The tensile plastic strain $\tilde{\varepsilon}_t^p$ corresponding to the stress value $\tilde{\sigma}_t$ is equal to

$$\tilde{\varepsilon}_t^p = -\frac{\ln(\tilde{\sigma}_t / f_{to})}{b_t} \tag{53}$$

Hence the resulting d_t parameter can be computed using the following expression

$$d_t = -\frac{\ln(1-\tilde{D}_t)}{\tilde{\varepsilon}_t^p} \tag{54}$$

Similarly to the compressive case the following condition must be satisfied $d_t \geq b_t$.

4. Numerical implementation

The general algorithm of stress evaluation for a given strain increment is given in Box.1.

Box.1. General algorithm of stress evaluation

• Transform nominal stress state at the last converged step N to the effective stress state

$$\bar{\sigma}_N = \frac{1}{1-D_N}\sigma_{\mathbf{N}}$$

• Compute trial effective stress state:

$$\bar{\sigma}_{N+1}^{\mathrm{tr}} = \bar{\sigma}_N + \bar{D}^e \, \Delta\boldsymbol{\varepsilon}_{N+1}$$

• Compute principal trial effective stresses: $\bar{\boldsymbol{\sigma}}_{N+1}$

• Set initial values of damage variables:

$$\kappa_{t,N+1} = \kappa_{t,N}$$

$$\kappa_{c,N+1} = \kappa_{c,N}$$

• If $F(\bar{\boldsymbol{\sigma}}_{N+1}, \kappa_{t,N}, \kappa_{c,N}) \geq 0$: perform plastic corrector algorithm (Box.2)

• If $F(\bar{\boldsymbol{\sigma}}_{N+1}, \kappa_{t,N}, \kappa_{c,N}) < 0$: update current stress state: $\bar{\sigma}_{N+1} = \bar{\sigma}_{N+1}^{\mathrm{tr}}$

• Update damage parametr: D_{N+1}

• Map current effective stress to the nominal stress state:

$$\sigma_{N+1} = (1-D_{N+1})\bar{\sigma}_{\mathbf{N+1}}$$

Box.2. Plastic corrector procedure

Set of independent variables: $\left\{\Delta\hat{\varepsilon}^{p}_{N+1}, \kappa_{t,N+1}, \kappa_{c,N+1}, \Delta\lambda_{N+1}\right\}^{\mathrm{T}}$

Stress-strain integration is carried out by solving the following set of nonlinear update equations (Newton-Raphson method is used)

1. $\mathbf{r}_{\varepsilon^p} = \Delta\hat{\boldsymbol{\varepsilon}}^{p}_{N+1} - \Delta\lambda_{N+1}\,\mathbf{b}(\hat{\sigma}_{N+1}, \kappa_{t,N+1}, \kappa_{c,N+1}) = 0$
2. $r_{\kappa_t} = \kappa_{t,N+1} - \kappa_{t,N} - \dfrac{\sigma_t(\kappa_{t,N+1})}{g_t}\, r(\hat{\sigma}_{N+1}) < \Delta\hat{\varepsilon}^{p}_{1} >= 0$
3. $r_{\kappa_c} = \kappa_{c,N+1} - \kappa_{c,N} - \dfrac{\sigma_c(\kappa_{c,N+1})}{g_c}\,(1 - r(\hat{\sigma}_{N+1})) < -\Delta\hat{\varepsilon}^{p}_{3} >= 0$
4. $r_F = F(\hat{\sigma}_{N+1}, \kappa_{t,N+1}, \kappa_{c,N+1}) = 0$

The stress-strain integration procedure of the modified Lee-Fenves model was developed in the principal stress space following the scheme proposed by Larsson and Runnesson [5]. This scheme can be adopted here as the principal effective stress directions, due to conical form of the plastic potential, remain unchanged during plastic correction.

The above procedure is used for plane-strain and 3D continuum finite elements. For shell elements (MITC-Q4 elements are used in ZSoil code) the stress component perpendicular to the midsurface is assumed to be zero ($\sigma_z = 0$) and the algorithm requires major modifications (see Lee and Fenves [6] where the plane stress formulation is proposed). To avoid rederivation of the plastic corrector procedure the $\sigma_z = 0$ condition is enforced in an iterative manner.

5. Numerical examples

To assess model capabilities Kupfer's tests are reproduced first (in 3D format), then the three-point bending test (see [3]) is carried out, as a plane-strain problem, and finally a reinforced concrete slab, discretized with aid of Q4-MITC shell elements, is analyzed.

5.1 Kupfer's tests

In this benchmark monotonic biaxial compression-compression and compression-tension tests (after Kupfer) are reproduced with aid of the plastic damage model. These tests are run with a 2x2 mesh of 8 nodes brick elements (low order EAS elements are used in ZSoil to model materials exhibiting strong dilatancy) of size 100.0 mm x 100.0 mm x 50.0 mm each (as in [7]) using spherical arc-length displacement control driver (node A is used to control displacements). The test setup is shown in Fig.(8). Three tests are considered i.e. $q_1/q_2 = -1/0$ (uniaxial compression), $q_1/q_2 = -1/-0.52$ (compression-

compression) and $q_1/q_2 = -1/+0.052$ (compression-tension). Material properties are as follows: $E = 33000$ MPa, $\nu = 0.2$, $\underline{f}_c = 32.4$ MPa, $\underline{f}_{co}/\underline{f}_c = 0.4$, $\underline{f}_{cbo}/\underline{f}_{co} = 1.15$, $\underline{\sigma}_{c,D}/\underline{f}_c = 0.5$, $\tilde{\sigma}_c/f_c = 1.0$, $\tilde{D}_c = 0.44$, $G_c = 4.5*10^{-3}$ MN/m, $f_t = 3.24$ MPa, $\tilde{\sigma}_t/f_t = 0.5$, $\tilde{D}_t = 0.5$, $G_t = 1.5*10^{-4}$ MN/m, $s = 0.2$, variable dilatancy is used with $\underline{\sigma}_{c,dil}/\underline{f}_c = 0.8$, $\alpha_p = 0.34$, $\alpha_{po} = 0.2$, $\alpha_d = 1.0$. The predicted stress-strain diagrams are shown in the following figures. A significant mismatch between the experiment and numerical prediction is observed for the reference model in the mixed tension-compression test for $q_1/q_2 = -1/+0.052$ (see figure 14). Modification of the yield condition (through parameter ρ) yields much better prediction shown in figure 13.

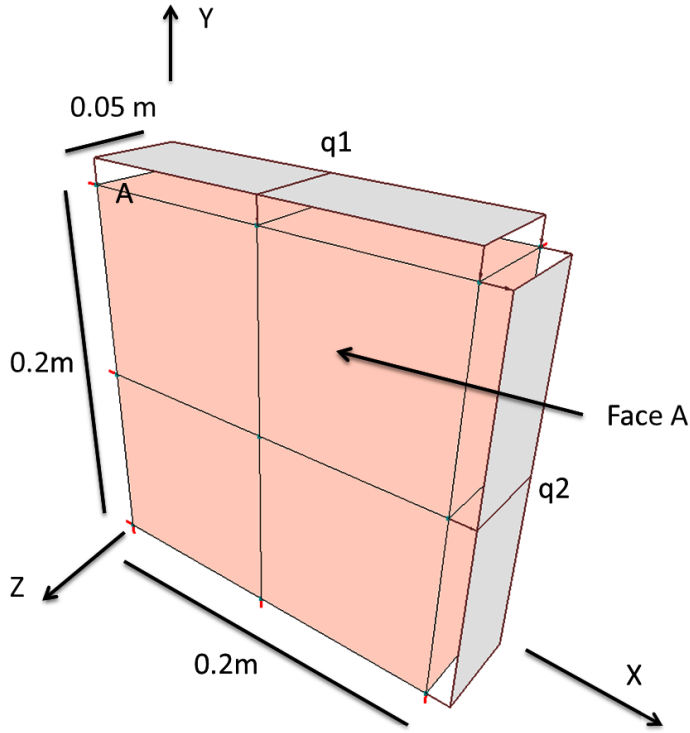

Figure 8: Kupfer tests: mesh and boundary conditions

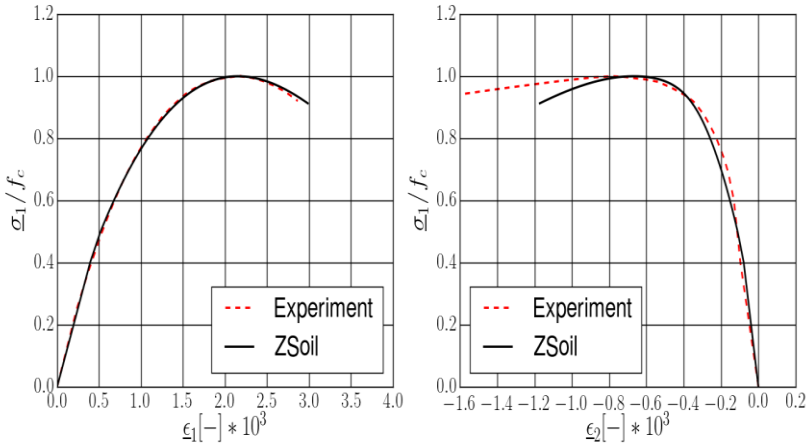

Figure 9: $q_1/q_2 = -1/0$: $\sigma_1 - \varepsilon_1$ (left) and $\sigma_1 - \varepsilon_2$ (right) diagrams

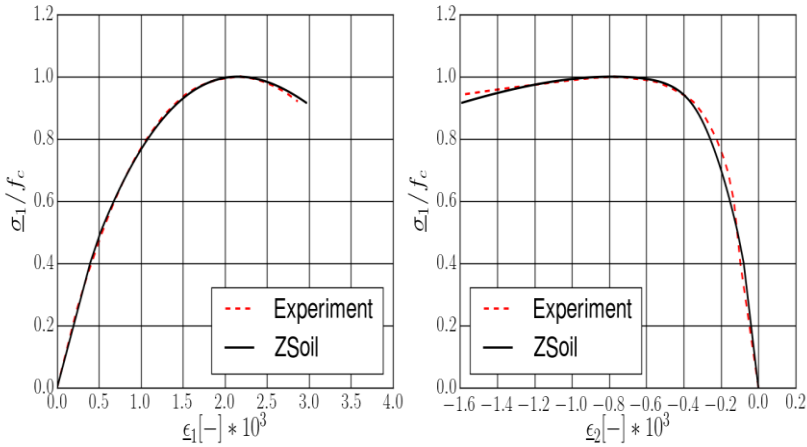

Figure 10: $q_1/q_2 = -1/0$: $\sigma_1 - \varepsilon_1$ (left) and $\sigma_1 - \varepsilon_2$ (right) diagrams for $\alpha_p = 0.5$

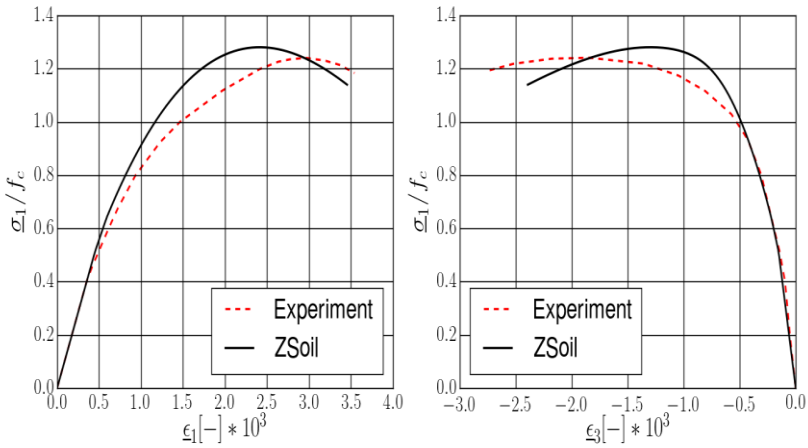

Figure 11: $q_1/q_2 = -1/-0.52$: $\sigma_1 - \varepsilon_1$ (left) and $\sigma_1 - \varepsilon_3$ (right) diagrams

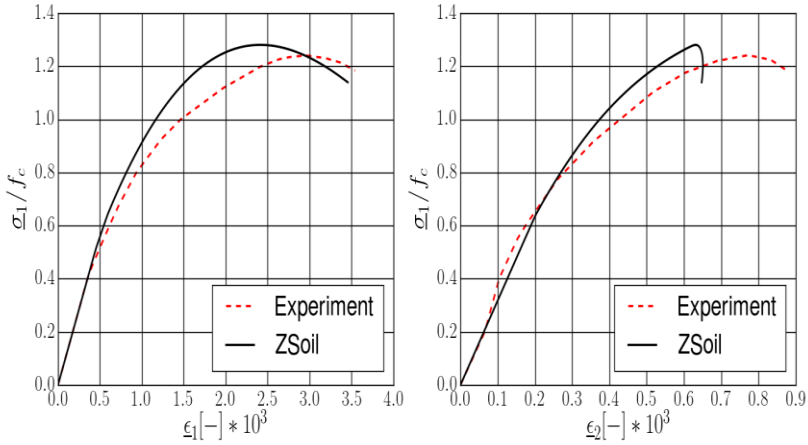

Figure 12: $q_1/q_2 = -1/-0.52$: $\sigma_1 - \varepsilon_1$ (left) and $\sigma_1 - \varepsilon_2$ (right) diagrams

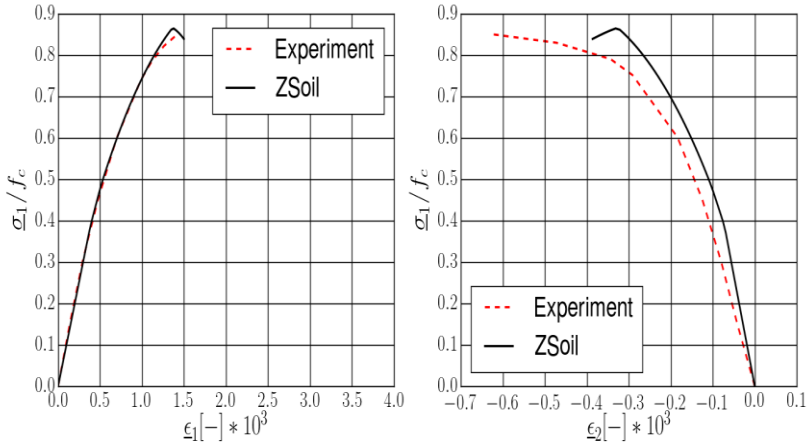

Figure 13: $q_1/q_2 = -1/+0.052$: $\sigma_1 - \varepsilon_1$ (left) and $\sigma_1 - \varepsilon_2$ (right) diagrams

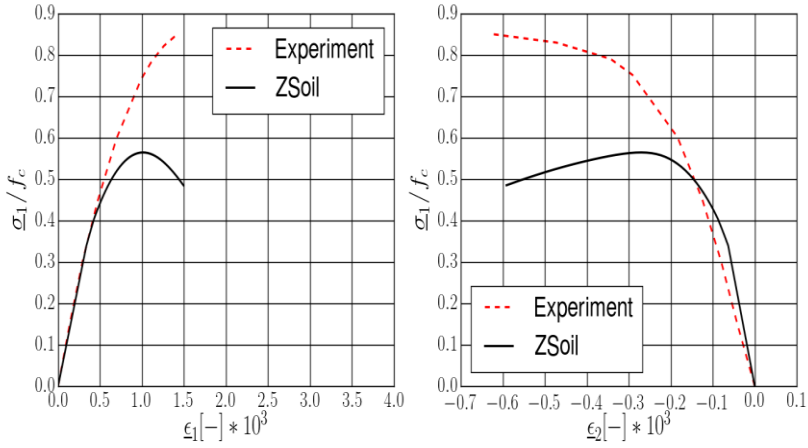

Figure 14: $q_1/q_2 = -1/+0.052$: $\sigma_1 - \varepsilon_1$ (left) and $\sigma_1 - \varepsilon_2$ (right) diagrams without modification of the yield condition (reference model, $\rho = 0.0$)

5.2 Three point bending test

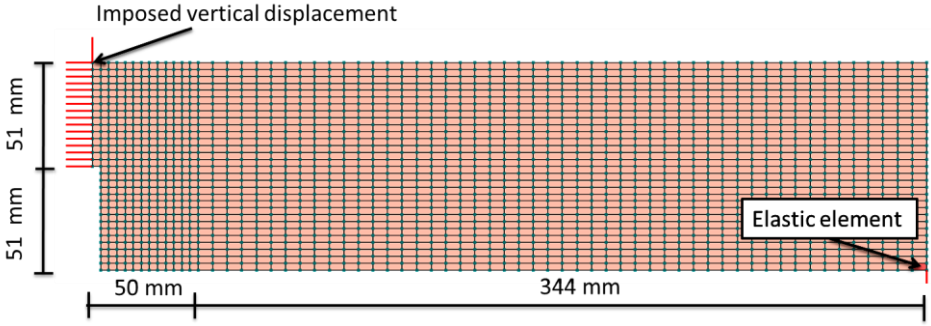

Figure 15: Three point bending test: geometry, mesh and boundary conditions

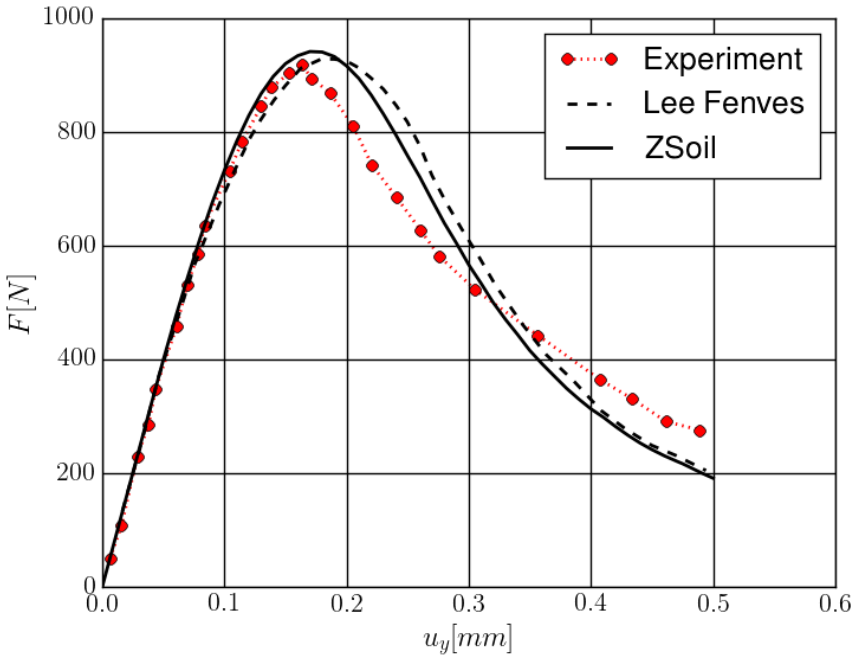

Figure 16: Three point bending test: comparizon of experimental and numerical force-deflection diagrams

Analysis of crack propagation in a three point bending test, carried out experimentally by Malvar and Warren [9], is the aim of this example. Geometry of the notched specimen, mesh and applied boundary conditions in the test, run as a plane-strain problem, are shown in Fig.15. To avoid local plastification near the vertical roller at the right side a fictitious elastic element is placed instead of the plastic-damage one.

Material properties are as follows: $E = 21700$ MPa, $\nu = 0.2$, $f_c = 29.0$

MPa, $\underline{f}_{co}/\underline{f}_c = 0.6$, $\underline{f}_{cbo}/\underline{f}_{co} = 1.16$, $\underline{\sigma}_{c,D}/\underline{f}_c = 0.5$, $\tilde{\sigma}_c/f_c = 1.0$, $\tilde{D}_c = 0.5$, $G_c = 4.5*10^{-3}$ MN/m, $f_t = 3.1$ MPa, $\tilde{\sigma}_t/f_t = 0.5$, $\tilde{D}_t = 0.55$, $G_t = 0.65*10^{-4}$ MN/m, $s = 0.2$, constant dilatancy is used with $\underline{\sigma}_{c,dil}/\underline{f}_c = 0.6$, $\alpha_{po} = 0.2$, $\alpha_d = 1.0$.

A displacement driven loading program, with a maximum assumed deflection of 5mm is applied with 50 equal steps. Comparizon of the experimental and numerical force-deflection diagrams is shown in Fig.16. The ZSoil prediction quite well matches the experimental curve reported by Malvar and Warren. The peak is predicted at same deflection as in the experiment and a small overshoot is visible just after the peak. This effect can be explained by the specific form of the softening described by an exponential function. It has to be mentioned that Lee and Fenves obtained their result by diminishing the tensile strength from 3.1 MPa to 2.4 MPa and tensile fracture energy from 70 [N/m] to 30 [N/m]. It seems that finite elements used by Lee and Fenves did suffer from severe locking phenomenon.

5.3 RC slab under point loading

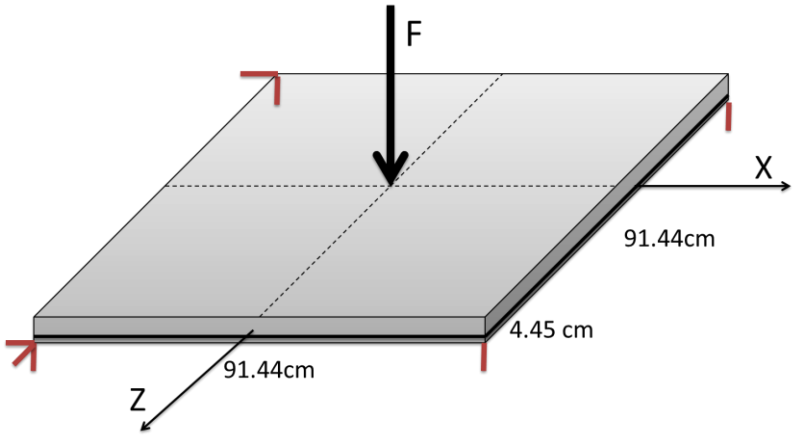

Figure 17: RC slab: geometry and boundary conditions

A square reinforced concrete slab with dimensions [3] 91.44 cm x 91.44 cm, 4.45cm thick, simply supported at four corners, and loaded by a concentrated force at the center, is analyzed here (see Fig.17). Exploiting symmetries only one quarter is discretized. The slab is reinforced by an orthogonal reinforcement with density $\rho = 0.85\%$ same in both directions. The average effective depth of the cross section is equal to 3.33 cm (to simplify the analysis both reinforcement layers are placed at 1.12 cm from the bottom fibers). It is very important to cancel membrane forces by proper setting of boundary conditions. Material properties for concrete, taken from the publication by Krätzig et al. [4], are as follows:

$E = 28613$ MPa, $\nu = 0.15$, $\underline{f}_c = 37.92$ MPa, $\underline{f}_{co}/\underline{f}_c = 0.6$, $\underline{f}_{cbo}/\underline{f}_{co} = 1.16$, $\underline{\sigma}_{c,D}/\underline{f}_c = 0.5$, $\tilde{\sigma}_c/f_c = 1.0$, $\tilde{D}_c = 0.5$, $G_c = 3.0*10^{-3}$ MN/m, $f_t = 2.91$ MPa, $\tilde{\sigma}_t/f_t = 0.5$, $\tilde{D}_t = 0.7$, $G_t = 1.5*10^{-4}$ MN/m, $s = 0.2$, constant dilatancy is used with $\underline{\sigma}_{c,dil}/\underline{f}_c = 0.6$, $\alpha_{po} = 0.2$, $\alpha_d = 1.0$. The corresponding properties for steel are: $E_s = 201300$ MPa, $f_y = 345.4$ MPa.

Comparizon of the experimental and numerical force-displacement diagrams is shown in Fig. 18. A typical mismatch between model and experiment is observed at deflections in the range $1 \div 2$mm. It can be reduced by diminishing the tensile strength down to $f_t = 2.3$ MPa (see Krätzig et. al). Another drawback of the model becomes visible when results of two different discretizations are compared. The observed response of the denser FE model is stiffer. This effect is caused by the applied softening scaling method in which the characteristic length is replaced by the finite element size. If the tensile fracture energy is to be preserved then smaller elements must exhibit larger ductility than the bigger ones. This deficiency disappears in case of reinforced concrete, when a fixed value of a characteristic length l_c^* is used instead of one equivalent to the finite element size ($l_c = h^e$). In the considered case $l_c = 0.13$ m yields a good match between experiment and numerical predictions with small influence of selected finite element grid size.

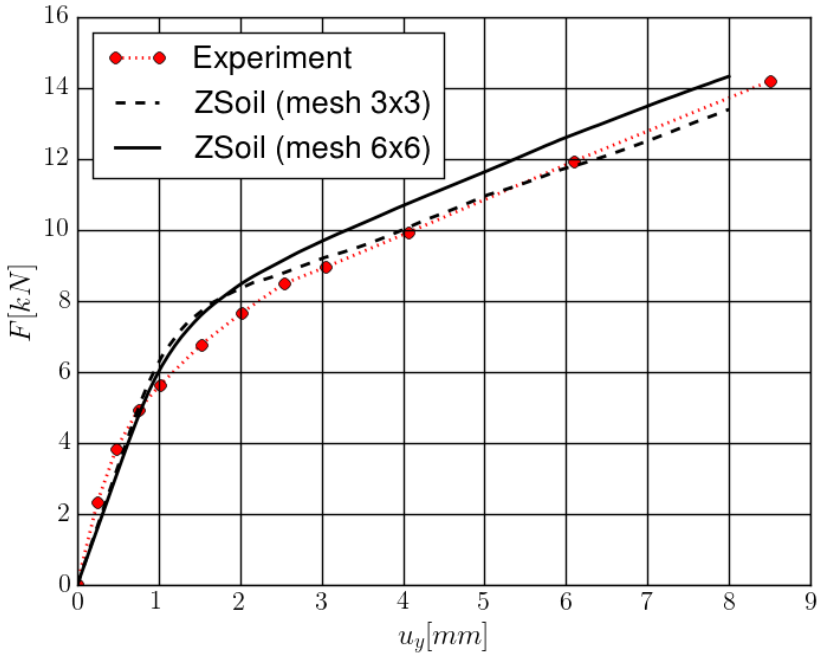

Figure 18: RC slab: comparizon of experimental and numerical force-deflection diagrams ($l_c = h^e$)

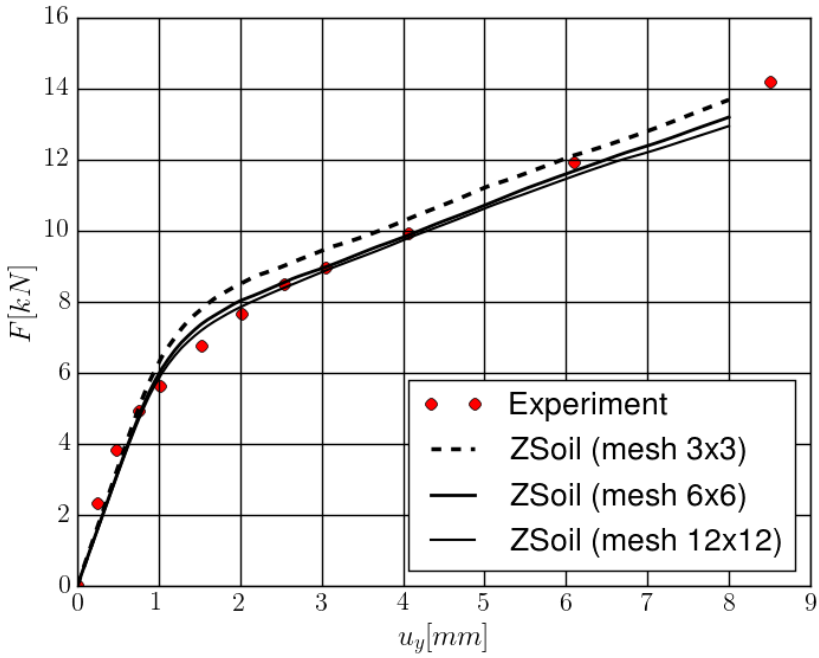

Figure 19: RC slab: comparizon of experimental and numerical force-deflection diagrams for fixed value of characteristic length $l_c = 0.13$ m

6. Conclusions

The proposed modified Lee and Fenves plastic-damage model for concrete can reproduce complex concrete behavior. The important modifications introduced by the authors include correction of the yield surface in the mixed tension-compression zone of the strength envelope, a modified plastic potential, in which variable dilatancy was introduced, a delay of stiffness degradation and dilatant behavior at the beginning of damage initiation. Model was implemented in plane strain and 3D format and its use for MITC-Q4 shell elements is possible but requires an iterative procedure to satisfy zero out of plane normal stress condition. Benchmarks show that the model can properly reproduce structural behavior of plain and reinforced concrete. In case of reinforced concrete an assumed constant characteristic length should be used rather than the directional finite element size in order to avoid significant mesh dependency. The model was implemented in ZSoil 2016 code.

References

[1] P. Grassl and M. Jirásek, "Damage-plastic model for concrete failure," *International Journal of Solids and Structures*, vol. 43, pp. 7166–7196, 2006.

[2] P. Grassl and M. Jirásek, "A plastic model with nonlocal damage applied to concrete," *International Journal for Numerical and Analytical Methods in Geomechanics*, vol. 30, pp. 71–90, 2006.

[3] J. C. Jofriet and M. McNeice, "Finite element analysis of reinforced concrete slabs," *J. Struct. Division (ASCE)*, vol. 97, 1971.

[4] W. B. Krätzig and R. Pölling, "An elasto-plastic damage model for reinforced concrete with minimum number of material parameters," *Computers and Structures*, vol. 82, pp. 1201–1215, 2004.

[5] R. Larson and K. Runesson, "Implicit integration and consistent linearization for yield criteria of the Mohr-Coulomb type," *Mechanics of Cohesive-Frictional Materials*, vol. 1, pp. 367–383, 1996.

[6] J. Lee and G. Fenves, "A return-mapping algorithm for plastic-damage models: 3-D and plane stress formulation," *IJNME*, vol. 50, pp. 487–506, 2001.

[7] J. Lee and G. Fenves, "Plastic-damage model for cyclic loading of concrete structures," *Journal of Engineering Mechanics*, vol. 124, pp. 892–900, 1998.

[8] J. Lubliner, J. Oliver, S. Oller, and E. Oñate, "A plastic-damage model for concrete," *International Journal of Solids and Structures*, vol. 25, 1989.

[9] L. Malvar and G. Warren, "Fracture energy for three-point-bend tests on single-edge-notched beams," *Experimental Mechanics*, vol. 45, pp. 266–272, 1988.

[10] S. Oller, E. Oñate, J. Oliver, and J. Lubliner, "Finite element nonlinear analysis of concrete structures using a plastic-damage model," *Engineering Fracture Mechanics*, vol. 35, 1990.

[11] O. Omidi and V. Lotfi, "Continuum large cracking in a rate-dependent plastic-damage model for cyclic-loaded concrete structures," *IJNMG*, vol. 37, pp. 1363–1390, 2012.

An orthotropic elasto-plastic-damage model of masonry. Implementation as ZSoil user model.

Aleksander URBAŃSKI[a] , Filip PACHLA [b,c] , Karolina WARTAK-DOBOSZ[b]

[a]*Cracow University of Technology, Dept. of Environmental Engineering, Poland*
[b] *KROZ Henryk Pachla, Poland*
[c]*Cracow University of Technology, Dept. of Civil Engineering, Poland*

Keywords: masonry, numerical modelling, orthotropy, plasticity, damage

Abstract

A computational model of masonry belonging to the class of homogenized models is presented. It takes into account orthotropy of elastic, plastic and damage response of 3D masonry media. Full description of the above features is given, as well as some details of its implementation as ZSoil user model. Finally, examples of practical applications are shown.

1. Introduction

Numerical modelling of masonry by means of finite elements is a subject of large number of research work. The "state of the art" reports, may be found in [2],[3]. There are two concepts of computational analysis of masonry:
1. direct, single-scale modelling
2. with use of homogenized models.

The first way of modelling is, in fact, fully available in ZSoil since its early versions (V5), see p.4.1, where mortar layers are represented by contact interface elements. FE meshing should closely correspond to brick and mortar spatial setup. However, application of this kind of approach, successful in analysis of small structures or structural details, has a natural limit, caused by the computational and man-work cost increasing beyond any acceptable level for medium or large scale structures. The other way, based on homogenized masonry model is free of the above limitations.

Presented model, belonging to the class of homogenized models is destined mainly to analysis of massive masonry structures. It is formulated as fully 3D

constitutive model, what makes it different from the majority of models which describe masonry as 2D media submitted to plane stress.

The assumption has been made that main feature which should be represented by the homogenized model of masonry is its orthotropy of elastic, plastic and damage response. Principal orthotropy axes are directed as shown in the Fig.1. Note, that first axis of orthotropy corresponds to the direction of "horizontal" layers. Together with the second axis they determine "plane" (of the wall, or tangent to the vault) in which action of forces is predominant.

In the paper, detailed description of its components is given, as well as some details of its implementation and testing. Finally, practical application is shown.

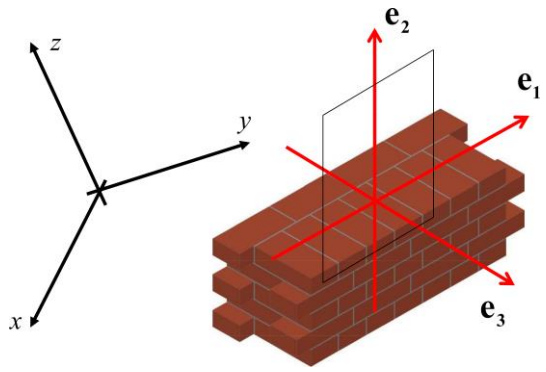

Figure 1. Global and material orthotropy coordinate systems.

2. Components of orthotropic elasto-plastic-damage model of 3D masonry

2.1 Orthotropic elasticity model

Constitutive equation for elasticity can be stated as:

$$\boldsymbol{\varepsilon} = \mathbf{C} \cdot \boldsymbol{\sigma} \tag{1}$$

where **C** is the compliance matrix, which has 21 independent components[1]. In the case of orthotropy, which is a special case of anisotropy, the number of unknowns is reduced to 12 components, of which 9 are independent. The compliance matrix is inverse of the stiffness matrix **D** and is commonly written as:

[1] in recent work vectors of strains and stresses are given in ZSoil standard notation ($\boldsymbol{\varepsilon} = \{ \varepsilon_{xx}, \varepsilon_{yy}, \gamma_{xy}, \varepsilon_{zz}, \gamma_{zx}, \gamma_{zy} \}^{\mathbf{T}}, \boldsymbol{\sigma} = \{ \sigma_{xx}, \sigma_{yy}, \sigma_{xy}, \sigma_{zz}, \sigma_{zx}, \sigma_{zy} \}^{\mathbf{T}}$)

$$\mathbf{C} = \mathbf{D}^{-1} = \begin{bmatrix} \frac{1}{E_1} & -\frac{\nu_{21}}{E_2} & 0 & -\frac{\nu_{31}}{E_3} & 0 & 0 \\ -\frac{\nu_{12}}{E_1} & \frac{1}{E_2} & 0 & -\frac{\nu_{32}}{E_3} & 0 & 0 \\ 0 & 0 & \frac{1}{G_{23}} & 0 & 0 & 0 \\ -\frac{\nu_{13}}{E_1} & -\frac{\nu_{23}}{E_2} & 0 & \frac{1}{E_3} & 0 & 0 \\ 0 & 0 & 0 & 0 & \frac{1}{G_{31}} & 0 \\ 0 & 0 & 0 & 0 & 0 & \frac{1}{G_{12}} \end{bmatrix} \tag{2}$$

where E_i, is the Young's modulus along axis i, G_{ij}, is the shear modulus in direction j on the plane whose normal is in direction i, and ν_{ij}, is the Poisson's ratio that corresponds to a contraction in direction j when an extension is applied in direction i. The compliance matrix (2) is symmetric and positive-definite, so it must satisfy the conditions:

$$\frac{\nu_{12}}{E_1} = \frac{\nu_{21}}{E_2}, \qquad \frac{\nu_{13}}{E_1} = \frac{\nu_{31}}{E_3}, \qquad \frac{\nu_{23}}{E_2} = \frac{\nu_{32}}{E_3} \tag{3}$$

$$E_1 > 0, \quad E_2 > 0, \qquad E_3 > 0, \qquad G_{12} > 0, \; G_{23} > 0, \; G_{23} > 0 \tag{4}$$

Two different coordinates systems are used (see fig. 1). The global coordinates are termed to be $\{x,y,z\}$. The second one, with $\{1,2,3\}$ axes is called material orthotropy coordinate system. In orthotropy case these coordinate systems are ortogonal, with e_{ij}, being coordinates of base versors $\mathbf{e}_i$ of material orthotropy set in $\{x,y,z\}$ coordinate system.

$$\mathbf{A} = \begin{bmatrix} \mathbf{e}_1^T \\ \mathbf{e}_2^T \\ \mathbf{e}_3^T \end{bmatrix} = \begin{bmatrix} e_{11} & e_{12} & e_{13} \\ e_{21} & e_{22} & e_{23} \\ e_{31} & e_{32} & e_{33} \end{bmatrix} \tag{5}$$

The transformation of stresses and strains, from one coordinate system to another is as given:

$$\mathbf{T}_{o,\varepsilon} = \begin{bmatrix} a_{11}^2 & a_{12}^2 & \beta a_{11}a_{12} & a_{13}^2 & \beta a_{11}a_{13} & \beta a_{12}a_{13} \\ a_{21}^2 & a_{22}^2 & \beta a_{21}a_{22} & a_{23}^2 & \beta a_{21}a_{23} & \beta a_{22}a_{23} \\ \gamma a_{11}a_{21} & \gamma a_{12}a_{22} & a_{11}a_{22} + a_{12}a_{21} & \gamma a_{13}a_{23} & a_{11}a_{23} + a_{13}a_{21} & a_{12}a_{33} + a_{12}a_{32} \\ a_{31}^2 & a_{32}^2 & \beta a_{31}a_{32} & a_{33}^2 & \beta a_{31}a_{33} & \beta a_{32}a_{33} \\ \gamma a_{11}a_{31} & \gamma a_{12}a_{32} & a_{11}a_{32} + a_{12}a_{31} & \gamma a_{13}a_{33} & a_{11}a_{33} + a_{13}a_{31} & a_{12}a_{33} + a_{12}a_{33} \\ \gamma a_{21}a_{31} & \gamma a_{22}a_{32} & a_{21}a_{32} + a_{22}a_{31} & \gamma a_{23}a_{33} & a_{21}a_{33} + a_{23}a_{31} & a_{22}a_{33} + a_{23}a_{32} \end{bmatrix} \tag{6}$$

where:

$$\beta = 1, \gamma = 0.5, \ [a_{ij}] = \mathbf{A} \text{ for } \mathbf{T}_{\varepsilon} \ ; \ \beta = 2, \gamma = 1, [a_{ij}] = \mathbf{A}^{T} \text{ for } \mathbf{T}_{\sigma}.$$

The transformation of stiffness matrix from the material to global coordinate system, is performed by a tensor-like transformation, as stated below:

$$\boldsymbol{\sigma}^{XYZ} = \mathbf{T}_{\sigma} \boldsymbol{\sigma}^{123} \tag{7}$$

$$\boldsymbol{\varepsilon}^{123} = \mathbf{T}_{\varepsilon} \boldsymbol{\varepsilon}^{XYZ} \tag{8}$$

The transformation of stiffness matrix from the material to global coordinate system, is performed by a tensor-like transformation, as stated below:

$$\mathbf{D}^{XYZ} = \mathbf{T}_{\sigma} \mathbf{D}^{123} \mathbf{T}_{\varepsilon} \tag{9}$$

2.2 Multi-surface plasticity model

In the recent work, while defining a plasticity condition for homogenized masonry-like media, the idea of clarity of meaning and what follows, simple identification of parameters was predominant. Also the simplicity of geometry and analytical expression of surfaces was the goal. A consequence of these assumptions is creation of multi-surface plasticity model, instead of building a model basing on one or two equation (example: Hill criterion, used in [2],[10]) in which meaning of parameters and their identification is not so straightforward. The stress return procedure used is Multi-surface Closest Point Projection (MsCCP) for the case of perfect plasticity, based on work of J. Simo and T.Hughes, see [6], with the extension allowing to handle possible non-associate flow rule.

The described elasto-perfectly plastic model of masonry use the following data:

f_{t1}, f_{t2}, f_{t3} - uniaxial tensile strength in all 3 principal directions of orthotropy,

f_{c1}, f_{c2} - uniaxial compressive strength, only in the first two principal directions of orthotropy, corresponding to in-plane directions of the masonry wall,

c - cohesion, understood as maximal in-plane shear stress, carried out by a sample in absence of compressive stresses in both directions,

$\mu_1 = \tan\phi_1, \mu_2 = \tan\phi_2$ - tangents of Coulomb friction angles,

$d_1 = \tan\psi_1, d_2 = \tan\psi_2$ - tangents of dilatancy angles,

R_1, R_2 - radii of cylindrical surfaces closing the elastic domain.

Basing on them, the whole set of seven yield surfaces, which are expressed in stress component related to orthotropy axes, is created. They are as follows:

– tensile cut-off condition planes normal to the orthotropy direction 1,2,3, respectively:

$$\begin{aligned} F_1(\boldsymbol{\sigma}) &= \sigma_{11} - f_{t1} = 0; \\ F_2(\boldsymbol{\sigma}) &= \sigma_{22} - f_{t2} = 0; \\ F_3(\boldsymbol{\sigma}) &= \sigma_{33} - f_{t3} = 0 \end{aligned} \tag{10}$$

– Coulomb type sliding plane for positive and negative σ_{12}, respectively:

$$\begin{aligned} F_4(\boldsymbol{\sigma}) &= \mu_1\sigma_{11} + \mu_2\sigma_{22} + \sigma_{12} - c = 0; \\ F_5(\boldsymbol{\sigma}) &= \mu_1\sigma_{11} + \mu_2\sigma_{22} - \sigma_{12} - c = 0 \end{aligned} \tag{11}$$

– cylindrical surface closing the domain along σ_{11} and σ_{22} axis, with $a_i = R_i - f_{ci}, i = 1,2$

$$\begin{aligned} F_6(\boldsymbol{\sigma}) &= (\sigma_{11} - a_1)^2 + {\sigma_{12}}^2 - {R_1}^2 = 0; \\ F_7(\boldsymbol{\sigma}) &= (\sigma_{22} - a_2)^2 + {\sigma_{12}}^2 - {R_2}^2 = 0. \end{aligned} \tag{12}$$

A view of multi-surface set in the 3D stress sub-space ($\{\sigma_{11}, \sigma_{22}, \sigma_{12}\}$) is shown in the Fig. 2. Some details of its creation and identification are shown in the Fig. 3.

Flow potentials Q_i, correspond to yield surfaces. For surfaces nr: 1,2,3 and 6,7 they have an associated form, as there is no physical evidence against it, but this is not the case of surfaces nr 4,5 as in general dilatation angles may be not equal to friction angles $\psi_i \neq \phi_i$, see [8],[11].

$$\begin{aligned} Q_1(\boldsymbol{\sigma}) &= \sigma_{11}; \\ Q_2(\boldsymbol{\sigma}) &= \sigma_{22}; \\ Q_3(\boldsymbol{\sigma}) &= \sigma_{33}; \\ Q_4(\boldsymbol{\sigma}) &= d_1\sigma_{11} + d_2\sigma_{22} + \sigma_{12}; \\ Q_5(\boldsymbol{\sigma}) &= d_1\sigma_{11} + d_2\sigma_{22} - \sigma_{12}; \\ &\text{note}: 0 \le d_i \le \mu_i \\ Q_6(\boldsymbol{\sigma}) &= (\sigma_{11} - a_1)^2 + \sigma_{12}^2; \\ Q_7(\boldsymbol{\sigma}) &= (\sigma_{22} - a_2)^2 + \sigma_{12}^2; \end{aligned} \tag{13}$$

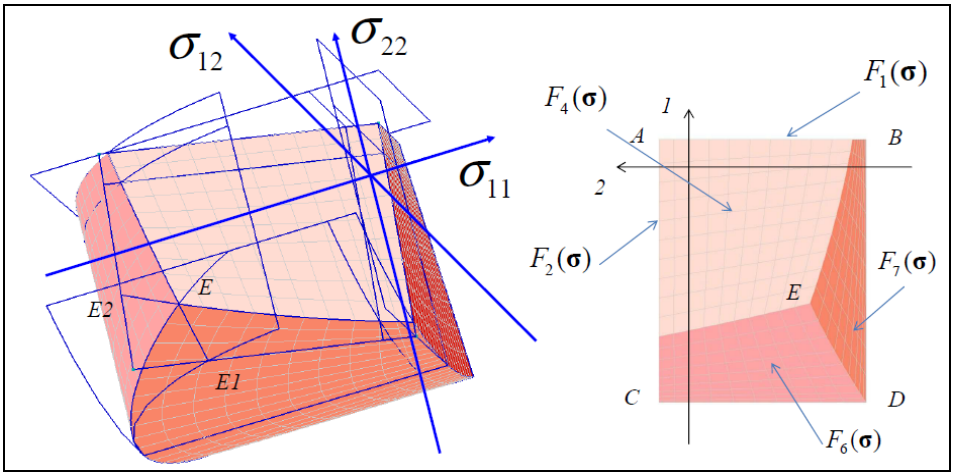

Figure 2. 3D view of the surface set.

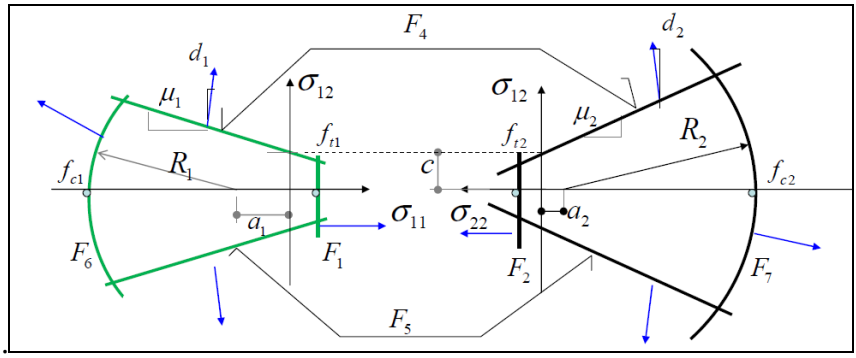

Figure 3. Meaning of parameters of the 3D plastic model.

To avoid an ambiguous situation, shown in Fig. 4, some additional relations must be fulfilled between the model parameters. The first one is a requirement of crossing the cylindrical surfaces F_6, F_7 by the most distant line of F_4, F_5, equivalent to the solvability condition in real numbers of equation system (14).

$$\begin{cases} (\sigma_{ii} - a_i)^2 + \sigma_{12}^2 = R_i^2 \\ \sigma_{12} + \mu_i \sigma_{ii} - \bar{c}_i = 0 \end{cases} \Rightarrow \left(\mu_i + \sqrt{1+\mu_i^2}\right) R_i > t_{\max} \qquad (14)$$

$$\bar{c}_i = c + \mu_j f_{cj} \qquad t_{\max} = c + \mu_1 f_{c1} + \mu_2 f_{c2}; \quad i = 1,2$$

Next, let us consider situations given as Fig. 4 b) and c). Requirement that crossing points lay beyond circle centre positions $s_i < a_i$, leads to the conditions given by eq.(15) for R_i, which override eq. (14).

$$s_i = \frac{a_i + \mu_i \bar{c}_i - \sqrt{\left(1+\mu_i^2\right)R_i^2 - \left(\bar{c}_i - \mu_i a_i\right)^2}}{1+\mu_i^2} < a_i \Rightarrow \left(1+\mu_i\right)R_i > t_{\max} \qquad (15)$$

For sake of an unambiguous definition of the set of surfaces needed by applied MsCCP algorithm it is necessary to prolong cylindrical surfaces as a planes beyond the crossing points as it is shown in Fig. 4 c). Otherwise, stresses may return on cylindrical surface everywhere, overriding other specified conditions (*F1, F2, F4, F5*) which should be active, as for MsCPP algorithm the most inner surface is the final goal. However analytical expressions for these parts of plasticity surfaces are different, obviously, see eq. (16), they do not constitute separate items in the set of multi-surfaces, because the continuity of their gradients along lines $\sigma_{ii} = s_i$ is preserved.

$$\sigma_{ii} > s_i : F_{6,7=5+i}^{prol} = 2\left((s_i - a_i)\sigma_{ii} + t_i\sigma_{12} - a_i(s_i - a_i) - t_i^2\right) = 0. \qquad (16)$$

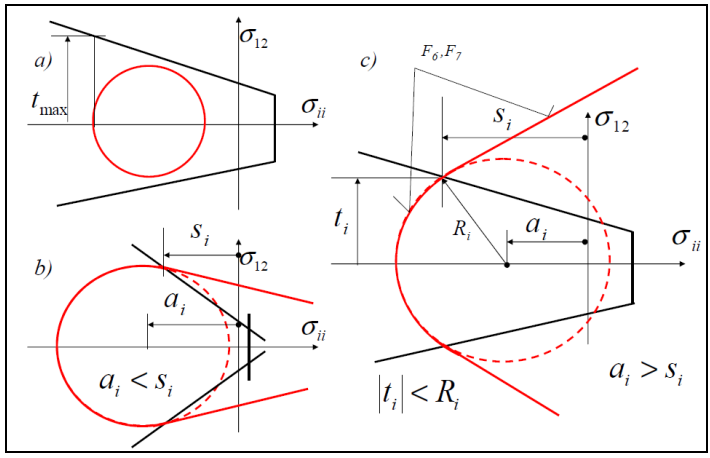

Figure 4: a) and b) Not allowed situation. c) Prolongation of cylindrical surfaces as a planes

Performance of proposed set of plasticity surfaces can be tested on experimental data given by Ganz and Thürliman [1]. Those data represent points in a tri-dimensional stress space of $\{\sigma_{11},\sigma_{22},\sigma_{12}\}$ for which plastic behaviour (ultimate state) was detected. In the Fig. 5a,b comparison between fitting data by a model given recently by Jemioło and Małyszko [2] and recent model is given.

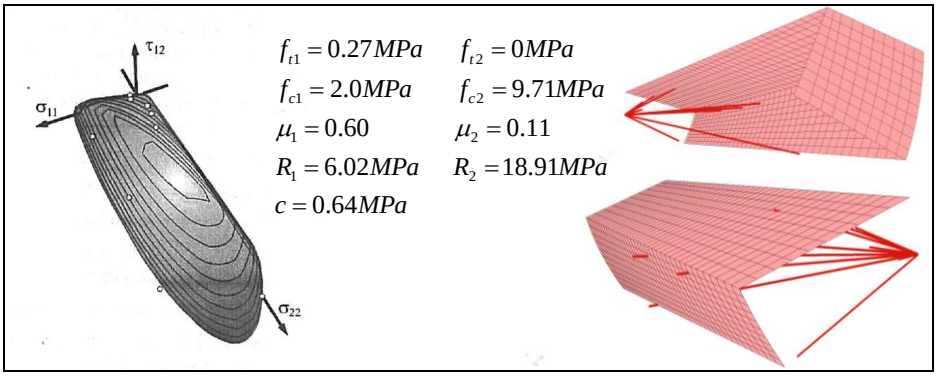

Figure 5a: Experimental data of [1] fitted by [2](left) and recent plasticity model.

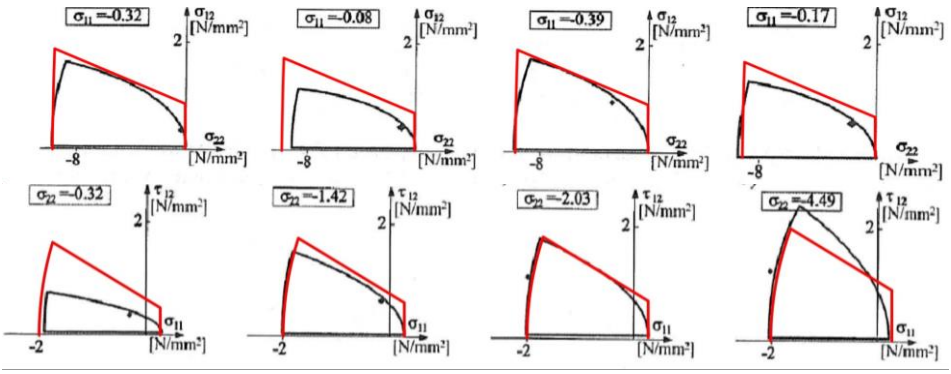

Figure 5b: Fitting data obtained in [1] by a model given in [2] (black graph) and recent model (red graph)

2.3 Continuum damage model of masonry

In order to describe the processes of appearance of cracks localized mainly in the mortar layers and accompanying loss of rigidity of masonry media by the model, a format offered by Continuum Damage Mechanics (CDM) has been chosen. Similar effects could be achieved by application of softening law in elasto-plastic model but it would complicate relations between the plastic surfaces and lead sometimes to non-acceptable (non-physical) effects. Strain-controlled damage is assumed as independent phenomena from plastic behaviour. Current CDM approach, outlined in the Fig. 6, with notion of effective stresses and strains acting in fictitious, undamaged continuum (here: elasto-plastic, see point 2.2), is based on the following assumptions:

1. Damage **factors** ω_i at *i*-th orthotropy direction (with A_0 -nominal area, $\overline{A_i}$ - effective area of damaged material at *i*-th orthotropy direction) are eigenvalues of damage tensor and **principal direction of second order damage tensor** are the orthotropy directions:

$$\omega_i = \frac{A_0 - \overline{A}_i}{A_0}, \quad 0 \le \omega_i < 1; \quad \boldsymbol{\omega} = \sum_i \omega_i \mathbf{e}_i \otimes \mathbf{e}_i \tag{17}$$

2. Equivalence of **forces** related to effective and nominal stresses:

$$f_j = \overline{\sigma}_{ij} \cdot \overline{A}_i = \sigma_{ij} \cdot A_0 \tag{18}$$

3. Equivalence of the **energy** expressed by effective and nominal stresses and strains:

$$dE = \overline{\sigma}_{ij} \cdot \overline{d\varepsilon_{ij}} = \sigma_{ij} \cdot d\varepsilon_{ij} \tag{19}$$

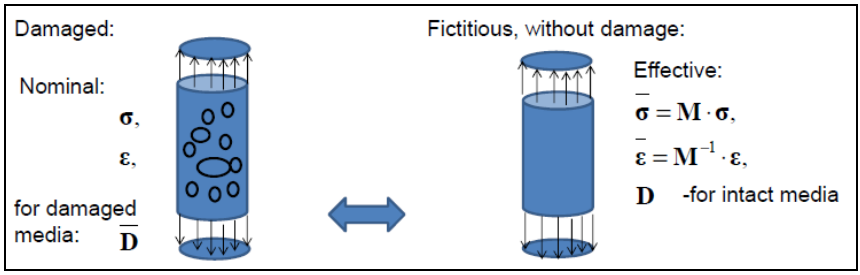

Figure 6: Relations for damage based on equivalence of forces and energy

A **damage effect tensor M**, of 4-order, following Voyiadjis and Deliktas work [7], is introduced, which considering the assumption 1, written in matrix notation, takes the simple diagonal form, see eq. 20:

$$\begin{aligned} M_{ii,ii} &= \frac{1}{1-\omega_i}, \\ M_{ij,ij} &= \frac{1}{\sqrt{(1-\omega_i)(1-\omega_j)}}, \quad i,j = 1,2,3, \quad \text{remaining } M_{ij,kl} = 0 \end{aligned} \tag{20}$$

The damage factors ω_i in each direction are functions of tensile strains:

$$\omega_i = \omega_i\left(\varepsilon_i^+\right) = 1 - \exp\left(-a_i \cdot \frac{h_{ei} \cdot \left(\varepsilon_i^+ - \varepsilon_{pi}\right)}{w_r}\right) \qquad 0 \le \omega_i < 1 \tag{21}$$

where: $\{\hat{\varepsilon}_1, \hat{\varepsilon}_2, \hat{\varepsilon}_3\}, \{\mathbf{w}_1, \mathbf{w}_2, \mathbf{w}_3\}$- eigen-values and eigen-directions of given strain tensor $\boldsymbol{\varepsilon}_n$,

$\boldsymbol{\varepsilon}_{3\times3}{}^+ = \boldsymbol{\varepsilon}_{3\times3}{}^+ + \langle\hat{\varepsilon}_i\rangle \cdot (\mathbf{w}_i \otimes \mathbf{w}_i)$ - positive part of strain tensor, $\boldsymbol{\varepsilon}^+ = \{\varepsilon_i^+\}^T = \mathbf{diag}\left(\boldsymbol{\varepsilon}_{3\times3}{}^+\right)$ - diagonal values of positive part of strain tensor related to orthotropy directions.

Adopted way of treating strains assure that in case of pure shear a damage in orthotropy direction may be induced.

The form of exponential function eq. (21) is similar to the function describing softening law in Menetrey-Willam model, see [4], [9], of

cementitious material, already (since 1994) implemented in ZSoil. It requires the following data: w_r -ultimate crack widths, a_i- steepness parameter, h_{ei}- element size in *i*-th direction. Damage threshold strain: $\varepsilon_{pi} = \alpha_i \cdot \frac{f_{ti}}{E_i}$ where the factor α_i indicates if damage at *i*-th direction take place prior $(\alpha_i < 1)$ or after $(\alpha_i > 1)$ tensile strains reach the values of tensile strength by Young modulus (also related to *i*-th orthotropy direction), see Fig. 7.

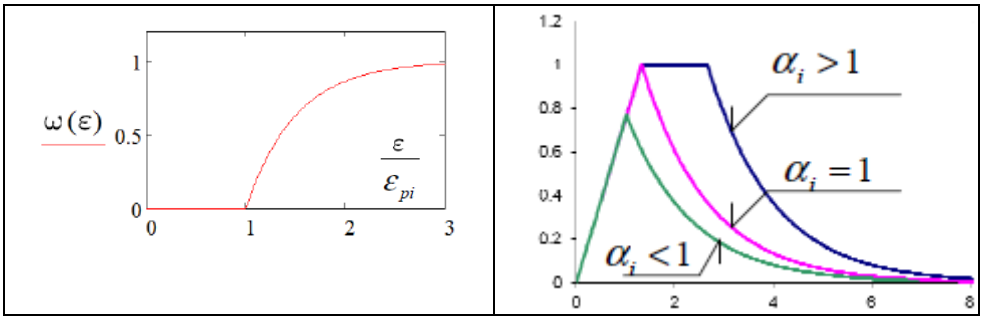

Figure 7: a) Damage factors b) Uni-axial tensile stress-strain (dimensionless) relations for damage with different factors α_i

The general schema of algorithmic treatment of the material submitted to damage independently of its plastic behavior, which seems to be the simplest formulation, is as follows. For given $\boldsymbol{\sigma}_{n-1}$-stresses at previous step, $\Delta\boldsymbol{\varepsilon} = \boldsymbol{\varepsilon}_n - \boldsymbol{\varepsilon}_{n-1}$ strain increment at recent step (both in orthotropy axes), set:

$$\overline{\boldsymbol{\sigma}}_{n-1} = \mathbf{M}_{n-1} \cdot \boldsymbol{\sigma}_{n-1}, \quad \Delta\overline{\boldsymbol{\varepsilon}} = \mathbf{M}_n^{-1}\boldsymbol{\varepsilon}_n - \mathbf{M}_{n-1}^{-1}\boldsymbol{\varepsilon}_{n-1} \tag{22}$$

The above effective stresses and strains increment consist, as well as elastic constitutive matrix $\mathbf{D}_e$, entries to the Multi-surface Closest Point Projection (MsCCP) routine which returns current effective stresses $\overline{\boldsymbol{\sigma}}_n$ and constitutive (elasto-plastic) matrix for the intact material $\mathbf{D}_{ep}$. Thus a return to the nominal stresses $\boldsymbol{\sigma}_n = \mathbf{M}_n^{-1}\overline{\boldsymbol{\sigma}}_n$ and to the constitutive matrix of damaged material $\overline{\mathbf{D}}_{ep} = \mathbf{M}_n^{-1}\mathbf{D}_{ep}\mathbf{M}_n^{-1}$ is finally performed. Stress $\boldsymbol{\sigma}_n$, and damage factors ω_{in} are stored for the next load step.

3. Implementation. Handling principal directions of orthotropy as ZSoil user-model data

A method of setting of principal directions of orthotropy is given for three common types of masonry constructions: wall, cylindrical vault, copula. The

key point is, that orthotropy directions are delivered as a part of ZSoil material model data. If they change from point to point, as it is in the case of a vault or copula, it would need a tremendous amount of data to be generated by the user. The following procedures will substantially simplify data setting.

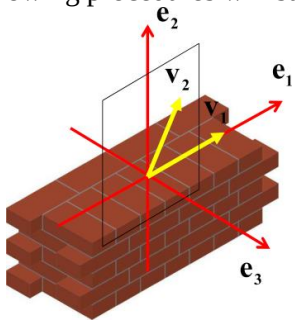

$$\mathbf{e}_1 = \frac{\mathbf{v}_1}{\|\mathbf{v}_1\|}$$
$$\mathbf{e}_3 = \frac{\mathbf{v}_1 \times \mathbf{v}_2}{\|\mathbf{v}_1 \times \mathbf{v}_2\|} \qquad (23)$$
$$\mathbf{e}_2 = \mathbf{e}_3 \times \mathbf{e}_1$$

Figure 8: Setting of principal directions of orthotropy for wall from given vectors in plane of the wall.

In the case of cylindrical vault the principal directions of orthotropy are set according to the assumptions presented on Fig. 9. Vector $\mathbf{v}_1$ defines the axis of the vault and $\mathbf{v}_2$ point lying on the axis of it. The orthotropy base is set according to eq. 24.

For a copula the procedure of obtaining principal directions of orthotropy (eq. 25) is analogical to the one for the cylindrical vault. Vector $\mathbf{v_1}$ defines the axis of the copula and vector $\mathbf{v_2}$ defines the point lying on this axis (Fig. 10).

Additionally in both algorithm, for each finite element of the vault or the cupola Gauss point coordinates $\mathbf{x}$ are known.

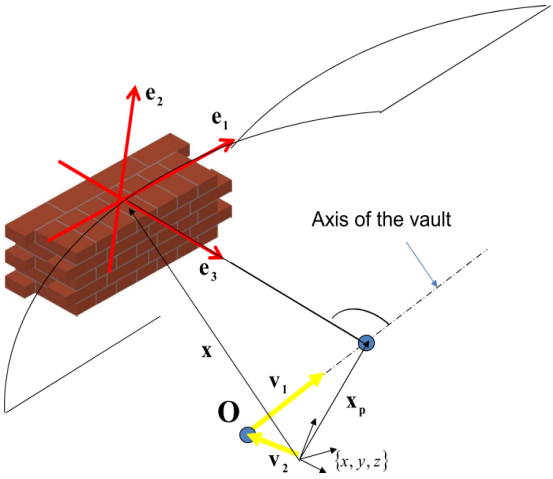

$$\left(\mathbf{x}_\mathbf{p}(\lambda) - \mathbf{x}\right) \circ \mathbf{v}_1 = 0$$
$$\Rightarrow \lambda = \frac{\left(\mathbf{x} - \mathbf{v}_2\right) \circ \mathbf{v}_1}{\mathbf{v}_2 \circ \mathbf{v}_2}$$
$$\mathbf{x}_\mathbf{p}(\lambda) = \mathbf{v}_2 + \mathbf{v}_1 \cdot \lambda$$
$$\mathbf{e}_1 = \frac{\mathbf{v}_1}{\|\mathbf{v}_1\|} \qquad (24)$$
$$\mathbf{e}_3 = \frac{\mathbf{x} - \mathbf{x}_\mathbf{p}}{\|\mathbf{x} - \mathbf{x}_\mathbf{p}\|}$$
$$\mathbf{e}_2 = \mathbf{e}_3 \times \mathbf{e}_1$$

Figure 9: Setting of principal directions of orthotropy for a cylindrical vault.

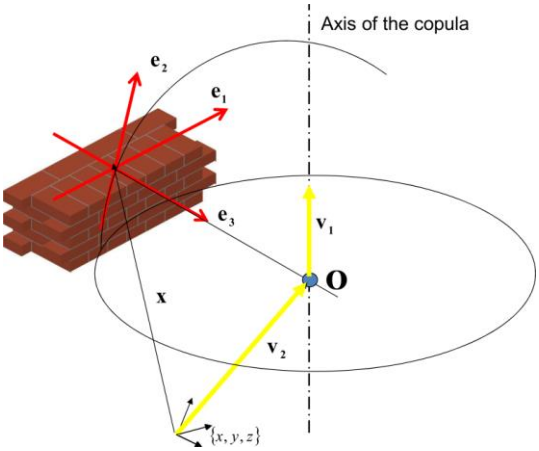

$$\mathbf{e}_3 = \frac{\mathbf{v}_2 - \mathbf{x}}{\|\mathbf{v}_2 - \mathbf{x}\|}$$
$$\mathbf{e}_1 = \frac{\mathbf{v}_1 \times \mathbf{e}_3}{\|\mathbf{v}_1 \times \mathbf{e}_3\|} \qquad (25)$$
$$\mathbf{e}_2 = \mathbf{e}_3 \times \mathbf{e}_1$$

Figure 10: Setting of principal directions of orthotropy for a copula.

4. Applications

4.1 Identification of homogenized orthotropic elastic model and its comparison with interface masonry model

In order to verify the programmed orthotropic elastic model it was compared with the results obtained from the masonry model with interface elements (Fig. 12). In this single-scale model bricks are elastic elements while the mortar joint are represented by the interface elements with normal and tangent stiffness $k_n = E_m / t, k_t = 0.5 k_n$, respectively.

A homogenized model was built from 3D solid elements, parameters of which were computed according to the analytical homogenization method proposed in papers [10], [11]. Representative Volume Element (RVE) for masonry structure is presented on Fig. 11. It is assumed that the displacements of mortar and brick under loading are equal. Given formulas may be generally useful in identification of elastic orthotropy data in the case of single leaf masonry. Evaluation of Young's modules for homogenized model (see Fig. 11) basing on constituent elastic properties is as follows:

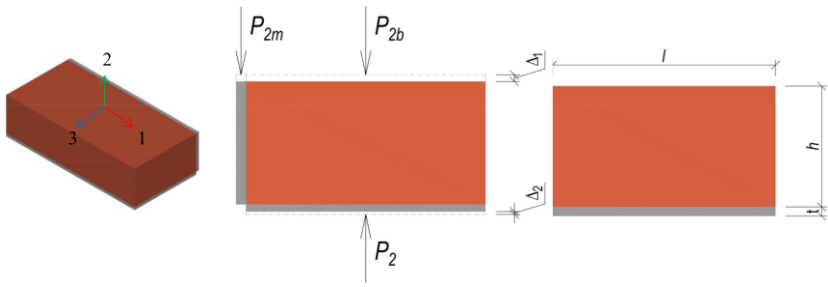

Figure 11: Representative Volume Element for masonry structure.

$$\Delta = \Delta_1 + \Delta_2$$

$$\begin{cases} P_2 = P_{2b} + P_{2m} \\ \Delta_1 = \Delta_b = \Delta_m \end{cases} \Rightarrow P_{2m} = \frac{P_2 E_m t}{E_b l + E_m t};\ \Delta_2 = \frac{P_2 t}{E_m l}$$

$$\Rightarrow E_2 = \frac{E_m l (E_b l + E_m t)(h+t)}{(t(E_b l + E_m t) + h E_m l)(l+t)}) \tag{26}$$

$$E_1 = \frac{E_m h (E_b h + E_m t)(l+t)}{(t(E_b h + E_m t) + h E_m l)(h+t)};\quad E_3 = \frac{E_m h (E_b h + E_m t)(w+t)}{(t(E_b h + E_m t) + h E_m w)(h+t)},$$

where P is a force acting on RVE, m- index represents mortar, b- index represents brick, l- brick length, h- brick height, t- thickness of mortar joint and w-width. Procedure for evaluation of shear modules according to [10] and [11] is following:

$$k = \frac{(l \cdot E_1 + 4 \cdot h \cdot G_b)}{l \cdot E_1 + 4 \cdot h \cdot G_b + E_1 \cdot \left(\frac{G_b}{G_m} - 1\right) \cdot \frac{l^2}{l+t}},$$

$$G_{13} = \frac{(t+l)(t \cdot G_m + h \cdot G_b)}{(t+h)\left[1 + \frac{(4 \cdot t \cdot h \cdot G_b) + (1-t) G_m \cdot t}{4 \cdot h \cdot G_m + (1-t) G_m} + l\right]} \tag{27}$$

$$G_{12} = \frac{l \cdot (t+l)(t+h)}{k \frac{t \cdot l \cdot (t+h)}{G_m} + \frac{(t+1-k \cdot t)(l \cdot h - t^2)}{G_b} + t(t+1)\frac{(t+1-k \cdot t)}{G_m}},$$

$$G_{23} = \frac{(t+h) G_m (l \cdot G_b + t \cdot G_m)}{(t+l)(t \cdot G_b + h \cdot G_m)}$$

Elastic parameters of a single-scale and homogenized models are given in the Table 1.

Table 1.

	Brick	Mortar	Homogenized model
Young modules [GPa]	E_b=1.0	E_m=0.1,	E_1= 0.672, E_2= 0.432, E_3=0.500
Shear modules [GPa]	G_b=0.38	G_m=0.05	G_{23}=0.190, G_{12}=0.318, G_{13}=0.182
Poisson ratio [-]	v_b=0.3	v_m=0	$v_{12} = v_{13} = v_{23} = 0.16$

Loading was applied to the part of the top surface of the wall, and along its lower edge vertical displacements are fixed (Fig. 12).

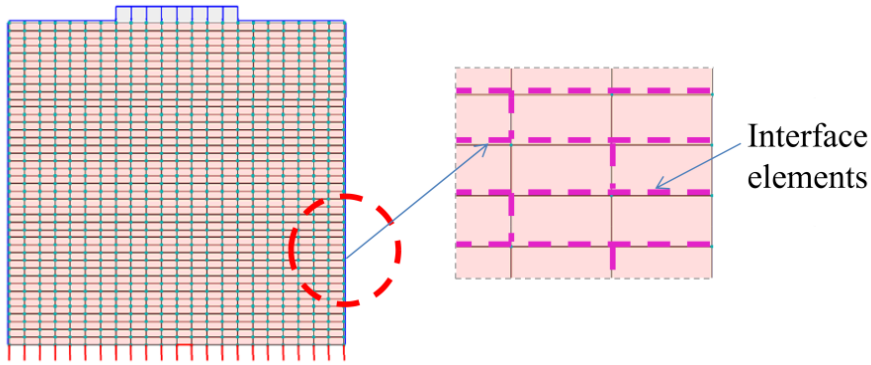

Figure 12: A single-scale model of masonry wall.

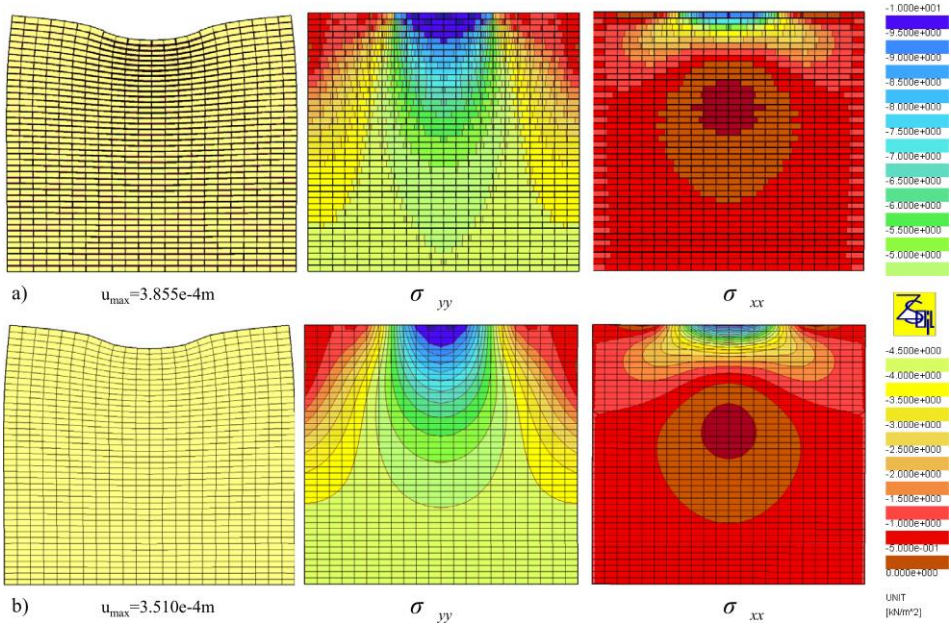

Figure 13: a) Results for a single-scale model of masonry wall b) Results for a homogenized elastic orthotropy model of masonry wall.

Results obtained from homogenized elastic orthotropic model are in good accordance with those obtained from single-scale model with interface elements. It can be seen on Fig. 13 that displacements are similar for both approaches (discrepancy about 10%). The maps of stresses σ_{xx} and σ_{yy} in the wall are also consistent (see Fig. 13).

4.2 Application: Bearing capacity of a thick masonry arch.

Massive masonry arches are the main structural component of the 150 years old railroad viaduct shown in Fig. 14a. Its geometrical shape is a skewed cut-off from a cylinder with length L=9.3m, radius R=5.7m, thickness t=0.85m. Estimation of bearing capacity was important part of the assessment of the structure, previously performed in [5], basing on elastic analysis exclusively. So, it may be seen as a complement of [5]. Schema of loads adopted for estimation of bearing capacity factor λ is given in Fig 14b. During data preparation, semi-automatic option of creating orthotropy principal directions for cylindrical vault, as described in point 3 (Fig 9.), has been extensively used.

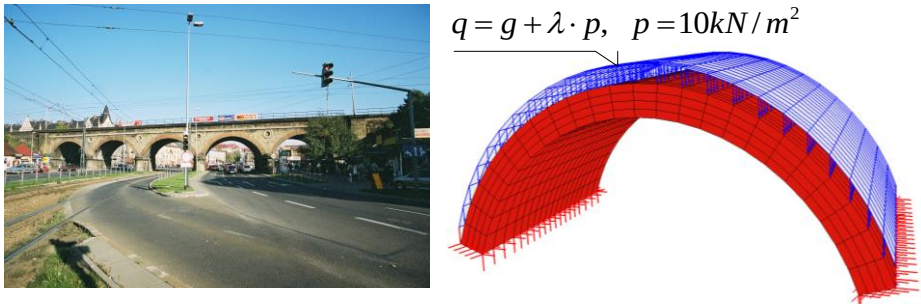

Figure 14: Railroad viaduct supported by masonry arch a) General view b) Schema of loads adopted for estimation of bearing capacity factor λ.

Elastic (E_i,G_i) and plastic (f_{ti},f_{ci}) material parameters were very roughly estimated by homogenization procedure based on data obtained from nondestructive testing of the masonry component. Damage data were set basing on experience from similar simulation for brittle media. Fig. 15a shows related ZSoil dialog windows containing masonry data gathered in two groups, i.e. *elastic* - orthotropy data, *nonlinear* - plasticity and damage.

Parameters elastic

Value name	Value
E1	7100000
E2	6000000
E3	4900000
v12	0.25
v13	0.25
v23	0.25
G1	2800000
G2	2800000
G3	2800000
vec11	2.68431
vec12	0
vec13	9.3
vec21	1.356
vec22	-2.018
vec23	4.7
mode	1

Parameters nonlinear

Value name	Value
fc1	10000
fc2	8000
ft1	1200
ft2	1200
c	1200
mi1	0.2
mi2	0.2
R1	100000
R2	100000
ft3	1200
dil1	0.1
dil2	0.1
alfa1	1
alfa2	1
alfa3	1
a1	5.26316
a2	5.26316
a3	5.26316
wr	0.001

all stress related values in [kPa]

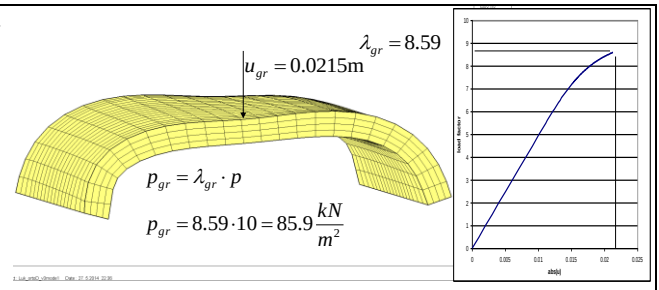

Figure 15: a) Model data b) Deformation of the masonry arch at ultimate load and simulated load-displacement path.

Figure 15 b) shows deformation of the masonry arch at ultimate load and simulated load-displacement path. Figure 16 shows plastic zones in the bottom and in the top surface of the arch.

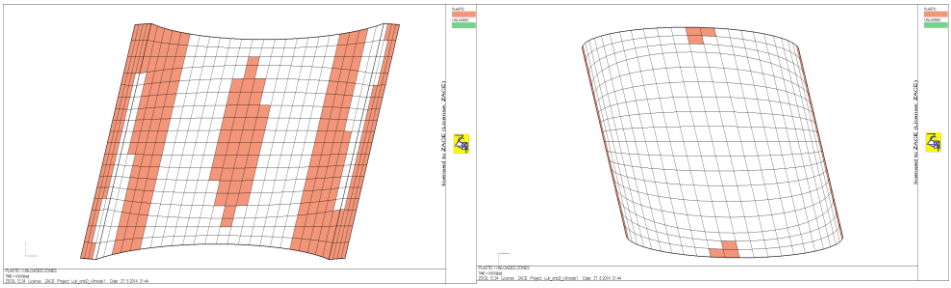

Figure 16: Plastic zones in the ultimate state.

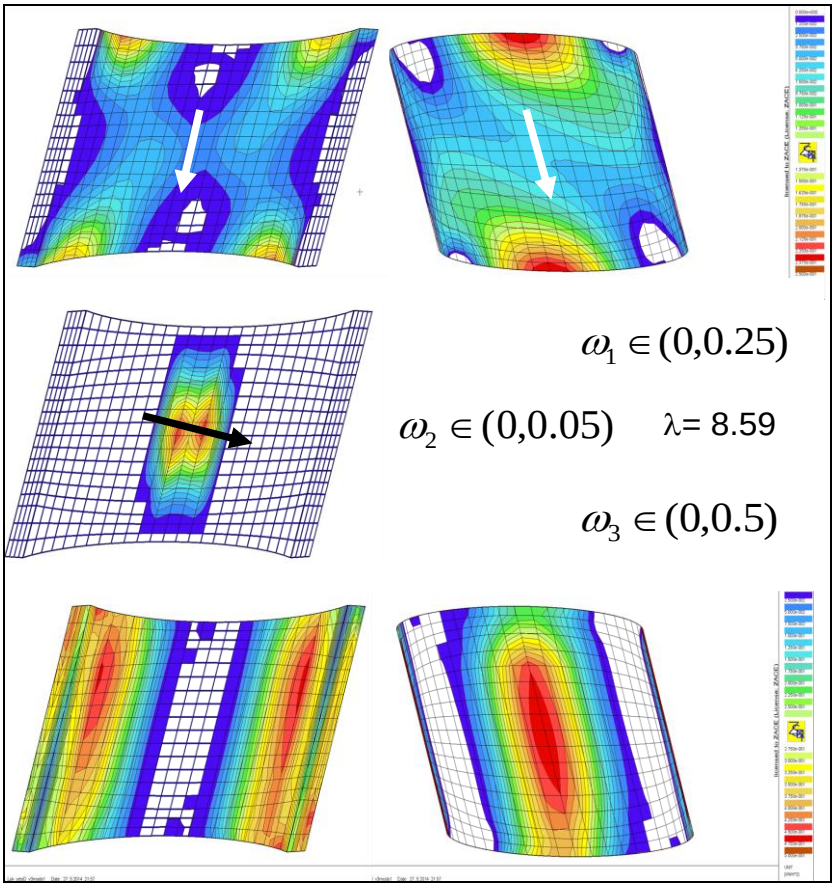

Figure 17: Damage factors ω_i in 3 orthotropy directions.

In Fig. 17, damage factors ω_i in all 3 orthotropy directions are shown. The 1-st and 2-nd direction is marked with arrow. For 1-st and 3-th direction damage factors are given on both sides of the arch. Analysis shows that splitting mechanism (in 3-rd direction, normal to the arch surface) might be, in this case, the most dangerous one. This conclusion agree with some disturbing observation of structure behavior, and confirms correctness of the measures recommended in [5] (anchoring in normal direction).

5. Conclusion

A simple material model for the simulation of the homogenized masonry like media has been presented. The model main feature is the orthotropy of elastic, plastic and damage response. Simplicity of geometry and analytical expression of limit state (yield) surfaces basing on Coulomb friction law with cut-offs on tensile and compressive sides leads to multi-surface elasto-plastic model. The orthotropic damage model adopted is governed by tensile strains. The model perform well in the problem of statics but its performance in problem of dynamics has not been tested yet. Application of the model in dynamics - requires some enhancements of the model (description of crack closure/opening).

Direction of future investigation will concentrate on:

- identification of the macro-model data basing on numerical homogenization and test data, for different types of masonry.
- gathering experience by undertaking more analysis of real masonry structures.

Acknowledgments

Project was co-funded by European Social Fund (ESF), European Union (EU) Agreement no. 11/2013 Nauka dla biznesu Szkolenia i Doradztwo dla Przedsiębiorstw

References

[1] H. Ganz, B Thürliman: *Versuche über die Festigkeit von zweiachsig beanspruchtem Mauerwerk,* Institut für Baustatik und Konstruktion ETH Zürich, 1982.

[2] S. Jemioło L. Małyszko: FEM and constitutive modeling in analysis of masonry structures. Theoretical basis (in polish: MES i modelowanie konstytutywne w analizie zniszczenia konstrukcji murowych. tom 1

Podstawy teoretyczne), Wyd. Uniwersytetu Warmińsko-Mazurskiego, Olsztyn. 2013.

[3] P.B. Lourenço, Computational strategies for masonry structures. PhD thesis, Delft University of Technology, 1996. Available from: www.civil.uminho.pt/masonry.

[4] Ph. Menétrey: *Numerical analysis of punching failure in reinforced concrete structures*, EPFL, Dissertation 1279, 1994.

[5] K. Ryż, A. Urbański: *Assesment of safety of a railway bridge supported by masonry arches* (in polish: *Ocena bezpieczeństwa zabytkowego wiaduktu kolejowego o konstrukcji murowej typu sklepionego*). Materials of VII Scientific Conference „Engineering problems of restoration of historic structures" (in polish: Inżynieryjne problemy odnowy staromiejskich zespołów zabytkowych") Kraków, may 2006.

[6] J.C. Simo, T.J.R. Hughes: Elastoplasticity and Viscoplasticity Computational Aspects, Stanford Univ., Division of Applied Mechanics, 1988.

[7] G.Z. Voyiadjis, B. Deliktas *A coupled anisotropic damage model for the inelastic response of composite materials*. Comput. Methods Appl. Mech. Engrg. 183 (2000) 159±199

[8] R.Zarnić, J.Selich. F.B. Damjanić, S.Gostic *Development of macro and F.E. models of masonry*. Proc. of the 3-rd International Symposium on Computer Methods In Structural Masonry- Lisbon. Ed. Books & Journal International p. 32-42m, 1995.

[9] ZSOIL, User Manual. Elmepress and Zace Services ltd, 1985-2010.

[10] A. Zucchini, P.B. Lourenço *A micro-mechanical model for the homogenisation of masonry* International Journal of Solids and Structures 39 (2002) pp. 3233–3255.

[11] A. Zucchini, P.B. Lourenço *Mechanics of masonry in compression: Results from a homogenisation approach* Computers and Structures 85 (2007) pp. 193–204.

Examples of large-scale simulations of soil-structure interaction with ZSoil

Rafał F. Obrzud*, Krzysztof Podleś**

** Karakas & Français, Switzerland and ZACE Services Ltd*
*** Cracow University of Technology and ZACE Services Ltd.*

Keywords: soil-structure interaction, large scale foundation, deep excavation, tunneling, ZSoil

Abstract

This paper illustrates selected capabilities of ZSoil for preparing and analyzing large-scale, soil-structure interaction simulations. Three examples of real, ongoing projects are presented. In the first example, a complete model of a large scale foundation for a multi-storey office building is illustrated. The soil-structure analysis includes all the construction stages prior superstructure construction in order to account for a realistic stress relief below the foundation. The prediction of settlements is obtained by accounting for combined rigidity of superstructure, foundation slab and, finally, a layout of rigid inclusions which are embedded in highly compressible soil layers.

In the second example, a verification of the feasibility of deep excavation in a close vicinity of an existing building is demonstrated. In this example, a direct SSI analysis allows the building settlement to be analyzed as the function of deflections of an anchored pile sheet wall.

Finally, the last example illustrates a SSI modeling of a tunnel intersection which is excavated below the existing railway tunnel, as well as the existing hospital building.

All the presented numerical simulations are performed with ZSoil, a finite element program which offers a unified approach to model natural processes which are associated with excavation and construction stages. A new ZSoil feature, a possibility of exporting results to the data set understandable by ParaView, a multi-platform data analysis and visualization application, is demonstrated with several customized graphical outputs.

1. Introduction

Deep excavations or tunnel openings in urban areas generally result in ground movements that can induce significant damages to adjacent buildings and services. In order to avoid such movements or reduce their impact, the excavations are supported by retaining walls, struts or anchors, or other temporary support which are installed as the excavation progresses. Unexpected damages or accidents related to excessive settlements can very often be predicted by performing numerical simulations before starting the construction works.

Many times, evaluation of settlements relies on foundation loads obtained from the structure analysis which is performed without allowance for soil settlements. Furthermore, the foundation settlements are often estimated assuming a perfectly flexible structure by applying the foundation loads directly to the subsoil model. However, it is commonly recognized that soil-structure interaction (SSI) can significantly affect the estimated settlements and alter internal forces of structural members. In order to account for an actual, stiffness-driven interaction between the structure and soil, these two distinct parts have to be included in a direct analysis. In the direct analysis, the soil and structure are included within the same model and analyzed as a complete system [1].

A rigorous SSI analysis should also include an adequate choice of constitutive laws describing both soil and structural elements, a reliable selection of parameters, as well as the adoption of the correct type of analysis [2]. These elements make static SSI analysis - particularly with the reference to serviceability limit states - one of the most challenging tasks in modern geotechnical engineering.

In this paper, the Hardening Soil model has been adopted to describe complex soil behavior [3, 4, 5, 6, 7]. This model has received a lot of attention of geotechnical engineers over the past fifteen years, as it is able to accurately predict the deformation and stress states for commonly-solved boundary problems, such as deep excavations, tunneling, shallow or deep foundations, and pile rafts. The rock mass in the tunnel excavation project, Section 4, is described with the original Hoek-Brown model [8, 9].

This paper illustrates examples of implementation of SSI within a design setting. In the first example (Section 2), a complete model of a large scale foundation for a multi-storey office building is presented. The SSI analysis includes all the construction stages prior superstructure construction in order to account for a realistic stress relief below the foundation. The prediction of settlements is obtained by accounting for combined rigidity of superstructure, foundation slab and, finally, a layout of rigid inclusions which are embedded in highly compressible soil layers.

In the second example, a verification of the feasibility of deep excavation in a close vicinity of an existing building is demonstrated. In this example, a direct

SSI analysis allows the building settlement to be analyzed as the function of deflections of an anchored pile sheet wall.

Finally, the last example illustrates a SSI modeling of a tunnel intersection which is excavated below the existing railway tunnel, as well as the existing hospital building.

All the presented numerical simulations are performed with ZSoil, a finite element program which offers a unified approach to model natural processes which are associated with excavation and construction stages. Utility of ZSoil in the context of large scale modeling is demonstrated. The presented simulations include between 400'000 and 800'000 degrees of freedom, but larger computations (1'500'000 DOFs are proved to be also feasible.

In order to obtain customized graphical outputs, some of the images were generated with the aid of ParaView, an open source, multi-platform data analysis and visualization application [10]. Paraview is known and used in many different communities to analyze and visualize scientific data sets. Since 2016, ZSoil has been offering the new feature that allows ZSoil results to be exported to the file formats that ParaView understands.

ParaView can be used to build visualizations to analyze data using qualitative and quantitative techniques. ParaView runs on distributed and shared memory parallel and single processor systems making the data analysis for large scale models very effective. Since ParaView is a multi-platform application (it has been successfully tested on Windows, Mac OS X, Linux, IBM Blue Gene, Cray Xt3 and various Unix workstations, clusters and supercomputers), ZSoil-produced data sets can be visualized using different operational systems.

2. Design of a multi-storey office building

This section presents an approach to design and verify a large scale foundation for a multi-storey office building. This example illustrates a complex global modeling of SSI which takes into account all the construction stages.

The presented project (Fig. 1) is part of the PONT-ROUGE property development project by Federal Swiss Railaways which foresees the creation of a new urban hub located less than two kilometers from the Geneva city center and will benefit from first class accessibility [11]. Aiming to enhance the perimeter around the Lancy-Pont-Rouge train station, it is one of Geneva region's biggest real estate projects. The creation of an urban area on both sides of the new Lancy - Pont Rouge railway station includes the construction of five buildings for different facilities. They correspond to a total surface of approximately 120'000 m^2 and will include office space, as well as space for complementary facilities such as restaurants, cafes, small businesses, leisure activities, public facilities and a hotel complex.

PROJECT FACTS

Location: Geneva, Lancy
Objective: 9 main office buildings divided into 5 lots (B1-B5)
Dates: 2012 - 2024
Client: Federal Swiss Railways
Structural engineers: EDMS - Geneva
Geotechnical engineers: Karakas & Français - Geneva/Lausanne

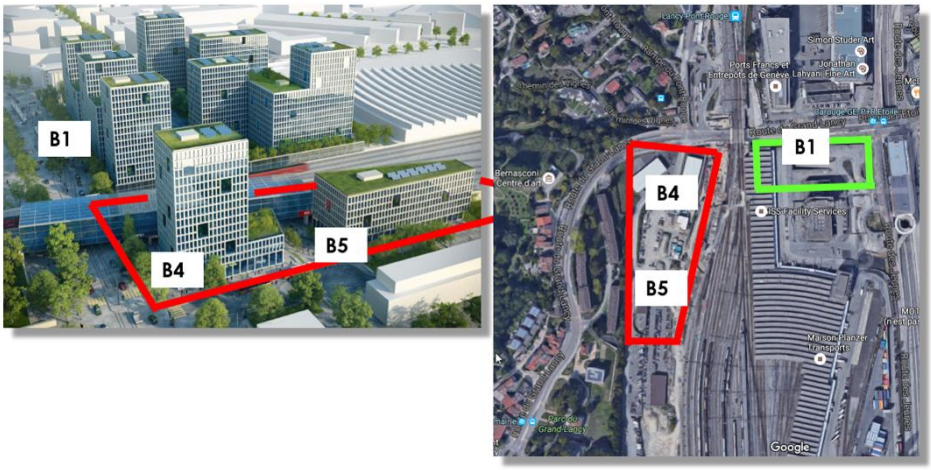

Figure 1: Architectural view model on the PONT-ROUGE property development project. B1 lot under construction, B4-B5 to be built.

With regards to numerical modeling, the first part of the project - lot B1 (Fig. 1) was presented in [12, 13]. Excavation works for a common underground structure for a complex of three towers in B1 lot are currently underway.

The numerical simulation which will be presented here, concerns two lots: B4 and B5 (Fig. 1). These two structures are two multi-storey office buildings, 13 and 5 floor-high, respectively (Fig. 2). Both buildings are core-supported outrigger structures: interior shear concrete shear walls and outriggers - concrete columns (cf. [14]). A complex of the two buildings and the underground structure was modeled with ZSoil and is presented in Fig. 3. It was deliberately decided to model the entire above-ground structure in order to take into account the global rigidity of the structures, as well as to automatically compute the body forces acting on the foundation (dead and live loads were initially not given by structural engineers).

One of the particularities of this complex of buildings is that they share a thick, continuous bottom slab. The continuity was designed to ensure waterproofing as, in the final stage, the underground structure will remain submerged below the ground water table which is located about 2.5 m above the bottom of the foundation. Depending on the load magnitude in particular zones,

the foundation slab has varying thickness: 120, 80 and 60 cm below B4, B5 and underground parking, respectively (see Fig. 9). In order to simulate a realistic stress redistribution, it was decided to model the bottom slab by means of 5, 4 and 3 rows of *Continuum For Structure* elements, respectively. In addition, all the underground walls were also discretized by means of continuum elements. In turn, the frame of the above-ground structure was modeled with the aid of elastic shells for walls and floors, and elastic beams for floors. It was assumed that the Young's modulus accounts for possible concrete cracking and a long-term creep.

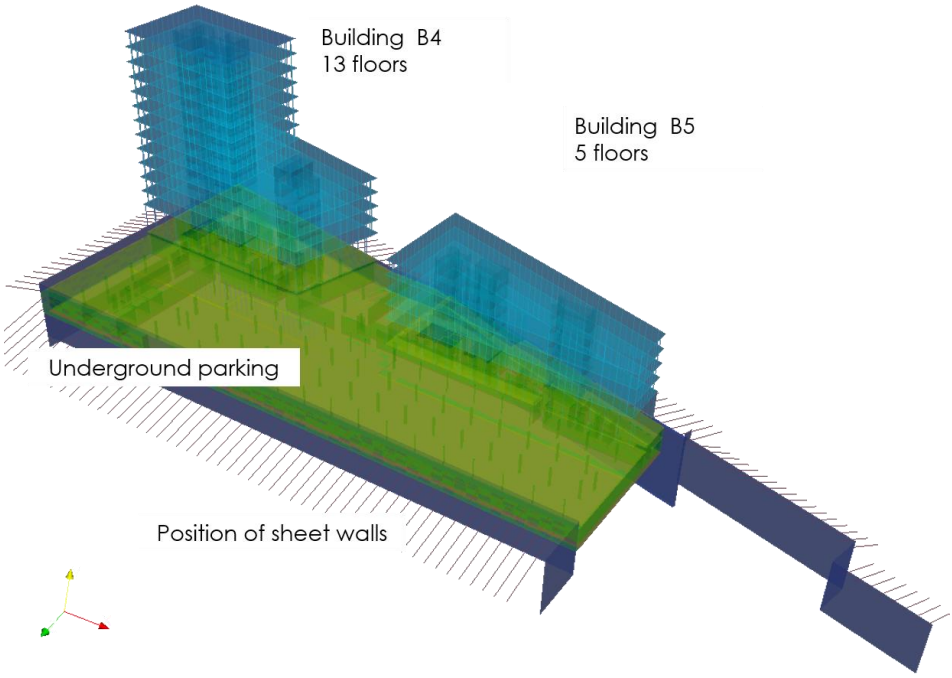

Figure 2: Main components of the structure. Visualization of the ZSoil-generated model by means of ParaView [10].

Since ZSoil offers a unified approach to model natural processes which are associated with construction phases, the excavation and construction stages were simulated explicitly. In order to support the excavation for below grade structures, sheet wall technique was designed and modeled along the planned excavation perimeter (Fig. 2). The interlocked sheet piles will form a wall for a temporary lateral earth support with reduced groundwater inflow. The anchors were included in the model to provide additional lateral support considering that the excavation depth is about 8 m.

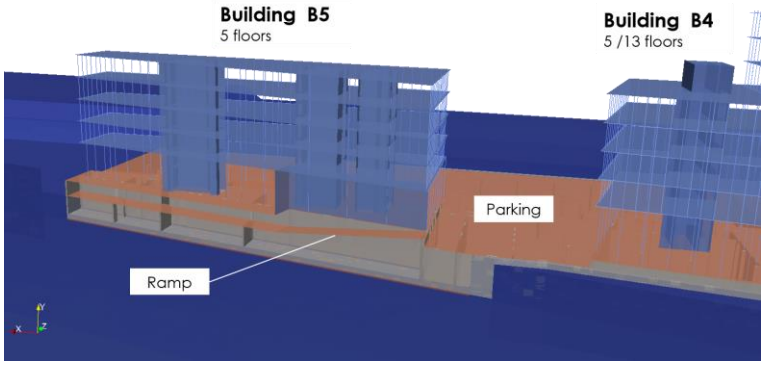

(a) Ramp

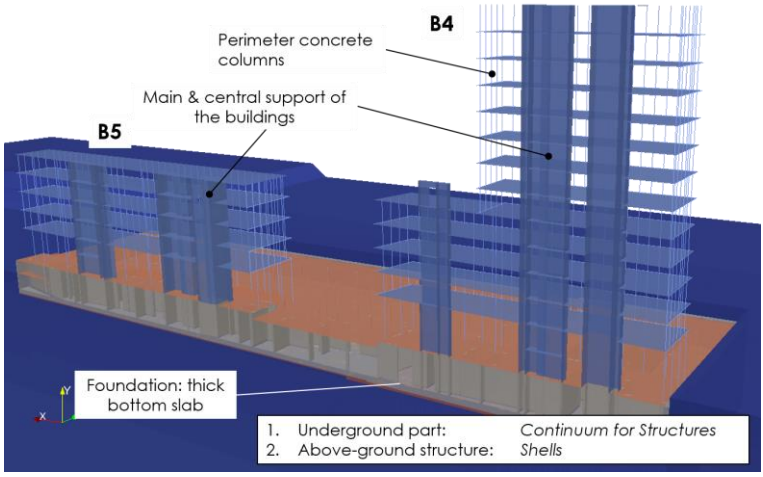

(b) Concrete cores

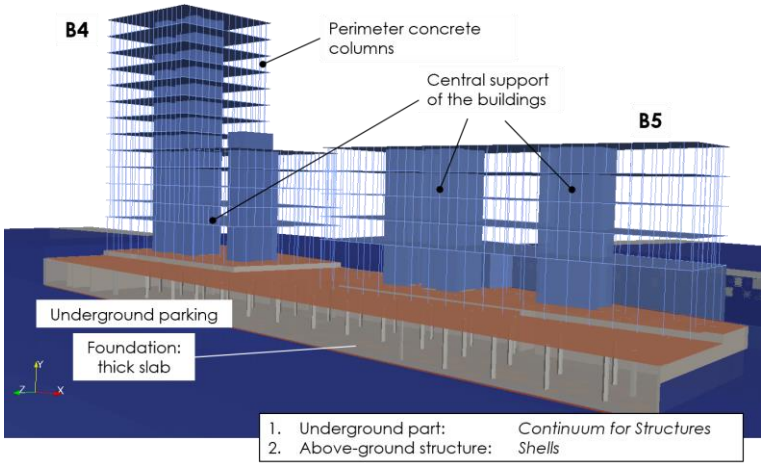

(c) Underground parking

Figure 3: Buildings B4-B5: longitudinal sections.

In this particular example, the global modeling approach to simulate the excavation and construction stages allowed the following issues to be computed and evaluated:

- efficiency of retaining walls during excavation
- realistic magnitudes of stress and deformation in the subsoil around the excavation
- long-term total and differential settlements resulting from dead and live loads by taking into account a global rigidity of the structure
- total stresses acting below the bottom slab, as well as the bending moments built up in the bottom slab due to dead and live loads, and ground water table rise after halting of water pumping
- effect of ground improvement with the aid of rigid inclusions (modeled with piles but not connected with the slab as the pile head are designed to be located below a compacted layer of gravel)
- stresses and moments acting on the bottom slab in the case of an accidental high level of the ground water table

One of the challenges in preparation of large scale model is the number of different members which are included in the FE model. In this context, FE models should be prepared using so-called macro modeling which allows the user to create macro zones for which a virtual mesh can be automatically generated and main attributes easily modified including automatic updating in the final FE mesh. It is also recommended to divide the main model components such as subsoil, system of anchors or on-ground structure, in separate files that can be assembled in the final stage of preprocessing. If needed, selections and action processes like copy, move, modify parameters, can be sped up by inactivating "Undo" in the preprocessor. Rapidity of preprocessing and, most of all, computing can be considerably boosted by applying advanced interpolation techniques, i.e. *mesh tying* or *nodal link* (see [3] for detail), which handle two incompatible meshes, typically fine and coarse, providing accurate solutions for the reduced number of finite elements, cf. Fig. 4(a).

One of strong points of ZSoil is that the preprocessing, computing and postprocessing are handled by separated modules. It allows the user to run the calculation for preliminary analyzes, postprocessing results during computing, as well as including new modifications in the preprocessor. It may sometimes result in the multi-opening of the preprocessor which in the case of a large scale-model, can be time-consuming. The development of the presented model revealed the need for speeding up the load time of input files. A close collaboration between the modeling engineer and software developer relying on the precise communication of drawbacks and needs has resulted in a dramatic speed improvement for file loading. Starting from ZSoil 2016 v16.03, the load time has been reduced by the factor of 10 for the components that suffered inefficiency in the previous versions, interfaces and subdomains, respectively (see Fig. 4(b)).

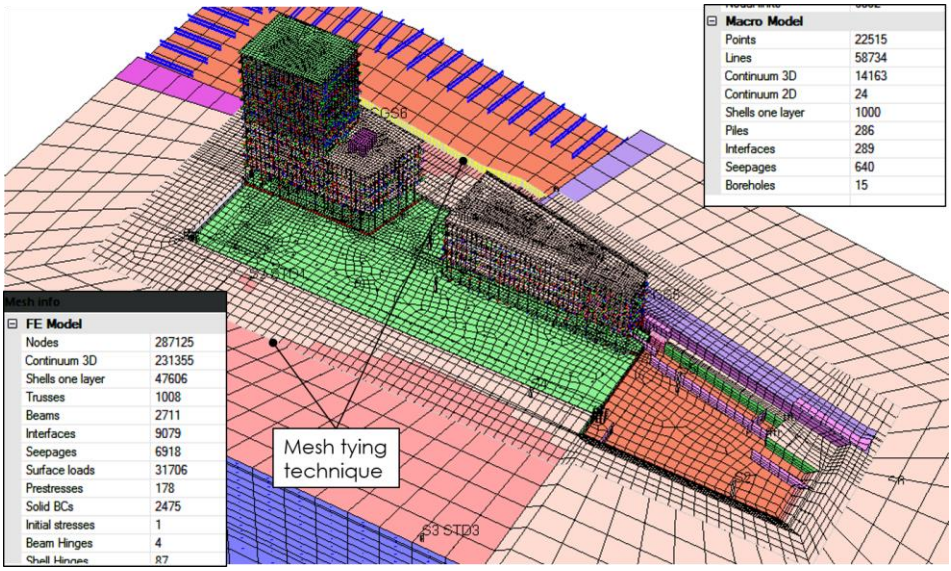

(a) 3D model data view. Number of components in Macro and FE models.

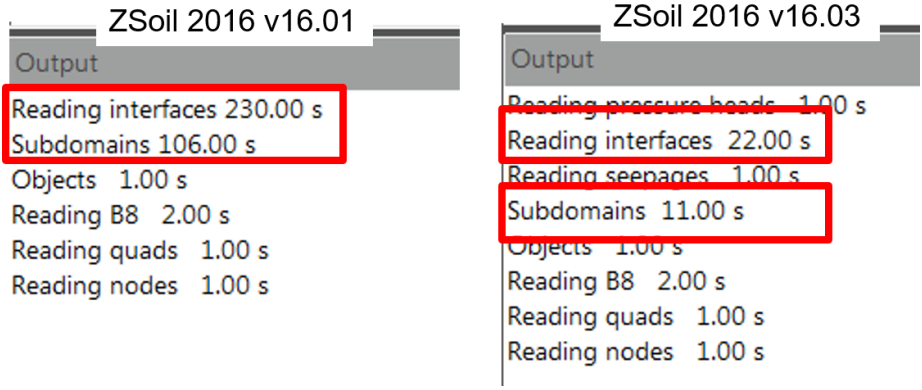

(b) Load file times in previous and new versions of ZSoil PrePro

Figure 4: View of large scale model prepared with ZSoil Preprocessor and improvements in data load time for the large scale model.

The main objective of the presented simulations was to qualitatively evaluate the effectiveness of the proposed foundation solution but also to predict building settlements. In order to establish realistic magnitudes of stress and deformation in the soil below and around the foundation, a realistic simulation of excavation stages was carried out. It was assumed in the preliminary analysis that the sheet pile walls remained in the ground over the whole simulation including the stage of building construction and application of live loads, see Fig. 5(a). As a result, the settlements are concentrated within the envelope defined by the planned excavation perimeter and they are distributed more or less uniformly below the main concrete core up to the sheet wall. It is so because, in such a configuration,

soil is constrained by the retaining wall which ensures discontinuity of the displacements with respect to the soil elements outside the excavation perimeter, as illustrated in Fig. 5(b).

The final analysis was carried out once the sheet pile wall removal had been placed within the construction schedule. For budgetary reasons, it is foreseen to remove the sheet wall once the underground and the back-filling on the underground parking have been completed. These are required to stop water pumping within the excavation perimeter. It can be easily guessed that the removal of The sheet wall will restore the continuity of displacements and pore pressures below the foundation level, inside and outside of the excavation perimeter. Since the sheet wall removal was carried out after a partial loading due to underground construction, a partial displacement continuity can be observed in the model, as shown in Fig. 5(c). Although the magnitude of maximal settlements does not change, the redistribution of displacement which can be noted on the color maps, have influence on the distribution of internal forces in the bottom slab and walls of concrete structure.

Fig. 6 explains how to explicitly discretize the interface elements within the time space. It is shown that the first contact apparition takes place after sheet wall installation on the both sides of the shell elements. A new contact has to be defined on the interface elements on the excavation side when the backfill occupies the space between the underground and sheet pile walls. Finally, the previously decoupled nodes at the interface are tied in terms of displacements and pore pressures, rendering the absence of the temporary sheet wall.

Verification of the effectiveness of the designed foundation system was carried out with the model that included 286 pile objects; the inner and outer layouts are shown in Fig. 7(a). The piles represent concrete rigid inclusions which are intended to transfer loads to underlying stiffer stratum and improve the global response of the soil in order to better control the settlement of the building, as illustrated in Fig. 7(c). The obtained results showed that well distributed settlements are inferior than 3.0 cm.

The proposed solution with the rigid inclusions was confirmed to be appropriate by running a model without piles. It can be noted in Fig. 8(a), that the base solution resulted in settlements about 4.0 cm. However, when applying additional extra load, the maximal settlement increases dramatically up to 6.2 cm, as shown in Fig. 8(d). Moreover, the zone of maximal displacements moves towards the building corner what can potentially lead to an inclination of the tower.

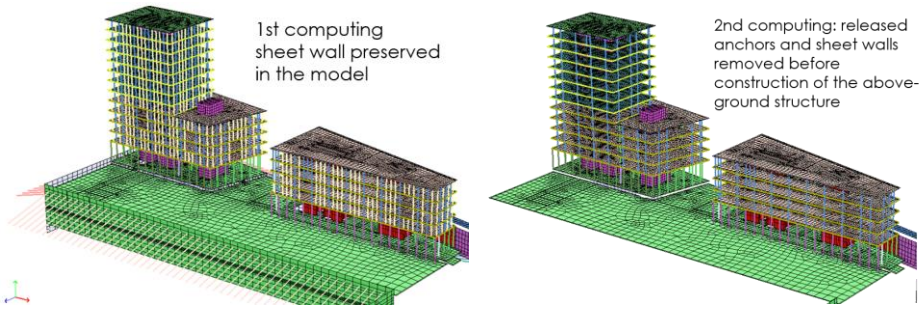

(a) Initial construction stage scheme (left) and final model (right)

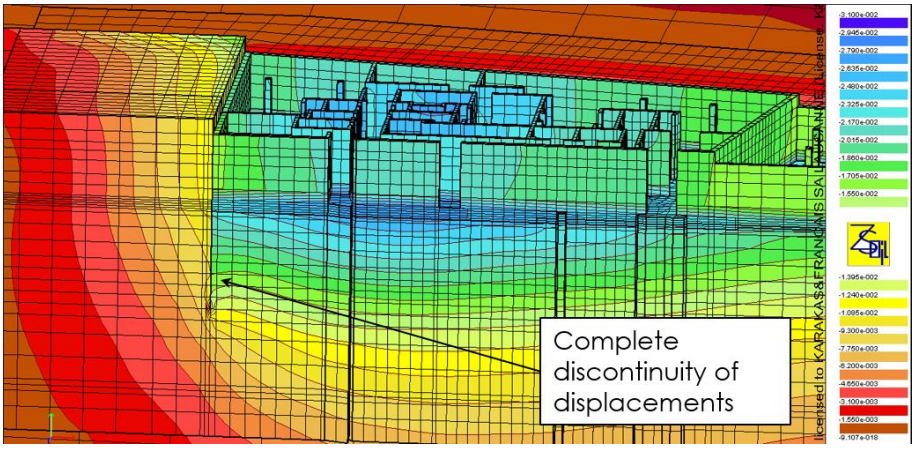

(b) Initial construction stage scheme

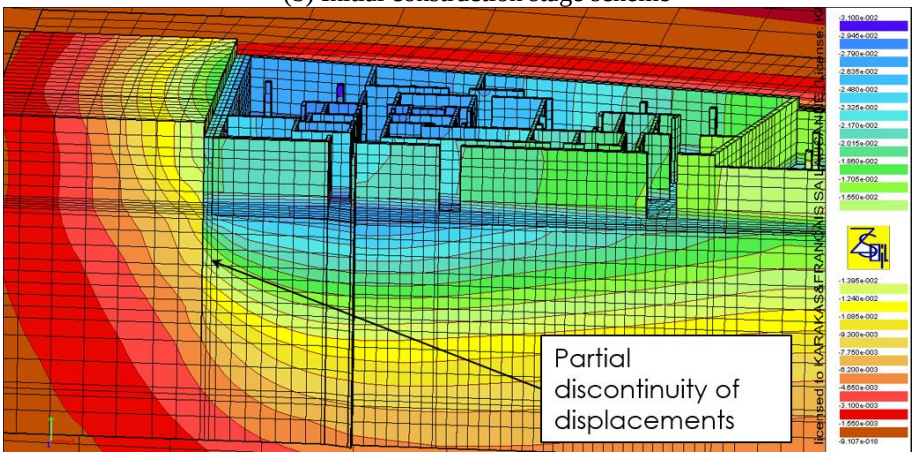

(c) Final construction stage scheme

Figure 5: Influence of discretization of construction stages on prediction of displacement field.

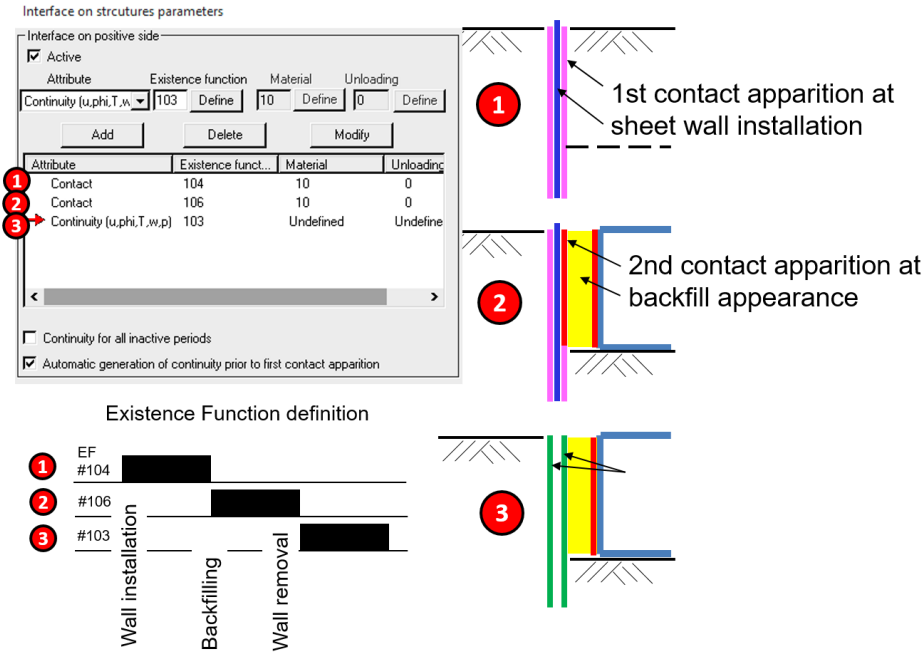

Figure 6: A complex discretization of interface elements accounting for backfilling and sheet wall removal.

The complete models can be successfully used to evaluate internal forces in the bottom slabs. The advantage of this approach is that the upward subgrade reactions are computed intrinsically being a function of the contact pressure intensities and soil settlements. As mentioned above, the bottom slabs were modeled using *Continuum for structure* elements which ensure a correct representation of flexural stiffness. In such a case, contrary to shell elements, retrieving of the bending moments is cumbersome, or sometimes even impossible using internal ZSoil's methods when the mesh is highly unstructured in the plane.

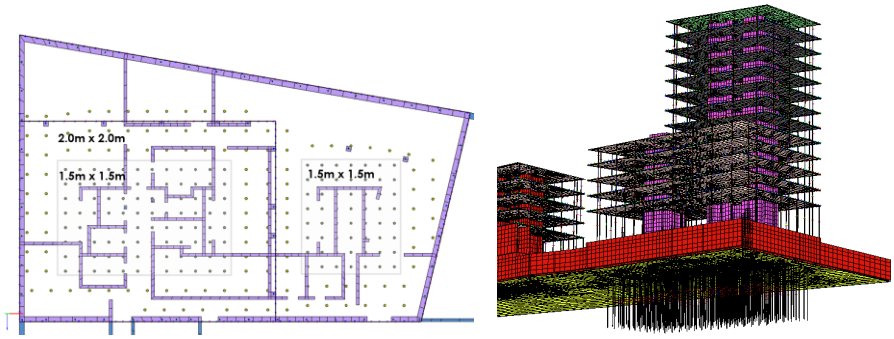

(a) View of rigid inclusions distribution (b) View of rigid inclusions from bottom

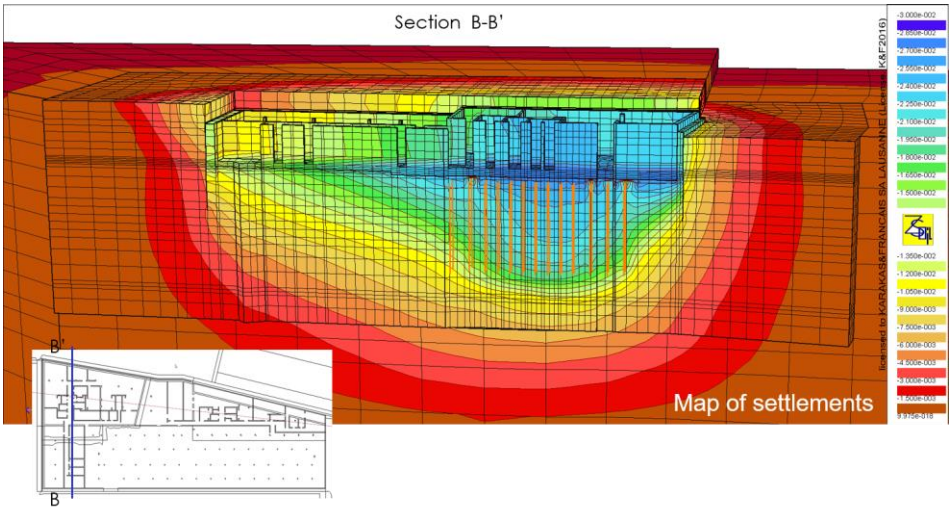

(c) Map of settlements - cross section through the concrete core

Figure 7: Solution with rigid inclusions below the concrete cores: load redistribution to deeper bedded soil layers.

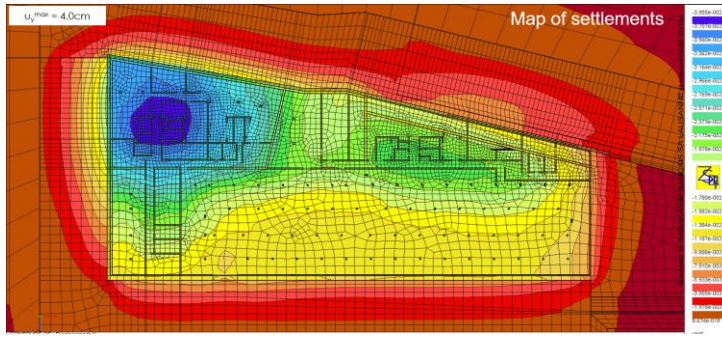

(a) 100% of dead+live loads

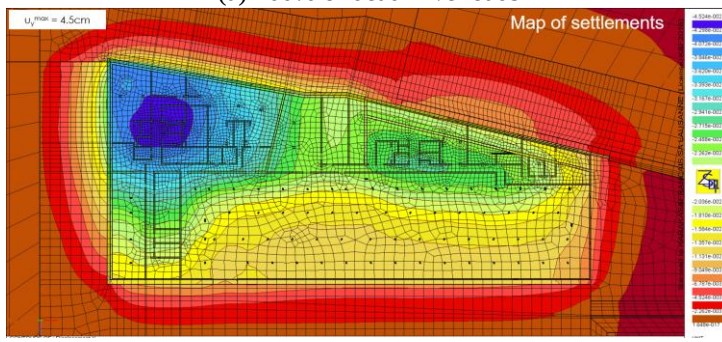

(b) 100% of dead+live loads + 20% of extra load

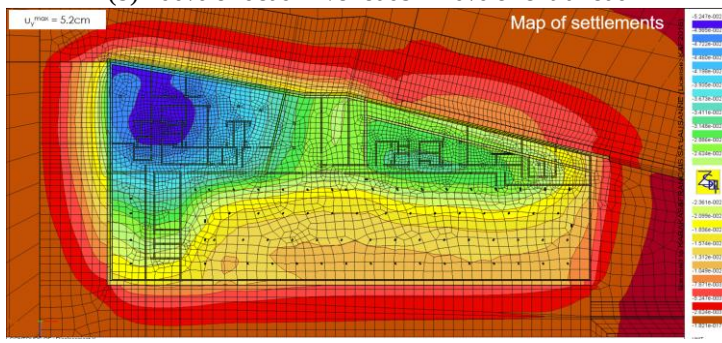

(c) 100% of dead+live loads + 40% of extra load

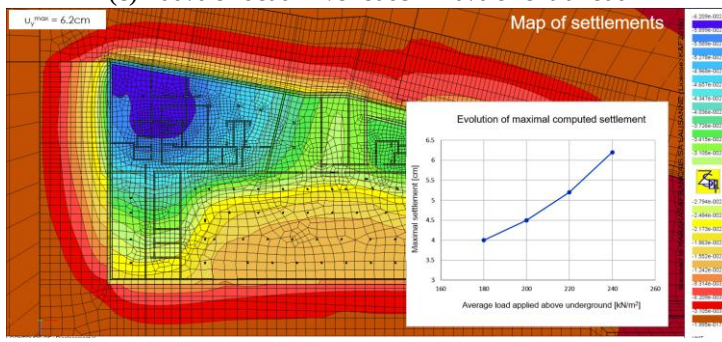

(d) 100% of dead+live loads + 60% of extra load

Figure 8: Solution without rigid inclusions below the concrete cores.

Fig. 9 presents a solution which consists of embedding auxiliary elastic

one-layer shells in continuum elements in the middle of the slab height. Note that the mesh compatibility is not required and the *nodal link* technique can be used if necessary. Thickness of the embedded shell should render the actual slab thickness but the Young's modulus has to be reduced so that it does not affect the flexural stiffness of continuum elements, say by factor of 1'000'000. Finally, in order to obtain the actual order of magnitude of bending moments, the computed results have to be increased by the same factor as the one used to decrease Young's modulus.

1. Assume:
a) shell thickness = thickness of bottom slab modeled with continuum
($I_{shell} = I_{continuum}$)
b) reduced Young's modulus for shell
$E_{shell} = E_{continuum} / 10^6$

2. Interpret results:
a) $M_{slab} = M_{shell} \cdot 10^6$

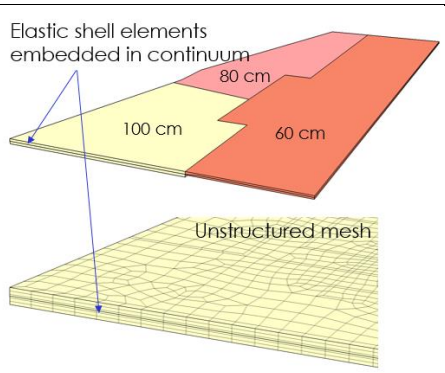

Figure 9: Retrieving bending moments from the unstructured mesh (bottom slab) by embedding one-layer shell elements in continuum elements (Continuum for Structures) -assumptions to be made.

An example of bending moments retrieved from embedded shells is illustrated in Fig. 10. The maps are plotted by a standard ZSoil's routine: *Maps -> Shells -> Moment*.

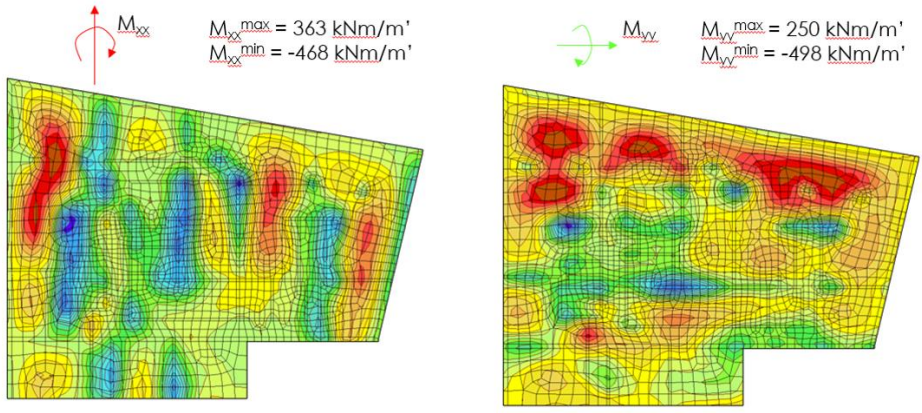

Figure 10: Maps of bending moments M_{xx}, M_{yy} computed for shell elements representing the bottom slab and the maximal values obtained as $M\ slab = M\ shell \cdot 10^6$.

3. Excavation supported with pile sheet

Built at the time of Expo'64, the sewage treatment plant in Vidy, Lausanne, no longer meets modern standards. Moreover, its capacity and performance no longer meet the needs of inhabitants of 15 towns which are included in the agglomeration of Lausanne. The renovation project contest launched in 2014 aims at improving the processing facilities to ensure impeccable quality of treated water. Maintaining high architectural, landscape and biological quality was a challenge faced by the winner project MONA by M+N architects (Fig. 11). The rehabilitation works started in 2016.

The presented modeling is a small part of a large scale project aiming at the construction of new buildings. Nevertheless, some of the existing facilities, which do not require to be completely renovated, will be maintained operational in the future. As a result, the construction works take place in close vicinity of the existing buildings.

PROJECT FACTS

Location: Lausanne, Vidy
Objective: Modernization of the sewage treatment plant
Cost: 300 millions CHF
Dates: 2016 - 2021
Client: City of Lausanne and Epura SA
Geotechnical engineers: Karakas & Français – Lausanne

Figure 11: Architectural view model of the new sewage treatment plant in Lausanne and the model perimeter for simulating an excavation next to the incineration building.

A verification of the feasibility of deep excavation in the light of admissible settlement of an adjacent existing building was the main goal of the presented simulation. Fig. 12 shows the FE model at the final stage of the excavation. The image illustrates a 7 to 10-meter deep excavation which is located 7 to 13 meters

from the incineration building. The excavation is supported by an anchored sheet pile wall which forms an outgoing corner. This makes this setup challenging to realize due to a complex intersection of the anchoring system in which the prestressed anchors are inclined in many planes. Moreover, often the first row of anchors has to be replaced with less efficient system of nails (long anchors cannot be installed because of the building walls).

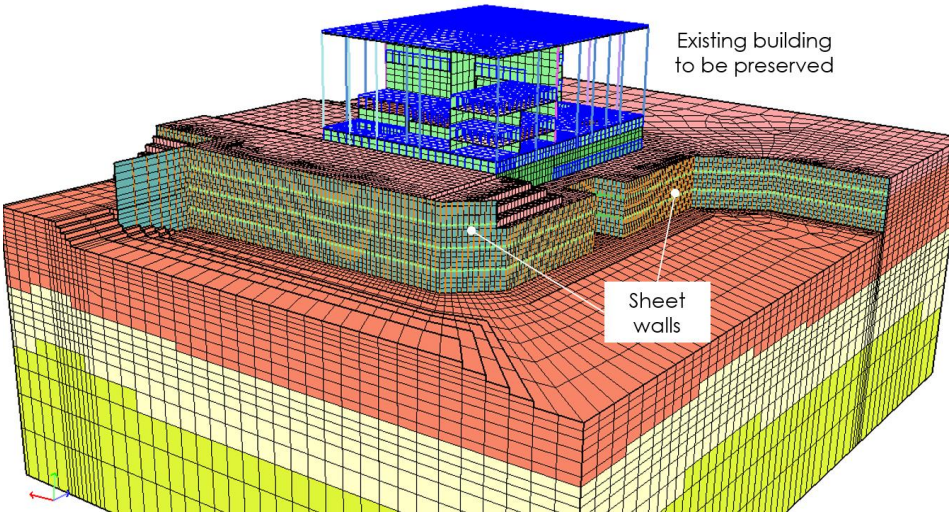

Figure 12: View of the model at the final stage of the excavation.

With regards to the FE model, it was constructed with a considerably smaller number of macro subdomains compared to the previously presented model. Moreover, mostly structured meshing was applied, which reduces the load time for macro models when the preprocesor is reopened. Nevertheless, the load time was still considerable for the interface elements (86 sec., see Fig. 13). The implementation of new algorithms for loading interface elements in ZSoil 2016 v16.03 allowed the load time to be reduced by the factor of 14 in this particular model, making the reopening large scale models less time consuming.

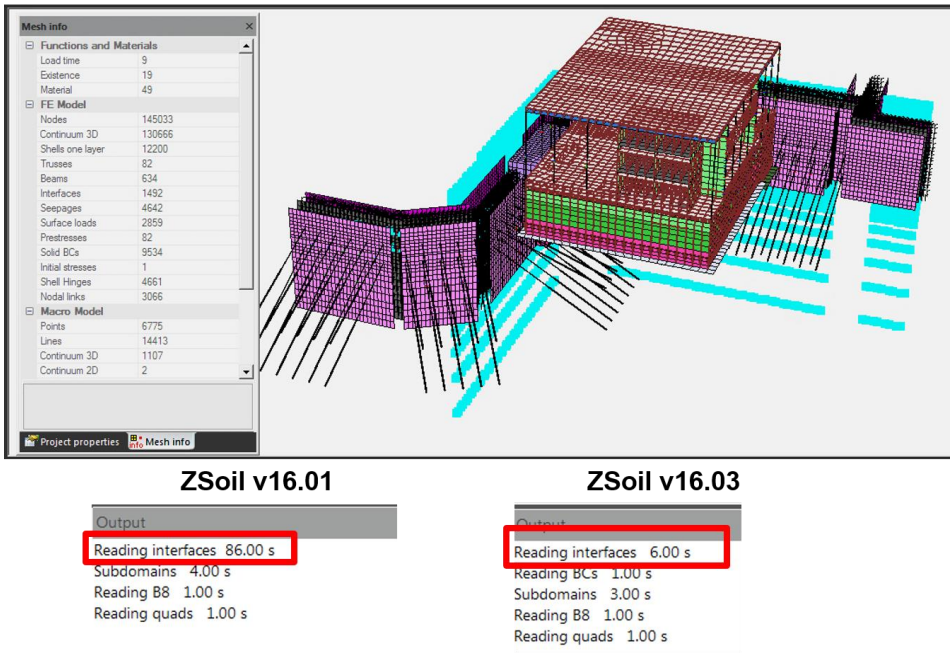

Figure 13: View of retaining wall system with 1492 interface elements and comparison of load times required for reading interface elements by ZPreProcessor v16.01 and v16.03.

In order to accurately predict wall deformations in the outgoing angle, attention had to be paid to an appropriate definition of horizontal flexural stiffness. Several approaches can be considered when modeling the sheet pile wall:

1. continuous isotropic shell - admissible for "infinitely" long excavations but inadequate in this case as it overestimates the stiffness of retaining structure in horizontal direction
2. continuous orthotropic shell - significantly reduced stiffness can be assumed in the horizontal direction
3. sheet pile width modeled explicitly assuming discontinuity between isotropic shell elements - introduction of plastic hinges along sheet pile connection - adopted approach (Fig. 14)
4. explicit modeling of geometry of each pile sheet - unnecessarily complex in this particular case

Since a fine mesh discretization was demanded around the outgoing corner, the third approach was adopted to model the sheet pile wall. An introduction of plastic hinges along the sheet pile connections allowed rotational constraints to be released (assumed perfectly plastic joint), as presented in Fig. 14. Moreover, in order to ensure possible relative displacements along the connections, uncoupling of translational degrees of freedom was assumed once deliberately chosen threshold of 5 kN had been achieved for small displacements.

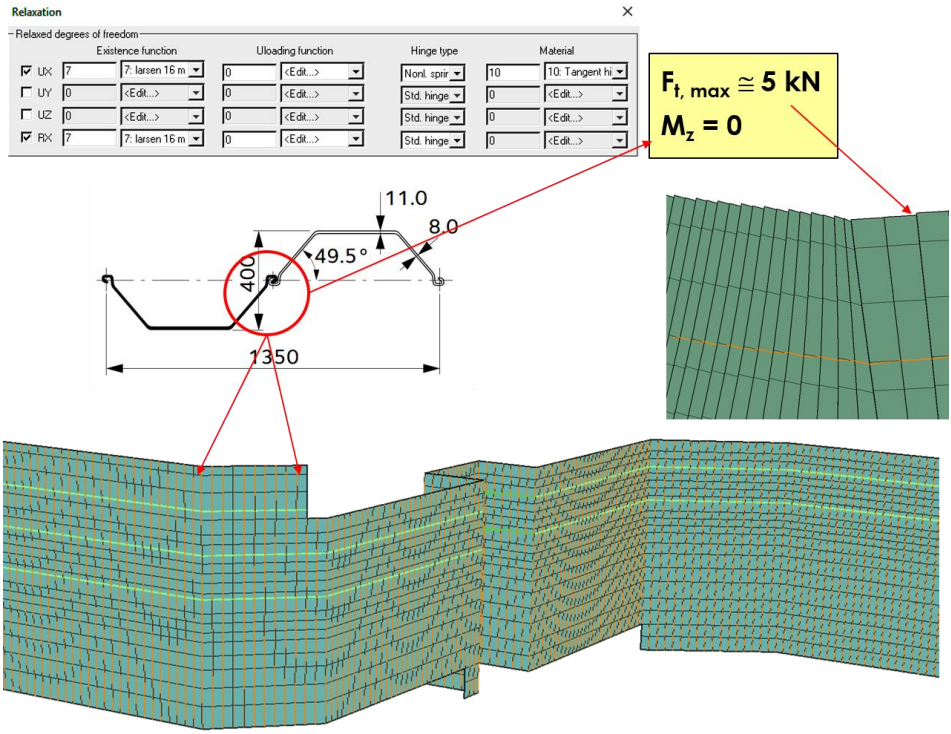

Figure 14: Adopted approach for modeling of sheet wall including explicit discontinuity between isotropic shell elements representing sheet pile width.

For the sake of comparison, computation assuming a continuous isotropic shell was also carried out resulting in 50 % smaller wall displacements than the one considered to be reference one, as depicted in Fig. 15.

The detailed model discretization in terms of both, geometries and excavation stages, allowed the following issues to be computed and controlled:

- global SSI response
- settlements of existing building
- efficiency of retaining wall and anchoring system in terms of soil deformations around the excavation
- internal forces in sheet piles, horizontal stiffeners, anchors and nails

Moreover, 3D modeling made it possible to optimally design the anchoring system starting from traditional 2D drafts Fig. 16 .

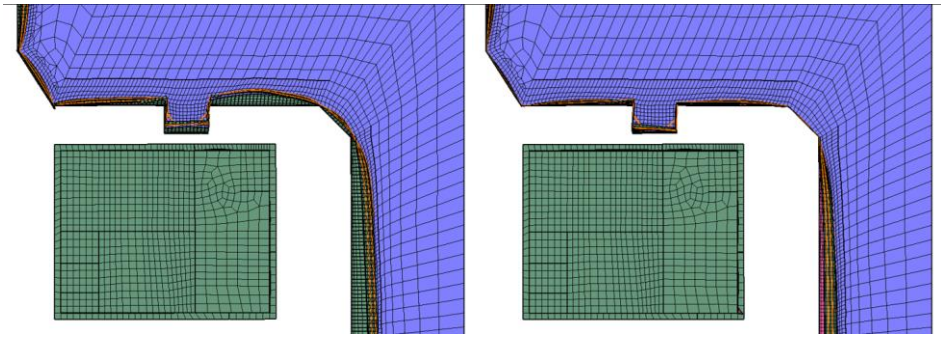

(a) Continuous isotropic shell elements (b) Discontinuous isotropic shells (plastic hinges)

Figure 15: Comparison of the deformed mesh for two models (amplification x100); the approach with discontinuous shells results in displacements 50% larger than those computed for continuous isotropic wall.

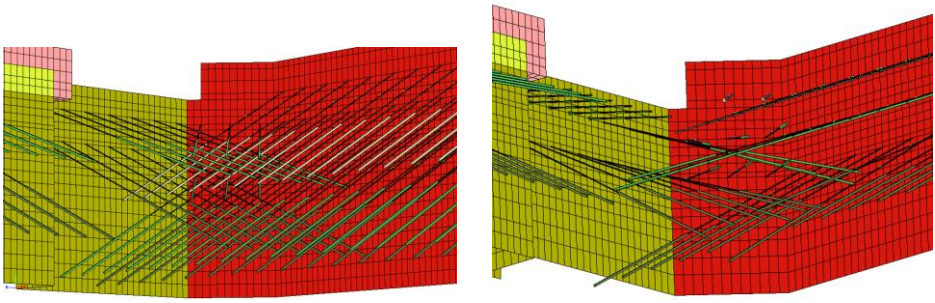

(a) Initial (b) Final

Figure 16: Implementation of anchor layout: a) preliminary based on 2D drafts (impossible to realize in practice), b) optimized with ZSoil PrePro, accounting for placement tolerances.

Fig. 17 illustrates an effective results exploration with the aid of ParaView. The magnitude of horizontal displacements, max. about 4.0 cm as shown in Fig. 17(b), was confirmed by observations in the adjacent sectors already excavated in the first half of 2016.

The cross-sectional view located right below the building foundation shows that the expected vertical soil displacements are very small, as shown in Fig. 17(c). Fig. 18(b) The obtained settlements of the building are small and do not exceed 6 mm, differential settlements are acceptable.

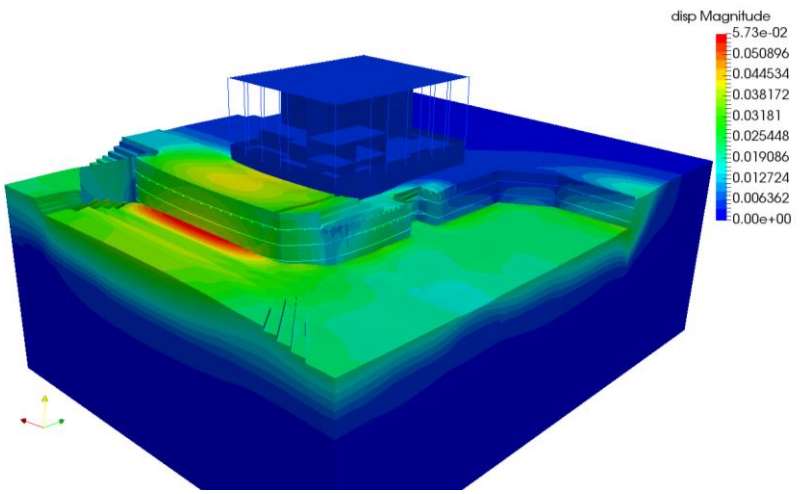

(a) Absolute displacement

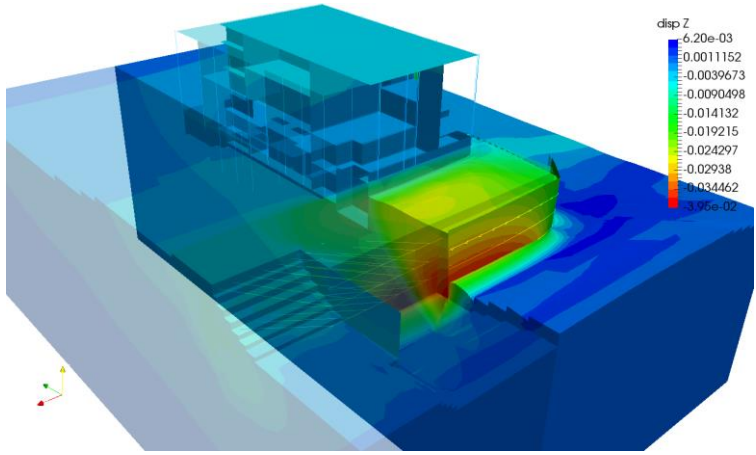

(b) Horizontal displacement in Z direction

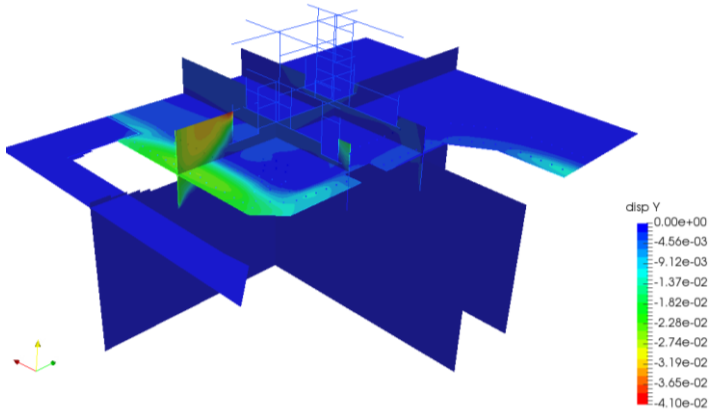

(c) Settlements

Figure 17: Visualization of displacement fields with ParaView.

Although ParaView is an excellent alternative solution for dataset visualization, ZSoil PostProcessor remains irreplaceable for rendering results specific to civil engineering, such as diagrams of internal forces. Sometimes it can be useful to present two different types of graphical interpretations on the same chart. Such a solution can be achieved by superposing two ZSoil screen shots in MS PowerPoint and making one of the white backgrounds transparent. An example is given in Fig. 18(a) and it illustrates the diagram of A bending moment along the most deflected part of the sheet pile wall.

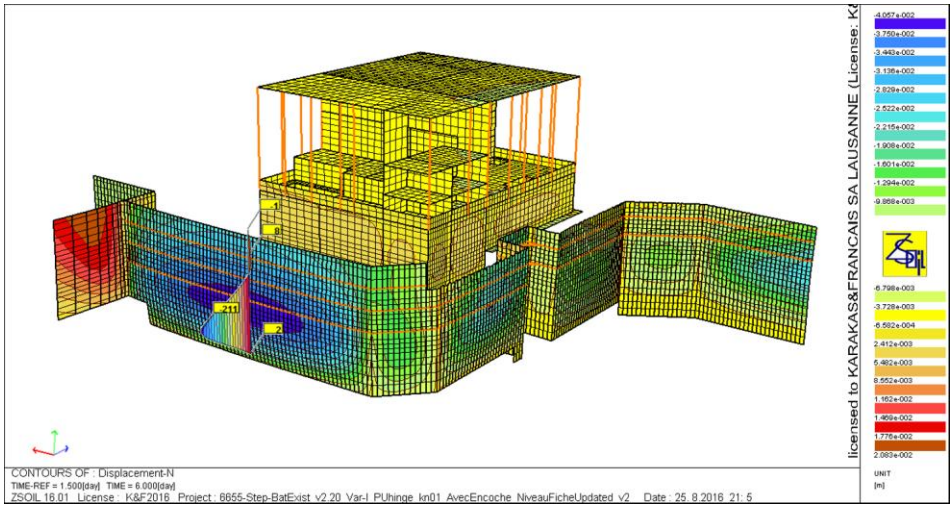

(a) Normal displacement of sheet wall and maximal bending moment

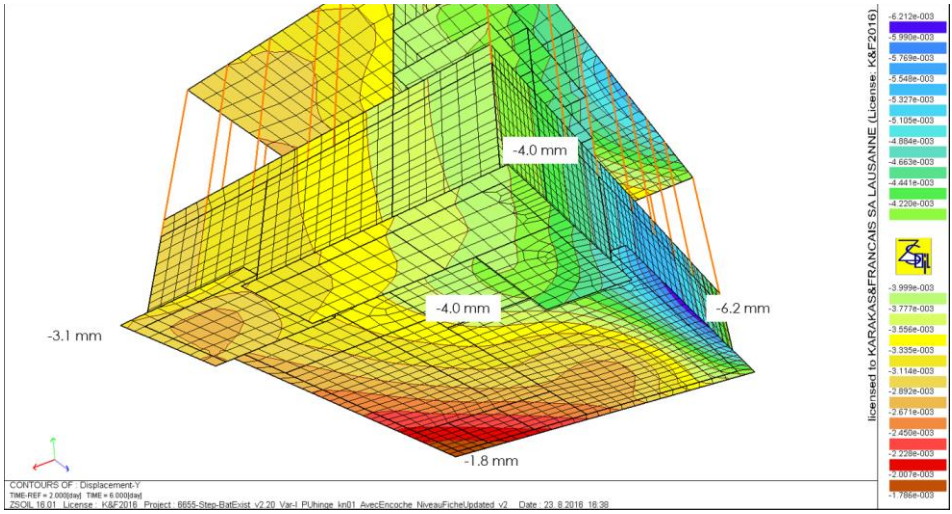

(b) Settlements below foundation of building

Figure 18: Visualization of displacement for retaining structure and foundation of building with ZSoil.

4 Interaction between excavated tunnels

The LEB train ensures a vital link between the center of Lausanne and its northwestern part and Gros-de-Vaud district. Since 2000 and since its extension to Lausanne-Flon, the frequency of the LEB train has continuously increased with the number of passengers 156 % higher than 10 years before.

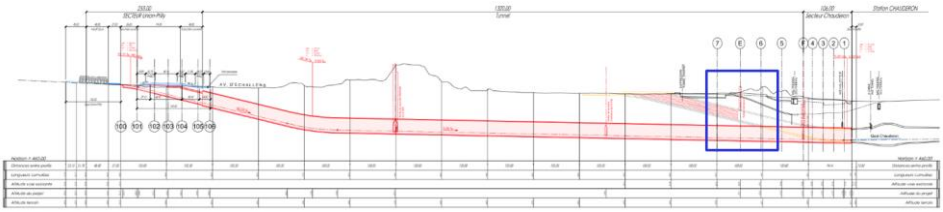

PROJECT FACTS

Location: Lausanne - Prilly
Objective: 1.4 km tunnel Lausanne Chaudron - Union-Prilly
Cost: 145 millions CHF
Dates: 2017 - 2020
Client: Canton of Vaud, City of Lausanne, T-L, LEB
Engineers: Monod & Piguet - Lausanne, Karakas & Français – Lausanne, CSD - Lausanne

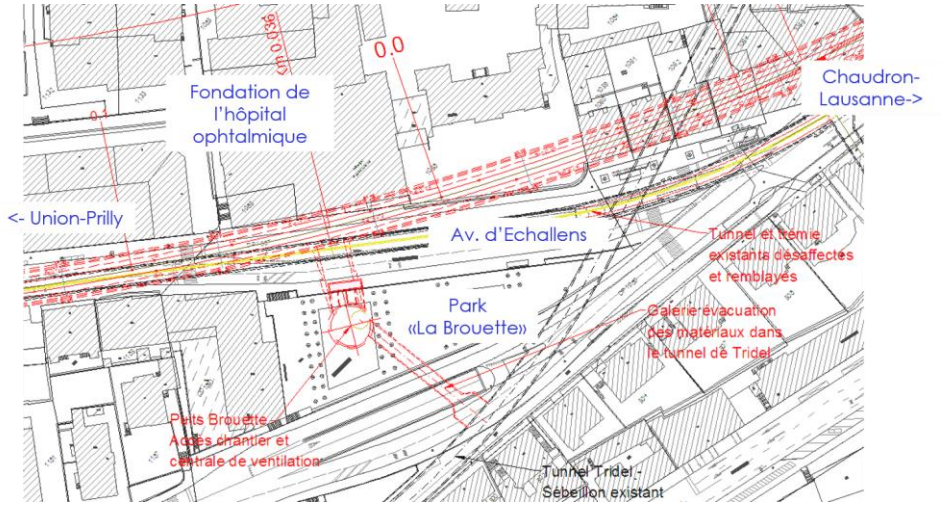

Figure 19: Longitudinal section of the designed tunnel and an aerial view zoom on the analyzed lot.

Despite many improvements, one of the weak points of this line is a dangerous sector which is located in Echallens Avenue. In this section, the railway shares the line with other road users: cars, bicycles and pedestrians. This unfavorable

configuration has led to numerous accidents including a fatal one. Despite urgent countermeasures that were taken between 2009 and 2014 in order to improve security, the risk of further accidents remains high.

For the authorities, transferring the railway underground was the most appropriate solution for the final elimination of the hazard. The new tunnel of about 1400 m will link the Chaudron station with the Union-Prilly station (see Fig. 19), and it will replace the current route above ground, ensuring effectiveness of the connection in terms of speed and punctuality.

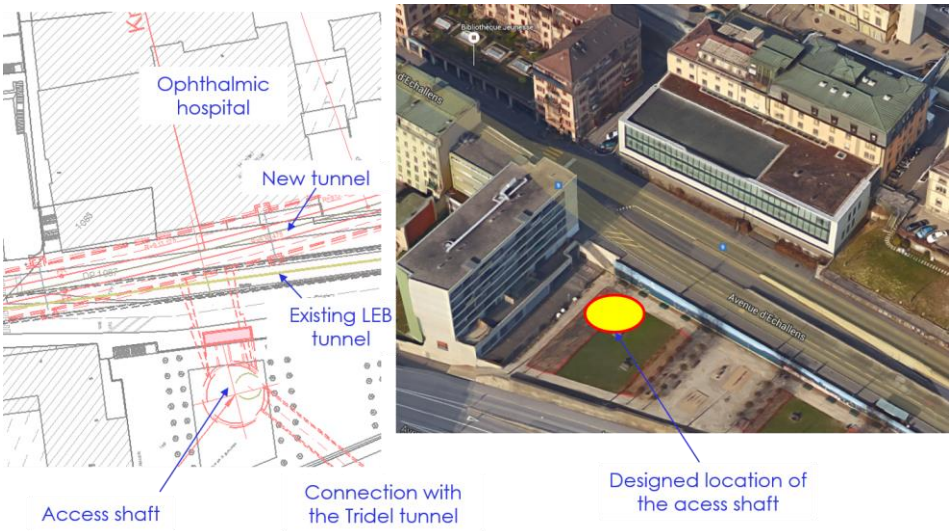

Figure 20: Designed location of the access shaft and new tunnel with respect to the existing buildings and tunnel.

The excavation of a tunnel is intrinsically associated with the need to evacuate soil masses. However, heavy truck transport would seriously disrupt the flow of already dense traffic in the center of the city. Therefore, it was conceived that the excavation for the new tunnel can be linked with the existing underground railway - the Tridel Tunnel - through which the excavated soil masses can be evacuated. The main access shaft, which will be realized in the Brouette Park, will connect the existing tunnel with the construction site by means of two auxiliary access tunnels, see Fig. 19 and 20. In order to connect the access shaft with the beginning of the excavation for the new tunnel, one of the access tunnelS has to be excavated under the existing LEB tunnel. In this configuration, the shortest distance between the vault top and the bottom of the existing tunnel is about 80 cm (see Fig. 21) creating A potentially hazardous situation.

Aware of the fact that any failure during excavation for the tunnel intersection can strongly affect excavation productivity or the traffic flow in the existing tunnel which will remain operational during the entire construction period, it was decided to perform a detailed 3D numerical simulation.

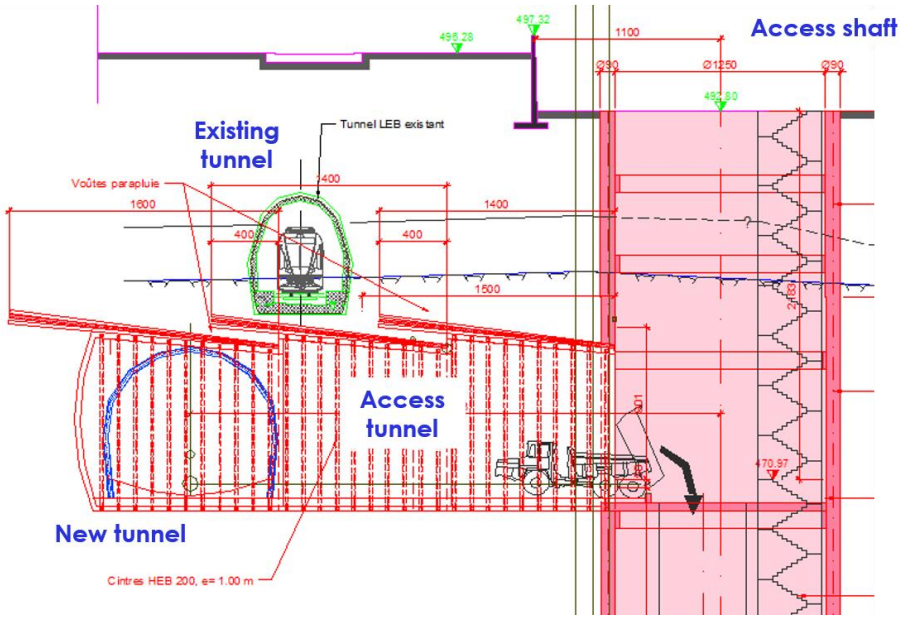

Figure 21: Longitudinal cross-section through the access tunnel which connect the access shaft and the excvation for the new tunnel.

The aim of numerical modeling which can account for excavation and construction stages was to evaluate the feasibility of the tunnel intersection in terms of:

- evolution of displacements of the existing tunnel during the excavation of the access and the proper new tunnel
- evolution of rail warp stemming from the convergence of the access tunnel (cross-level difference of the track in any segment in the existing tunnel)
- tensile stress zones in the concrete members of the final lining in the existing tunnel
- expected deformation around newly excavated tunnels
- internal forces in the mixed steel-concrete section designed for the temporary support in the access and new tunnels
- internal forces in the Gothic vault and internal forces
- evolution settlements at the terrain surface
- differential settlements of the hospital foundation

The 3D model of the tunnel intersection is presented in Fig. 22. Considering the good quality of the excavated rock mass, it was decided to place the beginning of the access tunnel excavation at a border of the model which coincides with the perimeter of the access shaft. A full-face technique is foreseen to excavate A 32m long access tunnel assuming a mixed section, i.e. HEB steel

brace every 1m (elastic beam elements) and a 30cm shotcrete layer (one-layer shell elements). Three lots of forepole umbrella, which are intended to ensure stability of the above-passing existing tunnel, were modeled with the aid of nail elements which ensure flexural rigidity and allow to take into account the ultimate resistance of the grouting.

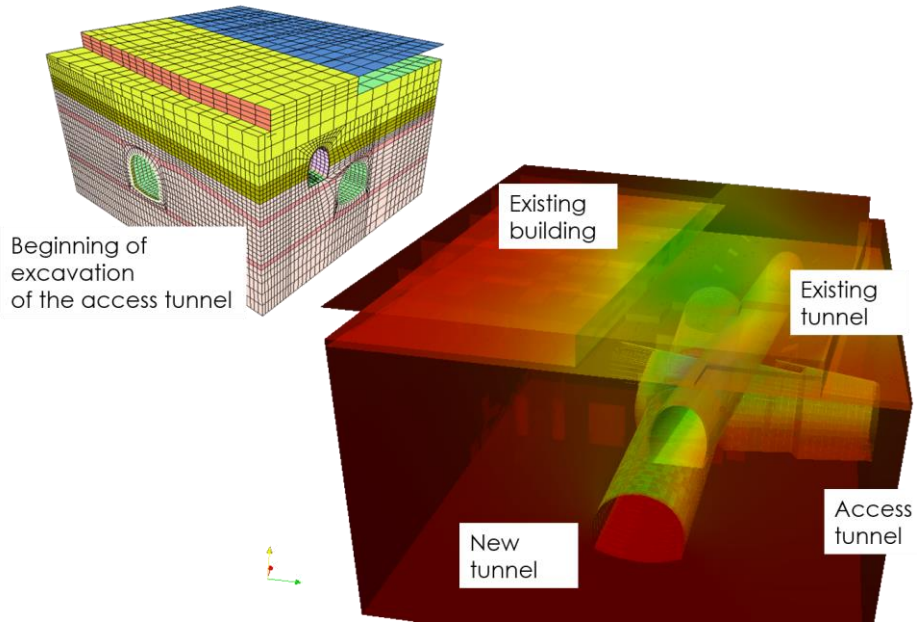

(a) Views of 3D model

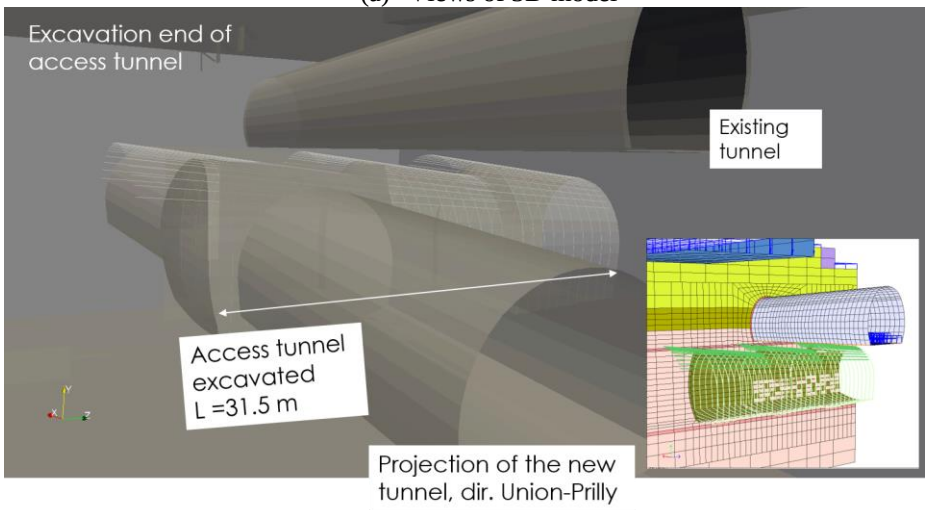

(b) Tunnel intersecion

Figure 22: Numerical model of the tunnel intersection visualized with ZSoil's PostPro and a transparent preview produced using ParaView.

Once the access tunnel has been completed, the preparatory works for the opening of the new tunnel in two directions are scheduled. They consists of an installation of Gothic vault cross-ribs and cutting the access tunnel steel braces in order to open the tunnel towards the first direction, i.e. Union-Prilly. From this moment, most of overload due to the tunnel excavation is redistributed to the Gothic vault. The vault is modeled with the aid of beam elements, whereas the filling concrete is represented by fictive stiff truss elements which ensure a rigid link between the access tunnel's walls and HEB cross-ribs. This is so because the complex intersection between three openings including meter-by-meter excavation of the access tunnel, made it impossible to preserve the mesh compatibility in this zone.

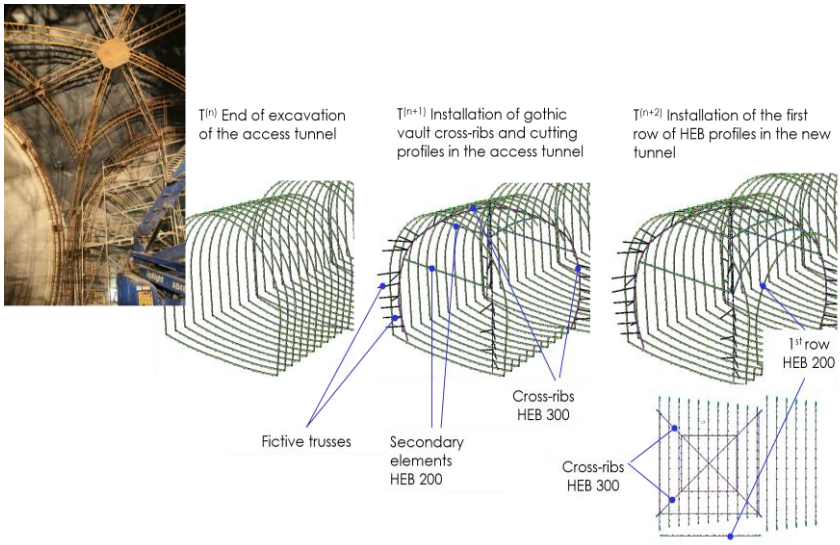

Figure 23: Principle of the Gothic vault, its discretization in the FE model and the excavation of the new tunnel in the first direction.

In order to analyze the sensitivity of the numerical model, a parametric study was carried out by varying the most uncertain parameters, *in situ* ratio between horizontal and vertical stresses K_0, as well as rock mass stiffness represented by the modulus E_{rm}. Fig. 25 illustrates the deformation of the existing tunnel obtained for the simulated openings of the access and main tunnels. The results obtained for the most pessimistic combination of $K_0 - E_{\mathrm{rm}}$ parameters show that the maximal vertical displacement of the existing invert is expected to be between 3.8 and 6.6 mm. It can be noted that the cross-section of the existing tunnel undergoes a torsion-like deformation during excavation works.

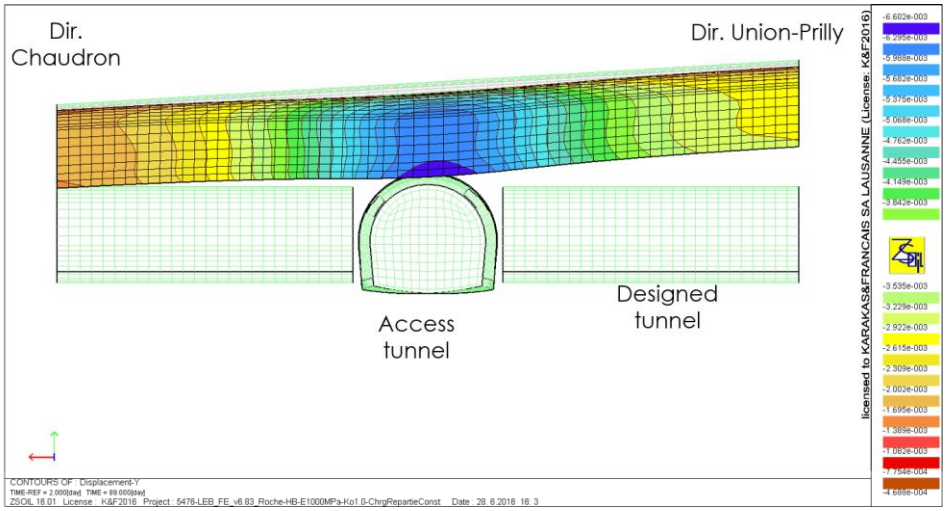

(a) Deformation of the existing tunnel in longitudinal direction

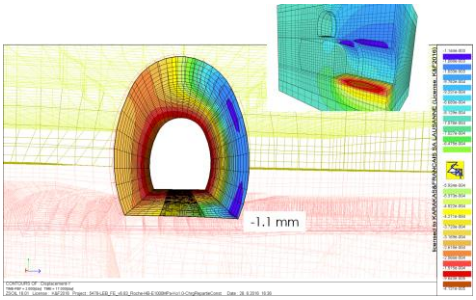

(b) Access tunnel approaching to the existing tunnel

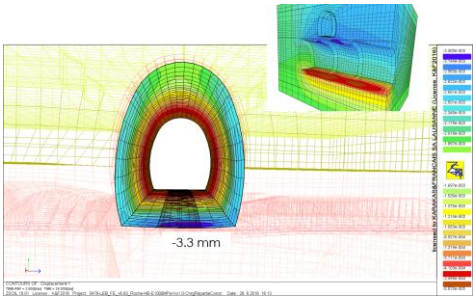

(c) Excavation front below the existing tunnel

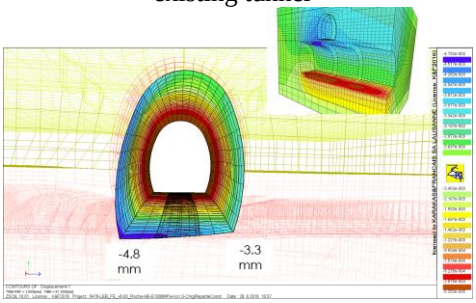

(d) Completed opening of the new tunnel in the first direction

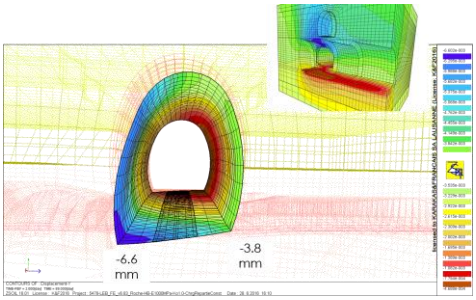

(e) Completed opening of the new tunnel in the second direction

Figure 24: View of the existing tunnel deformed during openings of the access and main tunnels.

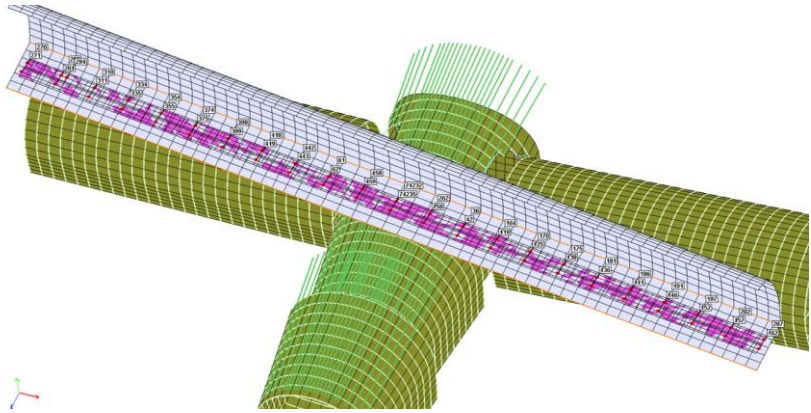

(a) Selection of measurement points located at rails position

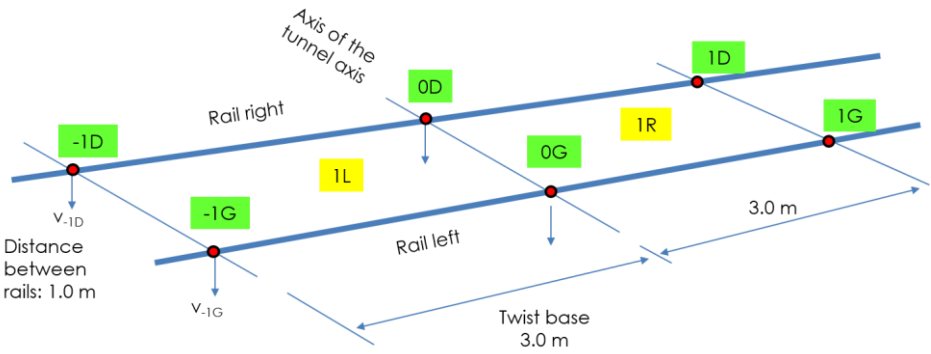

(b) Distances between measurement points in vertical transverse and longitudinal planes

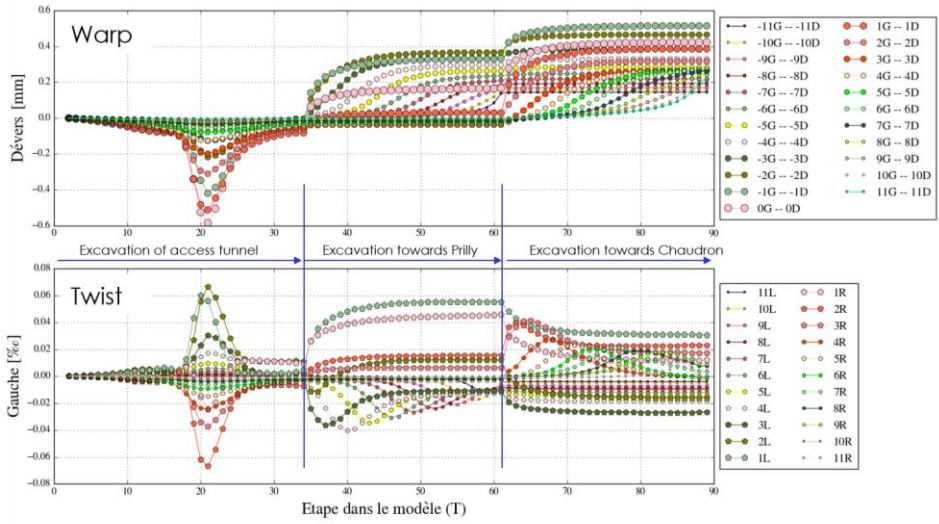

(c) Evolution of the rail warp and twist

Figure 25: Quantification of the tunnel deformation by the rail warp and twist.

These deformations can be quantified by computing the magnitude of changes in track geometry in the existing tunnel. Track geometry is three-dimensional geometry of track layouts and associated measurements used in design, construction and maintenance of railroad tracks. The subject is used in the context of standards, speed limits and other regulations in the areas of track gauge, alignment, elevation, curvature and track surface. Warp, d is the difference in crosslevel of any two points within the specific distance along the track and is measured in transverse vertical plane, cf. Fig. 25(b), whereas twist, N is calculated based on adjacent warp measures and distance L between two sections $N = (d_i - d_{i-1})/L_i$, and can by expressed in percentage (for detail see [15]).

Fig. 25(c) shows the evolution of the rail warp and twist which are calculated for each excavation stage. From the technical point of view, this analysis was carried out with the aif of Matplotlib environment [16] (for graphical representation), and python-based post-processing package for data retrieval from ZSoil binary results files (e.g. *.s00). The open-source package is addressed to the users with intermediate level in programming, who wish to retrieve the data without opening the ZSoil PostPro and treat them according to their specific needs. On-demand package distribution is available on ZSoil's hotline (hotline@zsoil.com).

5. Summary

Selected capabilities of ZSoil in the context of pre- and post-processing for large-scale, soil-structure interaction analysis have been demonstrated on three ongoing projects. It has been illustrated that the direct analysis for soil-structure interaction analysis allows to qualitatively and quantitatively evaluate effectiveness of the design settings in terms of both, soil and structural members performance.

Growing interest of engineers in the direct analysis for SSI encourage developers to constantly improve algorithms in FE codes. The illustrated high accuracy interpolation techniques which are implemented in ZSoil, i.e. nodal linking and mesh tying, allow the number of elements in the FE mesh to be reduced. This may considerably speed up both data preparation, computational time, and result analysis. Effective experience exchange between consultants and developers results in adapting the software to user's needs. Post-processing can be more effective when using specialized visualization application. Since 2016, ZSoil has made it possible to export data sets to the format understandable by one of the leading applications in data analysis and visualization. ParaView complements ZSoil with customized graphical outputs and rapid generation of animations. Finally, advances in constitutive modeling and the growing number of constitutive laws available in ZSoil to describe the behavior of both, soils and concrete, take modeling closer to reality.

6. Acknowledgment

Implementation of large scale models in the context of SSI requires close collaboration between structural, field geotechnical engineers and specialized computer consultants. Neither discipline alone is likely to have sufficient knowledge of structural, foundation, geology and site considerations necessary to properly complete a meaningful analysis for the design setting.

The first author would like to show his gratitude to Pablo Gebel, Thibaud Meynet, Sébastien Schneider (Karakas & Français), Yves Bach and Solène Tossa (EDMS), and Olivier Hey (Monod & Piguet) for the valuable exchange during development of the presented simulations.

References

[1] NEHRP Consultants Joint Venture (2012). Soil-Structure Interaction for Building Structures. Report NIST/GCR 11-917-14, prepared by the Applied Technology Council and Consortium of Universities for Research in Earthquake Engineering for the National Institute of Standards and Technology, Washington, D.C.

[2] Obrzud, R.F., Hartmann, S., Podles K. (2016). Selected aspects of designing deep excavations. *Studia Geotechnica et Mechanica*, 38(3). DOI: 10.1515/sgem-2015-0021.

[3] Truty A., Zimmermann Th., Podles K., Obrzud R.F. with contribution by Urbanski A., Commend S. and Sarf J.-L. (2016). *ZSoil manual* Elmepress and Zace Services Limited, Lausanne, Switzerland.

[4] Schanz, T. (1998). Zur Modellierung des mechanischen Verhaltens von Reinbungsmaterialien. In *Mitt. Inst. für Geotechnik 45*. Universitat Stuttgart.

[5] Schanz, T., Vermeer, P., and Bonier, P. (1999). Formulation and verification of the Hardening Soil Model. In *Beyond 2000 in Computational Geotechnics*. Balkema, Rotterdam.

[6] Benz, T. (2007). *Small-strain stiffness of soils and its numerical consequences*. Ph.d thesis, University of Stuttgart.

[7] Obrzud, R. and Truty, A. (2011). The hardening soil model - a practical guidebook. Edition 2016. Technical Report Z Soil.PC 100701, Zace Services Ltd.

[8] Hoek E., Torres C. C., and Corkum B.(2002). Hoek-Brown failure criterion - 2002 edition. In Proceedings of the North American Rock Mechanics Symposium, Toronto.

[9] Truty, A. and Zimmermann, Th. (2014). Hoek-Brown model for rocks Technical Report Z Soil.PC 140617, Zace Services Ltd.

[10] ParaView. http://www.paraview.org/

[11] Pont-Rouge. http://www.pont-rouge.ch/en/the-project/presentation/

[12] Obrzud, R.F. and Preisig, M. (2013). Large scale 3D numerical simulations of deep excavations in urban areas - constitutive aspects and optimization. In publications of Géotechnique Suisse 167, pp. 57-67.

[13] Obrzud, R. and Meynet, T. (2014). The use of ZSoil for complex, large scale 3D simulations of a deep excavation in soft soils. Presentation in ZSoil Day, August 2014, Lausanne, Switzerland (http://www.zsoil.com/zsoil_day/2014/R_Obrzud-Excavation3D.pdf)

[14] Ali, M.M. and Moon, K.S. (2007). Structural Developments in Tall Buildings: Current Trends and Future Prospects. *Architectural Science Review*, 50(3):205–223.

[15] Surveillance des installations de technique ferroviaire á proximité de chantiers DMS ID: 7247893 (Version réglementation CFF 1-0) (2011)

[16] Matplotlib. http://matplotlib.org/

Computational Strategies for Retaining Structures in Steep Slopes

Jörg-Martin HOHBERG[a,1]
[a]*IUB Engineering Ltd., Underground Structures Dept., Berne, Switzerland*

Keywords: Back analysis, primary stress state, instable slopes, shear bands, backfilling, soil-structure interaction, ultimate limit state, phi-c-reduction, convergence

Abstract

While excavation problems are well covered in the literature, the opposite computational task of backfilling retaining structures is less frequently discussed. Building in steep slopes emphasizes the question of the initial stress state and its influence on soil-structure interaction. Typical soil data given by geologists are rather conservative, so that it is often difficult to prove why existing structures are still standing up. Altering such structures involves computations close to the physical stability limit with difficult numerical convergence.

In the debate of how to apply the partial safety factor concept of Eurocode 7 or SIA 267 – with preference to factoring the output of an analysis, for ease of computation – the analysis for very low "characteristic" values amounts, in fact, to input factoring in order to cover the uncertainty range. While the phi-c-reduction method is quite accepted for slope stability analysis, the effect of reducing strength properties for retaining structures is rarely shown.

1. Introduction

Building road or railway infrastructure in mountainous areas like the Alpes is infeasible without cutting into steep slopes, either temporarily like in cut-and-cover construction of tunnels (Fig. 1) or permanently with anchored retaining walls or galleries. Even in mechanized tunneling, before the TBM finds competent rock, lose debris at hill sides need be traversed and require ground stabilization methods like pipe umbrellas or jet-grouting.

[1] email: martin.hohberg@iub-ag.ch .

Figure 1. Example of a cut-and-cover tunnel along a hillside (IUB)

1.1 Soil-structure interaction – true or false?

Such a cut-and-cover construction can be approximated by a plane-strain 2D model in two steps: The temporary retaining wall is dimensioned as continuous beam with limit-analysis software (like LARIX, DC-BAUGRUBE, QWALLS or similar); thereafter the earth pressure is applied to the tunnel section, modelled with beam elements on Winkler springs, by using a structural FEM package (e.g. STATIC or AXISVM). Stress resultants are calculated with characteristic properties for an earth pressure between active and at-rest conditions, from where the Ultimate Limit States (ULS) is derived by applying the partial safety factors to these stress resultants. Such split analysis is often sufficient in practice; only the Serviceability Limit State (SLS) would require an FEM analysis with characteristic properties.

Figure 2, however, shows a more complicated example, where the unclear soil-structure interaction (SSI) advocated an integrated FEM analysis: First, the excavation was modelled using shotcrete & rockbolts in the debris layer, followed by a bored pile wall & prestressed anchors in the underlying sandy stratum. Subsequently, the tunnel section (with a technical chamber uphill) was represented with beam elements, against which the backfilling and the long-term transfer of the earth pressure took place by removing the temporary supports.

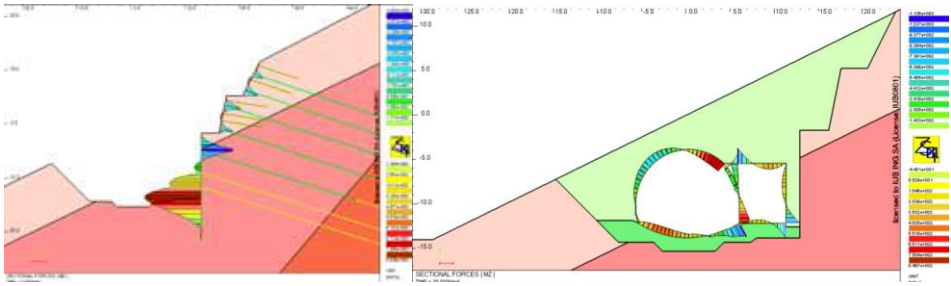

Figure 2. Bending moments in the retaining wall and the tunnel (IUB 2008)

In reality the situation was three-dimensional, as the tunnel crossed the slope at an oblique angle, but an integrated 3D SSI analysis would have taken too long in those days, the more as last-minute geological probing revealed that the tunnel had to be founded on piles [1]. The earth pressure was therefore computed from a 2D SSI analysis and thereafter applied to a 3D shell model (Fig. 3a). In order to avoid torsional deformation of the tunnel tube and its bending effect on the piles, permanent pre-stressed rock anchors were installed in the right tunnel sidewall (Fig. 3b).

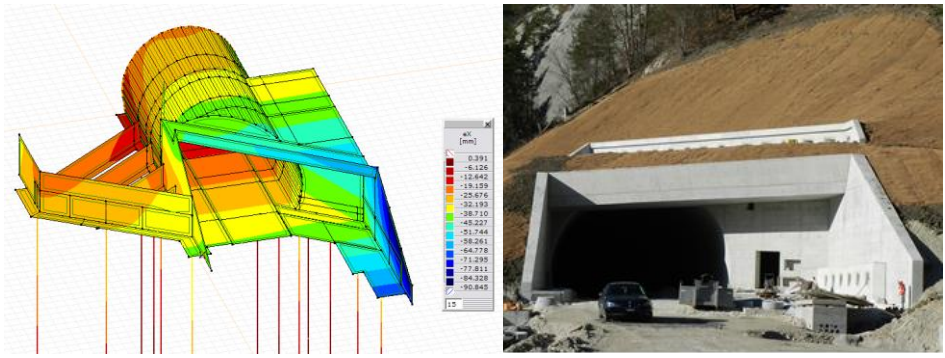

Figure 3. (a) Torsional displacements computed in AXISVM, (b) finalized tunnel portal (GVH 2009)

1.2 'Enhanced 2D' by modelling thick slices

As shown in earlier ZACE publications, 3D SSI models are feasible for excavation problems, even with a large number of different existence and unloading functions [e.g. 2]. Depending on the soil properties, the nonlinear behaviour will remain limited, as the settlement behind the retaining wall usually governs the design (SLS). The dimensioning of props or anchors is performed again by factoring the output of an FEM analysis using characteristic soil properties. A rather demanding 3D application including backfilling was presented in [3], but with limited plasticizing in the soil.

In steep slopes close to the stability limit the degree of nonlinearity is more severe. The combination of a large number of steps for excavation and backfill in conjunction with lengthy iterations virtually prohibits 3D SSI models. A

good alternative may be the model of a "thick slice", where the plane-strain stress state is enforced by sliding boundary conditions perpendicular to the slice faces. Ideally, the thickness is determined by the spacing of symmetry axes along the structure. Such *local 3D* SSI models permit to account e.g. for stiffening ribs designed to prevent ovalization of tunnels under earth pressure.[2]

Figure 4 shows the example of an entry tunnel, where the stiffening rib of the structure was modelled by continuum elements, to better capture the diaphragm action in the rib. Compared to using beam elements to represent tunnel walls, the sequence of excavation / building the structure & backfilling necessitates a much more elaborate mesh with extensive replacement of materials (elements of excavated rock becoming concrete and others becoming backfill).

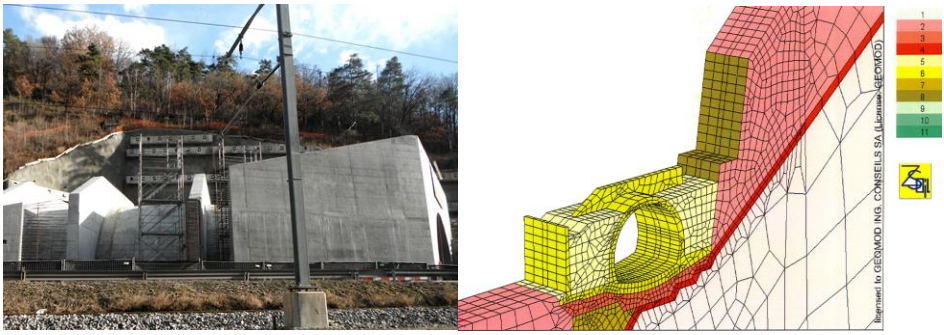

Figure 4. Cut-and-cover tunnel under construction (IUB), and local 3D model (GEOMOD 2007)

The same modelling principle was applied to a gallery, which was to be re-analysed according to the new ASTRA Directive on cut-and-cover tunnels. Issued in 2013, this directive attempts to reconcile the conventional beam analysis under predefined earth pressure with true SSI analysis in FEM. The particular challenge lies in the philosophy of applying partial safety factors to the soil strength parameters (input factoring) and not to the stress resultants in the structure (output factoring).[3] This brings about a more pronounced nonlinearity than backfilling with characteristic soil properties. Moreover, if the structural deformation must be expected to activate passive resistance – i.e. bedding instead of loading –, SIA 267 demands also reduction of the soil stiffness by a partial safety factor.

Again, the shell structure is stiffened by a rib, and we demonstrated that this feature as well as the proper representation of the pillar foundations required a

[2] Other applications are models to investigate local 3D effects at anchors, around piles in a pile wall, etc.

[3] The reasoning is that input factoring may bring about shifts of the neutral point of the bending moment, whereas output factoring does not affect the internal lever arm $e = M/N$.

local 3D analysis (Fig. 5), whereas a simplified 2D analysis gave misleading results [4].

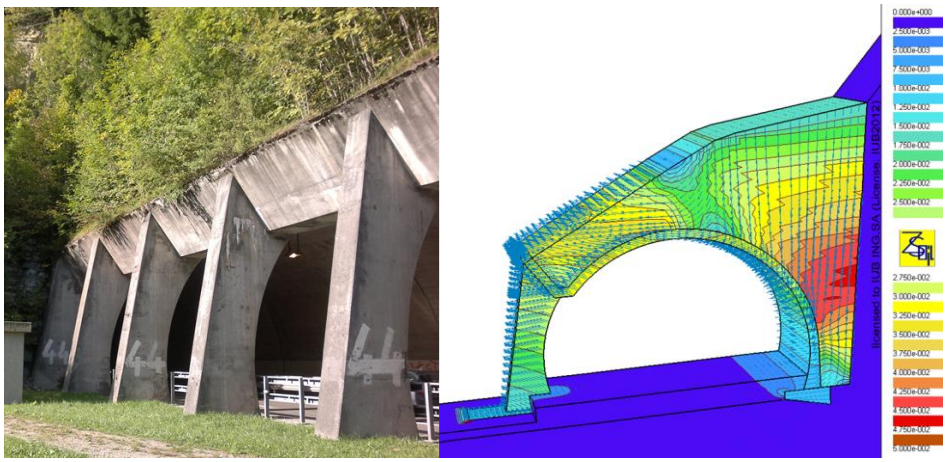

Figure 5. Gallery with high overburden, and local 3D model with abs. displacements (IUB 2013)

As can be told from the zig-zag appearance of the colours in the soil in Figure 5, the backfilling was performed layer by layer, allowing to assess critical intermediate loading configurations in which the crown of the arch raised before it sagged under full overburden.

1.3 Base practises to be developed

Analysis of structures in steep slopes requires a number of additional thoughts with regard to stress regimes, strength parameters and safety concepts. The findings to be presented are grouped in three so-called Base Practices:

BP1 Establishing a primary stress state in the slope without excessive plastic zones;

BP2 Establishing an acceptable initial stress state around existing retaining structures (so-called "secondary stress state") with an efficient pre-calculation;

BP3 Finding a convincing design concept for input factoring, especially where the uncertainty inherent in "prudent characteristic" (rather: residual) values outweighs the familiar magnitude of partial safety factors.

These are supporting skills that need to be adopted on the way to the ultimate objective, that is the analysis of structural alterations or rehabilitations of such retaining structures situated in steep slopes.

All computations are performed with the classical Mohr-Coulomb model, as advanced constitutive models (such as HSS), accounting for hysteretic elastic effects, are not available for coarse granular materials or soft rock.[4]

Thus the seeming up-thrust of the ground during excavation – due to the missing distinction between loading and unloading modulus – is also of concern. Chapter 3 presents a case were such 'buoyancy' mislead the analysis of a tunnel to be excavated in a steep slope.

2. Modelling gravity retaining walls

The following study was motivated by a project of ascertaining the structural stability of an existing gravity retaining wall of varying dimensions, where the lower sections of 8.1 m maximum height have a conventional shape, whereas higher sections of up to 9.9 m are composed of two gravity walls sitting on top of each other (Fig. 6).

Figure 6. Double gravity wall (note the fence demarcating the crest of the upper wall)

This particular combination constitutes a mechanism, in which sliding of the upper wall would induce toppling of the lower wall. Geological investigations behind the wall indicated a very low strength of the Moraine deposits (φ'_{Mo} =33°, c'_{Mo} = ~0 ÷5 kPa), in which the space for constructing the retaining wall had been excavated. The soil-structure interaction thus involves both the backfill and the grown Moraine deposits of the hill side.

2.1 Plausibility check on strength parameters

An exploratory analysis for the topography of the undisturbed slope is always to be recommended. Not only does such an analysis give confidence in

[4] A practical approach sometimes taken by GEOMOD is to use the Cap Model in Z-SOIL, even though this is based on a Drucker-Prager cone, necessitating a compromising circle fitted to the MC compression-extension surface in the deviatoric plane.

the characteristic strength values given by the geologist (or grounds for questioning them), it also reveals obstacles for a successful stability analysis and gives first hints as to mesh size, boundary conditions, and the incrementation/iteration strategy (Fig. 7). Note that the deformation depends on the layer thickness, the base rock profile, and on the uphill continuation of the slope.

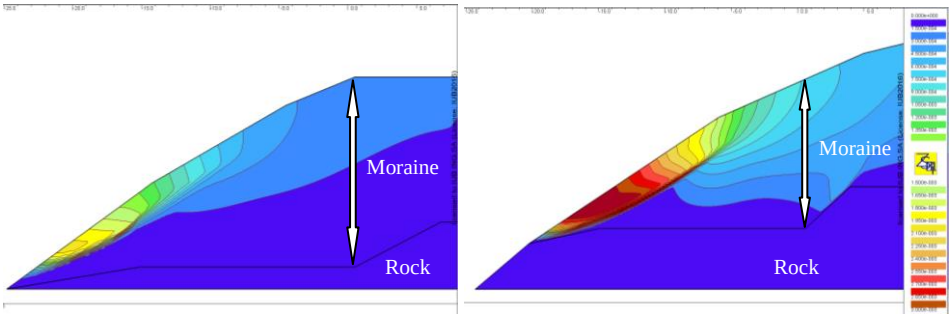

Figure 7. Presumed pre-existing slope (2 sections) with φ'= 33° after c-reduction to c' = 1 kPa (abs. displ.)

It may be necessary to start with an elevated strength for Z_SOIL's initial gravity algorithm to cope. For the given slope and with φ'_{Mo} = 33° and c'_{Mo} = 2 kPa, the initial gravity algorithm produces almost no plastic zones. The likely initial state with plastic zones and shear bands is subsequently computed with the time-dependent driver by means of using internal load functions on the strength properties (**BP1**).

Note that in all examples shown in this paper, no locally elevated 'vegetal' cohesion was employed, as often done by practitioners to avoid shallow surface instabilities.

2.2 Effects of construction assumptions

What we really look for is the secondary stress state around the existing retaining wall. The different possibilities to arrive at this 'initial state' are discussed for the mono-wall section (as existing in the left-hand part in the photography of Fig. 6).

The exact excavation procedure is unknown, but the two drillings behind the wall give an idea of both the slope of the excavation pit and the level of the bedrock. As no shotcrete was found in the cores, it is assumed that the upper part of the cut stood up unsupported, while the lower part was excavated in bays. For φ'_{Mo} = 33° and 33% supporting pressure (meant to model the adjacent berms), an initial cohesion of $c'_{Mo,ini} \approx$ 12 kPa was found necessary; with zero supporting pressure, the cut failed for $c'_{Mo,ini} \approx$ 20 kPa (Fig. 8 left). Note the drop in horizontal stress due to impending wedge failure.

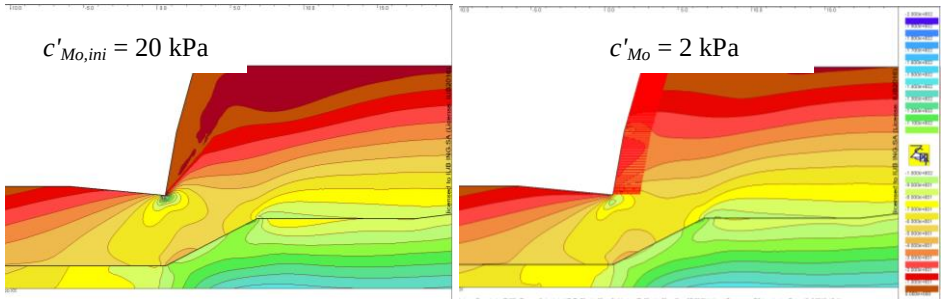

Figure 8. Horizontal stress unsupported (left) and with temporary restraints after 40% stress release (right).

The advance stress release (e.g. 40%) is controlled by the unloading time at which the auxiliary restraint is activated. During further unloading due to excavation, the primary stress state in the Moraine is by and large preserved, even though the auxiliary restraint allows for vertical settlement. After the retaining wall is in place, the auxiliary restraint is gradually removed. This **BP2** procedure was found to converge better than bringing a high initial cohesion of 12 kPa down to 2 kPa. Moreover, the earth pressure on the retaining structure can be expected to be more conservative when using this procedure.[5]

By employing a temporary horizontal restraint from the beginning (i.e. 0% advance stress release), no excavation process would be needed at all. However, the lack of preloading stress due to overburden causes higher plasticizing under the heel of the retaining wall.

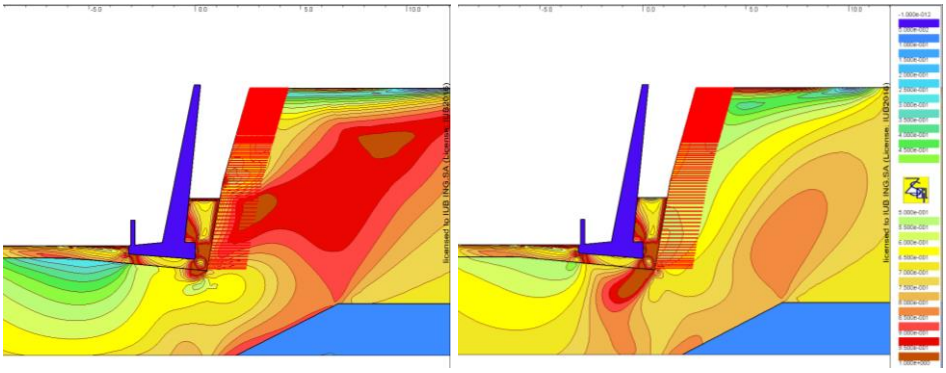

Figure 9. Stress level with 50% stress release (left) vs. a computation neglecting the excavation (right)

2.3 Backfilling procedure and load transfer

Unlike for excavation processes, where a continuous (un)loading function can be applied to the equivalent nodal forces of the elements killed, a similar

[5] The initiation of shear bands already during construction – as in Figure 8 (left) – may reduce the ultimate collapse load of the retaining structure. Cf. the high stress level (in red) in Fig. 9 left.

option for smoothing banking and backfilling steps does not exist. One may think of placing the entire backfill in one go and incrementing the gravity by an internal load function applied to specific weight. However, the simultaneous lack of confining pressure will lead to a large number of overstressed integration points and failing convergence, regardless of the portion of gravity applied.

Moreover, it is highly unlikely that gravity turn-on can produce the same stress pattern in the backfill as stepwise filling does (cf. Fig. 10 below). The height of the fill layer needs to be smaller with increasing total height of the backfill, because each weight increment causes additional displacements in the frictional interface to the concrete wall as well as plastic straining in the continuum. The layer height was chosen small enough to allow BFGS or at least initial-stiffness iterations to converge.

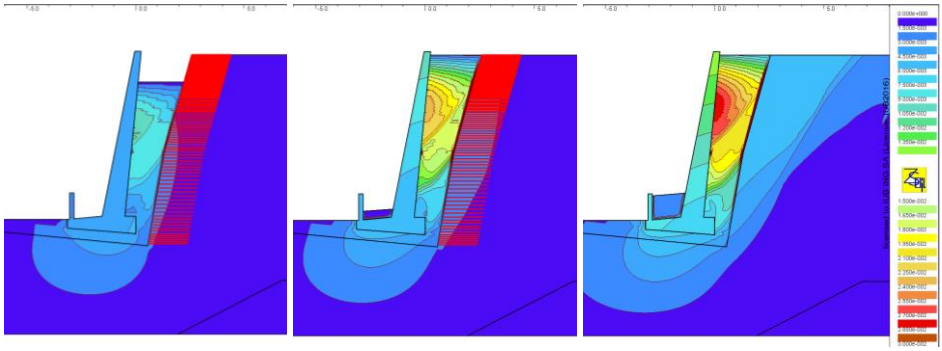

Figure 10. Abs. displacements for c = 2 kPa before and after releasing the temporary BC (50% stress relief)

Shear-banding commences in the backfill when the height reaches about 7 m; at this step the initial leaning of the wall towards the slope due its overhang is compensated and starts to reverse to tilting. Shown are the absolute displacement after excavation (reference time). This effect is enhanced by the 1:10 batter of the rear surface of the retaining wall, which allows the backfill to slump and spread more than with other wall geometries. If interface elements are used between concrete and backfill, the default for computing the penetration penalty from the surrounding continuum stiffness (κ_n *multiplier* = 0.01) can be kept, but the stick penalty ratio should be reduced to κ_t/κ_n =0.1.

After complete release of the intermediate horizontal restraint between backfill and Moraine, the remaining safety can be evaluated by *c*-reduction, applying either an internal load function to $c'_{Mo,cal} = 2 \rightarrow 0$ kPa, or through the Stability driver (option '*c*-reduction only'). The ultimate capacity is seen to be limited by yielding under the toe of the foundation (Fig. 11).

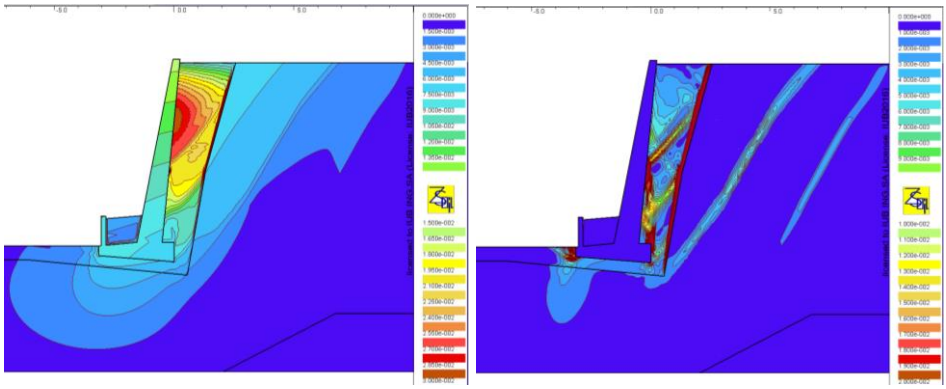

Figure 11. Abs. displacements and deviatoric strain for c = 0.583 kPa (SF_c = 3.43)

2.4 Articulated retaining wall in slope

A second cross-section of the retaining wall exhibits a peculiar articulated system of a second retaining wall sitting on top of the lower one. This situation is more complex, but treated in the same manner as the monolithic wall. Again, a nearly unsupported excavation (requiring c_{ini} = 12 kPa) was compared with use of a temporary horizontal restraint in combination with $c'_{Mo,cal}$ = 7 kPa or 5 kPa, resp.

Of particular interest is the behaviour of the berm used during construction. Its depends on the stiffness of the backfill and the Moraine – where E_{BF} : E_{Mo} = 50 MPa : 80 MPa was chosen – and the shear strength of the Moraine. Figure 12 shows a computation with $c'_{Mo,ini}$ = 7 kPa and 70% advance stress relief. After releasing the temporary restraint, the cohesion of the Moraine was reduced by an internal loading function to $c'_{Mo,cal}$ = 5 kPa.

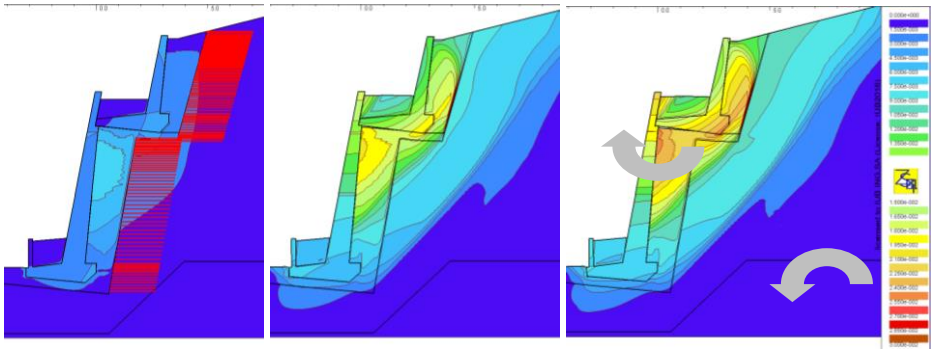

Figure 12. Abs. displacements for c = 7 kPa before/after releasing the BC, and after reduction to c = 5 kPa

Note that the foundation of the upper wall shields the lower backfill against additional pressure, because its toe rests directly on the lower wall. As the upper wall exerts a horizontal thrust on the lower wall, the lower backfill slumps and detaches from the foundation of the upper wall. Both walls continue to rotate in

opposite directions, with shear-banding in both backfills and beginning shear failure through the berm. For c' = 2 kPa instability is immanent.

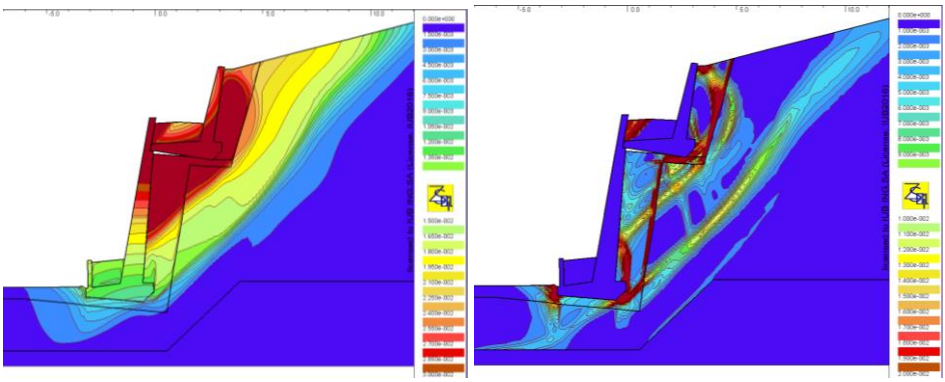

Figure 13. Abs. displacements and deviatoric strain after reduction to c = 2 kPa

From the deformation apparent in the numerical simulation, it seems plausible that during construction of the retaining wall the cohesion in the Moraine must have been considerably larger than 2 kPa (Fig. 13). As the core samples were taken from right behind the retaining wall, these may in fact have been disturbed by the shearing in the berm and thus lead to an underestimation of the cohesion in undisturbed parts of the Moraine. **BP2** as back-analysis of the initial state will thus provide the basis for questioning geotechnical parameters.

2.5 The effect of prestressed ground anchors

We are now coming to **BP3**.To prevent the rotational mechanism, a row of ground anchors would best be installed right underneath the foundation of the upper wall. A prestressing force of 50 kN/m is explored, which, of course, cannot reverse deformations already manifested but will increase the triaxial strength behind the retaining wall owing to additional confining pressure. The easiest way to vary the location of anchors is by simply approximating the pre-stress through a nodal force.

The computations are started with $c'_{Mo,ini}$ = 5 kPa and 40% advance stress relief, i.e. with a conservative assumption of shearing already in place before rehabilitation. After releasing the temporary BC, the nodal force is increased to 50 kN/m. The beneficial effect of the prestress lies in the reduction of the apparent stress level behind the wall (Fig. 14).

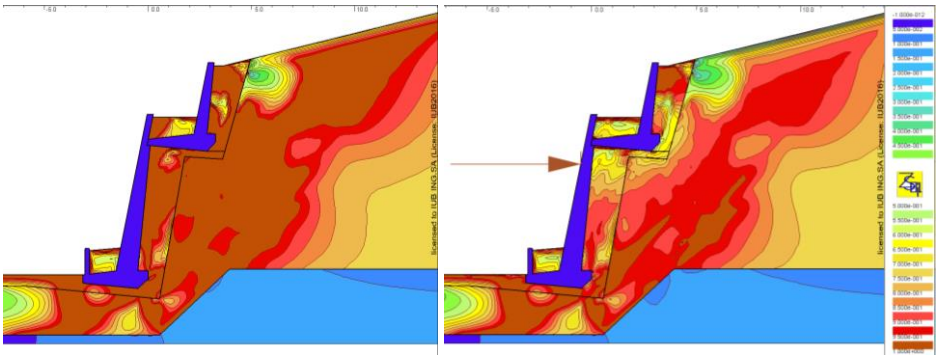

Figure 14. Stress level at c = 5 kPa, before and after prestressing (p =50 kN/m)

Figure 15 demonstrates that after prestressing the cohesion in the Moraine can indeed be reduced from 5 kPa to 1 kPa (and even lower) without triggering instability. By varying the prestressing force, different levels of safety (also against earthquakes) can be evaluated.

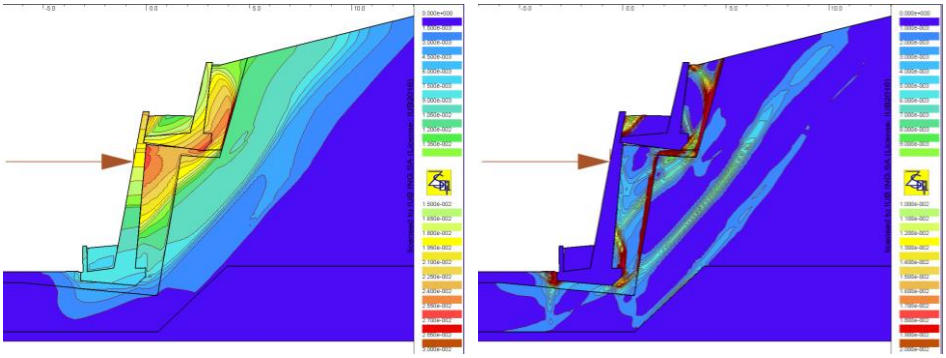

Figure 15. Abs. displacements and deviatoric strain at c = 1 kPa (with 50 kN/m prestress)

Not that this interaction between earth pressure and anchor force, optimizing the amount of prestress, cannot be captured in classical limit equilibrium analysis. In excavation problems, earth pressure and anchor force are activated simultaneously with increasing excavation depth. Whereas here the prestressing takes place against stiff passive behaviour of the ground, improving the overall stability with marginal alteration of the stress state in the existing wall.

3. Structures in instable slopes

The idea is to obtain a primary stress distribution with comes close to the in-situ consolidation of debris running down the hillside, rather than a 'gravity

turn-on'.[6] In the following two examples an alternative method for **BP1** is presented, involving **BP2** and **BP3** as well.

3.1 How to approximate the in-situ stress state?

The slope in question was estimated by the Geologist to be close to its natural stability limit, even though no indication of surface slipping was seen yet. Where the inclination was steeper than the estimated angle of friction, obviously some cohesion must exist. The project was to widen an existing road at the top of the slope (to improve traffic safety), which entailed that the traffic loads must now comply with the standards for a new road rather than with the reduced requirements for existing structures [3].

The slope was modelled with an idealized rough surface of the underlying bedrock due to folding of strata ("Hakenwurf"). A smooth interface with unknown properties (incl. wetness due to formation water) might not have given proper results, hence enforcing a shear failure line through the continuum was preferable.

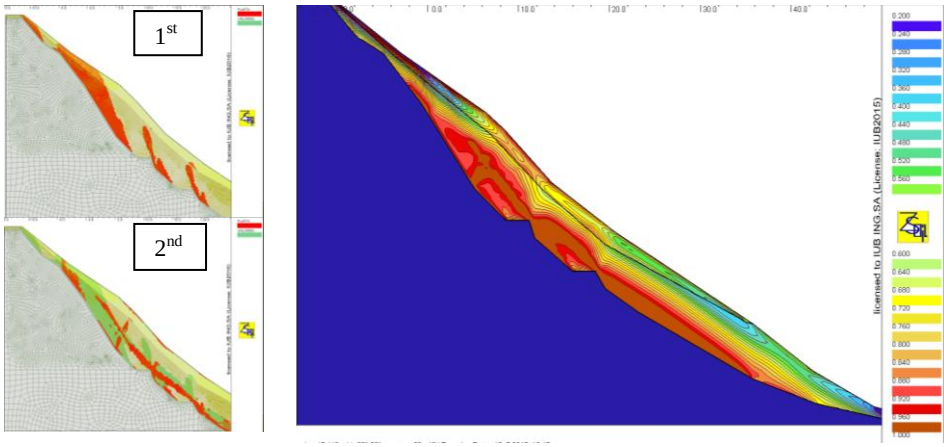

Figure 16. Stepwise computation of a valid primary stress state (1st tension cut-off, 2nd reduction of cohesion)

For the Gravity algorithm to converge, a fictitious cohesion of 200 kPa was assumed, such that only plastic zones due to the tension cut-off would be produced; the amount of integration points yielding was controlled by using only 25% of the self-weight. The remainder was applied in the Time-Dependent algorithm using a load function ($\rightarrow$ 100% weight). Thereafter the cohesion was gradually reduced with a second load function $c'_{Mo,cal} = 100 \rightarrow 20$ kPa for the Moraine and $c'_{Gr,cal} = 100 \rightarrow 10$ kPa for the overlaying gravel (rock debris).

[6] In older computations (like Fig. 2) "gravity turn-on" was used but mitigated by interface elements to the bedrock, in order to allow settlement of the gravel layer without producing plastic zones in the continuum elements.

Figure 16 shows the resulting initial stress state, which is not yet at the brink of instability and thus unconservative when the Geologist was to be believed, i.e. $\{\varphi', c'\}_{Mo,k}$ = {36°, 5 kPa} and $\{\varphi', c'\}_{Gr,k}$ = {38°, 0 kPa}. But because the initial state had to be recomputed for all further design studies, the margin to instability was computed only once by *c*-reduction and the difference between the pseudo-initial state and believed true initial state taken into account as 'model factor' on the unsafe side [3], i.e. all safety margins evaluated in later design alternatives had to be divided by this model factor, computed to be γ_S =1.16. Such considerations also form part of **BP2**.

3.2 Widening of an existing road above the slope

As a first step of investigation the existing road was back-analysed with the reduced traffic loads for existing structures. The load function employed included the partial safety factor.

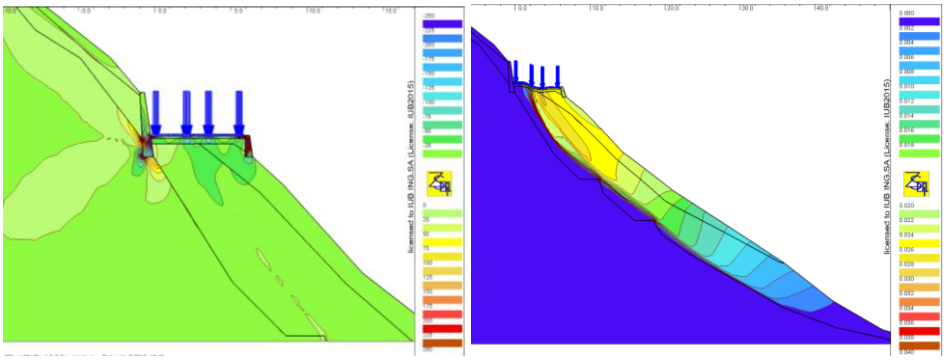

Figure 17. Vertical stress (ref. to excavated state) and abs. displacement increment under traffic ($SF_{\varphi\text{-}c}$ = 1.31)

The left-hand side of Figure 17 shows the existing stress due to service traffic load (with 70% reduction for existing structures), the right-hand side the additional displacements due to the design traffic load (factorized by 1.3) and φ-*c*-reduction to $SF_{\varphi\text{-}c}$ = 1.31, which amounts to {29.0°, 15.3 kPa}$_{Mo}$ and {30.8°, 7.6 kPa}$_{Gr}$. Dividing $SF_{\varphi\text{-}c}$ by the model factor γ_S gave a 13% (= 1.31 / 1.16) higher stability than for the 'natural' slope, as the design traffic load was less than the weight of the excavated material.

This was not the case for the refurbished road with 90% design traffic load. Prestressing to reduce the rotation of the cantilevering concrete slab introduced an unwelcome vertical force component with ensuing additional slope deformation (Fig. 18).

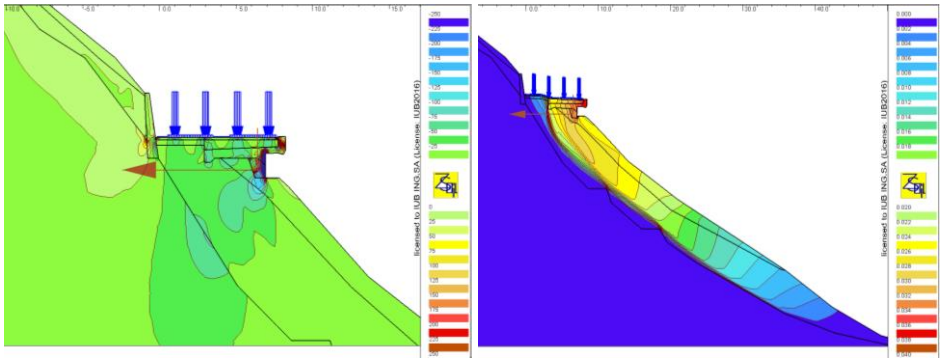

Figure 18. Vertical stress (ref. to excavated state) and abs. displacement increment under traffic ($SF_{\varphi\text{-}c}$ = 1.34)

BP3 may thus involve comparison of different solutions based on the same (perhaps uncertain) initial conditions. In this case the solutions investigated encompassed bored piles with ∅ 70 cm with and without a prestressed rock anchors and a foundation on micro-piles (Fig. 19). The latter was found to increase the slope stability to 121% (= $1/\gamma_S \cdot SF_{\varphi\text{-}c}$), i.e. $\{27.3°, 14.2\ \text{kPa}\}_{Mo}$ and $\{29.0°, 7.1\ \text{kPa}\}_{Gr}$.

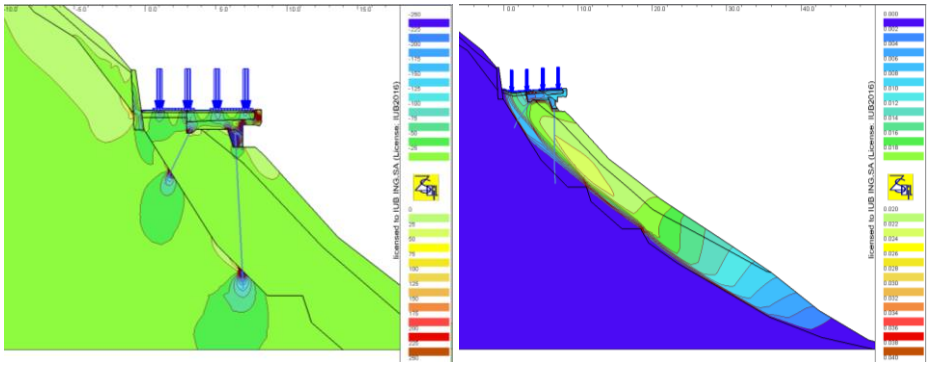

Figure 19. Vertical stress (ref. to excavated state) and abs. displacement increment under traffic ($SF_{\varphi\text{-}c}$ = 1.41)

Note that in a plain-strain model the piles are placed across the continuum mesh without contact to the elements in the instable layers. For closer investigation of the lateral interaction between piles and slope a local 3D model would have to be employed (cf. chapter 1.2).

3.3 Treacherous slope behaviour

The last example concerns a tunnel excavated in a steep slope close to the surface. The tunnel is advanced with fore-poling through the rock debris and crosses the rock interface at oblique angle. As the pipe umbrella itself – forming

an articulated arch – cannot be analysed as 2D model[7], the objective was to analyse only the loading on the concrete lining. But first a realistic stress state for soil-structure interaction need be established (**BP2**),

Figure 20 shows the results as computed by a young engineer with little experience in nonlinear FE analysis. It looks as though the tunnel would ovalize into the gravel. Is this due to the simple Mohr-Coulomb material law with exaggerated heave during tunnel excavation (unloading equal to loading modulus), or is it something else?

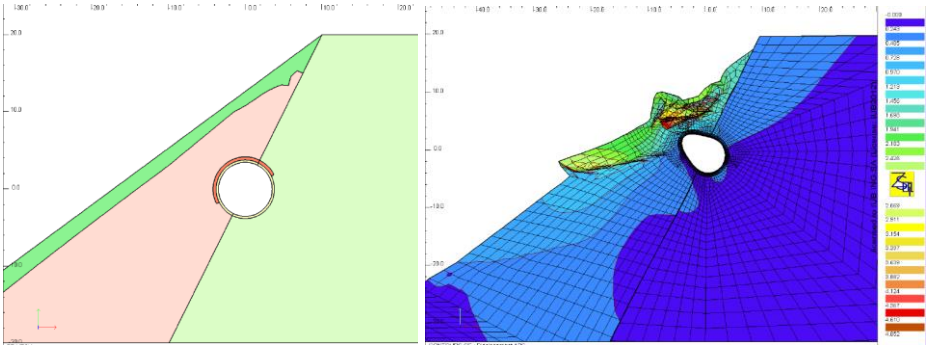

Figure 20. Computed failure mode of tunnel in gravel/rock transition zone

A variety of beginner's mistakes were made – too large load steps in full Newton-Raphson iteration, attempt to model stress relief at the tunnel face by reducing Young's modulus in the elements to be excavated, neglecting gravity in the rock. The cohesion in the gravel was reduced to zero without problem, because no friction was specified in the interface to the rock! This allowed the gravel to settle freely, developing plastic zones only near the surface, which resulted in the strange elastic expansion (Fig. 21).

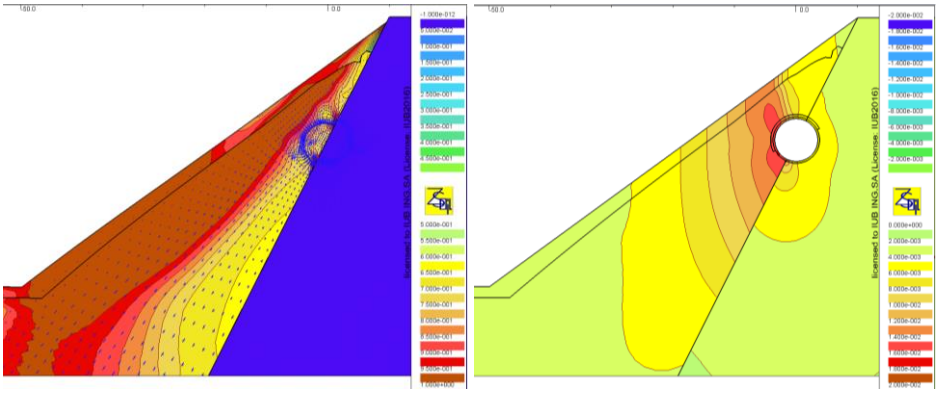

Figure 21. Plastic zones before excavation and elastic heave after excavation

[7] The steel pipes are usually dimensioned by means of an analytical or FE solution for a continuous beam resting on springs, both discrete springs representing steel arches as well as a Winkler foundation at the tunnel face.

The results were not thoroughly checked, believing that just displacement and stress resultants in the lining were of interest – a frequent shortcoming among structural engineers (but occasionally encountered also in geotechnical design reports).

A realistic initial state was achieved through gradual reduction of the cohesion (similar to the 2-step procedure in Fig. 15), checking the plausibility of the deformations before excavating the tunnel (Fig. 22).

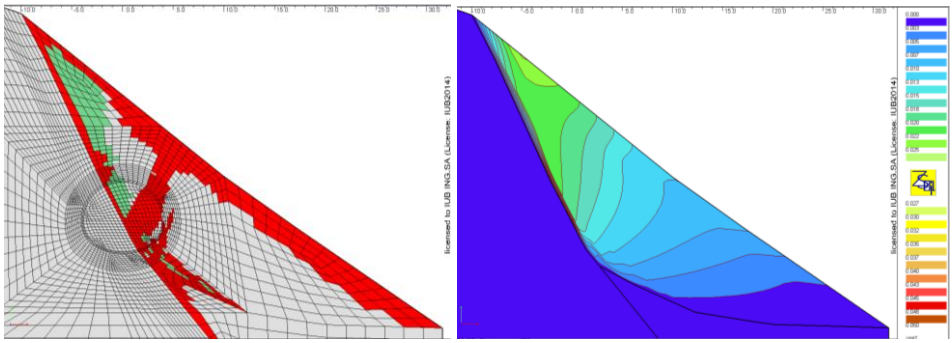

Figure 22. Abs. displacements and plastic zones for c_{Gr} = 5 kPa before excavation

Afterwards, the tunnel was excavated using an unloading function for the elements removed, for different assumed cohesion in the slope. The resulting deformations and spreading of plastic zones were studied first for the unlined tunnel in full-face excavation, in order to check the resulting failure mode (Fig. 23). The knowledge thereby gained about the cohesion needed for the unsupported case was then used to study the influence of advance stress relief before installing the shotcrete lining, partial excavation with different lead times of the crown against the bench, etc.

In this example **BP3** involves studying the failure mode of the unsupported cavity in order to design the right sequence and timing of intervention. The sensitivity to parameter variation helps to decide on an adequate safety margin.

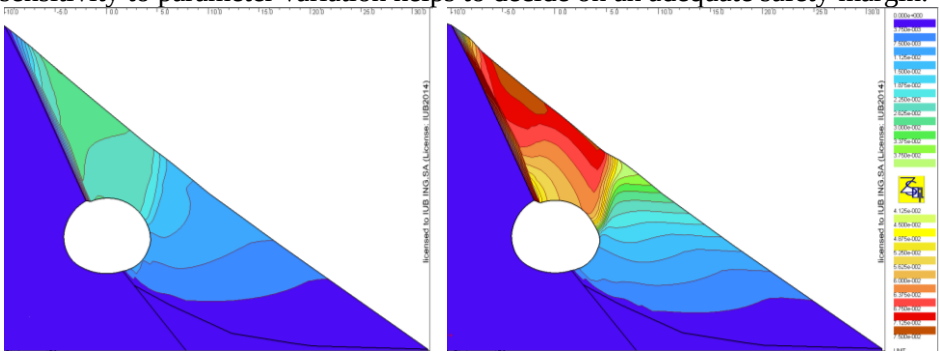

Figure 23. Abs. displacements of the unlined tunnel for c_{Gr} = 10 kPa and 5 kPa

4. Conclusions

This paper wants to raise the awareness for primary stress states involving pre-existing shear zones and impending instability. It was shown that even minor variations of cohesion may have very pronounced effects. Numerical analysis of structures in steep slopes means walking a fine line between producing unconservative results – or no results at all due to lack of convergence. Achieving convergence under difficult conditions is a prerequisite for detecting real instability.

Three 'Base Practices' are proposed, which are relevant also in design methods based on input factoring, i.e. computation with reduced (or naturally low) geotechnical strength parameters. Path dependency seems to be less critical as often thought; hence, analyses may start with optimistic parameters, followed by strength reduction later. This enables 'quick & dirty' exploratory computer runs to familiarize oneself with the physical problem, before entering into lengthy iterations.

Geotechnical FEM is a strong tool for investigating unclear failure modes and for testing the relevance of geotechnical parameters. The back-analysis of existing structures gives an opportunity for fruitful discussions between geotechnical engineers and geologists. Certainly, more work needs to be done on the translation of traditional safety philosophies from Design Codes to numerical analysis.

Acknowledgments

For earlier computations credits are given to former and present co-workers at IUB:
Jing-Wen Chen, Dr. Mohamed Oubelkas, Raphael Sonney, and Kai Mehnert.

References

[1] J.-M. Hohberg. *Anforderungen des Praktikers an die Aussagekraft numerischer Modelle.* SGBF Autumn Conference 2009, *SGBF Mitteilungen/Publications* no. 159, Zurich, 2010.

[2] F. Geiser, *Cut-and-cover study: 2D and 3D analyses.* Z_SOIL User Meeting, August 2011.

[3] M. Wszolek & P. Milczarek: *Analysis of folded steel-shell / earth bridge.* Z_SOIL User Meeting, August 2011.

[4] J.-M. Hohberg. *Gallerien als Hangstützung – 50 Jahre nach dem Bau.* 29th Cristian Veder Colloquium, *Mitteilungshefte der Gruppe Geotechnik*, no. 51, Graz, March 2014.

[5] J.-M. Hohberg. *Stability analysis for supporting structures and retaining walls in steep slopes.* DGGT Workshop Numerische Methoden in der Geotechnik, *BAW-Mitteilungen,* no. 98, Karlsruhe, Oct. 2015.

Tackling liquefaction problems with ZSOIL

Stéphane Commend*, Samuel Kivell*

** GeoMod ingénieurs conseils SA, Lausanne, Switzerland*

Keywords: cyclic loading, densification model (Sawicki's model), liquefaction, coupled transient dynamic analysis, pseudo-static analysis

Abstract

Seismic induced liquefaction can produce large settlements that can cause significant damage in urban areas. This paper presents the methodology and results of a liquefaction assessment that was completed during the design of a pile foundation for a new hospital. The assessment was conducted using finite element modeling with ZSOIL v2014 [1] and the densification constitutive model. Transient dynamic and pseudo-static analyses are used to estimate the influence of the pile length on the liquefaction induced settlement.

1. Introduction

During the foundation design of a new hospital in Rennaz, Switzerland (total estimated cost: 315 million CHF, see

Figure **1**), the question arose whether liquefaction could occur in sand layers located at different depths below the hospital. In 2012, an initial geological campaign concluded that liquefaction could occur at depths between 0 and 6 m, leading to a foundation system design based on 20 m long piles.

Then in 2014, a new geological campaign with CPTU tests showed another potential liquefaction zone at a depth between 15 and 25 m. The initial foundation design was no longer suitable, and the geotechnician and their expert proposed three different solutions in order to circumvent this effect:

- increase the pile length up to 35 m (cost: + 6 to 8 million CHF)
- vibratory compaction (cost: + 8 to 10 million CHF)
- drainage (cost: + 10 to 12 million CHF)

A pool of experts then discussed these measures. In particular, the contractor's expert proposed to use a finite element numerical model in order to:

- help understand if and how liquefaction could happen at a depth of 15-25 m under given seismic loading, for given stratigraphy and parameters

- estimate the settlement eventually induced by liquefaction
- evaluate the effect of long vs. short piles in order to optimize their length

Figure 1: Future hospital in Rennaz, Switzerland

GeoMod SA was therefore contacted by the contractor, and proposed the following methodology:

- show the possibility of reproducing mean effective stress decrease and pore pressure increase under cyclic loading on a single-element test with the densification model implemented in ZSOIL v2014
- perform 1D coupled transient dynamic analyses on soil columns subjected to different seismic loadings, in order to verify the liquefaction potential at a depth of 20 m for the local seismic demand
- use a 3D (cells and slices) pseudo-static approach, calibrated on the 1D coupled transient dynamic analysis, in order to estimate the efficiency of different piles to limit the settlement induced by liquefaction

2. Densification law in ZSOIL

In ZSOIL, the Densification constitutive law is proposed to reproduce the behavior of loose sandy soils that experience significant densification and are vulnerable to liquefaction [1]. The law is derived directly from the "Hardening Soil with Small-strain extension" (HSS) constitutive model by adding an explicit densification mechanism. Two formulations are available in ZSOIL, and in this case we use the Sawicki's approach.

According to studies completed with cyclic simple shear tests on loose sands, Sawicki and Świdziński found that a given loose sand has a so called common compaction curve that is independent of the amplitude of the shear strain cycles. Following their work, the following relation was proposed relating the accumulated volumetric strain (ε^{acc}) produced in N cycles of the cyclic

simple shear test, run at a constant shear strain amplitude (γ_0):

$$\varepsilon^{acc} = e_0 C_1 \ln(1 + C_2 z) \qquad \text{with:} \quad z = 0.25\, N\, \gamma_0^2 \tag{1}$$

where:

- C_1 & C_2 are constants that need to be determined
- e_0 is the initial void ratio
- N is the number of uniform shear strain cycles
- γ_0 is the amplitude of shear strain

The value of z, which depends on the number and amplitude of uniform shear strain cycles, gives a measure of the amount of accumulated shear straining that has occurred. For time domain applications where the number and amplitude of shear strain cycles is non-uniform, the Sawicki's model needs to be adapted. This is completed in ZSOIL with further details available in [12].

The general procedure for assessment of liquefaction induced settlement can be seen in the flow chart (see next page), and is explained in the following sections.

3. Definition/calibration of Sawicki's parameters

When using the densification model, apart from the standard HSS parameters, the two Sawicki's parameters (C_1 & C_2) need to be defined. To do this, first we must estimate the effective shear strain amplitude (γ_0) and the accumulated volumetric strain (ε^{acc}) for which liquefaction occurs. After putting these estimated values into equation (1), we now have a range of possible Sawicki's parameters. These can then be calibrated by simulating single-element cyclic shear tests for which failure/liquefaction should occur after N cycles of the defined uniform cyclic loading.

To do this appropriately, the following information is required:

- HSS soil parameters (can be obtained/estimated from a geotechnical report)
- Initial stress state/depth at which liquefaction could occur
- Local seismic demand, provided in [6]: magnitude M = 6 (therefore N = 6, see correlation in [10]) and peak ground acceleration $a_{g,max}$ = 2.14 m/s^2

3.1 Estimation of the shear and volumetric strain

Initially, the parameters were estimated for the soil material in the potential liquefaction zone at a depth of 25 m. To begin, the effective cyclic shear strain amplitude and volumetric strain for which liquefaction is induced were estimated following the relationships presented in [7] and [11] (see Figure 2).

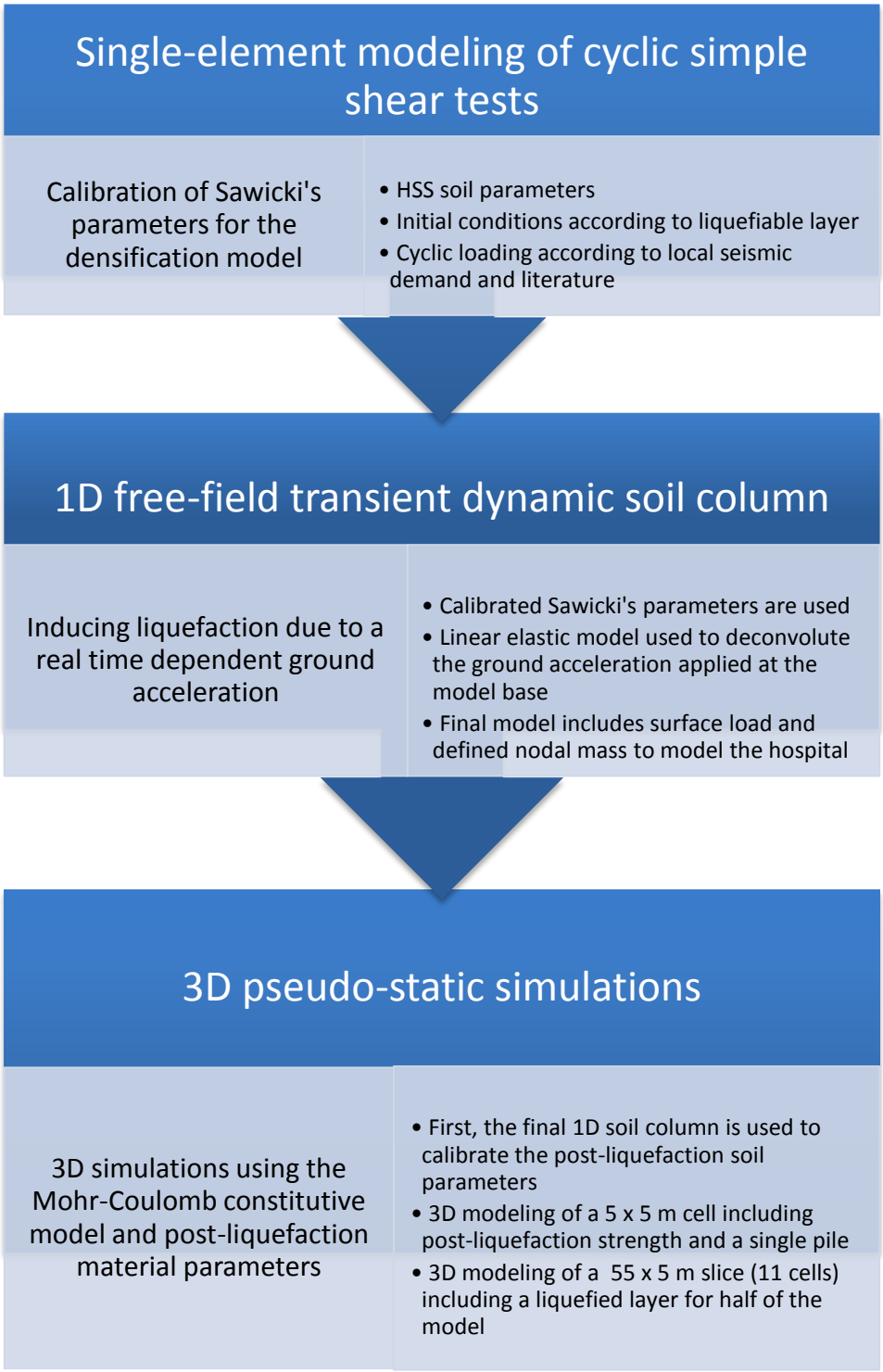
Single-element modeling of cyclic simple shear tests
Calibration of Sawicki's parameters for the densification model
• HSS soil parameters
• Initial conditions according to liquefiable layer
• Cyclic loading according to local seismic demand and literature
1D free-field transient dynamic soil column
Inducing liquefaction due to a real time dependent ground acceleration
• Calibrated Sawicki's parameters are used
• Linear elastic model used to deconvolute the ground acceleration applied at the model base
• Final model includes surface load and defined nodal mass to model the hospital
3D pseudo-static simulations
3D simulations using the Mohr-Coulomb constitutive model and post-liquefaction material parameters
• First, the final 1D soil column is used to calibrate the post-liquefaction soil parameters
• 3D modeling of a 5 x 5 m cell including post-liquefaction strength and a single pile
• 3D modeling of a 55 x 5 m slice (11 cells) including a liquefied layer for half of the model

The obtained values were then used in equation 1 to govern the possible values of the C_1 and C_2 parameters (equation 2 must be respected). Once this range of possible values was obtained, they could be calibrated with numerical modeling of single-element cyclic simple shear tests to define the values to be used in the following modeling.

With the following parameters,

$e_0 = 0.65$ $N = 6$ $\varepsilon_{acc} = 0.1$ $\gamma_0 = 0.0007$,

we obtain: $z = 0.25 \times 6 \times 0.0007^2 = 7.35 \cdot 10^{-7}$.

Substituting into (1):

$$0.1 = 0.65 \cdot C_1 \cdot \ln[1 + C_2 \cdot 7.35 \cdot 10^{-7}] \quad (2)$$

With: $a_{max} = 2.14\ m/s^2$, $\sigma_{v0} = 500\ kPa$, $r_d = 0.512$ [7],

$G_{max} = \frac{E_0}{2(1+v)}$ and $E_0 = 253\ MPa$[1]

$$\gamma_{eff}\ \frac{G_{eff}}{G_{max}} = \frac{0.65\ a_{max}\ \sigma_{v0}\ r_d}{g\ G_{max}} \cong 4.0 \cdot 10^{-4} \quad [10]$$

$$\gamma_{eff} \cong 8.2 \cdot 10^{-4} = 8.2 \cdot 10^{-2}\ \% \text{ (see Figure 2a)}$$

$$\varepsilon_{vol,M=7.5}(D_r = 50) = 0.16\% \text{ (see Figure 2b)}$$

$$\varepsilon_{vol,M=6} = 0.1\% \text{ (Table 9.4, [6])}$$

a) **b)**

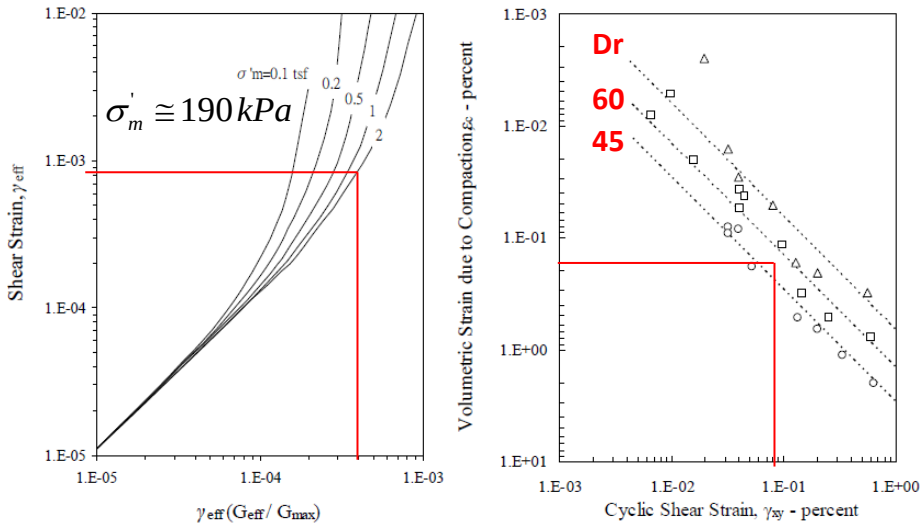

Figure 2. Estimation of the effective shear amplitude and accumulated volumetric strain

[1] Estimation by R, Obrzud basing on [Hicher and Biarez, 1994]

3.2 Single-element model geometry and boundary conditions

The geometry of the single-element axisymmetric problem can be seen in Figure 3. Vertical displacement is blocked at the base, with a constant horizontal confining stress equal to the initial in-situ stress conditions (σ'_{h0} = -117.5 kPa for K_0 = 0.47). The vertical stress applied at the top of the element is used to apply the uniform cyclic shear stress. After the initial stress state is established (σ'_{v0} = -250 kPa), the vertical stress is cycled with an amplitude equal to the deviatoric stress amplitude (Δq) which will be defined in the following section.

Note: to simplify the model, we have applied an initial pore water pressure u_w = 0 kPa instead of u_w = - 250 kPa. We are only interested in the change in pore water pressure, and therefore the initial pore water pressure is not significant as long as the initial effective stress state is correct.

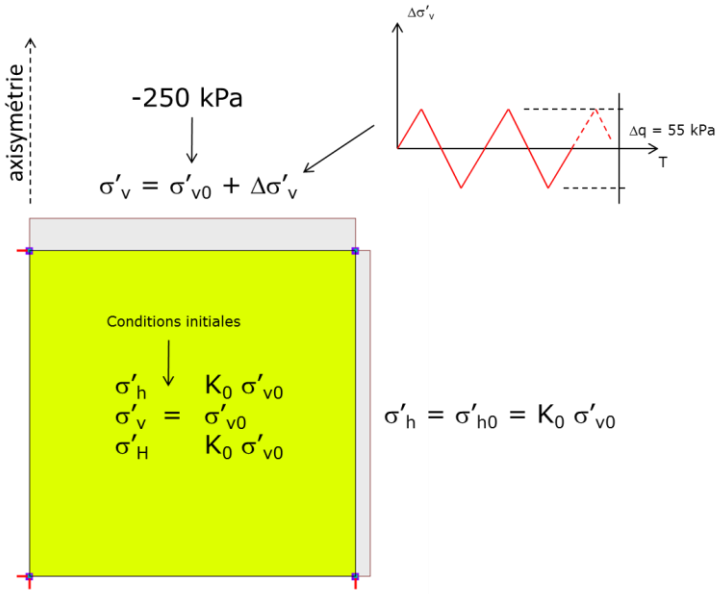

Figure 3. Elementary test description

3.3 Definition of the applied cyclic shear stress

In this simulation, the applied cyclic shear stress is uniform and regular and is simply characterized by the amplitude of cyclic shear stress. This value can be obtained through the notion of the Cyclic Stress Ratio (CSR) which represents the level of seismic shearing. It can be obtained by normalizing the amplitude of cyclic shear stress (τ_{cyc}) for cyclic simple shear tests with the initial effective vertical stress (σ'_{v0}):

$$CSR = \tau_{cyc}/\sigma'_{v0}$$

As the CSR is dependent on the initial effective vertical stress, it shows that as depth increases (or as σ'_{v0} increases), the level of seismic shearing decreases for a given amplitude of cyclic shear stress. A simplified approach can be used to estimate the equivalent CSR from the initial stress state (σ_{v0} and σ'_{v0}) and the local seismic demand ($a_{g,max}$, r_d and MSF) according to [7] (see Figure 4). Once this value for the CSR is obtained, the equivalent amplitude of cyclic shear stress to be applied in numerical model of the cyclic simple shear test can be back-calculated.

The local seismic demand provided in [6] includes a magnitude M = 6, and a peak ground acceleration $a_{g,max}$ = 2.14 m/s^2. For this single-element test, a depth of 25 m is considered giving: σ_{vo} = -500 kPa, σ'_{vo} = -250 kPa. The obtained cyclic deviatoric stress amplitude (Δq) is equal to 55 kPa (see Figure 4), and therefore the applied vertical stress varies between -222.5 and -277.5 kPa.

$$CSR_{7.5} = 0.65 \frac{\sigma_{v0}}{\sigma'_0} \frac{a_{g,max}}{g} r_d \left(\frac{1}{MSF}\right) = 0.11$$

$$CSR_{7.5} = \frac{\tau_{cyc}}{\sigma'_0} \text{ (eq. 9.4, [4])}$$

$$\tau_{cyc} = 27.5 \ kPa$$

$$q = \sigma'_1 - \sigma'_3 \quad \tau = \frac{\sigma'_1 - \sigma'_3}{2} \quad => \quad q = 2\tau$$

From which the variation of deviatoric solicitation is

$$\Delta q = 2\tau_{cyc} = 55 \ kPa$$

Figure 4. Estimation of the deviatoric stress amplitude

3.4 Calibrating the Sawicki's parameters

As we define the number of cycles (N) to be equal to 6 (for a M=6 earthquake according to [10]), we now calibrate the C_1 & C_2 constants, while respecting equation (2), until the element reaches failure after 6 cycles. This is achieved in this case for the following values: $C_1 = 0.01$ & $C_2 = 250'000$.

Note: the accumulated volumetric strain is the origin of the excess pore pressure (Δu) that causes liquefaction, and therefore larger C_1 & C_2 values will lead to a faster increase in ε^{acc} and Δu, resulting in liquefaction occurring after fewer cycles.

3.5 Results

After calibration of the Sawicki's parameters, we can see that failure has occurred in the model at the beginning of the sixth cycle (see Figure 5a). The applied cyclic shear stress can be seen in the *p'-q* space, with the cycles of deviatoric stress (q) and a reduction in the mean effective stress (p') until failure occurs.

In Figure 5b, a cyclic variation in the axial strain and excess pore water pressure can be seen. The trend is for the excess pore pressure to increase as the accumulated volumetric strain parameter increases, and this is the origin of the reduction in mean effective stress that is seen in Figure 5a.

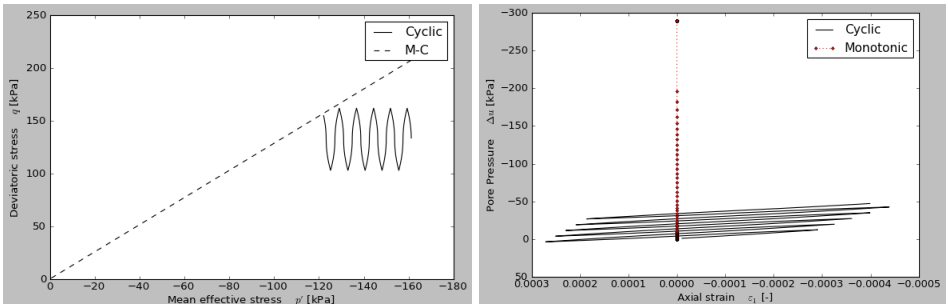

Figure 5. p'-q stress path (a) and axial strain vs. change in pore pressure (b) for the single-element test under cyclic loading

The results clearly demonstrate the build-up of excess pore pressure that is generated due to the induced cyclic shear strain. The increasing excess pore pressure reduces the mean effective stress, while the deviatoric stress cycles around a constant mean value. This continues until failure occurs and shows that using ZSOIL with the densification model, a good replication of liquefaction phenomena can be achieved.

4. 1D column coupled transient dynamic analysis

Once liquefaction had been generated with the single element test, the next step was to replicate this with a one-dimensional soil column (see Figure 6) subjected to a real non-uniform ground acceleration. The soil column included the site specific stratigraphy with the different material layers. The deconvoluted ground acceleration is applied to the base, and periodic boundary conditions are imposed on the vertical edges to obtain free-field behavior: u_x (left) = u_x (right).

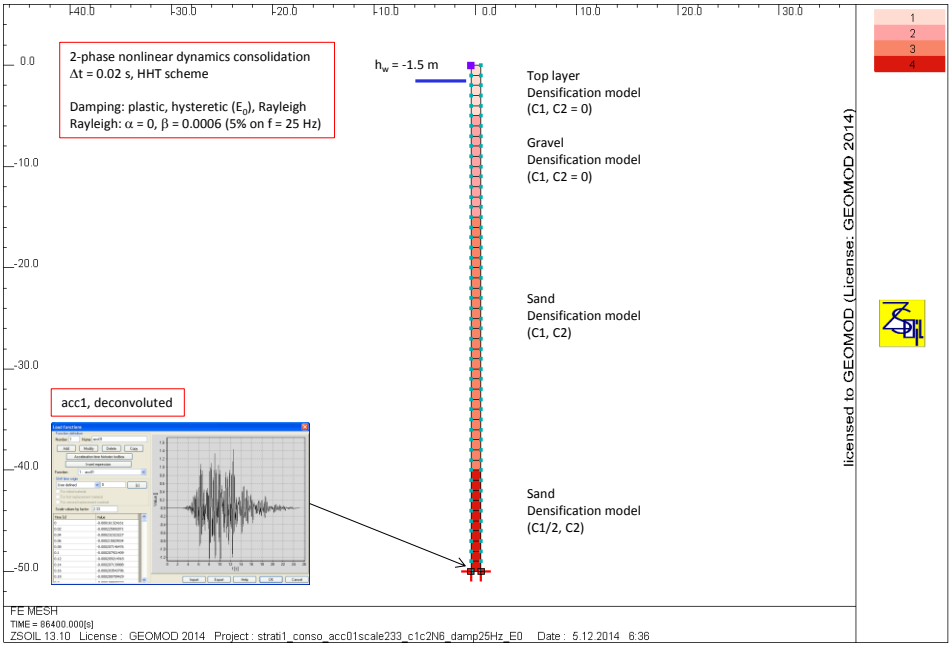

Figure 6. 1D soil column hypotheses

4.1 Parameter definition

The same calibration process as described in the previous section was completed to obtain the Sawicki's parameters with the following assumptions:

- Depth = 20 m with σ'_v =215 kPa, σ'_h = 104 kPa (K_0 = 0.47)
- Soil HSS parameters according to the geotechnical report [2]
- $CSR_{M=7.5}$ = 0.144 with r_d = 0.65 and a_{max} = 2.14 m/s^2
- $(N_1)_{60}$ = 12 N_{spt} according to the geotechnical report [2]

The obtained values are $\varepsilon_{v,7.5}$ = 2.1 %, $\varepsilon_{v,6}$ = 1.3%, $\gamma_{0,7.5}$ = 0.85 % and $\gamma_{0,6}$ = 0.5 %.

After calibration with the single-element model, the Sawicki's parameters were set to C_1 = 0.015 and C_2 = 50'000 for the material that is vulnerable to liquefaction.

4.2 Linear model

In the first stage, the 1D soil column is defined with a linear elastic constitutive model. This enables the eigenfrequencies to be obtained, as well as the definition of the correct accelerogram to be applied to the base of the model (through deconvolution). These steps are discussed below.

4.2.1 Estimation of the first eigenmode

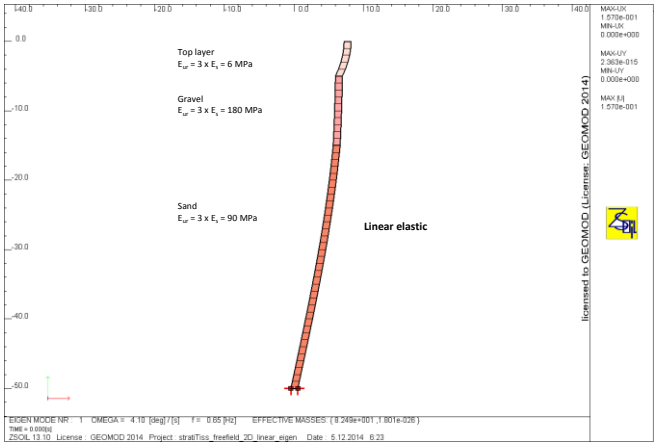

Figure 7. The first eigenmode

4.2.2 Applied ground acceleration

At this stage of the project, a micro-zonage site specific response spectrum was obtained along with a corresponding accelerogram (see Figure 8) [5].

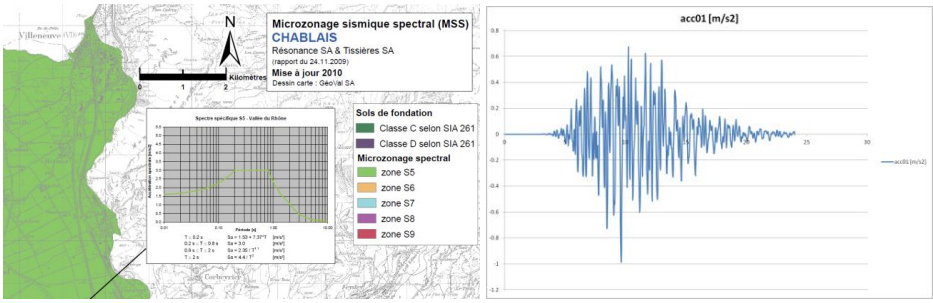

Figure 8. Specific spectrum and corresponding accelerogram

The accelerogram gives ground accelerations at the ground surface. As the accelerations that we impose on the model are applied at a depth of 50 m, they need to be modified in order to generate the correct surface motions. This can be completed using linear deconvolution in ZSOIL. For further details see the ZSOIL user manual [1]. After applying the deconvoluted accelerogram to the linear model, the resulting displacement and acceleration at the column's surface are shown in Figure 9.

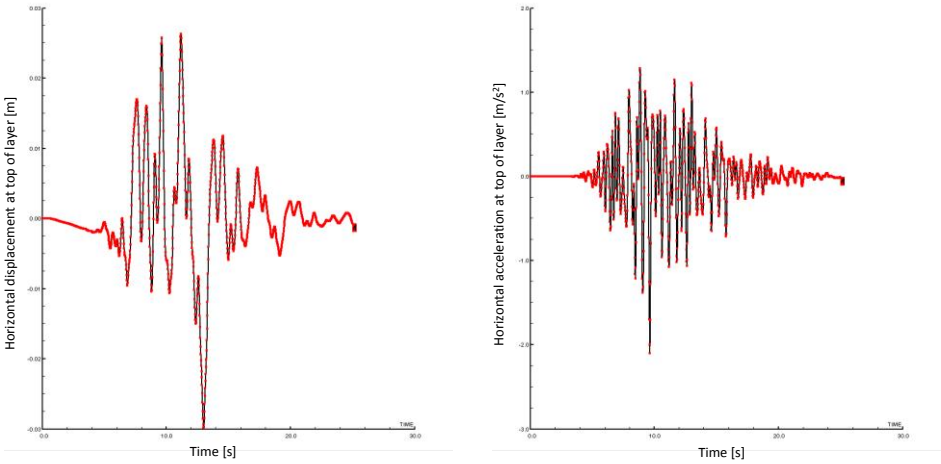

Figure 9. Linear model response after deconvolution of the ground acceleration: surface displacement and acceleration

4.3 Non-linear model

4.3.1 Soil parameters

The soil parameters for the HSS model are taken from the geotechnical report [2] and can be seen in Table 1. The extra parameters that require defining for the densification model (C_1 and C_2) can be seen for the different soil layers in Figure 6. It should be mentioned that in the top two layers, the parameters are set to zero to cancel the densification mechanism. Also, the C_1 parameter for the sand layer near to the model base was halved to eliminate boundary effects.

Table 1: HSS soil parameters

	Top layer	**Gravel**	**Sand**
Layer depth [m]	0 - 5	5 - 15	15 -
γ [kN/m^3]	18	21	20
γ_D [kN/m^3]	12.5	16.9	15.6
e_0 [-]	1.2	0.7	0.8
E_{ur} [kN/m^2]	6000	180000	60000
E_0 [kN/m^2]	20000	600000	200000
ϕ [°]	26	35	32
c' [kN/m^2]	4	0	0
k [m/s]	1e-5	5e-4	5e-6

4.4 Results

In Figure 10, the time histories at 15 m depth clearly show a buildup of excess pore pressure and a reduction in mean effective stress that occurs due to the shear strains induced by the base accelerations. As the mean effective stress rapidly goes to zero at T = 12 to 14 seconds, this indicates that the soil was liquefied and the total stress was fully taken by the excess pore pressure.

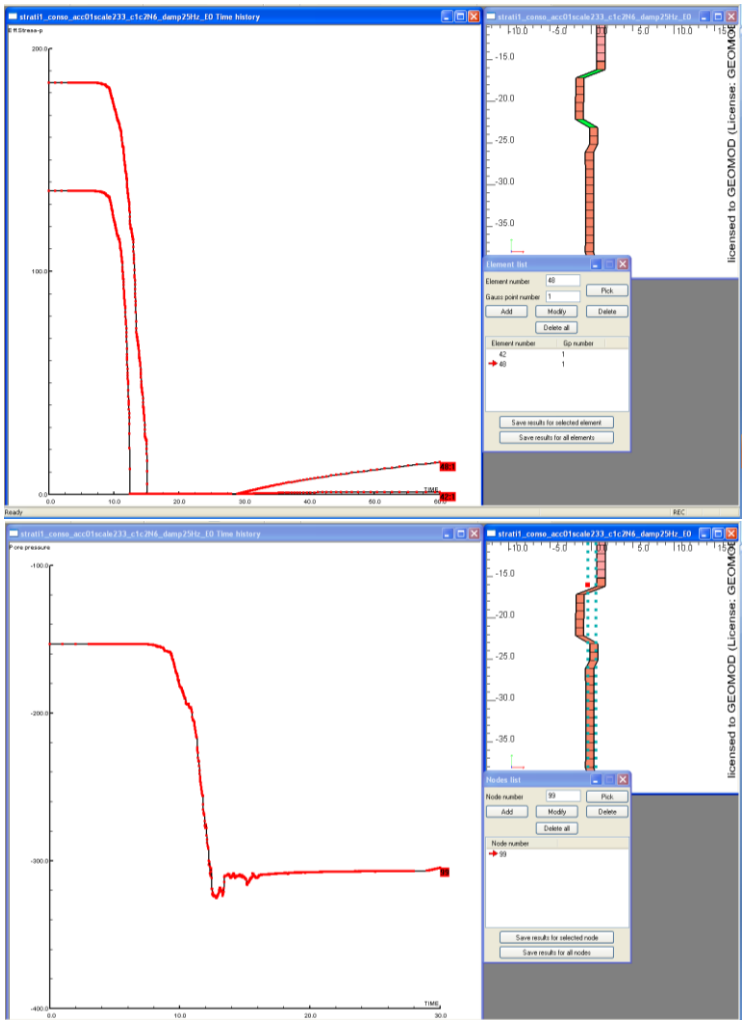

Figure 10. Time histories (T=0 to 30 s) of mean effective stress (p'), top and pore pressure at 15 m depth, bottom

Once the base acceleration stops, consolidation of the excess pore pressure (equal to the initial mean effective stress ~ 150 kPa) is further simulated over a one day period. The time histories of pore pressure and surface settlement show the dissipation of excess pore water pressure and the total stress being transferred back onto the solid skeleton (see Figure 11). This induces a surface settlement of approximately 18.5 cm.

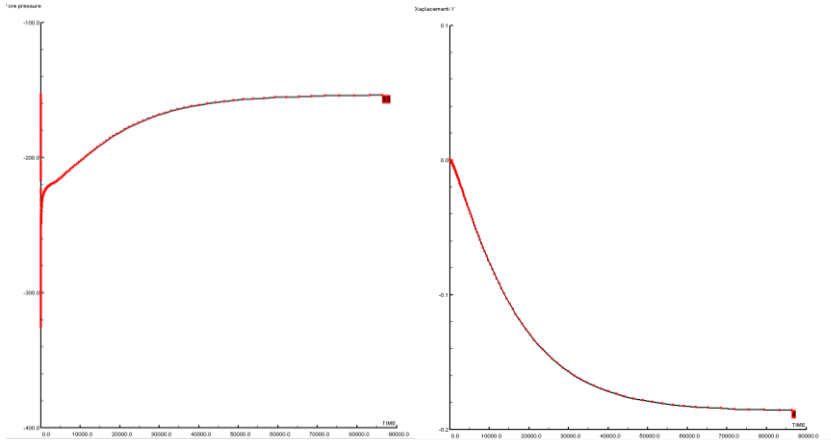

Figure 11. One day of consolidation: evolution of the pore water pressure and the surface settlement

Following this initial validation of induced liquefaction by seismic solicitation of a 1D free-field soil column, a parametric study was undertaken to investigate their influence on the surface settlement. The following factors were investigated (see Table 2 and Figure 14):

Table 2: 1D transient dynamic soil column simulations

Factor	**Result**
Size of the mesh (h-dependency)	10% difference in settlement by doubling the mesh density
Permeability	- 10% difference in final settlement by increasing permeability from 1e-6 to 1e-5 [m/s] - significant change in the rate the excess pore pressure is drained
Sawicki's parameters	- 20% range in final settlements for values tested - larger values for C_1 & C_2 increase the accumulated volumetric strain and therefore increase the densification and settlement
Amplitude of seismic solicitation (scaling)	- significant influence on final settlements
Different seismic solicitations of the same seismic demand	- no significant difference as expected for different accelerograms corresponding to the same seismic demand
Application of surface load (68kPa) and mass due to hospital	- after the initial settlement due to the application of the hospital load (5 cm), a further 21 cm of settlement occurred due to the earthquake solicitation (compared to 18.5 cm without modeling the hospital)

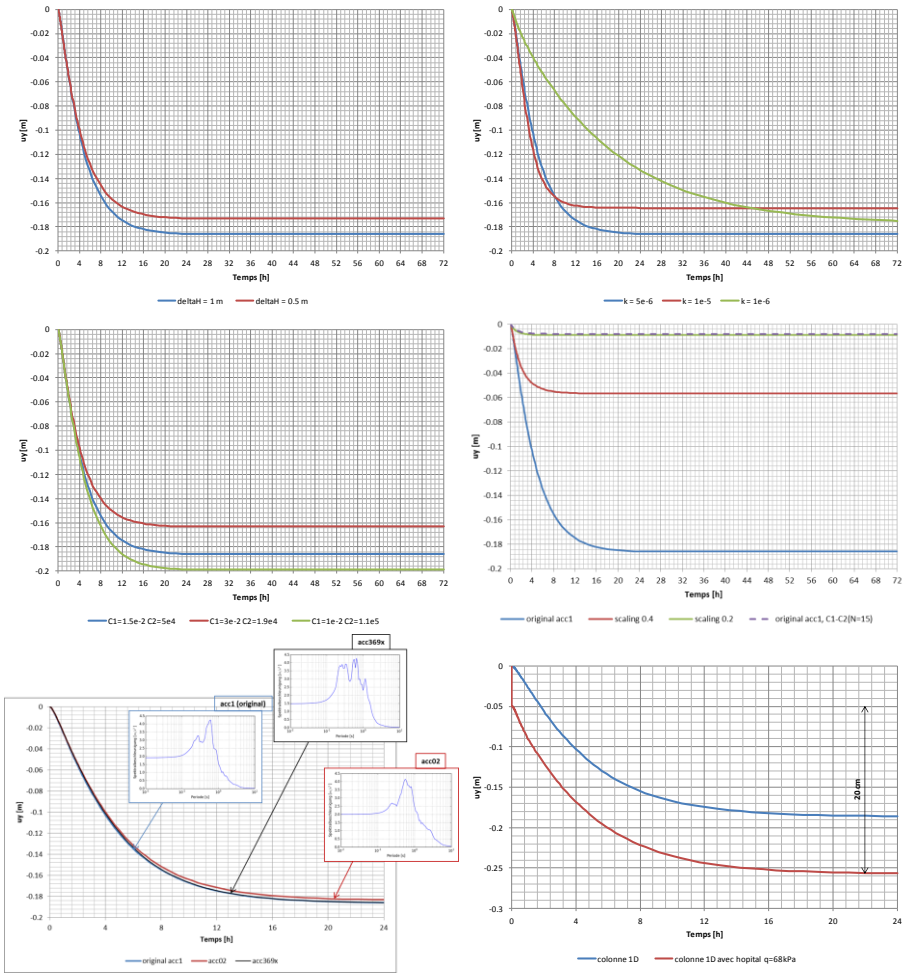

Figure 12. Surface settlements: parametric study

5. 3D Pseudo-static modeling

The initial foundation design included piles of 20 m length, and therefore the pile tip was located in the sand layer that was vulnerable to liquefaction. If liquefaction occurs in this sand layer, the pile tip resistance and the pile skin friction in the liquefied layer would reach a value close to zero, resulting in a reduction in the pile load capacity and significant pile settlements. One proposition to reduce the vulnerability was to increase the pile length to reach the stable sand layer below. The 3D pseudo-static modeling will investigate the influence the pile length has on post-liquefaction settlement.

5.1 5 x 5 m cell with a single pile

5.1.1 Pseudo-static post-liquefaction parameters

In this section, to better understand the effect caused by liquefaction on the pile capacity, a 3D model of a single loaded pile is simulated. Rather than running a dynamic simulation where liquefaction is induced by cyclic shear strains, a pseudo-static approach is used where the Mohr-Coulomb constitutive model is defined in the liquefiable zone. The strength and stiffness parameters of the Mohr-Coulomb model are reduced in this zone to simulate post-liquefaction soil strength and stiffness. The values of post-liquefaction strength parameters were approximated following recommendations found in [13] and [14]:

- $c_{res} = \sigma'_{v0} / 10$. Mid layer $\sigma'_{v0} = 200$ kPa, leading to $c_{res} = 20$ kPa
- $\phi_{res} = 0°$

and the post-liquefaction stiffness (E_{res}) was estimated by running a pseudo-static 1D soil column and calibrating the settlements with the settlements of the 1D transient dynamic simulation :

- 5 cm settlement after application of hospital charge for non-liquefied strength parameters.
- ~20 cm settlement induced by liquefaction.

5.1.2 Pseudo-static procedure

For all pseudo-static simulations, the simulation procedure is as follows:

1. T= 0: Establishment of the initial stress state prior to construction with parameters according to [2]
2. T = 1: Construction of foundation (pile and slab)
3. T = 2-3: Application of surface load due to hospital construction (q = 68 kPa)
4. T = 3-4: Removal of surface load due to hospital construction
5. T = 4-5: Reduction of strength parameters in the layer vulnerable to liquefaction to residual strength and stiffness values shown above
6. T = 5-6: Application of surface load do to hospital construction (q = 68 kPa)

The difference between the settlement at T = 3 and T = 6 gives the settlement induced by liquefaction. The time history of vertical settlement at the pile head can be seen in Figure 13 for the calibrated 1D pseudo-static soil column. The mesh and pile location for the 3D pseudo-static simulations can also be seen in Figure 13.

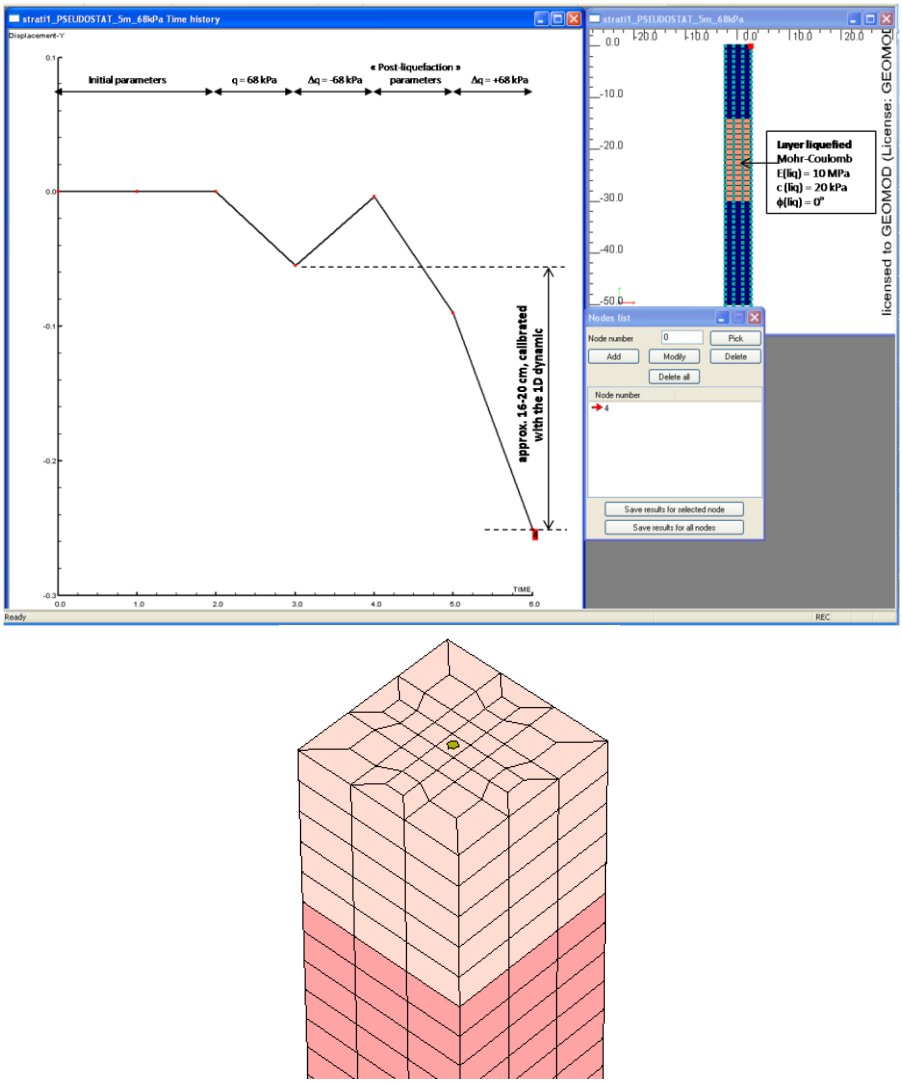

Figure 13: Time history of settlements for the 1D pseudo-static model and mesh for the 3D pseudo-static model

Following the calibration of the post-liquefaction stiffness parameters in the liquefiable layer with the 1D soil column model, a 3D pseudo-static model of 5 x 5 m cell was generated. The same simulation procedure was followed, and the parameters calibrated with the 1D pseudo-static model applied.

After the validation of this 3D model, a 0.85 m diameter pile of varied lengths was introduced into the center of the 5 x 5 m cell to investigate the influence of the pile length on liquefaction-induced settlement. The frictional pile-soil interface Coulomb law is dependent on the adjacent soil, and defined as follows: $\tau = c_{soil} + 0.7\ \sigma'_n\ tg\ \phi_{soil}$.

Following recommendations given by the geotechnician, the stiffness of the top layer was reduced to ensure that all of the hospital load was transmitted into the pile. This assumption was made considering that the top soil layer is also vulnerable to liquefaction, and therefore would not support any of the hospital load post-liquefaction.

5.2 Results

5.2.1 Settlements vs. pile length

An analysis of the influence that the pile length and the post-liquefaction cohesion (c_{res} = 1, 10 or 20 kPa) have on the results was made with the results shown in Figure 14. A clear reduction in the settlements can be seen as the pile length increases, with a significant reduction occurring when the piles are well bedded in the non-liquefiable sand layer (30 and 35 m long piles). For the cases with a post-liquefaction cohesion of 1 kPa, the calculations diverged for pile lengths that did not pass into the stable soil layer below (L_{pile} < 30 m).

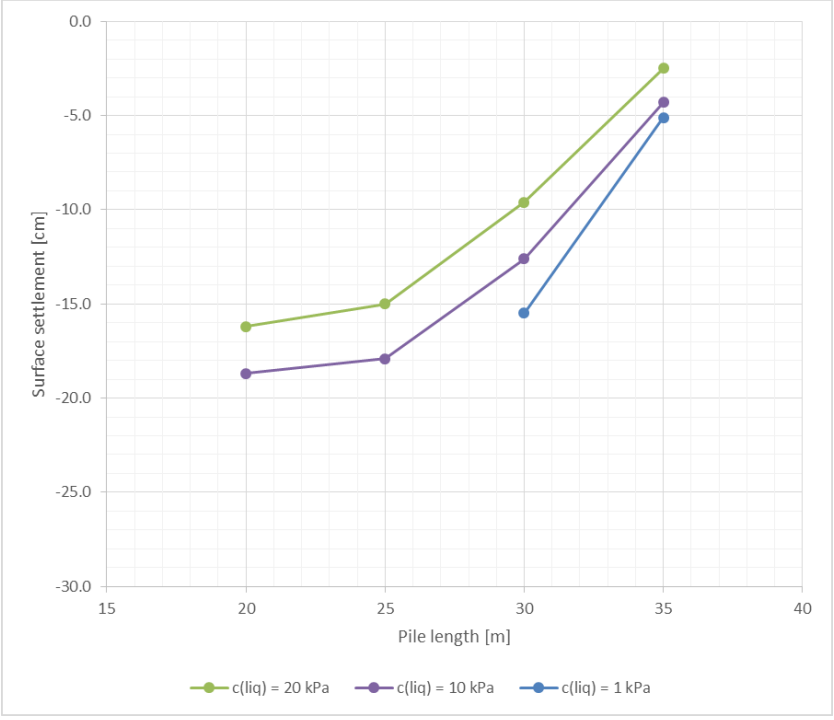

Figure 14: Settlement vs. pile length for various post-liquefaction cohesion values

In Figure 15, the normal force distribution in the pile is shown for 20, 25, 30 and 35 m pile lengths for the case with a post-liquefaction cohesion of 20 kPa. It is clear that :

- for the 20 m long pile, the load is taken by the layers above the liquefied soil. Significant pile settlement occurs in these top layers to generate the pile skin friction necessary to support the pile load. When comparing the surface settlements with the 0 m pile length case, the 20 m long pile reduces the settlement by less than 2 to 3 cm (see Figure 14).
- for the 35 m long pile, the load is transferred through the liquefied layer to the sand layer below. It also appears as though the pile experiences negaitve skin friction/drag down in the top sand layers, effectively supporting these layers as they settle due to the liquefaction (shown by maximum normal force occuring in the gravel layer).
- When the pile length is increased from 25 to 30 m and the stable sand layer is reached, a significant reduction in settlements occurs due to the transmission of pile loads down to the stable sand layer.

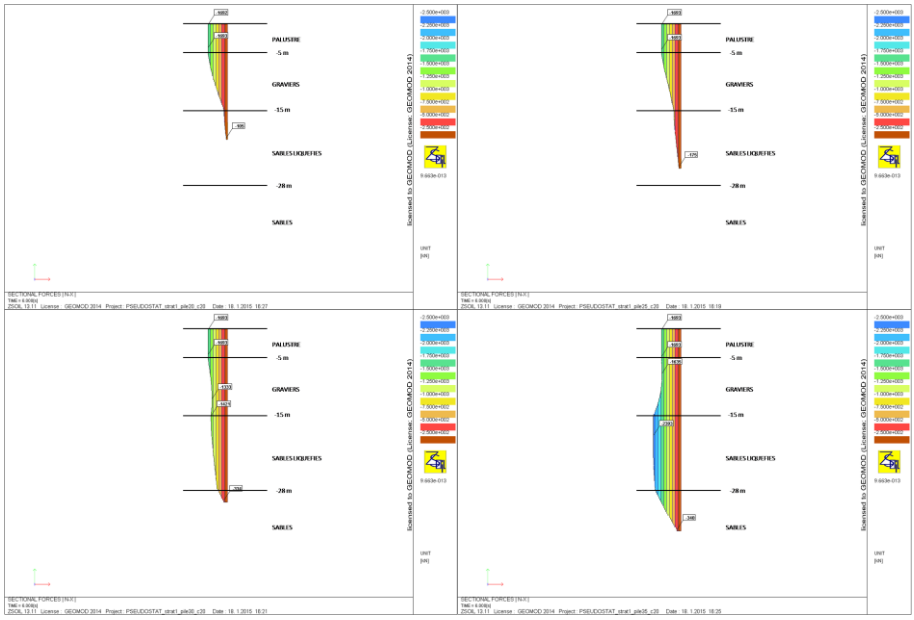

Figure 15: Normal force distribution in the pile for 20, 25, 30 and 35 m pile lengths

5.3 3D cross-section of foundation

To confirm the response of the pile foundation system, a cross-section of the structure was modeled. As shown in **Błąd! Nie można odnaleźć źródła odwołania.**, a 55 m slice of the foundation was modeled by copying 11 of the 5 x 5 m cells. The cross-section is located in the center of the foundation with half of the cross-section located above a stable sand layer, and the other half above a 10 m thick liquefiable sand layer (where post-liquefaction strength parameters will be introduced).

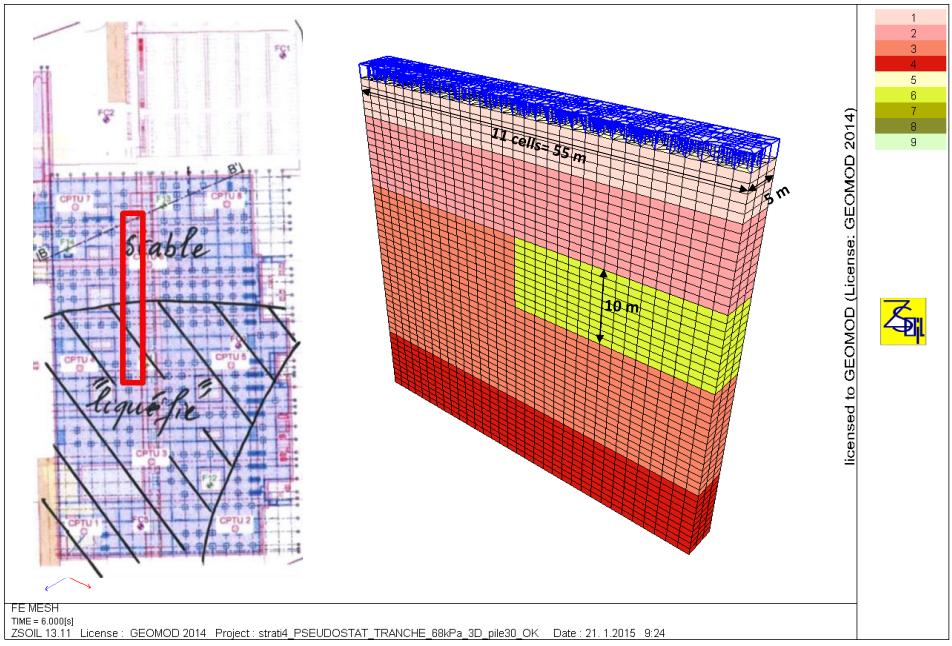

Figure 16: Geometry of 3D cross-section that was analysed

5.3.1 Results

The settlement contour plots for the cases with 20 and 30 m long piles are shown in Figure 16. They both clearly show a significant differential settlement between the stable and liquefied zones. Settlements in the center of the liquefied zone are approximately 12 and 4 cm larger than in the stable zone, for the 20 and 30 m long pile cases respectively. This also indicates a large reduction of the settlements when the piles pass through the liquefied layer and reach the stable sand layer below.

The influence on the pile axial force can also be seen in Figure 16. The case with 20 m long piles shows that the pile carries almost zero axial force as soon as it reaches the liquefied layer. However, for the case with 30 m long piles, the axial force is carried through the liquefied layer to the stable sand layer below.

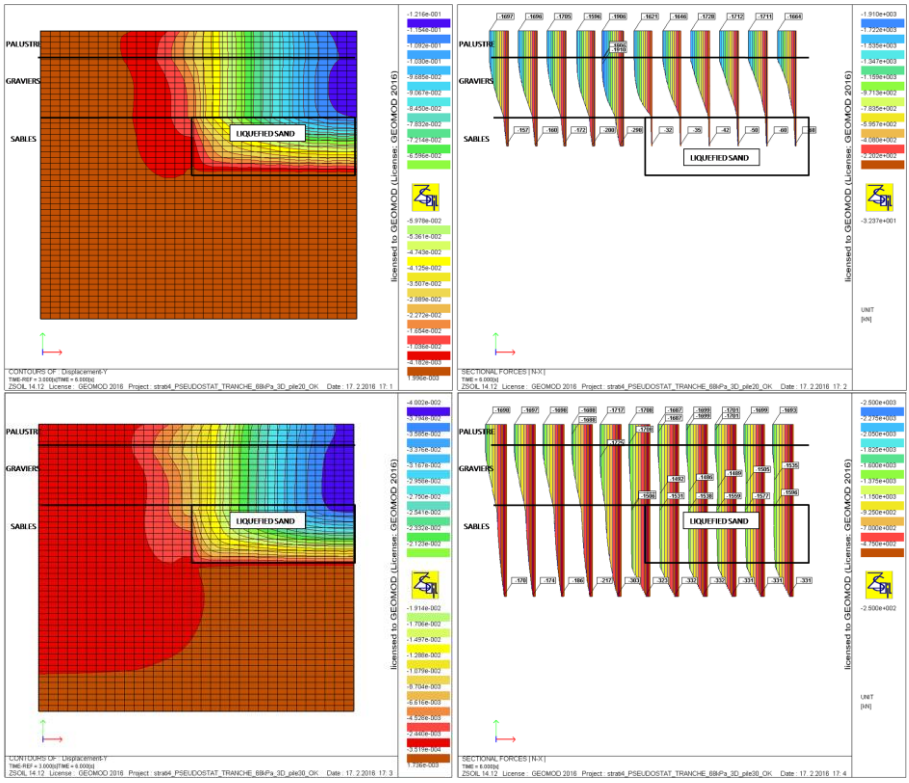

Figure 16: Surface settlements and pile normal forces for the analysed section with 20 and 30 m long piles

It appears that longer piles that reach the stable sand layer may not sufficiently reduce the settlement. They significantly reduce the magnitude of settlement, but some differential settlement still remains. Finally, after many discussions between the project experts, the final decision was to use vibratory compaction to reduce the likelihood of liquefaction occurring.

6. Conclusions and future work

In this report, it has been shown that liquefaction phenomena can be reproduced using ZSOIL with the densification model. Starting with single-element tests with data from a geotechnical report and the local seismic demand, appropriate soil parameters were estimated/calibrated. The use of several different levels of model complexity allowed further validation of the estimated parameters as well as the modeling approaches. Finally, the use of pseudo-static modeling allowed a parametric study of the pile length to be completed. Future work could include validating 3D transient dynamic analysis with the densification constitutive model, but this is yet to be completed. This will enable a better understanding of the soil-structure interaction that occurs during liquefaction under dynamic loading.

Figure 17: Final decision to use vibratory compaction to reduce the liquefaction risk

7. Actors and acknowledgements

The main contractor was HRC Vaud-Valais, the geotechnician was Karakas+Français SA, and the civil engineering office was Willi SA. Résonance SA (expert for the geotechnician) and Bureau Tissières SA (expert for the contractor) also participated in the discussions leading to the final foundation design, while GeoMod SA provided finite element models.

Many discussions with Prof. A. Truty (Zace Services Ltd. and CUT) helped us conduct these analyses in a very short period of time.

Finally we'd like to thank Prof. Th. Zimmermann (Zace Services Ltd.) for all his advice during this analysis and the writing of this paper.

8. References

[1] *Z_SOIL.PC 2014 user manual*, Zace Services Ltd, 2014

[2] *Etude géotechnique*, Karakas & Français SA, octobre 2012

[3] *Essai au pénétromètre statique*, GeoProfile, juin 2014

[4] *Etude du système de fondation en cas de séisme*, K&F SA, septembre 2014

[5] *Complément à l'étude de liquéfaction par sondages CPTU*, Résonance, octobre 2014

[6] *Notes de séance Tissières SA-GeoMod SA*, 17 novembre 2014

[7] *Geotechnical earthquake engineering*, Steven Kramer, 1996

[8] *An empirical method for predicting surface displacements due to liquefaction-induced lateral spreading in earthquakes*, PhD dissertation, A. Rauch, 1997

[9] *Evaluating soil liquefaction and post-earthquake deformations using the CPT*, P.K. Robertson, Proc. of the second international conference on site characterization, 2004

[10] *Semi-empirical procedures for evaluating liquefaction potential during earthquakes*, I. Idriss, R. Boulanger, Soil Dynamics and Earthquake Engineering, vol. 26, no 2, 2006

[11] *Evaluation of Earthquake-Induced Settlement in Dry Sand Layers*, Chen Yie-Ruey el al, The Electronic Journal of Geotechnical Engineering (EJGE) M, vol. 14, 2009.

[12] *Dynamics in ZSOIL*, A. Truty, Th. Zimmermann, 2013

[13] *Residual Shear Strength of Liquefied Soils*, M. Idriss, R. Boulanger, in proceedings of «Modernization and Optimization of Existing Dams and Reservoirs», 2007

[14] E-mail discussions between A. Pecker and S. Commend, 2010

Dynamic time-history analyses

Matthias Preisig

Geomod SA, Epinettes 32, 1007 Lausanne, SWITZERLAND
mpreisig@geomod.ch
www.geomod.ch

1. Introduction

Nonlinear time history analyses are a powerful tool for the design of new and the verification of existing geotechnical structures. If the structural safety of an existing structure cannot be proven with simpler methods, or if the complexity of the geometry does not allow the use of simpler methods, they provide an alternative. The application of nonlinear time history analyses requires, however, that the user has profound knowledge regarding algorithms, the use of suitable boundary conditions, seismic input methods and material models. Validation of the results also requires special attention.
This paper addresses several fundamental questions related to nonlinear time history analyses for seismic verification and design in geotechnical engineering:

- Discretization in space and time
- Different forms of dissipation in FE-models and material damping in commonly used material models for soils
- Boundary conditions and seismic input methods
- Validation of FE-models and results

1.1. Definition

The expression "nonlinear time history analysis" refers to numerical analysis methods that account for the nonlinear behavior of materials in time domain. It is equivalent to the expression "nonlinear dynamic method".
Although many considerations apply to soil dynamics in general, the focus in this paper is on earthquakes. As opposed to other soil vibration problems the source of the excitation lies outside the model domain. Structures are primarily subject to vertically propagating shear waves. Other actions such as deformations imposed by surface waves, which might be relevant for very long structures, will not be addressed.

2. Discretization

2.1. Discretization in space

Several requirements need to be considered in the elaboration of finite element meshes:

- A mesh should represent the geometry of a problem with its main features adequately in order to resolve relevant quantities such as deformations, internal forces in the structures, earth pressures etc. with sufficient accuracy.
- The mesh size has to be small enough to resolve for the problem relevant wave lengths with 5 to 10 nodes. For vertically propagating shear waves the following condition needs to be satisfied:

$$h \leq \frac{\lambda_{min}}{5 \text{ to } 10} = \frac{v_s}{f_{max}(5 \text{ to } 10)}$$

  where h is the nodal spacing, □ the wave length, v_s the shear wave velocity and f_{max} the largest frequency relevant for the simulation. In general a model should be able to represent frequencies up to 20 to 25 Hz (f_{max}).
- At the same time a discretization should not be too fine in order to keep the number of degrees of freedom low and therefore computing times reasonable. The horizontal nodal spacing can be larger than the vertical one, if horizontally propagating waves are mainly compression waves. This is, however, not the case if surface waves are important for the problem at hand.

2.2. Discretization in time

For explicit methods the time step length must be smaller than the time it takes for a wave to travel between two nodes. This condition is known as the Courant-Friedrichs-Lewy condition [1]. When using implicit methods, as is the case in most FE-codes used in geotechnical engineering, this condition does not have to be satisfied. It this case the time step requirement is usually given by the input signal that needs to be represented without losing any important frequency content. In general it is justifiable to use the time step of the input signal.
Algorithms with variable time step length should not be used since this would affect numerical (algorithmic) dissipation.

3. Dissipation

3.1. Physical forms of dissipation

Seismic energy is dissipated by material damping in structures and soil. Material damping leads to energy dissipation as a result of the following physical processes:

- **Permanent plastic deformation**: Strong earthquake excitation can lead to permanent deformation in structures and soil. In this process seismic energy is transformed into heat through friction.
- **Viscous damping**: Viscous damping occurs mainly in liquids. In soils it arises from pore water flowing through the soil matrix or it can result from liquefaction of loose sediments.

- **Hysteretic damping**: For nonlinear stress-strain behavior the loading stiffness is generally lower than the unloading stiffness. During repetitive loading-unloading cycles in soils energy is typically dissipated through hysteretic damping. Hysteretic damping is amplitude dependent; in the small amplitude range it can be caused by nonlinear elasticity, while for larger amplitudes it is mainly the result of plastic deformation.

For problems of soil-structure interaction or soil vibration the FE-model usually has to be limited by boundary conditions that do not correspond to a physical boundary, such as a stiff rock horizon. Outgoing waves represent a form of energy loss for the model domain. This form of dissipation is called **radiation damping**.

3.2. Dissipation in the FE-model

In order to represent the behavior of a soil-structure system as accurately as possible all previously mentioned forms of physical dissipation should be modeled appropriately. Adequate modeling of dissipation in soil is particularly important at low to medium seismic excitations, when only little energy is dissipated through plastic deformation. According to Seed et al. [7] the hysteretic damping coefficient in sands at shear deformations of up to 10^{-5} is less than 2 to 3%.

Methods available for modeling dissipation can roughly be divided into two groups: On one hand there are methods that represent physical processes more or less realistically. On the other hand there are purely numerical methods that cannot be associated with any real physical process.

The following physical forms of dissipation can be represented by numerical methods:

- **Permanent plastic deformation**: Elastic-plastic material models allow the simulation of seismically induced plastic deformation.
- **Viscous damping**, caused by pore water flowing through the soil matrix, can be represented through appropriate two-phase material models.
- **Hysteretic damping at small strains** can be modeled through advanced material models. The Masing-Rule, which is included in the Hardening-Soil Small-strain model (HSS), can fulfill this task.
- **Radiation damping** can be taken into account using absorbing boundary conditions.

The following numerical models cannot be associated with any real physical process:

- **Rayleigh damping** introduces a mass- and a stiffness proportional damping coefficient into the model. Rayleigh damping is frequency dependent: mass-dependent damping is active in the low frequency range while stiffness-dependent damping becomes active at high frequencies. Since Rayleigh damping does not represent any physical

form of dissipation it has to be calibrated specifically for the dynamic properties of every model.

- **Algorithmic damping** arises from time integration algorithms of the equations of motion. This form of damping is frequency-dependent and reduces amplitudes at high frequencies. Damping at high frequencies is useful in order to reduce oscillations that are non-physical and only due to the discretization in time and space. The Hilbert-Hughes-Taylor algorithm (HHT) with parameter □ = -0.3 is a commonly used. It is second-order accurate while being able to damp high frequencies effectively [4].

3.3. Quantitative investigations

3.3.1. Hysteretic damping in the HSS model

The Hardening-Soil Small-strain model (HSS) has largely become a standard for static problems in geotechnical engineering. Thanks to stress-dependent stiffness moduli, the distinction between loading and unloading stiffnesses as well as the activation of an initial stiffness modulus for small deformations it is capable of representing displacements of retaining walls and settlements under and in the vicinity of structures very accurately.
Through the use of an initial stiffness modulus for small deformations and a strain-dependent reduction of the tangential stiffness a hysteresis loop arises in the stress-strain diagram for cyclic loading (Figure 1). The surface enclosed by the loop is equal to the dissipated energy. According to the Masing-rule the loading and unloading branches are geometrically similar.

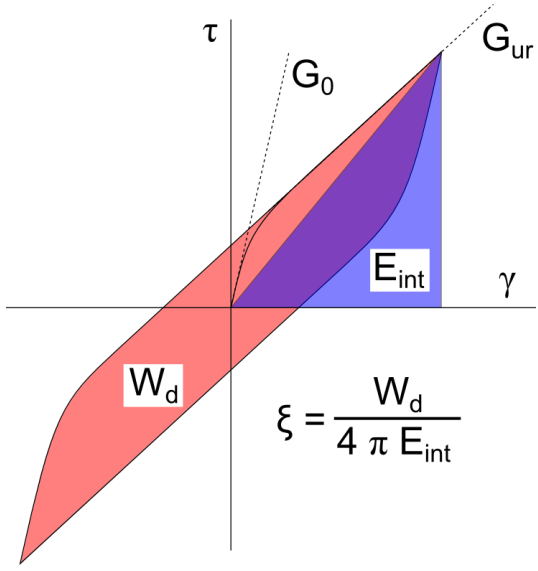

Figure 1: Hysteresis loop in the stress-strain diagram.

Based on the stress-strain curve the hysteretic damping coefficient is calculated as:

$$\xi = \frac{W_d}{4 \pi E_{int}} \tag{1}$$

where W_d is the area enclosed by the loop. The internal energy E_{int} corresponds to the area under the line from the origin to the point of maximum shear strain. G_0 is the initial shear modulus, G_{ur} the modulus for unloading and reloading.
The reduction of the initial stiffness modulus follows the relation after Hardin-Drnevich [3], up to a threshold shear strain of γ_c. Beyond this threshold the stiffness modulus remains constant and equal to the unloading / reloading stiffness, while the apparent tangential stiffness is reduced due to plastic deformation. The threshold shear strain is computed according to:

$$\gamma_c = \frac{\gamma_{0.7}}{0.385} \sqrt{\frac{G_0}{G_{ur}} - 1} \tag{2}$$

The coefficient 0.385 is the result of a calibration and is used in the ZSoil implementation of the HSS-model. $\gamma_{0.7}$ corresponds to the shear strain, at which the secant shear modulus amounts to 70% of the initial shear modulus G_0.
Equation (1) can be used to compute the hysteretic damping coefficient for numerical tests.
Numerical tests were performed using a quadratic, 2D plane strain model consisting of 10 by 10 elements (Figure 2). The displacements were applied to the boundary nodes as shown in the figure. In order to obtain results for a large strain range a cyclic excitation with increasing amplitude was applied.

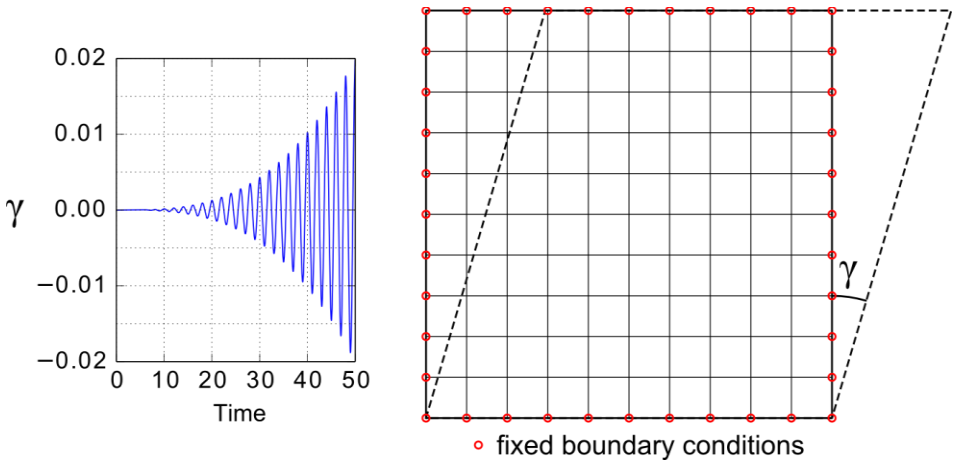

Figure 2: FE-model for numerical tests of the hysteretic behavior of constitutive models.

The stress-strain curves for three tests, HSS with and without plastic deformation as well as Mohr-Coulomb, are shown in Figure 3.

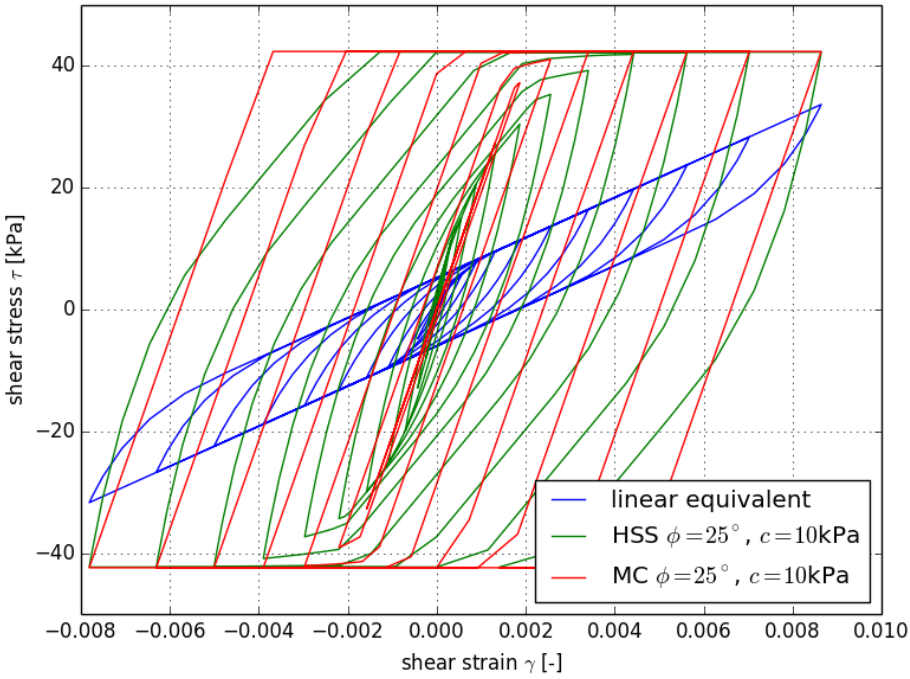

Figure 3: Hysteresis curves for three different material models.

On the basis of the stress-strain curves the secant shear modulus at maximum strain as well as the damping according to Equation (1) was computed for each hysteresis loop. Averaging stresses and strains over all the elements in the domain helped reduce boundary effects and made it possible to obtain meaningful results.

Three series of tests were conducted:

- For the tests presented in Figure 4 plastic deformation was deactivated. At large strains the curves tend to the ratio of unloading / reloading stiffness to initial stiffness. Because the threshold shear strain depends on the stiffness ratio the evolution of the damping ratios is also affected. Beyond the threshold shear strain γ_c the damping ratio decreases as a result of the secant shear modulus being constant (E_{int} increases faster than W_d).
- Figure 5 shows the results of a series of tests using HSS without plastic deformation (linear equivalent) and HSS and Mohr-Coulomb with friction angle of 25° and cohesion of 10 kPa. The Young's modulus for the Mohr-Coulomb test was selected between the moduli for primary loading (secant modulus E_{50}) and unloading / reloading. The main difference between Mohr-Coulomb and the other models lies in the existence of a cutoff shear strain, below which due to the absence of plastic deformation no damping is present. If the parameters of the HSS

model are calibrated appropriately the transition from small-strain hysteretic damping and damping through plastic deformation is smooth.

- In the third test series (Figure 6) the influence of the threshold shear strain γ_c is shown. The modulus reduction and damping ratio curves illustrate how the threshold shear strain affects the curves mainly in the small strain range.

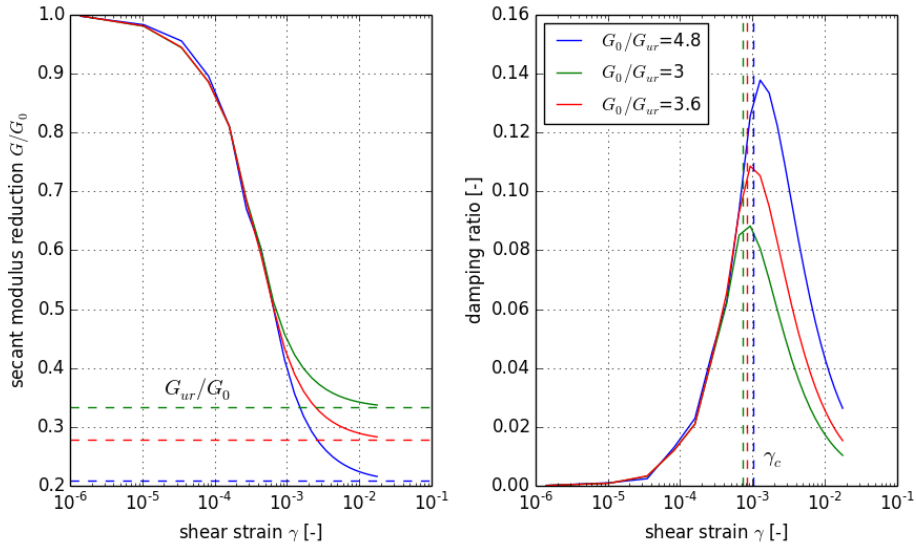

Figure 4: Reduction of secant shear modulus and hysteretic damping coefficient as a function of shear strain. HSS material model without plastic deformation.

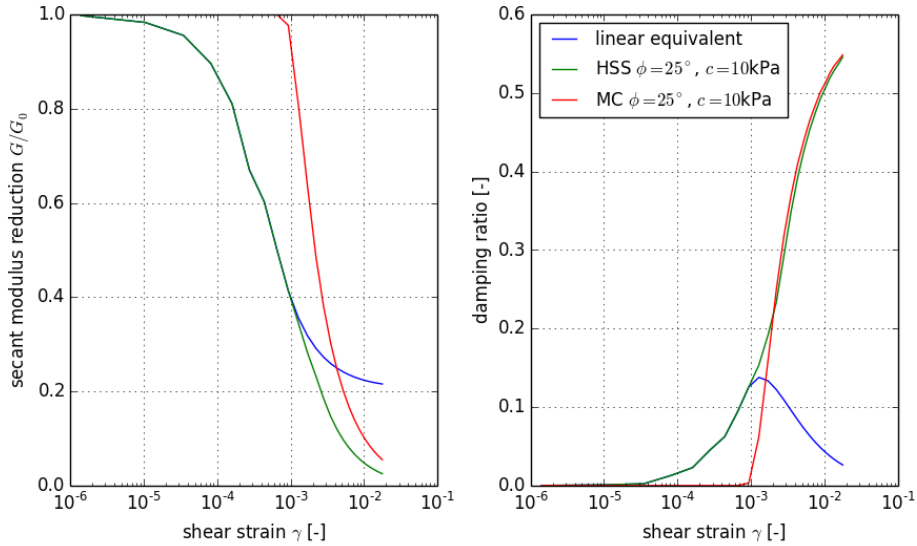

Figure 5: Reduction of secant shear modulus and hysteretic damping coefficient as a function of shear strain. With and without plastic deformation.

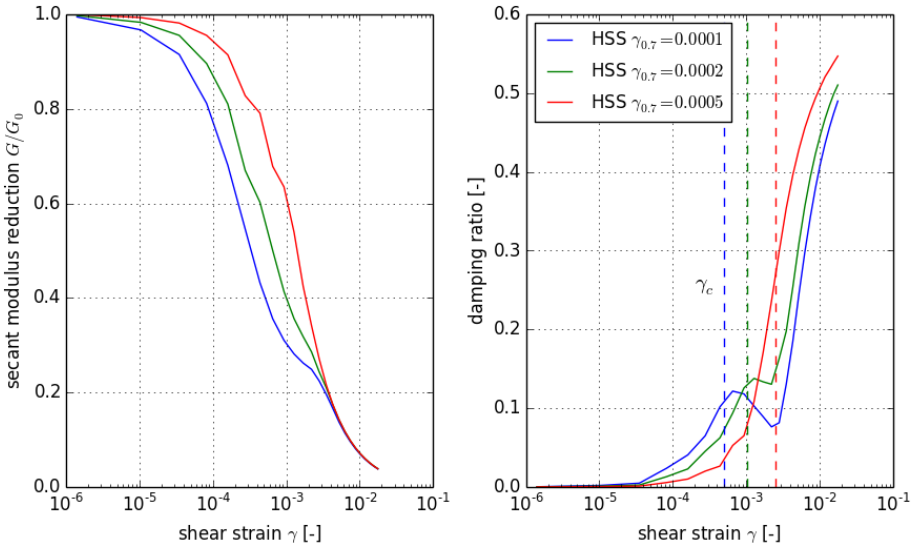

Figure 6: Reduction of secant shear modulus and hysteretic damping coefficient as a function of shear strain. HSS with different threshold shear strains.

For calibration of the material models experimental results are available for different types of soils. For cohesionless sands for example Seed et al. [7] present curves for modulus reduction and damping ratios.

4. Boundary conditions and seismic input methods

Selecting appropriate boundary conditions is of particular importance for dynamic problems. Since for seismic problems the displacements are non-zero throughout the model, special attention has to be paid in order not to disturb the natural wave propagation pattern. In particular, earthquake waves should be allowed to freely travel from the boundary to the structure of interest, while outgoing waves should be able to leave the model domain without generating reflected waves that might disturb the response of the structure.

In finite element methods there are two basic methods for applying boundary conditions: imposing displacements (Dirichlet boundary conditions) or applying forces (Neumann boundary conditions).

Setting either displacements or forces to values different from what they would naturally be will reflect waves. These reflected waves can, however, be reduced by imposing boundary conditions that are close to the motions/forces as they would be in reality. An overview of boundary conditions is presented in the following.

4.1. Displacement boundary conditions

Applying free-field motions to the model boundary can be a good way of reducing boundary effects. Only the perturbation created by the local feature will be reflected at the boundary, while the free-field part will be absorbed.
Several commercial software packages contain so called "free-field boundaries". Often they include viscous dashpots between the boundary nodes with imposed free field displacements and the adjacent nodes of finite elements. These dashpots are supposed to absorb part of the perturbation coming from the local feature.

4.2. Force boundary conditions

A multitude of methods apply forces to the model boundaries. These forces can either be determined from the motions of the free field, as is the case with the "Domain Reduction Method" (DRM, Bielak et al. [2]), or they can be computed using some specific force-displacement relation. In case of the second family of methods we can speak of boundary elements, whose force displacement relation adds terms to the global stiffness and mass matrices. The most commonly used method in this category consists in adding viscous dashpots (Lysmer boundaries) to the model boundary.
The DRM consists in applying forces to the nodes of an element layer on the model boundary that, if the interior of the model would be equal to the free-field, would generate free field motions on the inside and zero motions on the outside nodes. Perturbations, created by interaction of seismic waves with a structure, can be partially absorbed on the exterior nodes using viscous dampers. Hereby it is important to note that the layer of boundary elements has to behave linearly elastically for the principle of superposition to hold.
Most of the methods that fall within the category of force boundary conditions are not used very often, so there is not much practical experience available for realistic problems. Validation of their results is therefore not a simple task. In some cases it might even be preferable from a conservative standpoint to accept wave reflections at the model boundary, as opposed to using an inadequate method that absorbs too much energy.

4.3. Kinematic constraints

Instead of introducing a model boundary it is possible to enforce continuity of displacements and forces by the use of kinematic constraints. Doing this between the nodes of opposite model boundaries is equivalent with repeating the same finite element model laterally an infinite number of times.

5. Validation

Thanks to their versatility finite element methods are able to represent the behavior of very complex geometries and material behaviors. But this complexity can make checking the results by other people rather difficult. A

complete documentation of all input data, including details on discretization (nodal coordinates, time steps etc.) and algorithmic parameters is in general not useful. Even the complete documentation of all parameters for advanced material models can already be a formidable task. Certain standardization for validating and documenting numerical computations can therefore greatly improve the verifiability and facilitate timely detection of computation and modeling errors.

It is the obligation of the analyst to document his calculations clearly and with enough detail such that the main results can be reproduced. This documentation should also include some results that allow validation of the results. For instance, even if a client is only interested in cross-sectional forces in a structure an illustration of the displacement field will help understand the mechanism causing these forces.

Validation of numerical results includes the examination, whether the numerical model, that is the mathematical equations and material parameters, adequately represents reality. In contrast, **verification** of a numerical model is concerned with making sure that the mathematical equations are implemented right and are solved correctly by the numerical algorithms. Oberkampf et al. [6] treat the subject of validation and verification of numerical methods in detail. This section is exclusively concerned with validation, assuming that the employed software is thoroughly verified.

Validation of a model for nonlinear time history analyses includes the following aspects:

- Are the mathematical equations an adequate representation of reality?
- Is model size and mesh refinement adequate for a sufficiently precise resolution of the mathematical equations?
- Do the material parameters simulate the material behavior with satisfaction?
- Do the selected earthquake accelerograms appropriately represent the seismic risk?

Several possibilities for validating nonlinear dynamic simulations will be investigated in the following.

According to the Swiss norm SIA 267, results of FE-simulations have to be checked using a reliable comparative method. One option is the use of pseudo-static methods, such as the replacement force method. Such methods are generally known to be conservative. Since the replacement force method will generally activate one specific failure mode, and because inertial phenomena (resonance), soil liquefaction etc. are not considered specifically, the method might not yield conservative results in every case. Static methods are generally also not suitable for computing permanent plastic deformations. Empirical methods are available for computing displacements for some specific problems, but their value often does not go beyond comparison with historical evidence or experimental results.

Instead of trying to find an alternative method to solve the same problem statement it is often more useful to thoroughly validate the FE-computation by the following approaches:

5.1. Subdivision of a problem

It is good practice to validate aspects of a problem separately by subdivision into subproblems. Once all subproblems are validated one can assume that the complete model can be used for predictions.
The most important aspects of a nonlinear time history analysis requiring validation are: (1) the numerical discretization , (2) the vibration behavior of the soil-structure model and (3) the nonlinear material behavior.

1. Satisfaction of the conditions in the section on discretization should be sufficient for its validation.
2. Vibration behavior:
    - Vibrations at the surface of the FE-model without a structure or in safe distance from it have to conform to the demand spectrum specified in the norm (see Eurocode 8 part 1 §3.2.3.1.2)
    - The choice of model size and boundary conditions is important for reproducing a realistic vibration behavior. The model size can be validated by a comparison using a larger model. If significant differences persist the original model size or the employed boundary conditions are not adequate.
    - The analyst has to be sure that the considered loading is preponderant. For very long buildings surface waves or lateral variation of soil properties might have a strong impact on forces in the structure. Vertically propagating shear waves might not represent the highest risk for such a structure.
3. Nonlinear material behavior can be validated on simplified models:
    - Static tests: The computation of a safety factor by progressive reduction of soil strength can give an indication on the behavior that can be expected. The failure mode obtained can also give an indication on whether the discretization near the foundation is sufficiently fine.
    - Elementary tests with one or a few finite elements are useful for calibration of the material behavior, in particular if laboratory test results are available.
    - Dynamic tests: For complex material models such as the HSS model one-dimensional models using a soil column (one element width with periodic boundary conditions) are useful for investigating shear wave velocity and damping behavior.
    - Contact or interface elements can also have a strong influence on interaction behavior between soil and structure. Validation can, however, often only be done on the complete dynamic

model. Strong oscillations between individual time steps are an indication for numerical problems. The user manual of the software should provide help on how to avoid such problems for the specific interface elements.

5.2. Parameter sensitivity analyses

Sensitivity analyses allow an assessment of the influence of the variation of a single parameter while keeping all other parameters constant. This gives a bandwidth of possible results and allows an assessment of their overall precision.

For seismic problems the shear wave velocity profile often has a dominant influence on the vibration behavior of the soil-structure system. One has to keep in mind that a small difference in the shear wave velocity profile can by shifting the resonance frequencies have a considerable impact on the seismic demand on a structure.

5.3. Documentation

Clearly documenting all relevant input parameters and results is an important requirement for the validation of numerical computations. Errors in FE-models are often only detected in graphical representations of the resulting quantities. The following aspects should be considered:

- A graphical representation of displacements should always be included in the documentation. It illustrates if the displacement pattern is plausible, for instance if a clear failure mechanism in the form of an earth pressure wedge behind a retaining wall is visible. In the displacement field mesh dependency can be identified, or the presence of strong boundary effects can be seen, even if these do not necessarily need to affect the results.
- In a representation of shear strains or plastic levels no strong mesh dependency, such as checker board patterns, should appear. Such patterns can indicate the presence of locking phenomena, which lead to an underestimation of displacements.
- It is useful to define variables that will be computed for every model run and can be compared easily. Good parameters for comparison are displacements, for instance at the crown of a retaining wall, or section forces, for example the moment or the shear force at the base of a column of a building. It can also be useful to observe the evolution of integrated parameters, such as plastic strain energy or the earth pressure acting on a retaining wall.

References

[1] Belytschko, T., Liu, W.K., Moran, B., Nonlinear Finite Elements for Continua and Structures, Wiley, Chichester, 2000.

[2] Bielak, J., Loukakis, K., Hisada, Y., Yoshimura, C., Domain Reduction Method for Three-Dimensional Earthquake Modeling in Localized Regions, Part I: Theory. Bulletin of the Seismological Society of America, 93(2), 817-824, 2003.

[3] Hardin, B.O., Drnevich, V.P., Shear Modulus and Damping in Soils: I. Measurement and Parameter Effects, II. Design Equations and Curves. Journal of Soil Mechanics and Foundation Division, ASCE, 98(6):603-624, 1972.

[4] Hughes, J.T.R., The Finite Element Method, Dover Publications, Mineola (NY), 2000.

[5] Lysmer, J., Tabatabaie-Raissi, M., Tajirian, F., Vahdani, S., Ostadan, F., SASSI - A System for Analysis of Soil-Structure Interaction, Report No. UCB/GT/81-02. Department of Civil Engineering, University of California Berkeley, 1981.

[6] Oberkampf, W. L., Trucano, T. G., Hirsch, C., Verification, Validation, and Predictive Capability in Computational Engineering and Physics. 2004.

[7] Seed, H. B., Wong, R. T., Idriss, I. M., Tokimatsu, K., Moduli and damping factors for dynamic analyses of cohesionless soils. ASCE – Journal of Geotechnical Engineering, 112(11):1016-1025, Paper no. 21030, 1986.

[8] Zienkiewicz, O.C., Taylor, R.L., The Finite Element Method for Solid and Structural Mechanics. Elsevier Science, 2005.

[9] ZSoil 2013 (Finites-Element programm). ZACE Services Ltd, Lausanne, Switzerland, 1985-2013.

Fully coupled flow-deformation analysis on the impact of the dewatering confined water to the surrounding environment

YIN Ji [a], WU Jun[b], GUAN Fei[c]
[a] *Shanghai Geotechnical Investigations& Design Institute Co., Ltd, Shanghai 200070, China*
[b] *School of Urban Railway Transportation, Shanghai University of Engineering Science, Shanghai, 201620, China*
[c] *Shanghai GeoFem Consulting Co.,Ltd, 200433, China*

Keywords: Excavation, confined water, dewatering, Hardening soil with small strain, fully coupled analysis, finite element method

Abstract
In this paper, a fully coupled flow-deformation analysis using 3D FEM software ZSOIL.PC is conducted to simulate the entire construction stage of excavation in the 757 project, including the stage of removing base slab and dewatering confined water. The hardening soil model with small strain stiffness is employed to represent the behaviour of soil in excavation. The feasibility of the construction scheme is evaluated on the basis of the predicted numerical results. Numerical results show that the maximum settlement of the nearby BaoHua project caused by the stage of removing base slab and dewatering does not exceed 11.9mm. Hence, it is found that the construction scheme proposed in current study is acceptable. The monitoring results also show that the maximum settlement of buildings in BaoHua project is less than 7.6mm, which is within the predicted numerical value. It is then proved that the coupled influence of the removing base slab and dewatering confined water on the settlement of the surrounding environment can be predicted by the ZSOIL.PC with advanced soil model properly.

1. Introduction

The initial construction scheme of the 757 project in Zhabei district of Shanghai is to build a 10-story office building, with 3-story basement. Due to the change of the function of building, the position and height of the main building has changed accordingly. The proposed main building has 27-story above-ground structure and 3-story basement, while the shape of basement and the depth of the excavation remains the same. The location of the main building

in the initial and current design is given in Figure 1. The detailed change in the property of buildings for initial design and current design can be referred to Table 1.

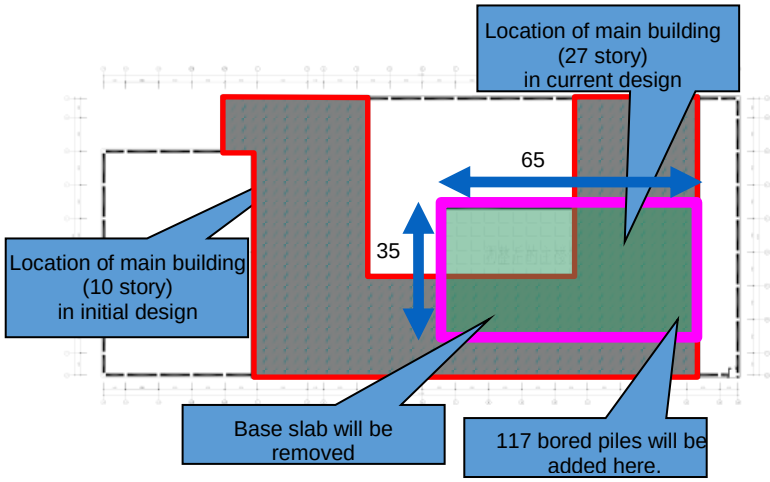

Figure1. Location of the main building of 757 project in initial and current design

Table 1. Property of buildings in initial and current design

Building	structural style	above-ground structure	underground structure	pile style/pile length/pile diameter	thickness of base slab
building in initial design	frame shear-wall structure	10-story	3-story	bored pile /40.0m/800 mm	1.1m/1.8m
building in current design	frame shear-wall structure	27-story	3-story	bored pile /40.0m/800 mm	2.3m

When the excavation has reached the formation level and base slab has been cast completely, the proprietor decided to change initial architectural design of 757 project. This leads to the suspension of the project for at least 6 months. After that, the authors are invited to analyze the impact of the dewatering confined water on the settlement of the surrounding area for the current design.

The scheme of the reinforcement of foundation for the main building in the current design is proposed as follows: (1) The base slab in the foundation of main building will be partially removed to form a "boring area"; and (2) The proposed bored piles will then be cast under the "boring area", with the penetration depth of 12m below the foundation slab. The supporting layer for the proposed bored pile in current design is the ⑧2 soil layer, and it is found the

proposed bore pile need to be penetrated through the ⑦ soil layer, which is the confined aquifer in Shanghai area. It is observed that the artesian head in the confined aquifer is 6~7m, which is 5~6m higher than the level of the bottom of foundation slab. It should be noted that for the current design, the installation of the proposed bored pile will damage the confined aquifer, and then the confined water will flow into the excavation pit. Hence, the artesian head in the confined aquifer must be dropped down below the bottom of base slab during the period of construction of the proposed bored pile. It is also found that the clear distance between the 3rd layer strut and top surface of base slab in the initial design is only 1.3m. Thus, in order to obtain enough space for piling equipment, the 3rd layer strut have to be partially removed over the "bore area " in the current design.

2. Background of the 757 project

The 757 project is located at the downtown, in which there are many above-ground buildings and underground facilities (i.e. gas pipeline and electrical tunnel). The BaoHua international business building (simplified as BaoHua project in the following) is located at the eastern side of the excavation of 757 project. The BaoHua project consists of a 25-story main office building with 2-layer basement and a 3-story skirt building. The type of the foundation for the BaoHua project is the pile foundation, which was constructed in 2010. The minimum distance between the excavation of 757 project and the exterior wall of the BaoHua's main building is 37.5m. The minimum distance between boundary of the proposed "bored area" in 757 project and the exterior wall of BaoHua's basement is 43.0 m. The layout of the excavation and surrounding buildings is reported in Figure 2.

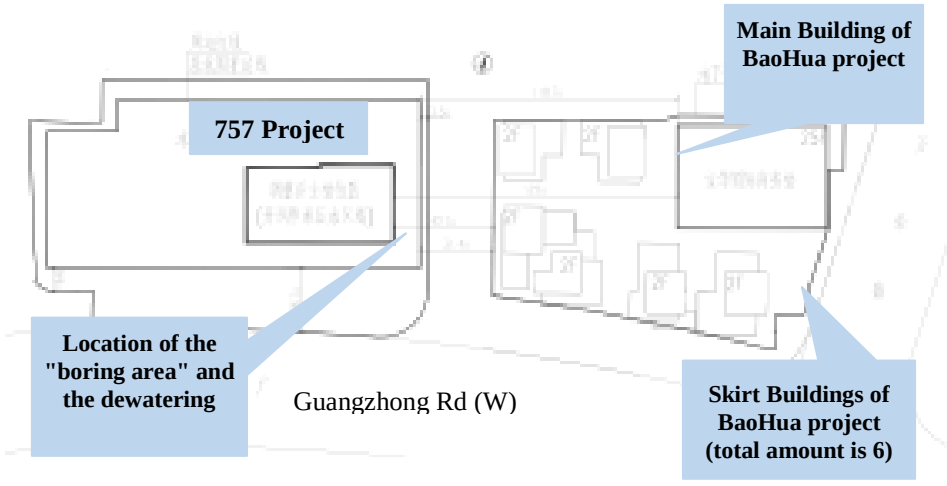

Figure 2. Layout of the excavation and surrounding buildings

3. Engineering geological conditions

3.1. Ground condition

In this project, the ground mainly consists of clayey soil, silt and sand. In terms of the soil sedimentation age, genetic type and the difference in the physical-mechanical properties, the ground can be divided into 9 main layers and several sub-layers. The characters of each soil layer is introduced in the following:

① -1 layer is miscellaneous fill. It mainly consists of construction waste, with uneven big gravels, concrete blocks and so on. The thickness of this layer is around 1.5m. This soil layer deposits in loose state. Part of this layer includes the terrace of factory building.

① -2 layer is plain fill. It mainly consists of clayey soil in loose state with little plants root and stem. The thickness of this layer is around 0.5~1.9m.

② -1 layer is auburnish yellow~grayish yellow silty clay. The base elevation for this layer is -0.92~-0.02m. The average thickness of this layer is 1.2m, and the maximum thickness is around 1.8m. This soil is in wet condition which has plastic to soft plastic state and medium compressibility.

② -3 layer is grey sandy silt with the base elevation of -1.58~-3.09m. The thickness of this layer is 2.00 to 3.30m. This soil is saturated and deposits in loose to slightly dense state with medium compressibility.

③ layer is grey muddy silty clay with the base elevation of -3.78~-4.99m. The thickness of this layer is around 1.30~2.70m. This soil is saturated which performs flow plastic state and high compressibility.

④ layer is grey muddy silty clay with the base elevation of -12.08~-13.32m. The thickness of this layer is around 7.80~9.40m. This soil is saturated which shows flow plastic state and high compressibility.

⑤ layer is grey clay with the base elevation of -16.06~-17.32m. The thickness of this layer is around 3.20~4.50m. This soil is in highly wet condition which shows soft plastic behaviour and high compressibility.

⑥ layer is dark green~straw yellow silty clay with the base elevation of -20.77~-21.76m. The thickness of this layer is around 3.80~5.20m. This soil is in wet condition which has plastic behaviour and medium compressibility.

⑦ layer is straw yellow~grey sandy silt and silty clay with the base elevation of -27.06~-28.38m. The thickness of this layer is around 5.70~6.70m. This soil layer is saturated and deposits in medium dense state with medium compressibility.

⑧ 1-1 layer is grey clay with the base elevation of -37.38~-39.02m. The thickness of this layer is around 9.60~11.20m. This soil has soft plastic behaviour and high compressibility.

⑧ 1-2 layer is grey silty clay with the base elevation of -45.58~-47.02m. The thickness of this layer is around 7.50~9.00m. This soil has soft plastic property and medium compressibility.

⑧ -2 layer is grey sandy silt and silty clay with the base elevation of -63.18~-63.94m. The thickness of this layer is around 17.40~18.00m. This soil is saturated which has the plastic to soft plastic property and medium compressibility.

⑨ layer is grey silt with the burial depth of 67m, This soil is saturated and deposits in dense state with medium to low compressibility.

Typical static cone penetration curve and geological section for the ground in current project can be referred to Figure 3.

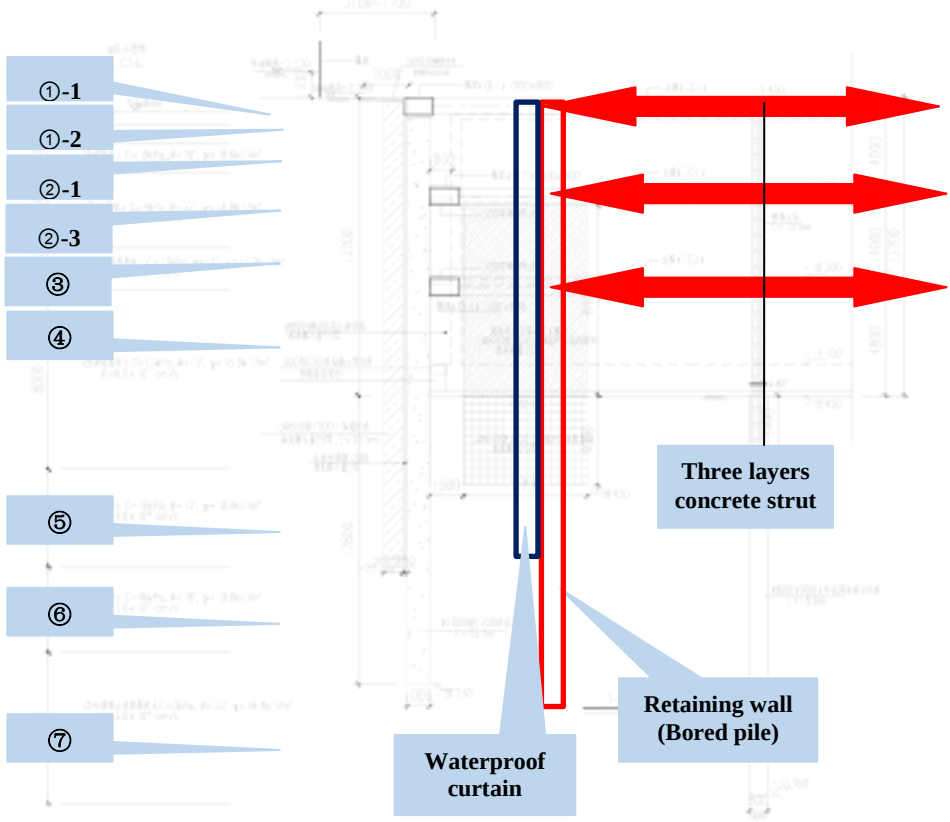

Figure 3. Sectional view of soil condition and supporting system in 757 project

3.2. Pile foundation and its reinforced scheme

In the initial design, the thickness of base slab for the skirt building and basement is 1.0m, in which the thickness of pile cap is 1.8m, and the thickness of base slab for main building is 1.8m. The bearing pile for the foundation of the main building is the bored pile with the diameter of 800mm, in which the post grouting method is adopted. The supporting layer for the bored pile is ⑧2 layer. Hence, the effective length of the bored pile is set to be 40m with the bearing capacity of 3600kN. The total amount of bored pile in the foundation of main building is 395. For the foundation of the skirt building and basement, the tension bored pile is adopted with the diameter of 800mm, in which the post grouting method is employed. The supporting layer for the tension pile is ⑧1-2 layer. Hence, the effective length of the tension pile is 31.0m with the bearing capacity of 900kN. The total amount of tension pile is 441. The layout of the pile foundation in initial design can be referred to Figure 4.

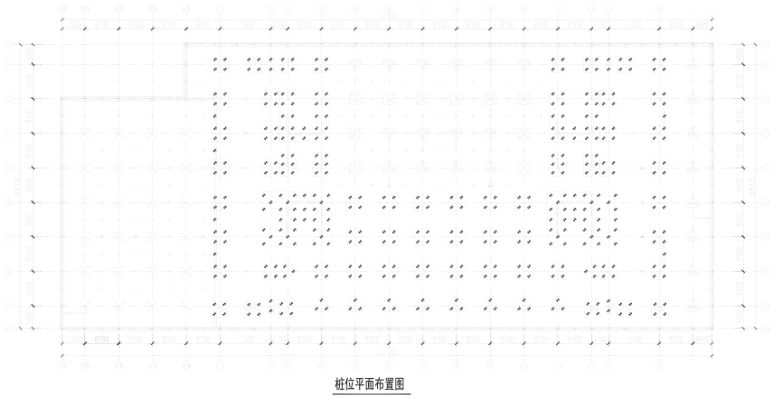

Figure 4 Layout of the pile foundation of 757 project in initial design

After the change of the location of main building in the 757 project, the thickness of the base slab for main building is increased to 2.3m. The area for the reinforcement of the pile foundation is about 2100m^2 of which the perimeter is around 193m. Hence, the total amount of 117 bored pile with the diameter of 800 mm need to be installed in the foundation area of main building in current design. This additional bored pile will be cast using the post grouting method. The supporting layer for the additional bored pile is ⑧2 layer. Thus, the effective length is calculated to be 40.0m with the bearing capacity of 3600 kN.

3.3. Pile foundation in BaoHua project

The depth of foundation in the nearby BaoHua project is around 7.0m. The thickness of base slab is 0.7m both in shallow area of skirt building and

basement, and 1.2m in thick raft area of main building. The bearing pile is the PHC-500（100）A. The supporting layer for the bearing pile is ⑦ layer. Thus the effective length of bearing pile is calculated as 20.0m with the bearing capacity of 1400kN. The total amount of the bearing pile is 409. The tension pile is the PHC-400（80）AB. The supporting layer for tension pile is ⑦ layer. The effective length of tension pile is set to be 20m and 24m with the bearing capacity of 420kN and 480kN, respectively. Hence, the total amount of tension pile is 782 and 4 for the length of 20m and 24m, respectively.

4. Numerical analysis

4.1. ZSOIL.PC software

The FE software adopted in this paper is ZSOIL.PC V2013 x64 which was developed by Zace Services Ltd in Lausanne [1]. This software has more than 3000 users all over the world, whose has made great accomplishments in design, consultation, and research area, and covers almost all the engineering problems that might be raised in the practical problems such as excavation in soil and rock, soil-structure interaction, dewatering underground water and temperature analysis. The software has been applied and validated in many significant projects in our company, such as deep excavation and pile foundation of Shanghai Hongqiao traffic hinge project, excavation and pile foundation of Shanghai tower project, accident investigation of property collapse in Lotus riverside, and settlement analysis of Wuhan Greenland Center, Dalian Greenland Center, and Suzhou South Central Center.

4.2. Constitutive model and its parameters for soil mass

The constitutive model in current project is proposed to be HSS model (Hardening soil model with small strain), which is derived from the Hardening soil model (HS). The Hardening soil model is firstly developed by the Schanz [2] on the basis of the double hardening model. The HS model consisted of a hyperbolic shear yield surface for shear hardening and an elliptic yield cap for compressive hardening in p-q stress space. The parameters in HS model has a clear physical significance, and can be obtained from the triaxial and oedometer test directly. Benz [3] developed the HSS model (Hardening soil with small-strain) with considering of the non-linear relation between shear stiffness and strain of soil in small strain range. The HSS soil model has been widely used and validated in the numerical analysis of geotechnical engineering in Shanghai area in recent years [4], and hence abundant practice experiences has been accumulated. Parameters for HSS model for the current project are given in Table 2.

Table 2 Parameters for HSS model

ground layer	unit weight	air voids ratio	moisture content	triaxial CD		parameters for HSS model deformation modulus			
	γ	e	w	C	Φ	E_{50}^{ref}	E_s^{ref}	E_{ur}^{ref}	E_0^{ref}
	$\frac{kN}{m^3}$		%	kPa	(o)	kPa	kPa	kPa	kPa
②-1	18.5	0.9	35	5	28.5	6933	4490	41601	208004
②-3	18.8	0.803	28.2	2	33.5	14571	9860	87426	437130
③	17.3	1.233	44.2	1	29.1	3761	2940	26327	131634
④	16.8	1.404	50.3	2	21.2	2293	2190	16052	80259
⑤	17.9	1.066	37.6	7	22.4	2219	3440	14425	72124
⑥	19.8	0.659	22.8	20	32.8	8060	7580	40298	201490
⑦	18.4	0.882	31.1	1	33	10492	9090	57703	288517
⑧-1-1	17.8	1.095	38.7	6	25	2559	3800	14076	70380
⑧-1-2	17.9	1.028	35.8	6	30	2562	4020	12812	64061
⑧2	18.8	0.847	29.5	1	32	4684	5170	28106	140530
⑨	18.9	0.65	22	1	35	12605	15920	81933	409666

4.3. Numerical model

Firstly, the stage of the dewatering confined water has a wide impact on the settlement of the surrounding environment, and hence the calculation model should be large enough to minimize the boundary effect on the analyzing area. Secondly, considering the balance between the element number and accuracy of result, the calculation model should not be too large. In current analysis, the centre part of the calculation model is set to be the "key area" which includes the model of current 757 project and nearby buildings. The length and width of the "key area" is equal to 5 times the depth of the excavation of the 757 project. The depth of the "key area" is set to be 5 times the burial depth of the basement

of 757 project. The bias mesh technology is adopted for the whole model, the mesh size is uniform with aspect ratio of 1 for the "key area", and then mesh size gradually increases away from the "key area". After convergent study, the numerical model is set to be 2015m in length and 1062m in width and 70m in depth, which is shown in Figure 5.

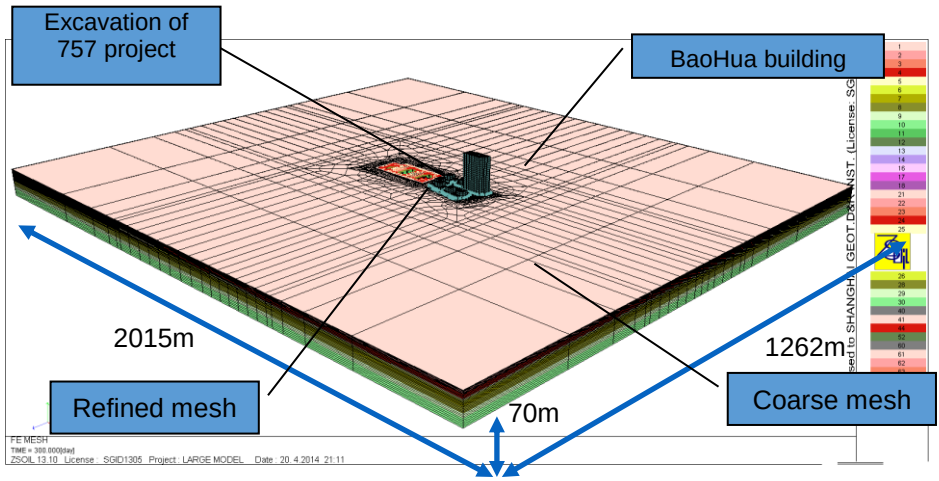

Figure 5. Finite element model

Boundary condition is settled as: (1) The horizontal displacement is fixed in the four side of the model, meanwhile both horizontal and vertical displacement is fixed at the bottom of the model; and (2) Water table for unconfined water is -1.0m (1.0m below the ground), and the artesian head for confined water is -3.0m (3.0m below the ground). In current analysis, the confined aquifer and ground water layer is isolated, and hence it is assumed that no seepage will happen between these two layers. In the numerical model, along the excavation a surface overload is taken into account. The overload is applied from 0m from the retaining wall up to 25 m from the wall (about 2 times of the excavation depth) and has the magnitude of 30 kPa. The FE model of supporting system and pile foundation in 757 project is shown in Figure 6.

In the numerical model of 757 project, the diaphragm wall element is used to model the retaining bored pile wall by adopting the equal flexural rigidity method. Due to the shear force and bending moment cannot be transferred among the retaining bored piles, the "hinge" element is inserted between the diaphragm wall to allow the rotational behaviour of the retaining wall. At same time, in order to save computational resource, the pile foundation is considered and simulated with pile element over the "boring area" and about 10m beyond the "boring area", and further the tension pile with larger spacing are not considered in the numerical model.

The location of the "boring area" and layout of the dewatering well (draining well and relief well) are illustrated in Figure 7. In the figure, the filter

tube of relief well is placed at the ⑦ layer to lower the artesian head of confined aquifer. In the numerical model the distance between the perimeter of "boring area" and sideline of the retaining structure is around 7.0~10.0m. The numerical model of underground structure and pile foundation of the main building in BaoHua project is given in Figure 8.

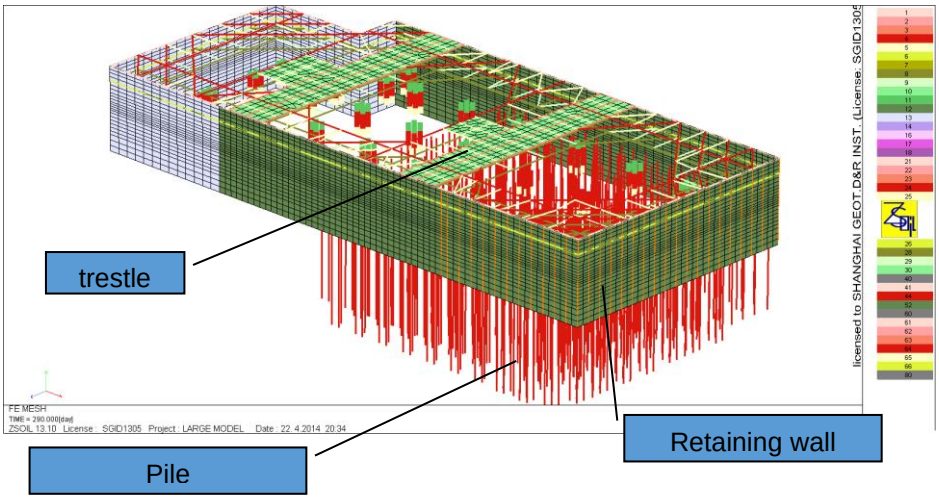

Figure 6. FE model of retaining structure and pile foundation of 757 project

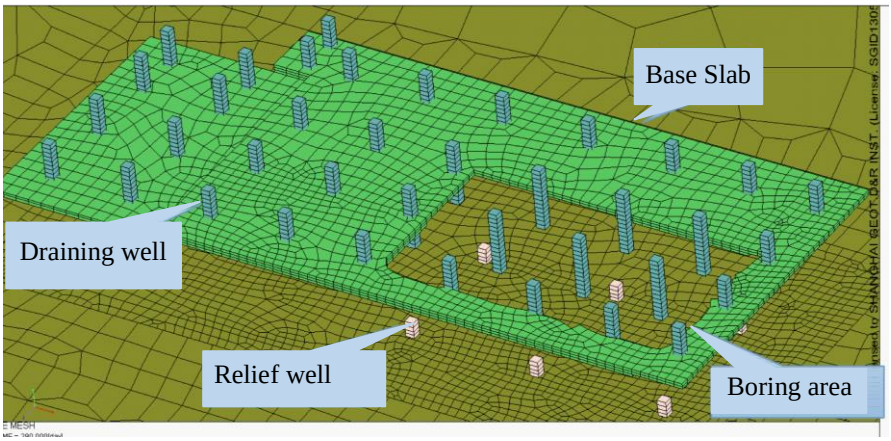

Figure 7. FE model of dewatering well and “hole” of the raft

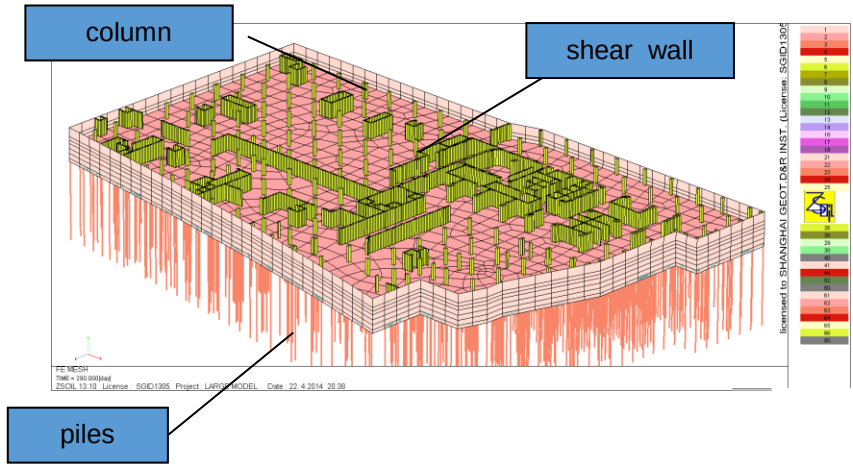

Figure 8. FE model of underground structure and pile foundation of BaoHua project

4.4. Loading step

In order to consider the accumulated influence of the excavation on the settlement of surrounding environment, the current simulation will be started at the beginning of excavation of 757 project. The main step of the simulation is stated as follows: (1) Calculation of initial stress state in ground, and at same time active the nearby buildings, including pile foundation, underground structure, main and skirt building of BaoHua project; and (2) Installation of the retaining wall, the 1st strut, trestle plate and excavation of the relief well; and (3) Excavation of the 1st soil layer ; and (4) Repeat steps of the excavation and installation of strut until the formation level reached; and (5) Casting the base slab and then suspension of construction for 3months; and (6) Removing the 3rd layer strut, and forming the "boring area"; and (7) Active the relief well and maintain water head for 4 months.

4.5. Numerical result

After the dewatering has been performed for 4 months, the distribution of water level for the confined aquifer is reported in Figure 9 and 10, respectively. From the figure, it is clearly shown that: (1) The dewatering of confined water performs large influence on the surrounding environment. The influence zone extends to the boundary; and (2) The water level of confined aquifer under the "boring area" is maintained at -14.0m; and (3) The water level of confined aquifer in BaoHua project is maintained within the range of -5.5m to -9.5m. Considering the permeability of the waterproof curtain has the certain impact on the ground water table, the amplitude of the phreatic level in BaoHua project is found to be 3.0m

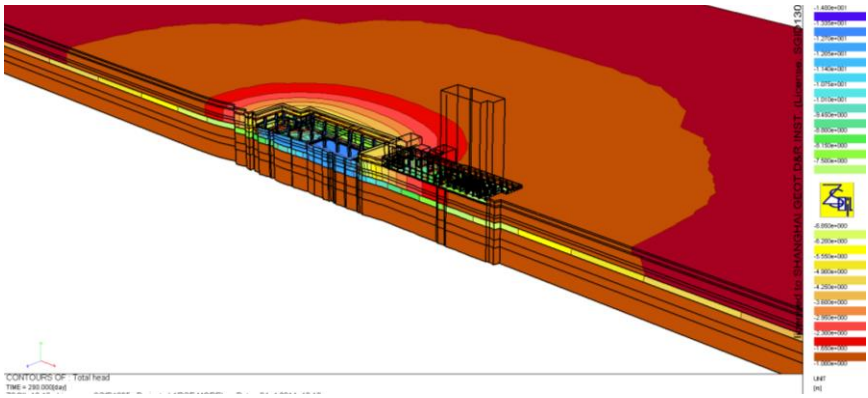

Figure 9. Sectional view of confined water head

Figure 10. Plain view of water head contour for confined aquifer

After the dewatering has been last for 4 months, the settlement in BaoHua project is given in Figure 11. From the figure, it is observed that the maximum settlement of BaoHua project is around 14.3mm, which occurred at the nearby "boring area" of 757 project. The settlement of the main building in BaoHua project is about 6.1~7.7mm.

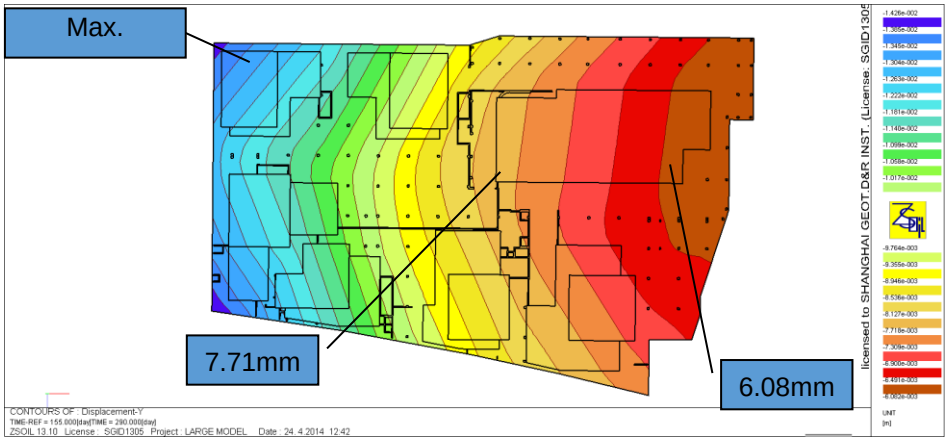

Figure 11. Settlement of Buildings in BaoHua project

5. Monitoring result

The monitoring plan for the settlement of BaoHua project and the water level of the confined aquifer is given in Figure 12 and 13, respectively.

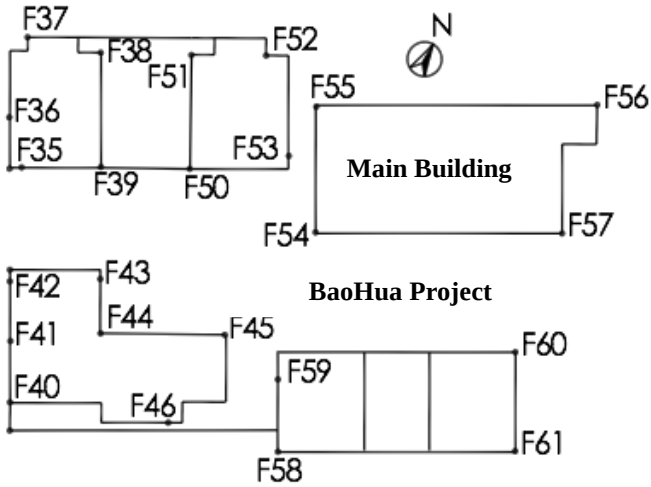

Figure 12. Monitoring plan for BaoHua project

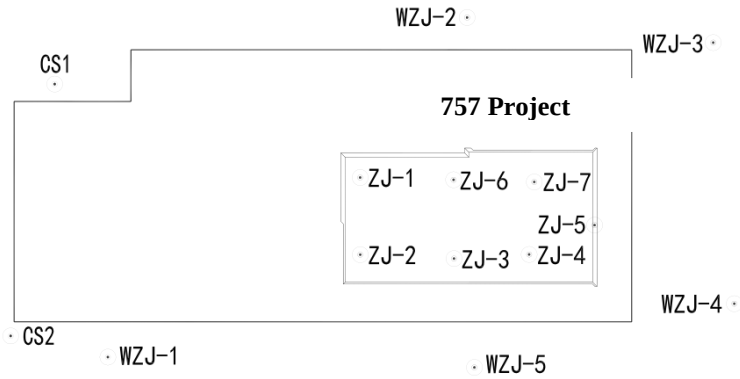

Figure13. Monitoring plan of the confined water head for 757 project

Table 3 illustrates the relation between the construction stage of 757 project and the monitoring index. For the BaoHua project, the monitoring started at No. 242, while for the confined water head in the "boring area", the monitoring began at No. 260, which is later than the starting time of the dewatering.

Monitoring data for the confined water head is shown in Figure 14. From the figure, it can be found that the confined water head at initial time is around -5.69~-15.41m, and remains at -3.0~-6.0m when the installation of bored pile and dewatering is finished.

Table 3 Construction stage versus monitoring Index

beginning and ending time	construction content	Corresponding monitoring index number
6/7/2014~6/15/2014	Removing base slab	242~250
6/16/2014~8/25/2014	Dewatering confined water, filling bore pile	251~305
8/26/2014~10/18/2014	Casting new base slab	306~357
10/19/2014~4/12/2015	Construction of underground structure,	358~438

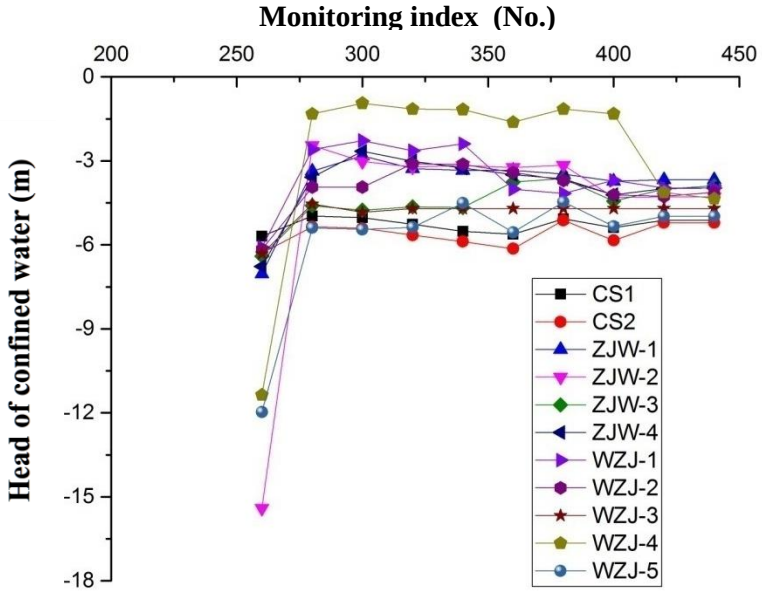

Figure 14. Monitoring data for the head of confined aquifer

Monitoring data for the settlement of BaoHua project is given in Figure 15. From the figure, it is observed that during the period of removing the base slab in 757 project, the settlement occurred in BaoHua project is around -0.1~-2.7mm. During the period of dewatering confined water in 757 project, the velocity of the settlement in BaoHua project increases, and then returns to be stable after the dewatering is ended. During the stage of the removing base slab and dewatering confined water in 757 project, the settlement of main building and skirt building of BaoHua project is measured to be -2.6 ~ -6.8mm and -2.4 ~ -7.6mm, respectively.

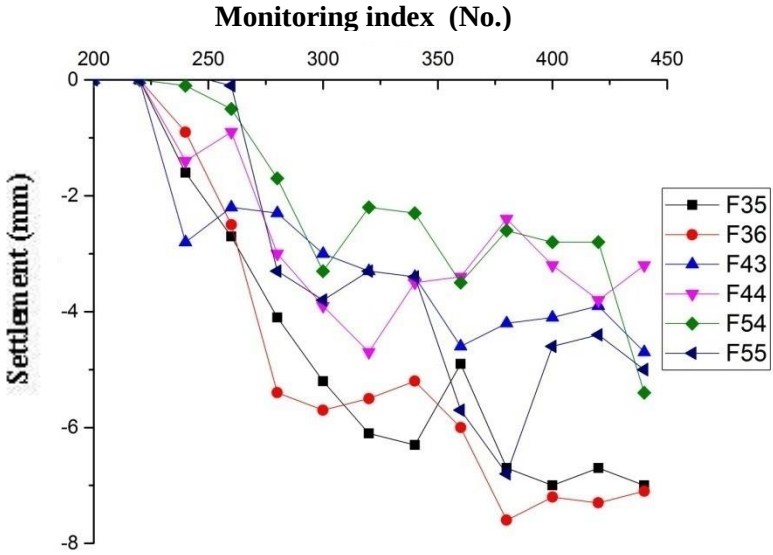

Figure 15. Monitoring data of settlement in BaoHua project

The calculation and monitoring value for the confined water head and the settlement of BaoHua project due to the removing base slab and dewatering confined water in 757 project is summarized in Table 4. Based on the table, it is found that the calculation value of the confined water head is less than the measured data for about 3~4m, while the calculation value of the settlement is bigger than the measured value for about 2~4mm.

Table 4 Calculation value vs. monitoring value

observation well	water level of confined aquifer		monitoring site	settlement of BaoHua project	
	measured value	calculated value		measured value	calculated value
	m	m		mm	mm
CS1	-5.69	-9.05	F35	-6.7	-11.5
CS2	-6.29	-9.05	F36	-7.6	-11.9
WZJ-1	-6.09	-9.6	F43	-4.7	-10.8
WZJ-2	-6.16	-10.7	F44	-4.7	-10.8
WZJ-3	-6.32	-9.05	F54	-5.4	-7.4
WZJ-4	-11.36	-9.6	F55	-6.8	-8.1
WZJ-5	-11.97	-11.25			

There is a big difference between the calculation and measured value for the confined water head. This might be possible that: on the one hand, the water level of the dewatering well in the "boring area" does not reach the expected value of -14.0m in practical engineering; On the other hand, there is a big error between the suggested value and real data for the permeability of soil which will affect the change of confined water head. However, due to the calculation value is lower than measured value for the confined water head, the calculated settlement of BaoHua project should be bigger than measured value as stated in Table 4. Further, in current study the numerical analysis is used to guide the construction, and the parameters adopted in analysis is expected to be conservative in order to cover the various kinds of unforeseeable factors.

6. Conclusion

In this paper, the numerical analysis is conducted to simulate the entire construction stage of excavation, including the stage of removing base slab and dewatering confined water. The advanced soil model is used to represent the soil behaviour and dewatering phenomena. The numerical results is then compared with the field observation, from which the main conclusions can be drawn as follows:

(1) A fully coupled flow-deformation analysis with HSS (Hardening soil with small strain) in 3D FEM software ZSOIL.PC, can predict the impact of the excavation and dewatering confined water on the settlement issue of surrounding environment properly. The process of conducting the analysis and the results showed the reasonable feasibility of the methodology taken in this paper. Hence, the numerical results can be used as the guideline for the construction of the project.

(2) Dewatering confined water is the main reason for the settlement of the building in which the supporting layer for pile foundation is at the confined water layer.

References

[1] T. Zimmermann, A. Truty. *Z. Soil PC 2013 manual[R]* . Lausanne: ZACE service Ltd, 2013

[2] R. Obrzud, A. Truty. *The hardening soil model - a practical guidebook [R]*. Lausanne: ZACE service Ltd,2014

[3] T.Benz. *Small strain stiffness of soils and its numerical consequences [D]*. University of Stuttgart, 2006

[4] Yin. J. *Application of hardening soil model with small strain stiffness in deep excavation engineering in Shanghai [J]*. Chinese Journal of Geotechnical Engineering, 2010, **32**(S1): 166–172. (In Chinese)

Settlement prediction of super high-rise building based on the soil-foundation-superstructure interaction analysis

YIN Ji[a], XIE Dongwu[b],LU Zhinai[c]
[a]*Shanghai Geotechnical Investigations& Design Institute Co., Ltd, Shanghai 200070, China*
[b] *Shanghai GeoFem Consulting Co.,Ltd, 200433, China*
[c]*Powerchina Huadong Engineering Co., Ltd, Hangzhou 311122, China*

Keywords: Super high rise, settlement prediction, soil-foundation-superstructure interaction, ZSOIL.PC, consolidation, hardening soil model with small strain stiffness, Hoek-Brown model.

Abstract
Prediction of settlement of two super high-rise buildings using the soil-foundation-superstructure interaction analysis are presented in this paper. Two methods for the prediction of settlement have been suggested: (1) in soft clay area the coupling of consolidation and the soil-foundation-superstructure interaction analysis is recommended to predict the settlement of the super high-rise building, in which the simulation of the excavation and refilling is included; and (2) in rock foundation area the total stress analysis with Hoek-Brown model can be applied to predict the settlement of super high-rise building, in which the influence of excavation resilience and consolidation on settlement can be ignored.

1. Introduction

1.1 Method for settlement analysis of super high-rise building

Super high-rise building has the characters of the large self-weight, large base loading, high requirements for the foundation bearing capacity and uniformity, and strict control on building's settlement and inclination. The normal method in China for settlement analysis of super high-rise building is the Equivalent Deep Foundation Method based on Chinese design codes. In this method, the subsoil is firstly taken as an elastic material, and secondly the analytic solutions such as Boussinesq's solution and Mindlin's solution is used to obtain the stress and settlement in the soil mass, and then the settlement can be modified based on the empirical coefficient. However, in practice it is well known that under the high base pressure from the superstructure, some parts of the surrounding soil have already been in the plastic state. When the plastic

zone is generated and developed, it is not proper to predict the settlement of the building based on the linear elastic stress-strain behavior of soil. It might be correct that the prediction of settlement with the elastic theory can be modified by the empirical coefficient. However, there are few examples of the super high-rise building to valid this coefficient. It should be noted that different buildings have different mechanical properties of subsoil, which make it difficult to summarize the rules from the statistical analyses. Further, the empirical coefficient of the settlement recommended by Chinese design codes is based on the data majorly from the buildings below 300 meters, which has the smaller base loading compared to the that of the super high-rise building discussed in this article. It still needs to be proved whether the empirical coefficient can be applied in predicting the settlement of buildings beyond 300 meters. Hence, it is necessary to develop a new method to predict the settlement of super high-rise building based on the practical soil behavior

1.2 Method for soil-foundation-superstructure interaction analysis

Dong and Zhao[1] introduces the method of the soil-foundation-superstructure interaction analysis (also called substructure method in the following part). The key of this method is that soil, foundation and superstructure should not be analyzed separately, and the influence of the interaction among these three parts is larger than the total impacts from the individual one. The Substructure method is normally adopted to analyze the interaction among the soil-foundation-superstructure, in which the superstructure is taken as the ‘substructure' with the flexible constrain to the foundation. The Substructure method can avoid generating a huge global stiffness matrix, and make the interaction analysis available. However, in this method the soil is treated as an elastic body, which fails to describe the complicated mechanical characteristics of soil in reality. Nowadays, with the development of the hardware of computer and calculation algorithm in finite element method, it is possible to carry out the analysis on the interaction among the soil, foundation and superstructure using the commercial FEM software. The authors have once analyzed the three-dimensional soil-foundation-superstructure interaction problem with 2.5 million DOF on a desktop computer, which has a configuration of dual process (16 cores) and 128G memory. In addition, based on the comparison of the predicted settlement data and the observed settlement data, Dong and Zhao[1]suggests that the distribution of the stiffness in the superstructure could be represented by the stiffness of 5-layers of superstructure. Therefore in current study, the numerical model will only consider the underground structure and 5-layers of superstructure to save computational time.

2. ZSOIL.PC and hardening soil model with small-strain stiffness

2.1 Brief introduction of ZSOIL.PC

ZSOIL.PC, a 64-bit 3D geotechnical FE software developed by ZACE Service Ltd., is employed to predict the settlement of the super high-rise building. The software achieves great success in the fields of engineering design, consultation and research, and offers unified approach to engineering analysis in soil and rock mechanics, underground structure, excavation, soil-structure interaction, ground water , temperature and dynamics issue. Many advanced geo-material constitutive models are implemented in this software.

2.2 Hardening soil model with small-strain stiffness

The Hardening Soil model [2] (HS model) consisted of a hyperbolic shear yield surface for shear hardening and an elliptic yield cap for compressive hardening in p-q stress space. The parameters in HS model has a clear physical significance, and can be obtained from the triaxial and oedometer test directly. Benz [4] developed the HSS model (Hardening soil with small-strain) with considering of the non-linear relation between shear stiffness and strain of soil in small strain range.. Generally, with the increase of the loading the settlement of buildings will cause the strain of soil with the scale from 0 to 0.001, during which the degradation of stiffness of soil performs a 'S' shape. The HSS model can represent this characteristics of the deformation in soil mass, and thus the predicted settlement obtained from this model conforms to the reality.

2.3 Hoek-Brown rock constitutive model

Hoek-Brown model [3] is a mature model to simulate rock characteristics with considering of the integrity of rock mass, of which the yield criterion is stated as follows:

$$f(\sigma_1,\sigma_3) = \sigma_1 - \sigma_3 - \sigma_{ci}(m_b \frac{\sigma_3}{\sigma_{ci}} + s)^{\alpha} \tag{1}$$

where σ_{ci} is the compression strength of the intact rock; α, s, and m_b can be obtained from GSI(Geological Strength Index), and expressed as:

$$m_b = m_i \exp(\frac{GSI - 100}{28 - 14D}) \tag{2}$$

$$\alpha = \frac{1}{2} + \frac{1}{6}(\exp(-GSI/15) - \exp(-20/3)) \tag{3}$$

$$s = \exp(\frac{GSI - 100}{9 - 3D}) \tag{4}$$

in which m_b is a reduced value of m_i, which reflects the degree of rock stiffness; D is an disturbed index related to the disturbing degree of rock with value from 0.0 (rock is not disturbed) to 1.0 (rock is severely disturbed).

In Hoek-Brown model, the elastic modulus can be expressed by GSI, as shown in the following:

$$E[GPa] = \left(1 - \frac{D}{2}\right)\sqrt{\frac{\sigma_{ci}}{100}}10^{\left(\frac{GSI-10}{40}\right)}, \quad \sigma_{ci} \le 100MPa \tag{5}$$

$$E[GPa] = \left(1 - \frac{D}{2}\right)10^{\left(\frac{GSI-10}{40}\right)}, \quad \sigma_{ci} > 100MPa \tag{6}$$

3. Settlement prediction of Shanghai Tower project

3.1 Background of the project

Shanghai Tower is located at the financial center of Lujiazui, Pudong District, Shanghai. It is one of the highest buildings in China, which has 121 story above ground with the total height of 632m. It also has 5-layer basement in which the buried depth of foundation is 31.4m, and the thickness of base slab is 6.0 m. The tower is the mega space frame-core tube-outrigger structure system in which the self-weight is 9200000kN and the base pressure from the core tube is over 2500kPa. The foundation of the tower is the bearing bored pile with the diameter of 1.0 m. The effective length of the bored pile is about 52.0~56.0m with the designed bearing capacity of 10000 kN. The bored pile is penetrated into the bearing soil layer with the depth of 5.0 ~ 9.0 m. The layout of the core tube and pile foundation of Shanghai Tower is given in Figure 1.

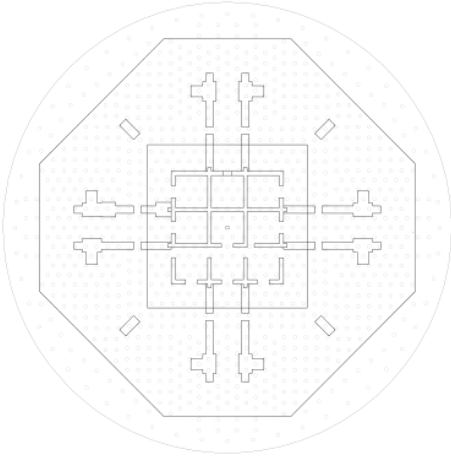

Figure 1. Layout of the core tube and pile foundation of Shanghai Tower

3.2 Ground condition and parameters for HSS model

The site condition in current project has the Quaternary cover with the thickness of 274.8m, which is the sediments between Quaternary Early Pleistocene Q1 and Holocene Q4. The Quaternary cover mainly consists of clayey soil, silty soil and sandy soil and is followed by the granitic layer. In terms of the soil sedimentation age, genetic type and the difference in the physical-mechanical properties, the ground in Quaternary cover can be divided into 14 main layers. Table 1 reports the characters of the each soil layer in current project. In the table, the designed value of ultimate frictional strength of pile, fs, and the ultimate toe bearing strength of pile, fp, are also given.

The HSS soil model has been widely used and validated in the numerical analysis of geotechnical engineering in Shanghai area in recent years [7], and hence abundant practice experiences has been accumulated. Parameters for HSS model for the current project are given in Table 2.

Table 1. Skin frictional strength and pile toe bearing strength

Layer Order	Name of Layer	Depth of Layer Bottom (m)	Ps(CPT) (MPa)	Bored Pile fs (kPa)	Bored Pile fp (kPa)
②	Silty Clay	2.7~4.5	0.64	15	
③	Mucky Silty Clay	7.3~10.0	0.82	6m above 15 6m below 25	
④	Mucky Clay	15.8~18.0	0.62	20	
$⑤_{1a}$	Clay	19.4~21.5	0.98	35	
$⑤_{1b}$	Silty Clay	23.5~28.5	1.34	45	
⑥	Silty Clay	28.1~30.5	3.08	60	
$⑦_1$	Sandy Silt with silt	34.8~40.5	12.33	60	
$⑦_2$	Silt	63.0~65.5	26.91	70	2500
$⑦_3$	Silt	67.2~71.6	17.16	70	2200
$⑨_1$	Sandy Silt	76.0~80.5	16.34	70	2500
$⑨_{2\text{-}1}$	Silt	87.0~92.1	18.62	70	2500
$⑨_{2t}$	Silty Clay with Clayey Silt	91.2~100.8	7.44	60	
$⑨_{2\text{-}2}$	Silt	98.5~101.5	21.87	70	2500

Table 2. Parameters for HSS model

Layer Order	γ $\frac{kN}{m^3}$	c kPa	Φ (°)	E_{50}^{ref} kPa	E_s^{ref} kPa	E_{ur}^{ref} kPa	E_0^{ref} kPa	m (-)
②	18.4	2	29.0	4445	3970	33337	173107	0.95
③	17.1	4	31.3	5436	3800	27181	128077	0.95
④	16.7	3	24.7	3297	2170	24725	129762	0.95
⑤1a	17.6	4	29.3	4485	3570	33636	174815	0.95
⑤1b	18.4	3	28.0	6584	5260	55966	287004	0.95
⑥	19.7	2	28.0	11493	6950	80453	393473	0.95
⑦1	18.5	2	32.5	22495	10350	101229	339235	0.70
⑦2	19.1	0	33.5	25097	14850	87841	433558	0.65
⑦3	19.1	2	33.5	17899	13280	89497	455811	0.70
⑨1	19.1	5	32.0	15838	11040	95030	466759	0.70
⑨2-1	20.2	0	33.5	16214	12550	97283	504512	0.70
⑨2-2	19.3	0	33.5	16373	12890	106423	521879	0.70

3.3 Numerical model

Two phase analysis (deformation-consolidation) is employed to predict the settlement of Shanghai Tower. The entire construction stage are considered and simulated, which includes the installation of bored piles and retaining structure, excavation (bottom-up method for main tower and top-down method for podium), dewatering, construction of the underground structure and the loading from superstructure. In order to avoid the boundary effect in the simulation of dewatering, the calculated domain size is set to be 1295 m in length and 1230 m in width and 145m in depth.

Beam and one layer shell elements are utilized to simulate the beam-plate system of underground structure, floors and diaphragm walls. Hexahedron elements are adopted to simulate the shear wall core tube, mega columns, and frame columns in tower area. The numerical model of underground structure and core tube structure are presented in Figure 2.

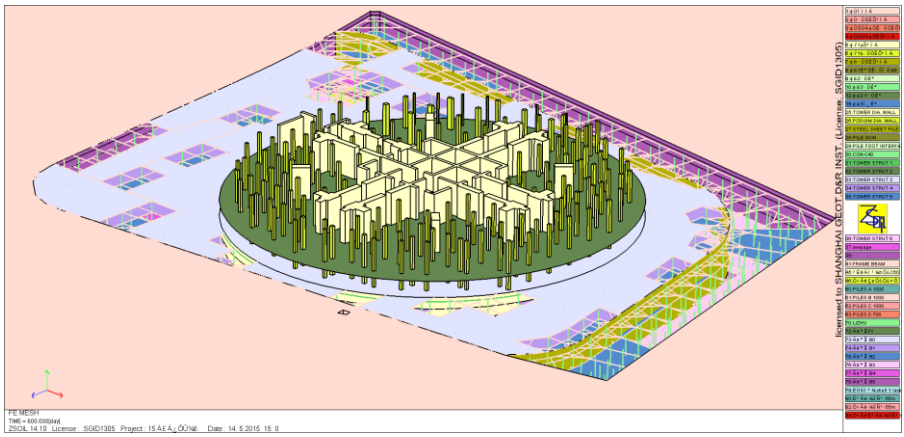

Figure 2. FE model of underground structure-soil-core tube structure

Pile elements are used to simulate the bored piles over the region of tower and podium. The essence of pile element is the combination of beam element and interface element, in which the tangential and normal interfaces between pile and soil can be assigned. The stiffness of interface is automatically determined from the stiffness of the surrounding soil. In the numerical model, the 'mud skin' of the bored pile is simulated with the interface element, of which the stiffness is assigned by a reduction factor of the stiffness of surrounding soil. The numerical model of piles (including piles for supporting strut system and uplift piles) is shown in Figure 3.

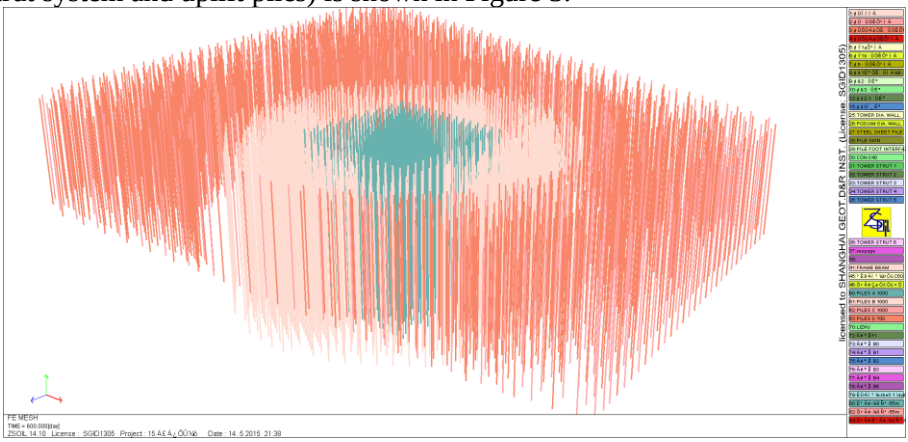

Figure 3. FE model of engineering piles of tower and podium building

Uniform surface load is assumed to be applied on the mega columns and core-tube structure using the method of the self-adapting with stiffness of tower.

3.4 Result of settlement prediction

After the structure's roof-sealing, all the load of superstructure acted on the foundation, and the consolidation settlement tends to be steady, the settlement at the center of tower raft is about 11.7cm, and there are 6.0cm at the edge of tower raft. The maximum differential settlement is about 5.7cm. The contour of the settlement in tower raft is shown in Figure 4.

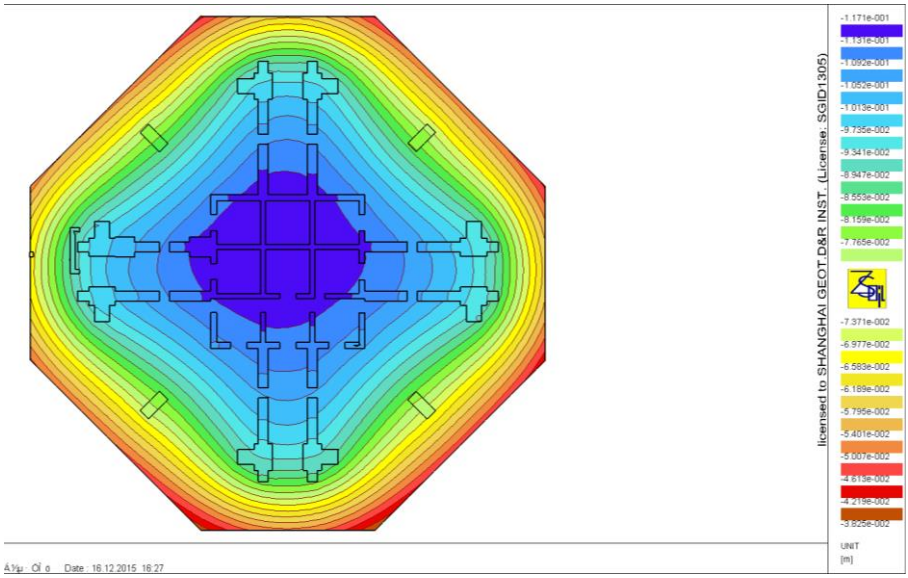

Figure 4. Contour of the settlement in tower raft

Along the two perpendicular directions through the center of the raft, the settlement of the raft is given in Figure 5. From the figure, it is found that the pattern of the settlement seems as a 'pan', of which the bottom is the center of the raft.

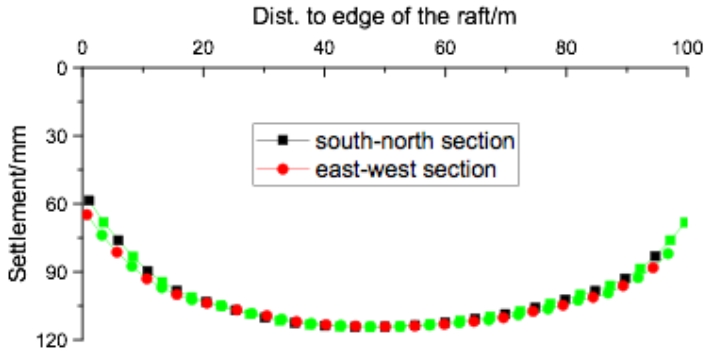

Figure 5. Sections of tower raft settlements

The predicted settlement and the observed data cannot be compared at present due to no release of the official observed settlement data. However, according to Zhao[4]'s settlement study on the nearby Jin Mao Tower and Shanghai World Financial Center, the settlement of super high-rise buildings in this area still has an increment of 20~30% after roof-sealing. ,

4. Settlement prediction of Ji'nan Greenland Puli Center

4.1 Project description

Ji'nan Greenland Puli Center is located at Gongqingtuan road, Puli street, and is the highest super high-rise building in Ji'nan area. The height of building is about 260 m, with 62 floors above ground and 3 floors underground. The depth of excavation of the building is about 18.0m. The average base pressure is 1200 kN/m^2. The building adopts the raft foundation with bottom-enlarged manual hole digging piles. The thickness of raft is 3.2m. The layout of the foundation is shown in Figure 6.

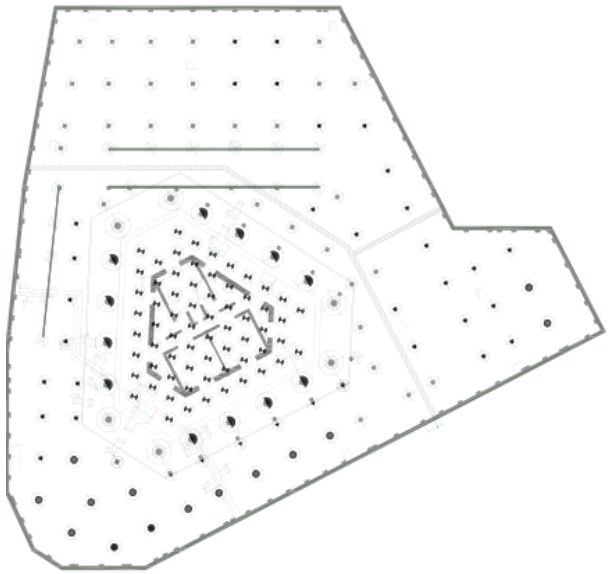

Figure 6. Core tube and pile foundation layout of Puli Center

The designed parameters of the manual hole digging pile, such as pile diameter, the length of pile , the depth of embedded into bearing stratum (medium weathered diorite) and the designed bearing capacity of single pile are shown in Table 3.

Table 3. Parameters for pile design

Pile Type	Diameter of Pile Body (m)	Diameter of Pile Tip (m)	Depth of Entry into Bearing Stratum (m)	Characteristics Value of Single Pile Bearing Capacity (kPa)
RZ1	1.5	2.7	2.0	21000
RZ2	2.4	4.3	3.0	54000
RZ3	2.8	5.0	3.0	73000

4.2 Stratum and parameters for Hoek-Brown model

The ground condition for the foundation is the rock layer, which mainly consists of ⑧ strongly weathered diorite and ⑨moderately weathered diorite. The latter one is the bearing layer for piles. The ⑧ strongly weathered diorite is a kind of broken rock with the shear wave velocity of 420m/s, SPT value of 63.9 blow and DPT value of 41 blow (63.5kg), and can be classified as the grade "Ⅴ" according to Chinese design codes. The ⑨ moderately weathered diorite is hard, with the massive structure and moderately developed fracture, RQD value of 50~70, and shear wave velocity of 725m/s. The constitutive parameters of Hoek-Brown model for ⑧ strongly weathered diorite and ⑨ moderately weathered diorite are presented in Table 4.

Table 4. Parameters for Hoek-Brown model

Layers	γ kN/m^3	D	σ_{ci} MPa	GSI	E kPa
⑧	24.0	0.0	19.70	24.39	338688
⑨	24.0	0.0	19.70	43.35	1009200

4.3 Numerical model

The numerical model of Puli Center is shown in Figure 7. In the numerical model, underground structures and part of superstructure are modelled without simulating the stage of the excavation. The 3D stratums are generated by BOREHOLE technique implemented in ZSOIL.PC to reveal the spatial

distribution of stratum. The length of piles is determined by the depth of bearing strata, and is shown in Figure 8. The method of modelling the structure and pile is same as that in Shanghai Tower. The consolidation settlement of bearing stratum is neglected and thus the total stress analysis is adopted in current analysis, which is different from the prediction of settlement of super high-rise building in soft clay area with high water level.

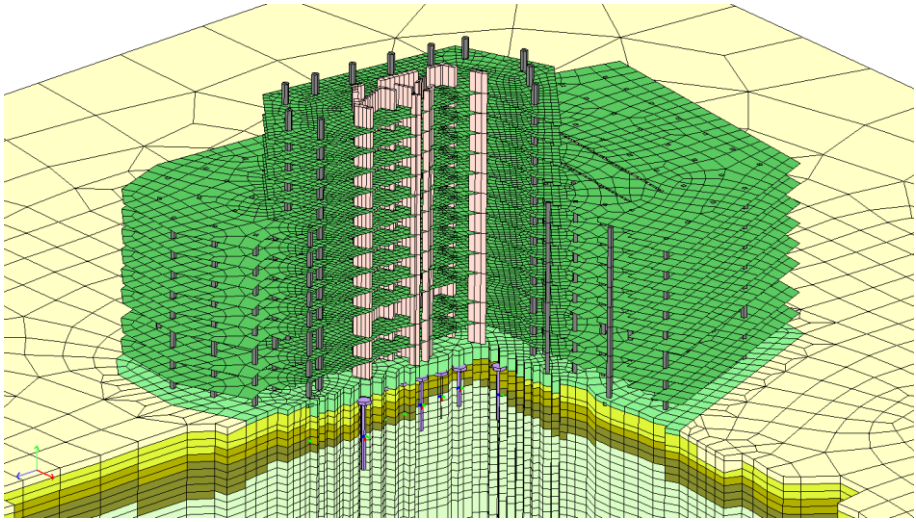

Figure 7. FE model o the Puli Center

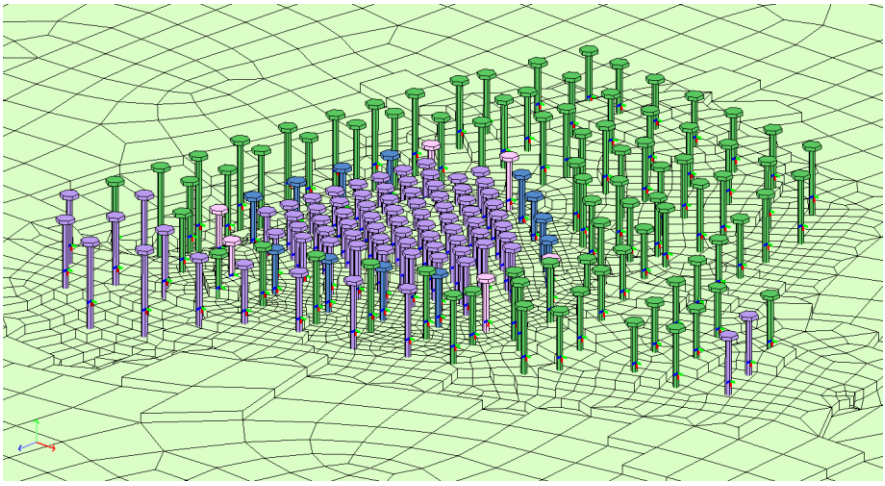

Figure 8. FE model of engineering piles of tower and podium building

Uniform surface load is assumed to be exerted on the mega columns and core-tube structure using the method of the self-adapting with stiffness of building.

4.4 Result of settlement prediction

After the roof-sealing of the structure and total load of superstructure acted on the foundation, the settlement at the center of tower raft is about 2.98cm, and the settlement is about 1.0~1.63cm at the edge of tower raft. It can be found that the differential settlement is 1.35~1.98cm. The pattern of the settlement in the raft looks like a ‘pan', which is shown in Figure 9.

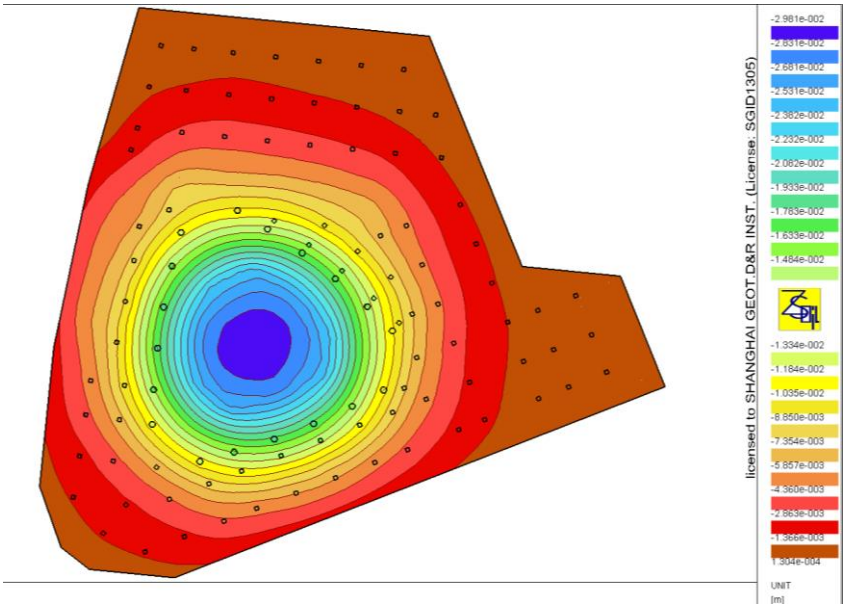

Figure 9. contour of the settlement of the raft

The structural top-sealing of the project was done in December, 2013. The plan of the monitoring of the settlement on the top of raft are given in Figure 10.

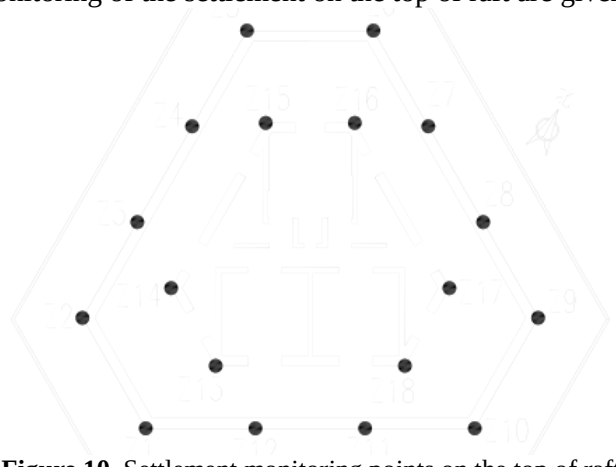

Figure 10. Settlement monitoring points on the top of raft

Comparing the settlement data between the predicted and monitored is summarized in Table 5. The predicted data agrees well with the monitoring data for the points Z1~Z12 at the raft edges, while the observed data at core tube area differs from the predicted. The possible reasons for the differences are: (1) the plate size in the plate loading test which is used to determine the bearing capacity of the layer, is only 300mm in diameter, and may cause the magnificent size effect on the obtained results; (2) the load exerted on the structure in the prediction are the approximate values from the method of the self-adapting with stiffness of building, which might be different from the actual load distribution.

Table 5. Tower settlement prediction vs. monitoring

Monitoring Points	Observations mm	Predictions mm	Monitoring Points	Observations mm	Predictions mm
Z1	12.58	12.98	Z10	13.7	11.16
Z2	13.01	13.13	Z11	15.3	18.28
Z3	12.85	19.64	Z12	13.3	18.55
Z4	14.18	19.34	Z13	15.52	23.66
Z5	15.18	12.91	Z14	16.63	23.52
Z6	14.01	10.12	Z15	15.73	23.34
Z7	15.31	17.48	Z16	16.63	22.51
Z8	14.57	17.48	Z17	16.13	22.56
Z9	15.50	11.77	Z18	16.30	23.84

5. Conclusions

In this paper, the prediction of settlement of two super high-rise buildings using the soil-foundation-superstructure interaction analysis are carried out, from which the main conclusions are drawn as follows:

(1) It is recommended to adopt two-phase (deformation-consolidation) analysis and soil-foundation-superstructure interaction analysis, including the simulation of the excavation and refilling to predict the settlement issue for super high-rise building in soft clay area. While in the rock foundation areas, the total stress analysis can be used to predict the settlement of super

high-rise building, neglecting the influence of excavation resilience and consolidation

(2) The "self-adapting" method of exerting uniform loading on the shear wall of core tube and mega columns of tower is efficient and acceptable but result in less accurate. The “correct” way seems to apply the precise load for the superstructure.

(3) The use of the ZSOIL.PC with the advanced soil and rock constitutive models in the soil-foundation-superstructure interaction analysis, can properly predict the settlement of super high-rise building within an acceptable time frame.

References

[1] Dong Jian-guo, and Zhao Xi-hong. *‘A theoretical practice of soil-foundation interaction of super high rise,’ Design of Super High Rise Series*, Shanghai: Tongue University Press, 1997.(in Chinese)

[2] T. Benz. *Small-strain stiffness of soils and its numerical consequences*, Universitat Sttutgart, 2007.

[3] E. Hoek, C. C. Torres, and B. Corkum. *‘Hoek-Brown failure criterion - 2002 edition,’ In Proceedings of the North American Rock Mechanics Symposium*, Toronto, 2002.

[4] Zhao Xi-hong, Gong Jian, and Zhang Bao-liang. *Integrated Study of Pile-raft Foundation In-situ Test of the 101 Floors of Shanghai World Financial Center*, Shanghai: China Architecture & Building Press, 2014.(in Chinese)

[5] T. Benz, R. Schwab, R. Kauther, and P. Vermeer. *A Hoek-Brown criterion with intrinsic material strength factorization*, International Journal of Rock Mechanics and Mining Sciences, 2008.

[6] ZSOIL, User Manual. Elmepress and Zace Services ltd, 1985-2014.

[7] Yin. J. *Application of hardening soil model with small strain stiffness in deep excavation engineering in Shanghai [J]*. Chinese Journal of Geotechnical Engineering, 2010, **32**(S1): 166–172. (In Chinese)

Steel Fiber Reinforced Concrete Beams and Slabs – a case record

Ulf Ekdahl[a]
[a]*Ekdahl Geo, Lomma, Sweden*

Keywords: Steel fiber reinforced concrete, Beam, Slab, ZSOIL.

Abstract
Usage of steel fiber added reinforced concrete (SFRC) in load-carrying structural members is gaining popularity because of its positive contribution to both energy absorption capacities and concrete strength. The shear capacity of concrete increases when steel fibers are added.
This paper presents experimental and finite element analysis of SFRC beams and slabs. The load capacities in buckling for driven SFRC piles installed in soft and very stiff clay till has also been analysed with finite element as well as load tests in the field. But this work will be shown in a coming paper.
The finite element program ZSOIL and the non-linear material model Hoek-Brown (Menetrey-Willam) is used to model the reinforced concrete. This model is a multi-surface elasto-plastic model with softening.
The result obtained from the finite element and experimental analyses are compared to each other. It is seen from the result that the simulated finite element behaviour indicates a good agreement with the experimental load test results.

1. Assignment

Eleven floors, over 400 working places and 20 000 square meters. There you have Malmö University's new building Niagara at Universitetsholmen in Malmö, see **figure 1**. Niagara consists of three buildings of five, seven and eleven floors of glass and wood facade that is connected by an open atrium.
On behalf of Akademiska Hus, Ekdahl Geo, has been responsible for all the ground engineering work done for the Niagara project. A part of the work has consisted of a study using nonlinear 3DFEM analyses of

- Determination of the size of the equivalent modulus of subgrade reaction, which can be used in the design of the bottom slab in static interaction with the structure of the building.
- Determination of the moment capacity of the base slab, whereby bending moment resulting from differential shrinkage is also taken into account.

- Determination of the characteristic crack width as a function of the size of the bending moment.

The design of the base must be performed in accordance with Eurocode.

Figure 1. Malmö University's new building Niagara.

2. Design Requirements

The thickness of the base slab is set to 400 mm and concrete quality of C40/50. The concrete slab shall be reinforced with steel fibers with minimum 30 kg/m^3 with the dimension 1 * 49 mm. The steel fiber shall be provided with hooked ends. In addition, the base slab shall be reinforced with mesh reinforcement Ø16 s100, B500B, at the top and bottom of the slab. Coverage shall be 50 mm at the bottom edge and 35 mm on the top edge of the slab.
The load capacity of the base slab shall be verified in the ultimate and the serviceability limit states. Verification in the ultimate limit state intends to

ensure load capacity so that there is adequate security against material failure. The requirements of the serviceability limit state intend to limit crack width and deformations.
The building has been founded with a bottom slab and on drilled shafts which will act as so called settlement brakes. The bottom slab shall be designed for water pressure equivalent to an overflow level equal to an intermediate ground water level, which shall be secured by pressure control pipes, so-called swan necks. Uplift forces from ground water pressure are taken care with installed ground anchors. The bottom slab shall be designed with respect to static interaction between the structure of the building and the subgrade.
In the 3D FEM analyses of the structure of the building, performed by the company WSP, the foundation and subgrade is connected with linear elastic springs.
The stiffness of the springs between the base and subgrade is described by the modulus of subgrade reaction, which is defined by the relationship

$$k = \frac{q}{s}$$

where q = contact pressure between base and surged
s = settlement of the bottom slab

The size of the equivalent bed modulus, which can be used when considering full static interaction, shall be determined using nonlinear 3DFEM analyses based on the average values of the material properties of soil and rock as stated in the geotechnical investigations.

2.1. Safety Principles

”Non-linear FEM analysis” provides description of the structure’s response to an increasing load. This allows both the serviceability limit state and ultimate limit state to be handled in a single calculation.
The disadvantage of such ”non-linear FEM analysis” is that the safety verification cannot normally be made through direct application of the partial factor method. Instead it is recommended that ”non-linear FEM analysis” shall be implemented using the mean values of material properties.
Safety verification can be made using a global safety factor γRg, which can be calculated as

$$\gamma_{Rg} = exp(\alpha_R \beta V_R)$$

Where α_R is the sensitivity factor for resistance, which can conservatively be assumed to be 0,8 and β is the norm target value of the safety index. When designing in accordance with Eurocode, β is set to 4,7.
Coefficient of variation V_f can be equated to the coefficient of variation for the ruling material parameter linked to the failure mode. In more general case, the coefficient of variation V_f is determined based on two separate non-linear analysis in which mean values and the characteristic values of material

properties are used as input. These analysis provide resistances R_m and $R_{k,}$ from which the coefficient of variation V_f can be calculated as

$$V_f = \frac{1}{1.65} ln\left(\frac{R_m}{R_k}\right)$$

For the estimation of the coefficient of variation V_R the model uncertainty shall also be taken into account in the analysis. Model uncertainty is described by the coefficient of variation $V_{C.}$ For the designed proposed foundation three criteria shall be considered together for estimation of the model uncertainty:

1. Accuracy in the calculation model (i.e., how well the analysis describes real behavior).
   This is considered normal.
2. Divergence between the strength in the real structure and that of the test body.
   This should be regarded as small since we have been using proven models for the in-situ properties of soil, rock and concrete.
3. Scope of control in the construction process.
   Scope of control in the construction process is good.

Weighing up of these parameters means that the coefficient of variation V_C for model uncertainty could be set at 0,07. The overall uncertainty related to the resistance R can then be calculated as

$$V_R = \sqrt{V_f^2 + V_C^2}$$

2.2. Shrinkage of concrete

Design with respect to the effect of uneven shrinkage of the bottom slab shall be based on the conditions set out in the Swedish Design Handbook for Concrete Structures. This means that the final value of shrinkage difference between the upper and lower surfaces of the base slab will be 2,375 * 10^{-4}.

3. Selection of material properties

3.1. Soil and rock

Mean values of material properties for soil and rock have been summarized in the Geotechnical Investigation reports. Characteristic values (5% quartile) of the material properties is determined taking into account that strength parameters are considered to be log-normally distributed, which means

$f_m = f_k \cdot \exp(1{,}65 \cdot V)$

where f_m = mean value of the material property
f_k = characteristic value of the material property
V = coefficient of variation

The coefficient of variation of material properties is assumed equal to 10%. This means that

$f_k = 0{,}85 \cdot f_m$

3.2. Strength and stiffness of the steel fiber reinforced concrete

The quality of the concrete must meet the requirements of strength class C40/50.

The mean compressive strength of the concrete, $f_{cm,}$ in the actual structure (base slab) is set to 40,8 MPa and the average tensile strength, $f_{ctm,}$ to 2,25 MPa. These values have been calculated as follows:

The relationship between the characteristic cube and cylinder compressive strength is described by the relation

$f_{ck,cyl} = 0{,}8 \cdot f_{ck,kub}$

The mean value of the concrete cylinder compressive strength is calculated as

$f_{cm,cyl} = f_{ck,cyl} + 8\ MPa$

The relationship between in-situ strength and cylinder strength is set to 0,85.

The mean compressive strength of concrete in the actual structure can then be calculated with

$f_{cm} = 0{,}85 \cdot [0{,}8 \cdot f_{ck,kub} + 8]$

The average value of the tensile strength in the actual structure shall be calculated with the relationship

$f_{ctm} = 0{,}215 \cdot f_{ck,cyl\ is}^{2/3}$

where $f_{ck,cyl\ is} = 0{,}85 \cdot 0{,}8 \cdot f_{ck,kub}$

In the determination of the coefficient of variation for the bearing capacity for the actual structure (the base slab), the following characteristic strength values are applied in the non-linear FEM analysis.

$f_{ck} = 0.85 * 0.8 * f_{ck,\ kub} = 34$ Map

$f_{ctk} = 0.7 * f_{ctm} = 1.57$ Map

The mean modulus of concrete's elasticity E_m and the characteristic modulus of elasticity E_k in the actual structure are calculated as follows

$$E_m = 22000 \cdot \left(\frac{40{,}8}{10}\right)^{0{,}3} = 33500\ MPa$$

$$E_k = 22000 \cdot \left(\frac{34}{10}\right)^{0{,}3} = 31750\ MPa$$

Crack energy ($G_{f)}$ of the steel fiber reinforced concrete, min 30 kg steel fiber/m^3, can conservatively be set equal to 1600 Nm/m^2.

3.3. Fracture energy of the concrete

Calculating the extent of the fracturing of the concrete is performed with FEM analyses, using a deformation softening concrete model. This means that the material's load bearing capacity decreases with increased deformation, causing

micro cracks to occur. This causes the tensile capacity to change with increased deformation. A so called ”smeared crack approach” has been used, which means that the cracks occur in the elements with a deformation equivalent with the strain in the fracture zone.
Concrete is a brittle material. The fracture energy of concrete is only about 120 Nm/m^2. When reinforced with 20 - 50 kg/m3 steel fibres, the flexural behaviour of the concrete improves and the fracture energy increases to at least 1600 Nm/m^2.
By plotting the tensile stress over the crack as a function of the crack width, the fracture energy can be determined as the area under the curve, see **figure 2**.

Various methods of determining the fracture energy of concrete are based on laboratory experiments. In this project, the fracture energy of steel fibre reinforced concrete has been estimated indirectly in a three-point bending test in accordance with RILEM TC-162 TDF. In this method a free supported beam (150*150*550 mm), which is sawn 25-30 mm and 2-3 mm wide on the lower edge, is loaded by a line load at the centre of the beam element. The extent of the displacement at the centre of the beam and the load are measured. The extension of the crack width can also be recorded. Photos of the experimental setup of the test performed at Lund Institute of Technology (LTH) are presented in **figure 3** and **figure 4**. The fracture energy has been conservatively estimated to be at least 1600 Nm/m^2.
In accordance with ”High Performance Concrete Structures, Design Handbook”, the fracture energy for concrete without steel fibre reinforcement is set equal to 120 Nm/m^2.

3.4. Strength and stiffness of the reinforcement

The quality of reinforcements must meet the requirements of strength class B500B.
The mean reinforcement yield strength, $f_{ym,}$ is set to 500 MPa.
The characteristic value of the reinforcement's yield strength, $f_{yk,}$ is set to 500 MPa.
The mean reinforcement modulus, $E_{m,}$ is set to 200 GPa.
The characteristic value of the reinforcement modulus of elasticity, $E_{k,}$ is set to 200 GPa.

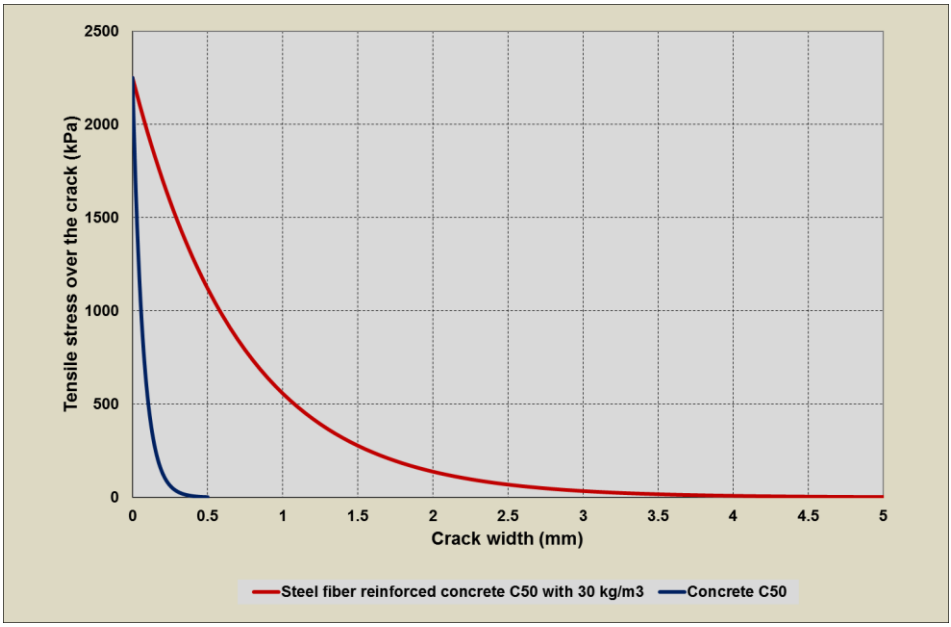

Figure 2. Fracture energy for concrete C50/60 with and without steel fibre reinforcements.

Figure 3. Three-point bending test in accordance with RILEM TC-152 TDF.

Figure 4. A crack occurs after load testing with a three-point bending test.

4. FEM analyses of the steel fibre reinforced bottom slab

4.1. Determination of the bending moment capacity

Calculation of the extent of the cracking of the concrete is performed using FEM analyses and using a deformation softening concrete model. This means that the material's load-bearing capacity decreases with increased deformation, which occurs due to micro-cracks. This means that the tensile strength capacity changes with increased deformation. A so called "Smeared crack approach" has been used, which means that cracks form in the elements as a result of deformation by a strain corresponding to the size of the crack width.
Concrete is a brittle material. The crack energy for concrete is only 120 Nm/m^2. With the addition of min 30 kg/m^3 steel fiber, flexural behavior of the concrete improves and the crack energy increases to at least 1600 Nm/m^2.
Validation of the deformation softening concrete model as implemented in the FEM program ZSOIL has been performed by comparing the expected behavior of the test load results from concrete beams tested using the four-point bending test at Lund Institute of Technology (LTH), see **figure 5**. The quality of the concrete meets the requirements of strength class C30 which has been verified with seismic tests measuring the resonance frequency, see **figure 6**.

The concrete beams were reinforced with min 30 kg/m^3 (characteristic value) steel fibers and had dimensions of 0,3 * 0,4 * 2,0 m. The bottom and top edges featured a longitudinal reinforcement of 3 Ø 12 mm and with a reinforcement quality of B500B. The concrete covering the reinforcement was 50 mm at the lower edge and 30 mm for the upper edge reinforcement.

Figure 5. Four point bending tests, deformation controlled, on steel fiber reinforced concrete beams.

Figure 6. The resonance frequency is determined with seismic measurements.

The result from the deformation driven load tests and comparison with predicted behavior with 2D FEM is reported in **Figure 7.** The bending moment that arises due to the deformation driven load test is reported as a function of the deflection at the beam centre. With 2D FEM, the test load curve has been predicted for both mean and characteristic values of the material properties.

It is clear from the comparison between test load results and performed FEM analyses with ZSOIL that the applied deformation softening concrete model can very accurately predict the behavior of the test loaded concrete beam. The predicted crack width is also in good agreement with test measurement results, see **Figure 8**.

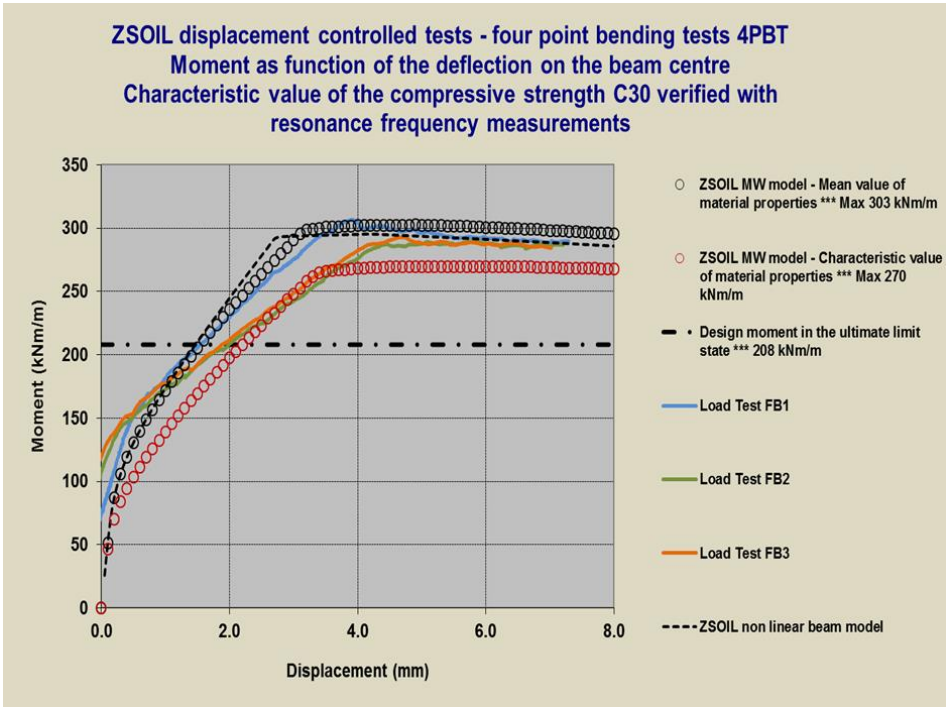

Figure 7. Comparison between predicted behavior with 2D FEM and load test results.

A so called "class A" prediction of the displacement controlled load tests has also been done by *Ekdahl Geo*, *Acerol Mittal* and *Professor Sven Thelandersson at LTH*. The predictions and the results from the displacement controlled load tests is shown in **figure 9**. The best prediction has been made by *Ekdahl Geo* using the finite element program ZSOIL and the non-linear material model Hoek-Brown (Menetrey-William) to model the steel finer reinforced concrete.
The load capacity of the base slab shall be verified in the ultimate limit state and it must be shown that the design load effect is less or equal to the design load capacity.
The performed FEM analysis of the base loading capacity in the ultimate limit state is shown in **figure 10**.
The coefficient of variation V_f is determined based on two separate non-linear analysis in which mean values and the characteristic values of material properties is used as input. These analyses gave the moment capacity R_m = 471 kNm/m and R_k = 433 kNm/m from which the coefficient of variation V_f was calculated as 8,7%.

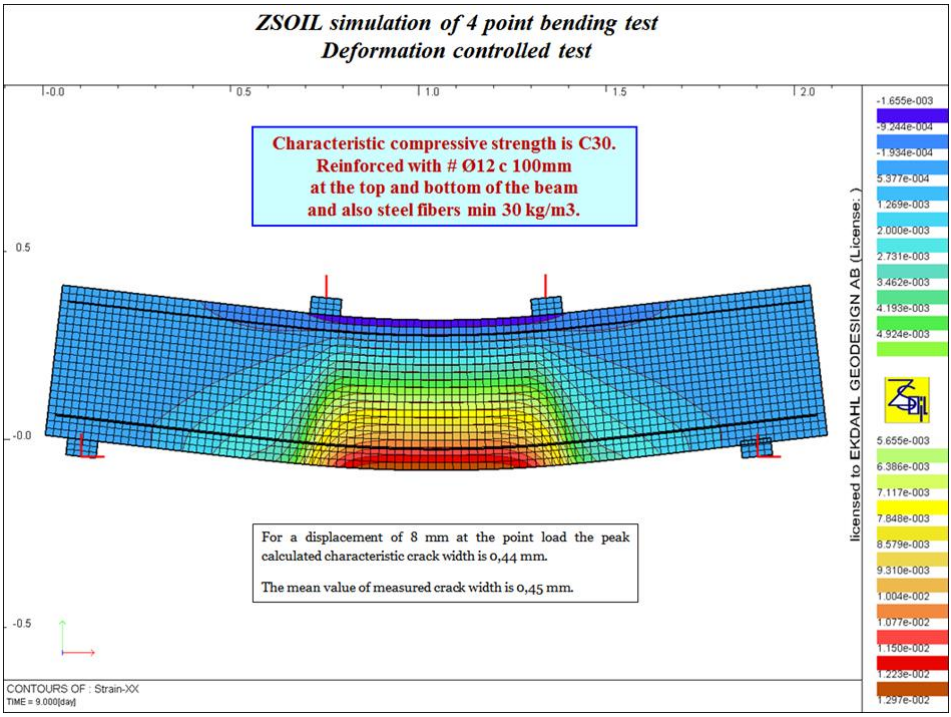

Figure 8. Comparison between predicted and measured crack width.

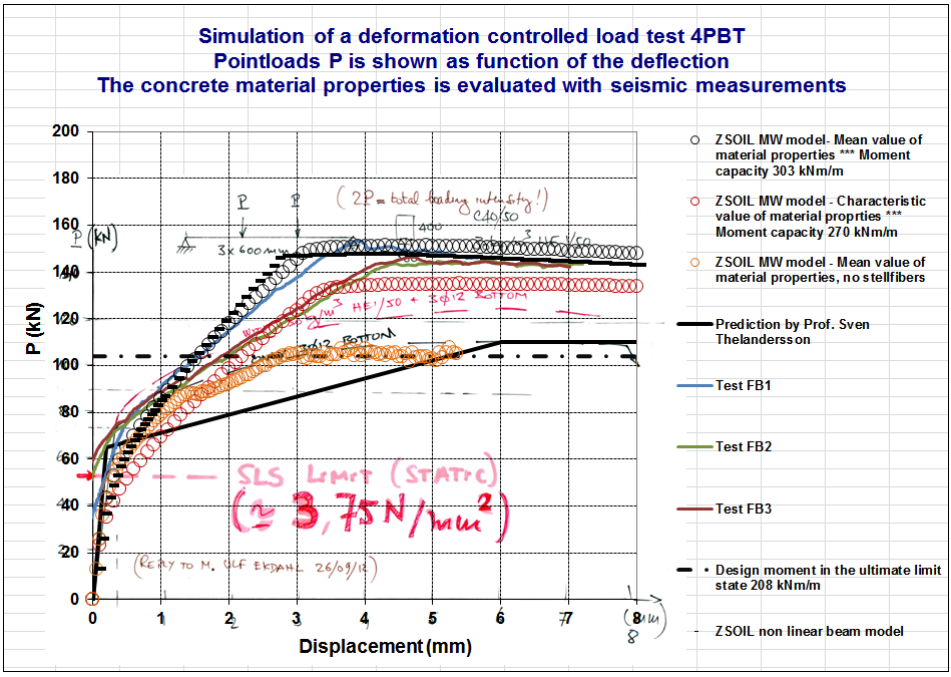

Figure 9. Class A predictions of the displacement controlled load test.

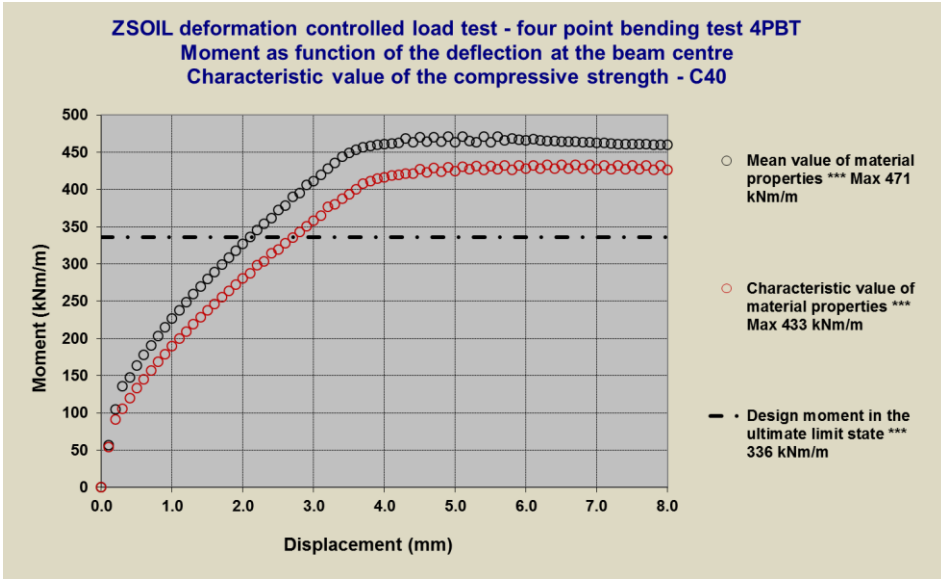

Figure 10. FEM calculated load test curve for both mean and characteristic values of material properties.

The global safety factor, including the effect of model uncertainty, is thereby according to Eurocode equal to 1.4. This means that the design moment capacity according to Eurocode is equal to 336 kNm/m.
In the serviceability limit state the maximum allowed characteristic crack width at the reinforcement level is 0,2 mm. Calculated bending moment as a function of characteristic crack width is reported in **figure 11**. Characteristic crack width at the design moment capacity of 336 kNm/m is 0,08 mm.

4.2. Calculation of the moment distribution in the bottom slab

Design load effect in the bottom slab is calculated by the company WSP using linear elastic shell elements connected to the foundation with a modular of subgrade reaction.
With 3D FEM and using nonlinear material properties of soil and rock, the maximum calculated moment in the bottom slab was calculated using both non-linear and linear material properties for the shell elements that model the concrete base. A c/c distance of 8 metres is assumed between the drilled shafts foundations. Ground water pressure against the bottom slab is determined by the secured overflow level.
Calculated moment distribution in the base slab for non-linear material properties is reported in **figure 12**. Maximum calculated moment, torque + bending moment is 175 kNm/m.

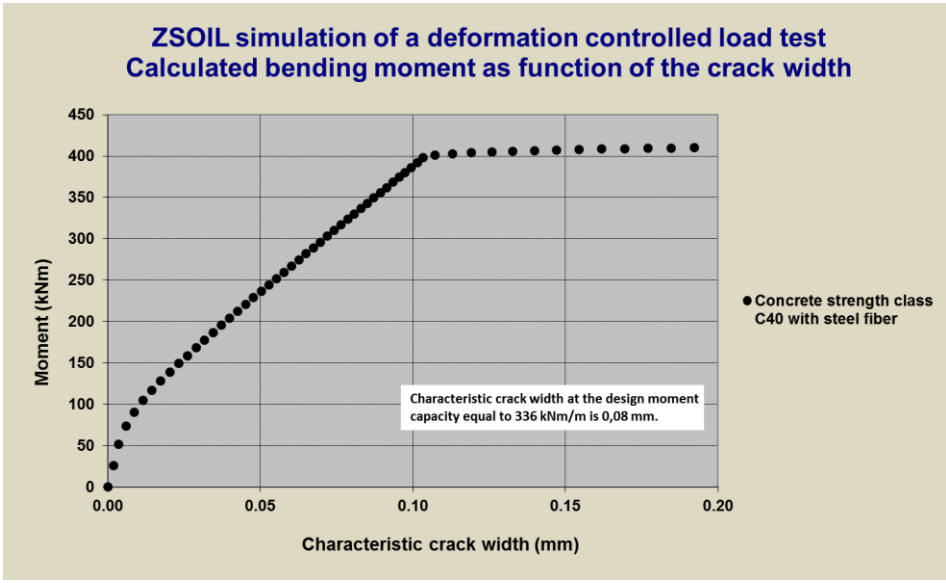

Figure 11. Bending moment as a function of the characteristic crack width.

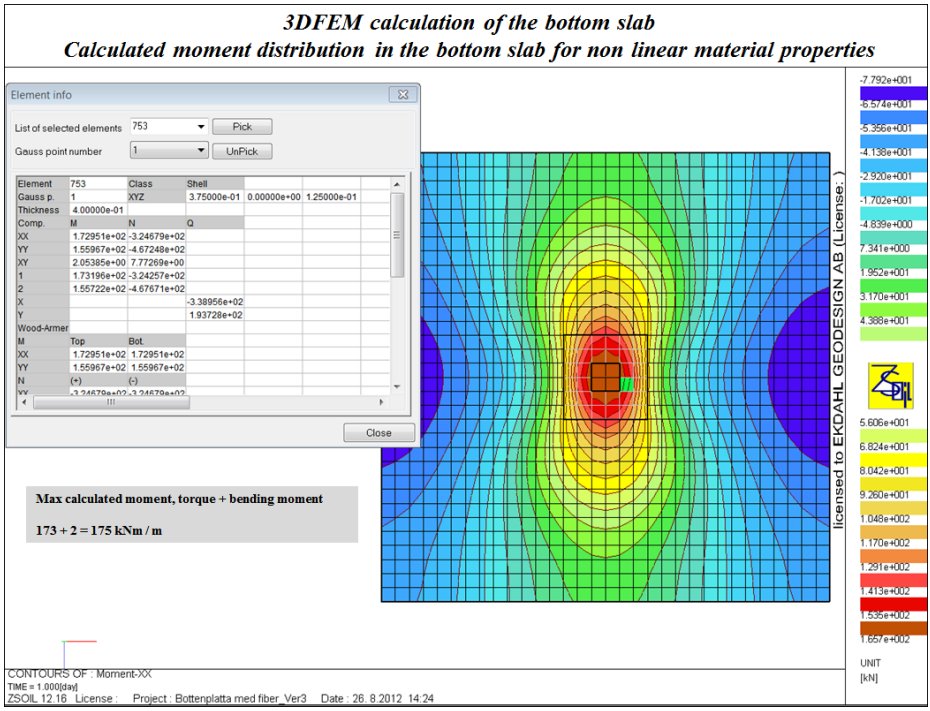

Figure 12. Calculated moment distribution using nonlinear material properties in the shell elements.

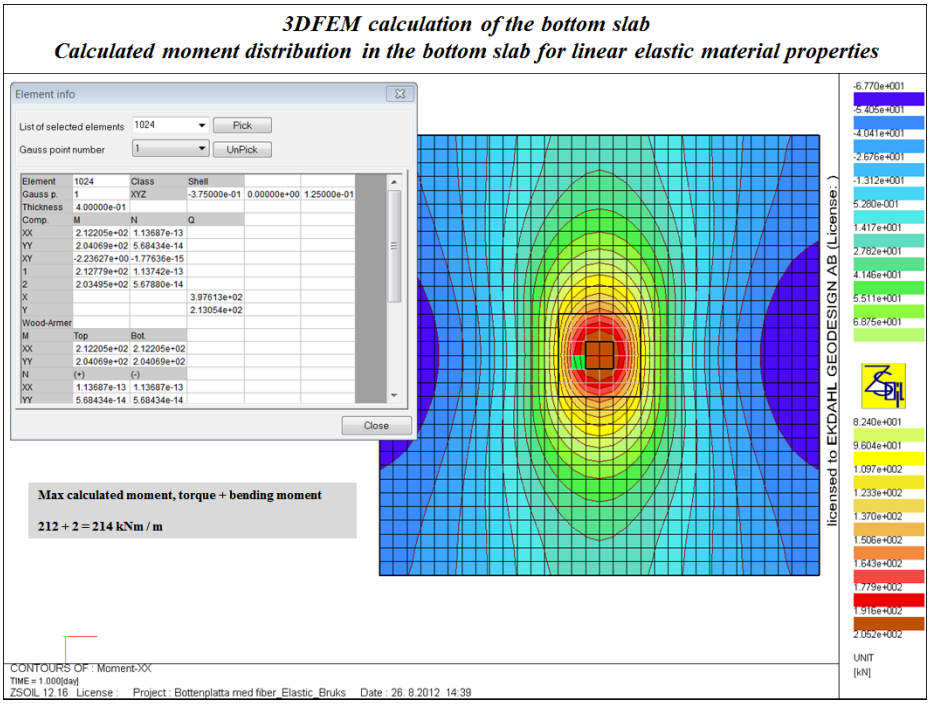

Figure 13. Calculated moment distribution using linear elastic material properties in the shell elements.

Calculated moment distribution in the base for linear elastic material properties is reported in **figure 13**. Maximum calculated moment, torque + bending moment is 214 kNm/m.
When modeling the base slab using linear elastic shell elements, maximum moment was overestimated by approximately 20% compared to when the concrete bottom slab has been modeled with nonlinear material properties.

4.3. Calculation of the moment in the bottom slab caused by uneven shrinkage

Moment due to differential shrinkage (M_{krymp}) can be calculated using the relationship

$$M_{krymp} = E_s A_s \cdot 0{,}9 \cdot d \cdot \varepsilon_{cs}$$

where $E_s = 200\,000$ MPa
$A_s = 2{,}011 * 10\text{-}6\ m^2/m$
$d = 0{,}35$ m
$\varepsilon_{cs} = 2{,}375 * 10^{-4}$

This means that bending moment due to uneven shrinkage is 30 kNm/m.
With regard to uneven shrinkage, the designed moment capacity must not exceed 336-30 = 306 kNm/m

4.4. Determination of equivalent modular of subgrade reaction

In the 3D FEM analyses of the buildings structure performed by the company WSP, there is a connection between the foundation and subgrade with linear elastic springs.
The stiffness of the springs between the bottom slab and subgrade is described by the so-called modular of subgrade reaction k, which is defined by the relationship

$$k = \frac{q}{s}$$

where

q = contact pressure between the base slab and the surged
s = the displacement of the base slab

The size of the equivalent modulus of subgrade reaction, which can be used in analyses taken into account the interaction between structure and subgrade, is determined using non-linear 3D FEM analysis based on the mean values of material properties for soil, rock and SFRC.
Calculation of equivalent modulus of subgrade reaction with 3D FEM simulations of the bottom slab and the drilled shafts in static interaction with the subgrade has been done using mean values of material properties.
The size of the modulus subgrade reaction distribution under the base can be evaluated as the calculated contact pressure divided by the calculated vertical displacement. Calculation of the modulus of subgrade reaction has been made for two extreme cases:

- Drilled shafts with diameter 1.0 metres and a maximum column load of 3600 kN in Safety Class 2 (SK2), see **figure 14**.
- Drilled shafts with diameter 1.5 metres and a maximum column load of 6100 kN in Safety Class 2 (SK2), see **figure 15**.

Performed non-linear 3D FEM analysis with ZSOIL shows that the modulus of subgrade reaction can with good approximation be set equal to 9.5 MN / m^3.

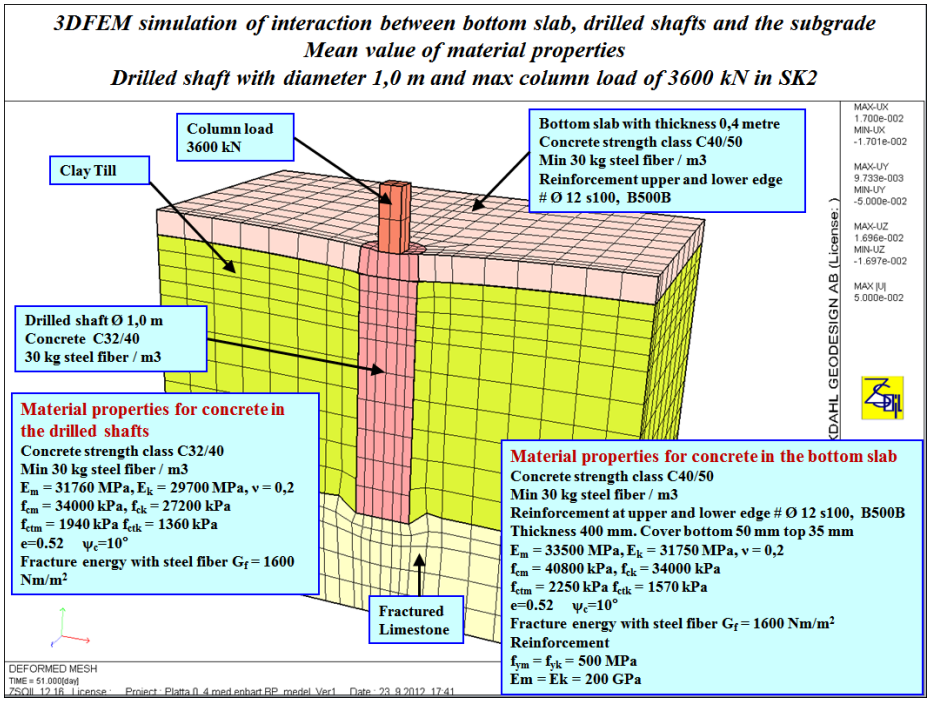

Figure 14. 3D FEM simulation of bottom slab and drilled shafts with diameter 1,0 m in static interaction with the subgrade.

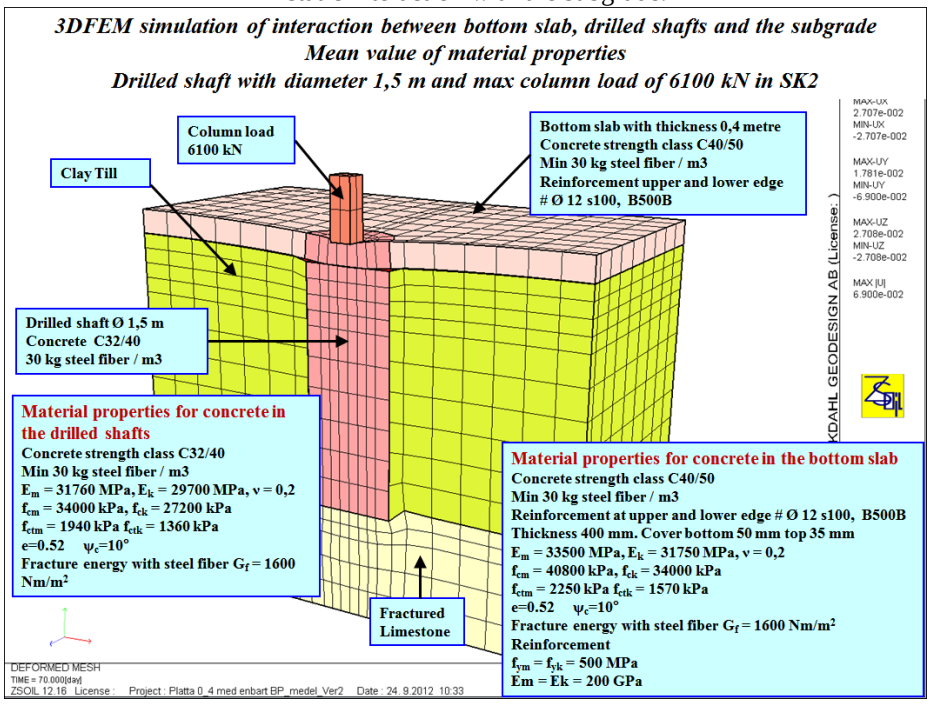

Figure 15. 3D FEM simulation of bottom slab and drilled shafts with diameter 1,5 m in static interaction with the subgrade.

5. Measurement of settlements during construction

During construction of the building settlement at one of the most loaded staircase where measured. The result of this levelling compared to calculated settlements with 3D FEM is reported in **figure 16**.
In the 3DFEM analyses of the frame of building the coupling between the foundation and the subgrade are done with linear elastic springs. The size of the spring stiffness and the modular of subgrade reaction are set by use of ZSOIL. Non-linear 3DFEM analyses are done using mean values of material properties.
Measured settlement at the staircase after the building construction is finished is 5,5 mm. The 3DFEM calculated characteristic settlement is 5,9 mm. It is clear that the performed analyses very accurately predict the behaviour of the foundation settlements.
It is clear that assumed evaluated geotechnical properties and the used ZSOIL 3DFEM model with consideration to interaction between the structure and the subgrade is verified.

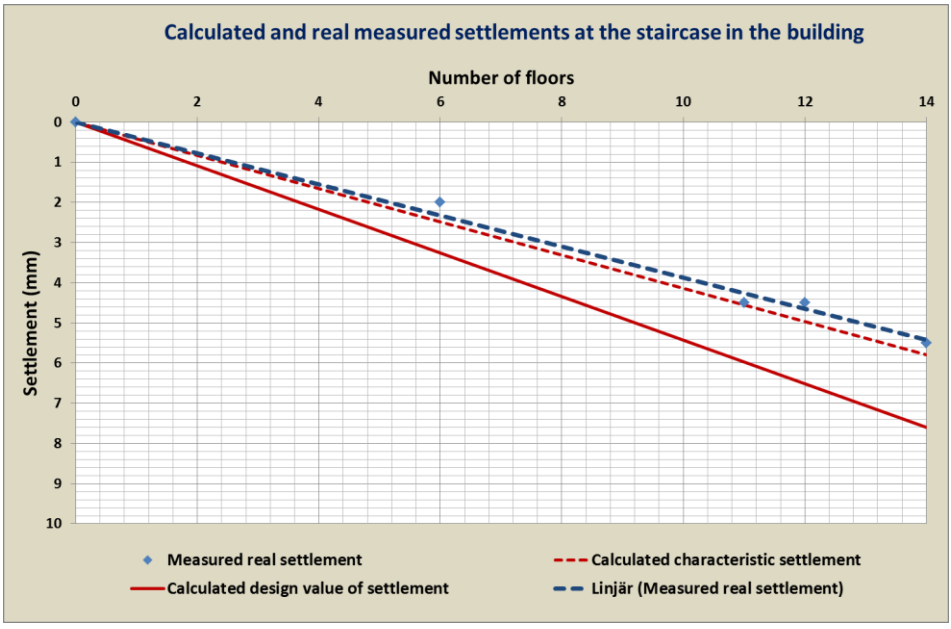

Figure 16. Measured and calculated characteristic and design value of settlement at the staircase in the building.

Non-Linear Force-Deflection Application on the Existing Underground Train Station of Berne

Christoph BERGER[a,1]
[a]*Emch+Berger AG Bern, Switzerland*

Keywords: non-linear bending-stiffness, settlement, existing structures, RC beam

Abstract
The project of the new underground station of Berne crosses the existing underground station with four new tunnels underneath. The excavation of these tunnels causes a settlement, which results in stressing the existing structure above additionally. As that structure is of great importance to the service of the main station and as that structure is relatively stiff and not completely ductile, an analysis of structural safety in function of the settlement is carried out. By the use of non-linear RC-beam-elements in ZSOIL, the structural safety margin in function of the settlement is assessed.

1. Introduction

The existing underground train station of Berne of the Regional Transport Bern-Solothurn (RBS) started its service in 1965, when the daily passengers numbered 16'000. Meanwhile, that number exceeded 60'000 by having an ongoing increase in demand [1]. A newly built underground station will accommodate the actual and future amount of passengers mainly due to longer platforms and more efficient passages to the platforms.
The new underground station includes new tunnels, which will cross the existing underground station underneath. The settlements by the excavation of these tunnels will stress the relatively stiff structure of the existing underground station to a critical situation. Moreover, the main tracks of the train station of Berne are directly above this structure and load it heavily. The key question relies on how much of a settlement can be accepted in order to avoid the risk of structural failure. Additionally to the life put in danger, a structural failure would disturb the service of the main tracks severely, as the main tracks are operated close to its maximum capacity. There are no main tracks to spare.
As for the given risk, the hereby presented structural analysis offers the required tool to define a maximum allowable settlement. Since the internal forces in the existing structure are plotted by the amount of settlement, the margin of

[1] Corresponding Author, email address: christoph.berger@emchberger.ch.

structural safety can be seen for different predictions of settlement and live at construction phase while measuring the actual values of settlement.

2. Problem

2.1 Project of the new underground train station

The existing underground station of Berne is used for the suburban trains by the Regional Transport Bern-Solothurn (RBS). The capacity for daily passengers of that station is going to be insufficient in the near future. Hence, a new underground station is projected. The new underground station will be built underneath the existing underground station and underneath the main station of Berne by the Swiss Federal Railways (SBB). The existing underground station will be specifically crossed below by the four connecting tunnels for the new underground station (Fig. 1). Because of the alignment of the new underground station, the connecting tunnels are approximately perpendicular to the alignment of the existing underground station.

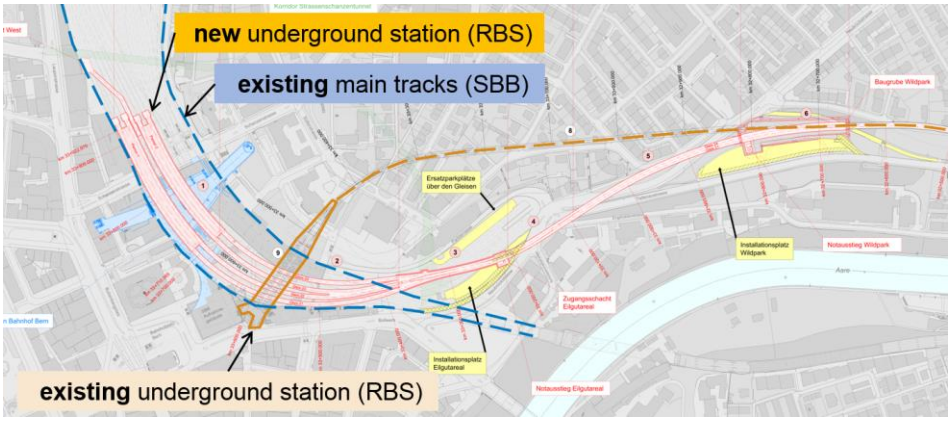

Figure 1. General plan of the new underground train station (RBS) underneath both the existing underground station (RBS) and the main station (SBB).

Considering the different layers of railway services, Fig. 2 clarifies the order. The four connecting tunnels for the new underground station cross below the whole existing structure. The existing underground station is the intermediate layer and directly covered by the tracks and platforms of the existing main station.

Even tough, the new underground station will be located deeply under the main station (difference in track levels of 23.5 m), it is not the cases for the existing underground station. The remaining rock between the foundations of the pillars for the existing underground station and the upper edge of the new tunnels measures 6.9 m (Fig. 2).

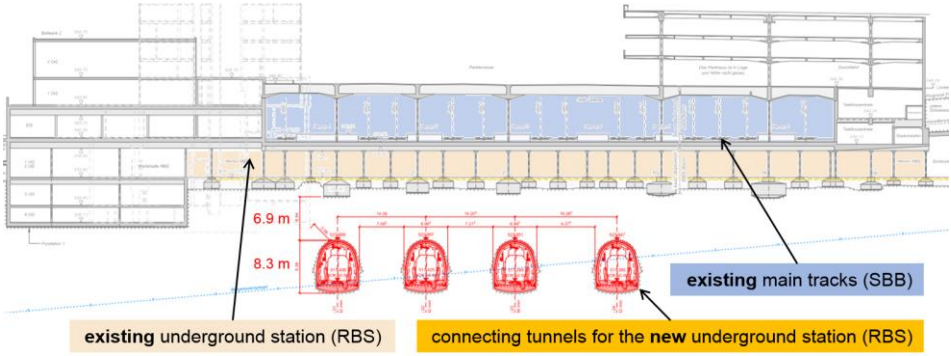

Figure 2. Cross-section of the four connecting tunnels for the new underground station. The existing underground station is located above these tunnels and directly covered by the tracks and platforms of the main station.

2.2 Settlements by new tunnels

The settlement troughs caused by the connecting tunnels stress the existing structure above. Therefore, special investigations on that topic [2] have outlined the variety of possible settlement troughs. Although the analysis was done by the use of ZSOIL, this analysis is not object of the present documentation. The four connecting tunnels including different excavation steps create more than 20 different settlement troughs. The maximum settlement for most-likely geological input values sets at roughly 8 mm. The locations of the settlement-peaks relative to the foundations of the existing underground station and the number of different settlement troughs generate a broad possibility of stressing the existing structure. The difficulties to detect the most stressing situation for the existing structure are obvious.

Since the existing underground station is not stressed by the maximum settlement but by the maximum differential settlement between two pillars of the structure, the various settlement troughs (> 20) are filtered by that latter aspect. Among the various settlement troughs, the one having the steepest slope is chosen as the critical situation for the structure above. In Fig. 3, this method is indicated by the point of inflection at the steepest slope. In order to cover the most critical situation of the structure above, the steepest slope is assumed to be constant for the span between two pillars. The resulting differential settlement for a span of 5.7 m values 3.3 mm.

In addition to the above mentioned definition of the critical differential settlement, a set of likely geological parameters was created. This set generated in [2] most-likely, possible and unlikely values of the differential settlement.

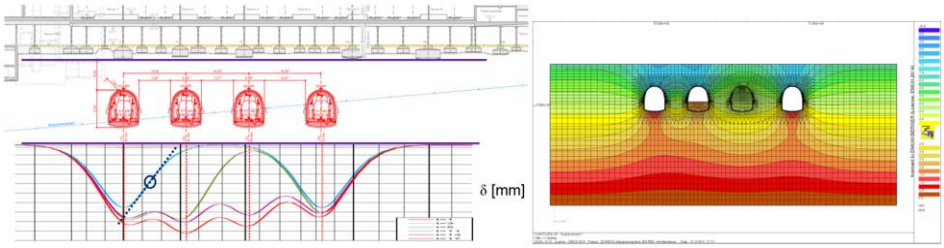

Figure 3. Settlements by the excavation for the four connecting tunnels. The different excavation steps generate a broad variety of settlement troughs. (For a better clarity, the picture shows only four excavation steps with the respective settlement trough).

3. Existing structure

3.1 The underground station in general

The existing underground station as well as the roof structure of the hall for the main tracks were built in the 1960s. That construction was done by ongoing service of the already existing main tracks. Only two to three tracks were temporarily closed at a time while a part of the existing underground station was built. As you can see in the middle picture of Fig. 4, the existing underground structure was built by cut-and-cover. The structure of the existing underground station consists in reinforced concrete. The slab itself is a strongly orthotropic structure as it shows two main beams over the two rows of pillars and an arched slab in cross-sectional direction. The arched slab and the continuous beams form a continuous RC-element as the concrete was poured into a single mould. Each construction stage forms one RC-element. These elements, including the arched slab, are connected by Gerber joints. In the present paper, the focus relies on the structural analysis in longitudinal direction. The two main beams over the pillars are analysed.

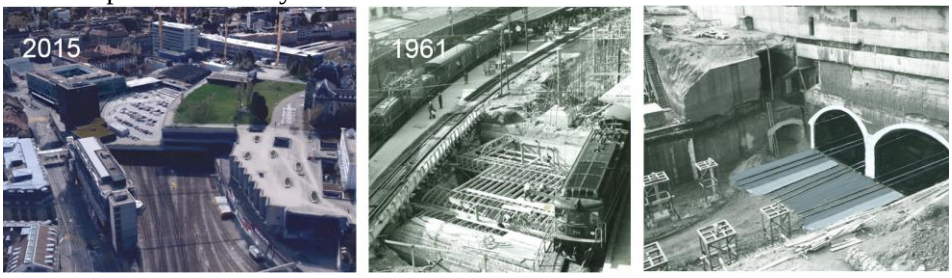

Figure 4. Left: The roof structure of the hall for the main tracks in present time. Middle and Right: The construction site in 1961 of the existing underground station by cut-and-cover. The construction stages allow an ongoing use of the main tracks above.

3.2 The main beam of the existing underground station

The two main beams in longitudinal direction are composed by continuous beams linked by Gerber joints. Each beam corresponds to a construction stage for the ongoing service of the main tracks above while constructing. Such a continuous beam covers three to four spans between pillars. The length of the analysed continuous beam sets at 14 m while having a height of 1.27 m. That height includes the arched slab, which has a minimal thickness of 0.52 m. (Fig. 5). Many of the longitudinal rebars switch layers between top and bottom in order to offer better resistance against shear and flexure.

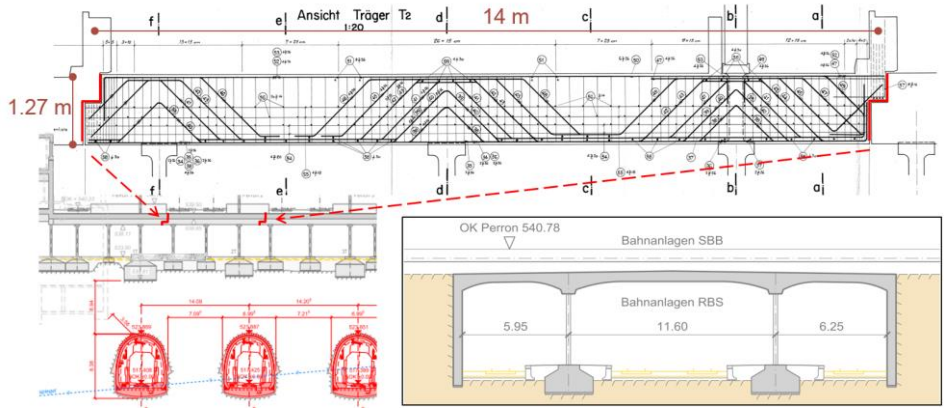

Figure 5. The two main beams are composed by continuous beams linked by Gerber joints. The arched slab and the continuous beams form continuous RC-elements as the concrete was poured into single moulds.

The continuous beams are strongly reinforced by rebars. 32 longitudinal rebars of 26 mm diameter are outlined in the upper part of the cross-section (Fig. 6). The steel is of high quality for that time and yields at 360 MPa. Two sets of stirrups of 14 mm diameter are put in dense spacing (150 mm, zones A and C in Fig. 7) close to the pillars and lose spacing (250 mm, zone B in Fig. 7) in mid-span. Thus, the structural design of this continuous beam is very sound and solid.

4. Structural behaviour

The differential settlement between two pillars stresses the continuous beam additionally. A constant shear force builds up along a span due to the implied deformation by the settlement (Fig. 7). An additional flexure is caused as well, but it can be accepted as the sound structural design allows plastic hinges at the beam. The influence of the of the bending moment relies on the bending stiffness and on the shear resistance according to the crack opening.

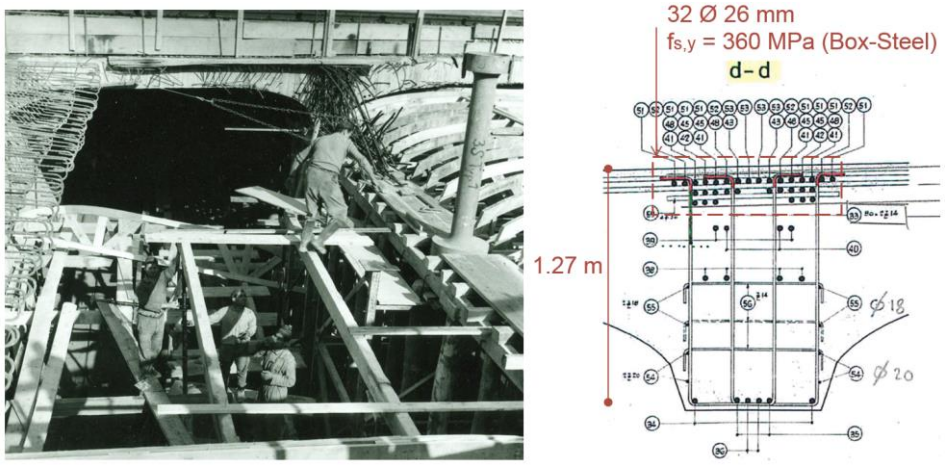

Figure 6. Left: Construction of the main beams and arched slab at once. Right: Cross-section of the main beam over a pillar.

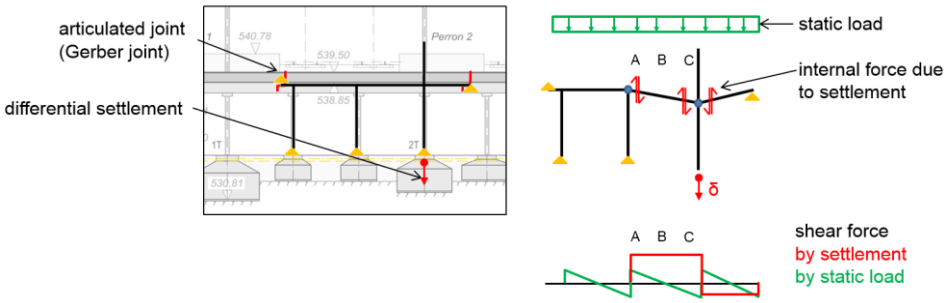

Figure 7. A continuous beam is subject to differential settlement. Shear force by settlement builds up additionally to the shear force by static load. The total shear force is increased heavily in zone A in opposite to zone C, where the two sources of shear force counterbalance each other.

The initial design is made to cover the internal forces only due to static load. Therefore, the key questions results in whether the existing resistance is solid enough to cover the additional shear force by settlement as well. This questions can be expressed by a global equation such as (1).

$$V_{Ed}(static\ load) + V_{Ed}(settlement\ \delta) \le V_{Rd}(settlement\ \delta) \qquad (1)$$

Considering the continuous beam subject to an additional constant shear force, there are different zones at the beam, named A, B and C. In these zones (Fig. 7), the addition of shear force by static load and shear force by settlement can either cumulate (zone A) or counterbalance each other (zone C). Therefore zone A is more critical than zone C. In zone B, there is basically only shear force by settlement. The total shear force in zone B is smaller than in zone A. But since the resistance in zone B is smaller than in zone A, it cannot be decided, whether

the structural safety of one or the other zone is more critical. Both zones must be analysed.

The additional shear force by settlement depends strongly on the bending stiffness of the continuous beam as the deformation is ensured by flexing the beam. Regarding to a realistic result, which cannot be too conservative for the given resistance, a non-linear structural analysis of the RC-beam must be carried out. This is the object of the present ZSOIL application.

5. Numerical model

The continuous beam is analysed by a beam in ZSOIL. Specifically, the tool of "reinforcement set for beam" is applied. (Fig. 8). There are two important cross-sections, which both represent a plastic hinge. They differ in positive and negative bending. The rebars are entered in the tool-box according to their quantity, diameter and location in height. The model is chosen to be of elastic-perfectly plastic behaviour. The yield stress for the steel is set at 360 MPa and the elastic stiffness according to a Young's modulus of 205'000 MPa. The concrete yields at 30 MPa of compression and has a cut-off value at 0 MPa of tension. The Young's modulus is put to 34'000 MPa. A check of plausibility of the non-linear bending stiffness show consistent results between ZSOIL and a structural analysis software for RC-cross-sections (Fig. 8, right graphs). For the given tension cut-off value of 0 MPa, there is no initial bending stiffness for uncracked cross-sections in the ZSOIL results. A tension stiffening for the bending stiffness is by the present application not modeled, which is in this case on the unsafe side.

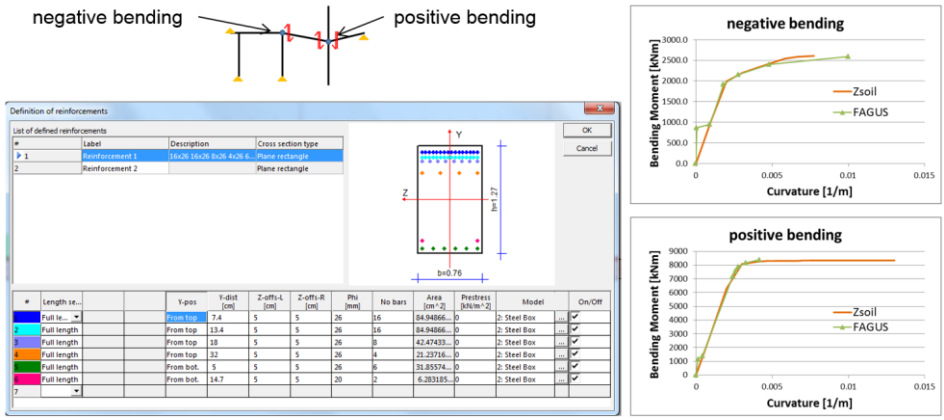

Figure 8. The ZSOIL tool of "reinforcement set for beam" is applied at the structural analysis. Right graphs: The bending stiffness is plotted by ZSOIL and by a structural analysis software for RC-cross-sections.

The continuous beam is only partly modeled in this ZSOIL application: The modeled beam starts at the second pillar from the left and then goes on for the two spans. There is a rigid restraint at the left end in order to ensure a plastic

hinge of negative bending at that end. The right end is a rotatable fixation as it represents the Gerber joint. The intermediate pillar is modeled by the implied vertical displacement as a boundary condition (Fig. 9). The beam is then analysed for differents steps of displacement until plastic hinges occur for negative and positive bending. The occurrence of both plastic hinges presents the maximum of additional shear force by settlement.

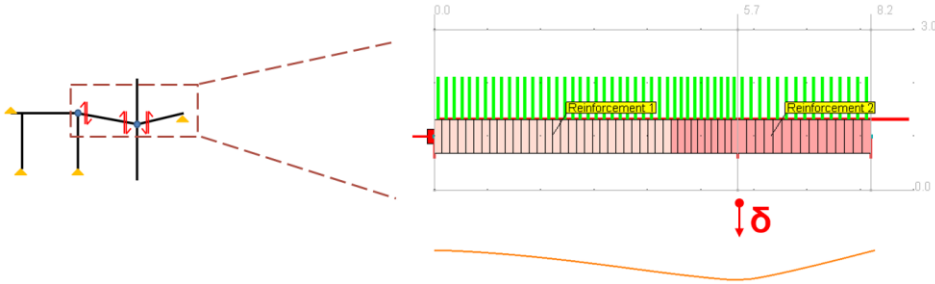

Figure 9. Only parts of the continuous beam are modelled in this ZSOIL application. The settlement is implied by boundary conditions.

6. Results

The resulting internal forces can be seen in Fig. 10 and Fig. 11. At small imposed displacement (< 7 mm), both cross-sections remain in the elastic domain of the rebars. Consequently, they are relatively stiff and cause a big increase of the shear force by settlement. By further displacement, first rebars start to yield and the stiffness decreases. The shear force by settlement increases less strongly. The first plastic hinge appears for a displacement of about 10 mm. It is the positive plastic hinge, which appears first. Finally, the second plastic hinge (negative) forms at a displacement of 30 mm.

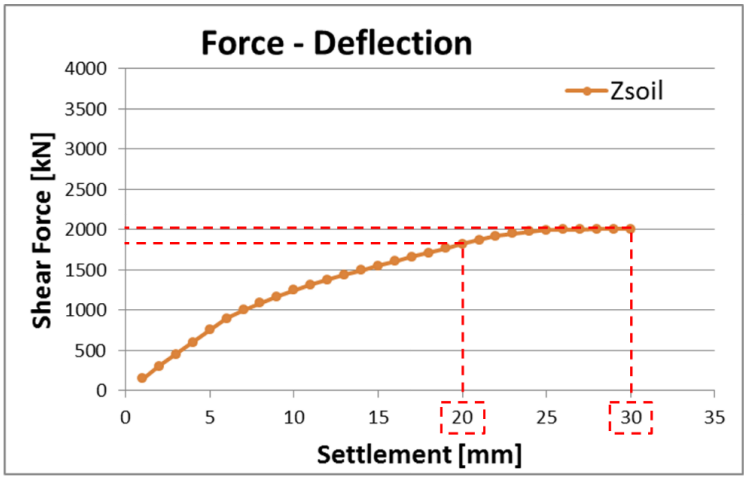

Figure 10. The shear force by settlement. Two points are outlined: A displacement of 20 mm causes a shear force of 1’818 kN and 2’004 kN at 30 mm.

The shear force in the left part of the beam corresponds to the shear force of interest. It goes to a maximum value of 2'004 kN at a displacement of 30 mm. The right part of the beam does not increase significantly after the formation of the positive plastic hinge.

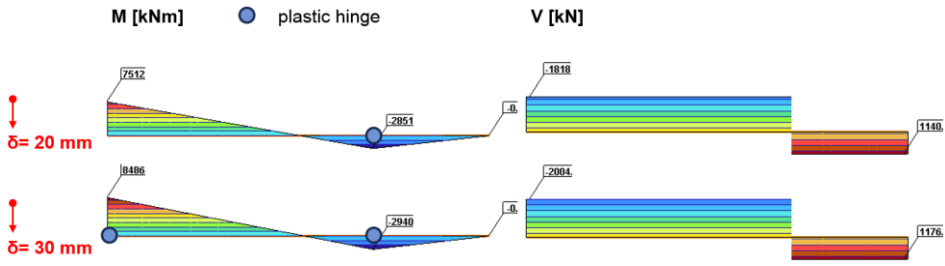

Figure 11. Resulting internal forces for the continuous beam. The second plastic hinge forms at a total displacement of 30 mm.

7. Structural analysis

Given the results by this ZSOIL application, the continuous beam can be analysed structurally. The additional shear force by settlement is overlaid to the shear force by static load. The total shear force in the continuous beam depending on the differential settlement can be seen in Fig. 12. The shear resistance is given in the same graphs as well. Considering the shear resistance at level III of the fib Model Code [3], the resistance reduces by crack opening respectively by settlement. The static load is presented in dead load with traffic load or only dead load. This allows to evaluate the gain of structural safety at worst case scenarios, when the main tracks above the structure must be closed because of unforeseen settlements.

Zone A shows high values of internal force and resistance. A critical situation appears for a differential settlement of approximately 20 mm. At that point, the total shear force reaches the shear resistance. Zone B on the other hand, is stressed less but also offers less resistance. It results that zone B is more critical than zone A, as the critical situation is reached at a differential displacement of approximately 15 mm. Zone B at mid-span is obviously less resistant to shear force than zone A close to the support of the beam. But the additional shear force by settlement is of the same value for both zones.

The dotted black line in Fig. 12 indicates the results for a linear structural analysis. The total shear force would reach the resistance for smaller differential settlements (~10 mm). Hence, a linear analysis would overrate the danger for structural safety by settlement. Even though this would be on the safe side, it would not result in satisfactory results as the subject is about existing structures.

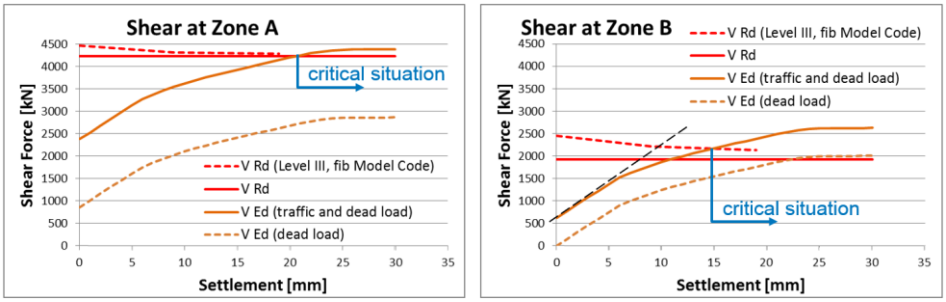

Figure 12. Structural analysis for zone A and B. The total shear force and the shear resistance are plotted in function of the differential settlement.

8. Conclusion

The structural safety margin in function of the settlement can be assessed with the above described approach. The structural safety depends on the additional stressing of the two main beams. The main beam is subject to a constant additional shear force by settlement. As the beam presents different zones with different values of resistance and different values of total shear force, it results that the most critical zone is at mid-span. For that zone, the resistance is relatively small, but the additional shear force by settlement is as big as near the supports of the beam. Finally, the use of non-linear RC-beam-elements allows to detect a realistic safety margin, as it implies a realistic bending-stiffness. A linear structural analysis would overrate the internal forces by a unrealistic bending-stiffness.

References

[1] Zukunft Bahnhof Bern, leaflet May 2015, www.zukunftbahnhofbern.ch

[2] Ausbau Bahnhof Bern RBS, Bahnhofeinfahrt Statische Berechnungen Regelquerschnitt Einspurtunnel, PLANERGEMEINSCHAFT RBS$^{\text{verbindet}}$, 19.01.2015

[3] fib Model Code for Concrete Structures 2010